UNIVERSIDAD COMPLUTENSE DE MADRID
FACULTAD DE CIENCIAS QUÍMICAS

TESIS DOCTORAL

Estructura molecular y hábitos cristalinos en interfases sólidas complejas: Un estudio por simulación molecular

MEMORIA PARA OPTAR AL GRADO DE DOCTOR

PRESENTADA POR

Pablo Llombart González

Directores

Eva González Noya Luis

González MacDowel

Madrid

Universidad Complutense de Madrid
Facultad de Ciencias Químicas

Departamento de Química Física I

Estructura molecular y hábitos cristalinos en interfases sólidas complejas:

Un estudio por simulación molecular

Memoria para optar
al grado de Doctor realizada por

Pablo Llombart González

Directores:
Dr. Eva González Noya
Dr. Luis González MacDowell

Madrid, 2019

UNIVERSIDAD COMPLUTENSE MADRID

DECLARACIÓN DE AUTORÍA Y ORIGINALIDAD DE LA TESIS PRESENTADA PARA OBTENER EL TÍTULO DE DOCTOR

D./Dña. Pablo Llombart González,
estudiante en el Programa de Doctorado Química Teórica y Modelización Computacional,
de la Facultad de Ciencias Químicas de la Universidad Complutense de Madrid, como autor/a de la tesis presentada para la obtención del título de Doctor y titulada:

ESTRUCTURA MOLECULAR Y HÁBITOS CRISTALINOS EN INTERFASES SÓLIDAS COMPLEJAS: UN ESTUDIO POR SIMULACIÓN MOLECULAR.

y dirigida por: Dr. Eva González Noya y Dr. Luis González MacDowell

DECLARO QUE:

La tesis es una obra original que no infringe los derechos de propiedad intelectual ni los derechos de propiedad industrial u otros, de acuerdo con el ordenamiento jurídico vigente, en particular, la Ley de Propiedad Intelectual (R.D. legislativo 1/1996, de 12 de abril, por el que se aprueba el texto refundido de la Ley de Propiedad Intelectual, modificado por la Ley 2/2019, de 1 de marzo, regularizando, aclarando y armonizando las disposiciones legales vigentes sobre la materia), en particular, las disposiciones referidas al derecho de cita.

Del mismo modo, asumo frente a la Universidad cualquier responsabilidad que pudiera derivarse de la autoría o falta de originalidad del contenido de la tesis presentada de conformidad con el ordenamiento jurídico vigente.

En Madrid, a 2 de septiembre de 2019

Fdo.: 

Esta DECLARACIÓN DE AUTORÍA Y ORIGINALIDAD debe ser insertada en la primera página de la tesis presentada para la obtención del título de Doctor.

Agradecimientos

Llegados a este punto y después de muchas alegrías y alguna que otra tristeza, es uno de los momentos en los que merece la pena pararse a echar un vistazo y recordar que esto no sería posible sin la ayuda de muchas personas.

En primer lugar, quiero agradecer a Alfonso Mateos Antón, antiguo profesor de Formación Profesional del I.E.S Lope de Vega, ya que nunca olvidaré la motivación para acudir a la facultad y adquirir la formación académica mas elevada.

A continuación quiero agradecer a dos de las mejores personas que he conocido y con las que he tenido la oportunidad de trabajar en estos años. Esas dos personas no podrián ser otras que mi director y directora de tesis, Luis y Eva.

A Luis tuve el placer de conocerle en mi primer año en la facultad. Pude tenerle como profesor en las asignaturas de Química Física I y II. La manera de impartir las clases y su forma de ver la ciencia hizo que me decantase por continuar con el trabajo fin de grado bajo su dirección, el trabajo fin de master y actualmente esta tesis. Gracias por la paciencia y la confianza depositada en mí durante estos años La crisis económica ha hecho que hayan sido unos años difíciles. No obstante, no tienen precio las discusiones científicas y personales que me han permitido finalizar con éxito esta tesis doctoral. De verdad, muchas gracias.

En relacion a Eva, la conocí por primera vez en un viaje a los famosos Workshops de Baiona. Tuve el placer de compartir el viaje de ida en coche y desde entonces me fascinó como científica, pero sobre todo como persona. Por supuesto, que decir de la confianza que depositaste para colaborar en el proyecto de nucleación. Es un proyecto es fascinante y ha hecho que durante este último año haya sido mas reconfortable finalizar la tesis. No tengo palabras para agradecer esta confianza, solo espero Eva que sepas que siempre podrás contar conmigo para lo que necesites. Sinceramente, muchas gracias.

Ahora quiero hacer un paréntesis para agredecer a los compañeros del Roca, Enrique y Antonio. A Enrique, aunque no has sido mi director, me has ayudado siempre de la misma forma cuando lo he necesitado. Que decir de Antonio, un experto informático y sobre todo magnífica persona. Además, no me olvidaré de los buenos ratos pasados con otros compañeros que también han pasado por el Roca durante mi estancia: Ariel, Itziar, Guillermo y Leandro. Gracias por siempre empezar el dia con unas buenas risas.

Es necesario en este punto realizar una mención muy especial para Guille y Andrés. Ambos son excelentes científicos y brillantes personas. Agradecerles su motivacion y he tenido la fortuna de poder trabajar con ellos, sobre todo mano a mano con Guille.

Por supuesto a los compañeros de la facultad Fer, Josue y Alejandro. Hemos pasado buenos ratos durante estos ultimos años compartiendo penas y alegrías. Otros dos grandes compañeros del

departamento han sido Jorge Reñe y Edu. No olvidaré esas enormes tertulias, siempre construyendo y empleando el humor como base de la pirámide. Mac, simplemente eres el mas grande y de las mejores personas que he conocido. Para JL, muchas gracias por esas charlas debatiendo sobre el agua y sobre GROMACS. Creo que mis directores coincidirán en el punto de que tu soporte ha sido incalculable. Que decir también de Jorge Benet, no coincidimos mucho en el tiempo pero los primeros tutoriales fueron de tu parte.

A continuación quiero agradecer a mi grupo de amigos (Miguel, Cristian, Juli etc. no puedo poner a todos) porque en parte, ellos también tienen la culpa de que ustedes hoy puedan estar leyendo estos agradecimientos.

A toda la familia, quiero que sepan que han sido un gran apoyo durante todos estos años. Mi madre, Pilar, y mi tia, Ángela, son las dos personas a las que les debo absolutamente todo. Son las personas que me han cuidado y educado. Mi padre Manuel desgradiadamente no llegará a leer nunca estos agradecimientos pero afortunadamente si pudo escucharlos.

Este último agradecimiento, y el más importante de todos ya que sin ella jamas se hubiesen escrito estos párrafos, lo he querido reservar para Arancha. Nos conocimos en el instituto y llevamos juntos desde entonces. Has estado siempre y me has dado todo el apoyo que he necesitado en situaciones que han sido muy difíciles. Eres la mejor persona que he conocido. Muchas gracias y TE QUIERO. Por supuesto no me olvido de tus padres Manuel y Ana, ni de tu hermana Ana y Carlos. Gracias.

De nuevo, para todos las más sinceras gracias, y sí deciden seguir leyendo este documento, recuerden que es por iniciativa propia y nadie les ha obligado a ello. Para quién me conoce, después de un momento tan emotivo (reconozco que alguna lagrimita se ha derramado mientras perpetuaba estas frases) no me podía despedir sin una broma. Un abrazo.

Los resultados de esta tesis han dado lugar a las siguientes publicaciones:

1. Capítulo 1: "Structure and water attachment rates of ice in the atmosphere: role of nitrogen", Pablo Llombart, Ramón M. Bergua, Eva G. Noya and Luis G. MacDowell. En revisión en PCCP

2. Capítulo 2: "Premelting-Induced Smoothening of the Ice-Vapor Interface", Jorge Benet, Pablo Llombart, Eduardo Sanz and Luis G. MacDowell, PRL, **117**, 96101 (2016)

3. Capítulo 3: "Surface phase transitions and the growth habits of snow crystals in the atmosphere", Pablo Llombart, Eva G. Noya and Luis G. MacDowell. En revisión en Science Advances

4. Capítulo 4: Rounded layering transitions on the surface of ice". Pablo Llombart, Eva G. Noya and Luis G. MacDowell. En preparacion

5. Capítulo 5: "Structural transitions and bilayer formation of CTAB aggregates", Pablo Llombart, Mauricio Alcolea Palafox, Luis G. MacDowell and Eva G. Noya, Colloids and Surfaces A, **580**, 123730 (2019)

6. Capítulo 6:

   (a) "Femtosecond laser reshaping yields gold nanorods with ultranarrow surface plasmon resonances", Guillermo González Rubio, Pablo Díaz Núñez, Antonio Rivera, Alejandro Prada, Gloria Tardajos, Jesús González Izquierdo, Luis Bañares, Pablo Llombart, Luis G. MacDowell, Mauricio Alcolea Palafox, Luis M. Liz Marzán, Ovidio Peña-Rodríguez, and Andrés Guerrero-Martínez, Science, **358**, 6363 (2017)

   (b) "Disconnecting Symmetry Breaking from Seeded Growth for the Reproducible Synthesis of High Quality Gold Nanorods"Guillermo González Rubio, Vished Kumar, Pablo Llombart, Pablo Díaz Núñez, Eva Bladt, Thomas Altantzis, Sara Bals, Ovidio Peña Rodríguez, Eva G. Noya, Luis G. MacDowell, Andrés Guerrero Martínez and Luis M. Liz Marzán. ACS Nano, **13**, 4424–4435 (2019)

Otras publicaciones no incluidas en esta tesis:

1. "Nanocapillarity and Liquid Bridge-Mediated Force between Colloidal Nanoparticles", Luis G. MacDowell, Pablo Llombart, Jorge Benet, Jose G. Palanco and Andrés Guerrero Martinez, ACS Omega, **3**, 1 (2018)

2. "Nucleation of pseudo hard-spheres and dumbbells at moderate metastability: appearance of A15 FrankKasper phase at intermediate elongations", Itziar Zubieta, Miguel Vázquez del Saz, Pablo Llombart, Carlos Vega and Eva G. Noya, PCCP, **21**, 4 (2019)

3. "Structure and fluctuations of the premelted liquid film of ice at the triple point", Jorge Benet, Pablo Llombart, Eduardo Sanz and Luis G. MacDowell, Mol Phys, Liblice 2018 Special Issue. doi: https://doi.org/10.1080/00268976.2019.1583388

4. "Water droplets on ice", David Sibley, Pablo Llombart, Eva G. Noya, Andrew Archer and Luis G. MacDowell. En preparación

ÍNDICE

Summary

Introduction

In this project that has given shape to my doctoral thesis, we have studied the habits of crystalline growth from the structural point of the ice–vapor interface and the gold–CTAB–water interface. From the experimental point of view, it can be very complicated to measure and interpret crystalline growth habits in complex solid interfaces.[1, 2, 3] By means of molecular simulation we have approached the study of the structure on the ice surface in coexistence with a thin water layer premelted on the surface of the crystal, where the thickness of the liquid evolves with temperature. The premelting film may be characterized in terms of two fluctuating solid-liquid and liquid-vapor interfaces. The correlated fluctuations may be studied using a model of interfacial Hamiltonians coupled by the interface potential. [4, 5, 6] This potential accounts for the equilibrium film thickness and greatly determines the properties of the interface.

On the other hand, depending on the structure of the solid surface, the temperature will cause disorder in the different surfaces and it happens that the properties can vary anisotropically depending on the ice surface we are studying. An example of anisotropy is the interfacial stiffness of an ice surface oriented in the basal face and in the prismatic primary face. The temperature produces disorder on the surface of the ice on both faces, being slightly higher on the latter and the solid surface presents capillary waves whose amplitude can diverge when the temperature approaches the triple point. This is the definition of a rough surface. In rough surfaces the amplitude of height fluctuations of small wavevector diverge. At the roughening transitions and below, the fluctuations remain finite at all wavelengths [7, 8, 9, 10]

The roughness transitions involve changes in the island formation the surface. When the surface is rough it is not necessary to form an island shaped nucleus and therefore it is not necessary to overcome the nucleation barrier of the islands. Due to this phenomenon the crystalline surface grows rapidly and is linear in the saturation.

On the ice surface the fusion of the most external planes takes place giving rise to the premelted liquid layer. This fusion of the most external solid planes does not take place in a gradual way with the increase of the temperature, finding that there are several solid planes that are desestabilized in favor of liquid formation. This is can be explained by the interfacial potential. Let's say by way of example that the liquid film is stable in a thickness of a single layer of water molecules: when the temperature is too low for the fusion of the solid planes, it happens that the liquid is not deposited homogeneously on the surface and forms patches. This will involve the formation of terraces and steps on the surface of the solid.

In relation to the gold-CTAB-water interface we need to understand its structure and prop-

erties to help us optimize the synthesis methods of gold nanoparticles. In last decades there has been an increase in resources due to the rise of nanotechnology and its applications in biomedicine, energy harvesting or data storage among others. [11, 12]

In this doctoral thesis we try to explain the role of CTAB aggregates in the morphology of gold nanorods synthesized from the seeding method by our experimental collaborators. [13, 14, 15] Two synthesis methods were proposed to obtain nano gold rods with exceptional optical properties. The first method is to synthesize gold nanoparticles and through a femtosecond laser to reshape the nanoparticles in the form of rods. [16] In the second method we generate the nano rods separating and controlling the processes of rupture of symmetry and crystalline growth through the selective diffusion of ions to each facet. [17] This is due to the presence of decanol in the colloidal solution. It is possible to stabilize a bilayer of surfactant on certain gold faces and thus control the diffusion of gold ions from the solution to the nanoparticle to thorugh the CTAB aggregates deposited in its surface.

In identification of the mechanisms is where molecular dynamics simulations have helped to establish a conceptual framework between experiments and results. We have validated the model potential. This model of charges has been validated in simulations for aggregates in solution with different concentrations of surfactant, salts and decanol.

Objectives

The general objective of this thesis is to reach a profound knowledge on the molecular structure of complex crystalline interfaces and their effect on the growth and habits of the resulting crystals. Given the ubiquity of water, we consider two important examples of solid complex interfaces with the presence of water that have much scientific interest per se, as well as a remarkable social and/or technological relevance.

On the one hand, the effect of the molten water on the interface of the ice with its vapour is studied. In short, the interface of the ice in the vicinity of the triple point is a complex interface, in which the ice and the vapor are separated by a layer of disordered water which can reach several nanometres thick. The formed water layer has an enormous influence on the properties of this important interface, whose behaviour determines the habits of growth of the ice crystals present in the atmosphere.

On the other hand, the interface of gold nanoparticles submerged in aqueous solutions of cationic surfactants will be studied, and in particular, the case of Cethyl-trimethylammonium bromide surfactant. In this other complex system, gold is separated from the volumetric phase of water by a surfactant layer, the structure of which is decisive in determining the shape and growth rate of gold nanoparticles.

In order to achieve these two major general objectives, we have divided them into a series of minor objectives that meticulously sum up this doctoral thesis project.

- Study of the interface of the ice with its vapor.

    1. Analyze in detail the structure of the water adsorbed on the ice surface.
    2. Determine the interfacial potentials of water adsorbed on ice.

3. Determine the accommodation coefficients of water molecules on ice surface and study the classic dispersion of water molecules over the ice interface as a function of nitrogene pressure.
4. Identify surface phase transitions at the ice/water and water/vapor interfaces and determine this relationship to the crystalline habits of ice in the atmosphere

- Interfaces of gold in aqueous surfactant solutions.

1. Study the micellization process of CTAB surfactant solutions as a function of concentration.
2. Determine the phase diagram of micellar structures as function of the concentration of additives such as alcohols and salts.
3. Determine the micellization process of CTAB surfactant on gold surfaces.
4. Study the effect of adsorbed micellar structures on the the kinetic growth of nanoparticles by deposition of gold precursors.
5. Linking the structure of the interface with the growth process and the resulting shape of the nanoparticles.

Results

Next, we will briefly comment on the main results obtained based on the objectives proposed above.

- Role of nitrogen in the growth rate of ice in the atmosphere

  Nitrogen slows the growth of ice. For the first time, we studied computationally the effect of nitrogen on the ice-vapour interface. In this study we determined the nitrogen adsorption energy shown according to the experimental results. In addition, we were able to demonstrate that nitrogen does not play a structural role on the ice surface, but rather reduces the flow of water molecules arriving at the surface, as shown by the coefficient of accommodation of water molecules depending on the pressure.

- Similarities between ice-water and ice-vapor interface

  Our study shows that the two distinct surfaces that limit the film behave at small wavelengths such as independent and atomically rough ice/water and water/vapor interfaces. For long wavelengths, we find that the two surfaces inhibit parallel fluctuations on a large scale. As result, the ice–vapor interface becomes smooth. The results of this work could help explain the complex structure of the ice crystals.

- Surface phase transitions in ice

  The forms of growth of snow crystals in the atmosphere are described in the Nakaya diagram. However, the physics behind this change in growth rates, and its relationship to the surface structure of the underlying equilibrium remains completely unknown. Here we show that in the range of -80 to 0 C, the main facets of the snow crystals undergo a sequence of alternate

surface phase transitions resulting in the anomalous increase of the step free energies and the crossing of the crystal growth rates exactly as required to explain the Nakaya diagram. As first postulated by Kuroda and Lacmann, our study highlights the importance of surface phase transitions and the film formed by the premelted planes of ice. They discussed the temperature dependence of the mechanism: (i) Vapor-quasi Liquid-Solid mechanism, (ii) Vapor Deposition, and (iii) Growth from bidimensional nucleation. Although unexpectedly, we observe the appearance of a succession of transitions of preroughening and smoothening induced by the premelted liquid, which we identify in an atomic model for the first time. For the premelted film we found two layering transitions that correlated with the surface smoothness. These results reveal the importance of the disordered surface phase, and we discuss it in the context of surface models known as solids on solids.

- Structural Transitions of CTAB Aggregates

  Firstly, we studied the stability and shape of CTAB preaasembled micelles with between 60 and 240 moleucules of surfactant. We found that micelles are stable up to about 150 molecules and that there is a transition from spherical to prolate ellipsoidal shapes at about 90 molecules. In addition, the presence of salts favours the formation of cylindrical micelles, whereas addition of decanol in a range of suitable concentrations favours the formation of bi-layers structured like a liquid crystal.

- CTAB adsorption on gold

  When we simulate the CTAB aggregates on the surface of gold micelles become hemispherical. Depending on the concentration of CTAB we find that the size of the micelles increases, but never form a perfectly developed CTAB bilayer. We found that the water channel between the gold and the CTAB is reduced with the increase of adsorption on the gold.

- CTAB and decanol adsorption on gold

  By simulating the addition of CTAB at several decanol fractions, we find that the formation of the bilayers is only possible on the gold faces {110} and {250}. On the other hand, for the faces {100} and {111} the order parameter shows the destabilization of the bilayer.

- Availability of gold and silver ions on the nanoparticle

  We quantified the availability of ions for each type of gold surface with the adsorbed aggregates and found low availability of gold ions on the crystallographic faces where CTAB and decanol form bilayers. Is often to employ methods assisted by silver ions. For this reason we studied the diffusion of silver ions, we did not find selectivity on the availability of silver ions.

Conclusions

At the beginning of this doctoral thesis, we set out to relate by means of molecular simulation the habits of crystalline growth with the properties of their solid interfaces. For this purpose we have studied the ice-vapor and the gold-CTAB-water interfaces.

In the case of water, we clarified that the atmospheric pressure exerted by nitrogen gas does not play any structural effect on the ice interface, and a kinetic effect through which the flow of water molecules arriving to the solid phase from the vapor is reduced. As a consequence, the experimental growth rate of ice crystals is reduced in the presence of nitrogen. In our study we obtained that the attachment rate of water molecules decreases at all temperatures as nitrogen pressure increases. Next, using the TIP4P/2005 model, we demonstrated that near the triple point, the thin layer of liquid adsorbed on the surface of the primary prismatic face of ice, the ice-film and film-vapor behave as two independent surfaces at small wave lenghts, but surfaces are coupled at long wavelengths of the capillary waves (smooth). A more detailed studied of the ice-vapor interface was then performed with the TIP4P/Ice water model. The TIP4P/Ice model predicts a melting temperature around 272 K, which allows us to explore the ice surface in a more consistent temperature range with the experimental situation. However, at this point I would like to emphasize that during this thesis numerous comprobations have been made between the Ice and 2005 models, and both models show consensus on the thickness of the liquid film if scaled with respect to the melting temperature of each model. The study of the interface is carried out through the analysis of the capillary waves and their propagation through the ice-liquid and liquid-vapor interfaces for an interval of temperatures from 190 K to 270 K. In this study we observed that the behavior of the step free energy is not monotone and presents very good aggreement with the experimental results measured in snowflakes. This non-monotone behaviour is due to the presence of different surfaces phases transitions, of which we highlight the preroughening transition by which we have a smooth surface with highly disorder steps and correlated at large wavelengths.

In relation to the second part of this doctoral thesis, we have studied the stability of CTAB aggregates in dissolution and the changes produced in aggregates when they are is adsorbed into a gold wall. In our work we find that micelles are stable up to an aggregate number of 150 surfactant molecules, and ceases to be spherical from 90 CTAB molecules. On the other hand, when the aggregate is in a solution with high ionic force, the micelles begin to elongate and become spherical from 90 molecules of CTAB, stabilizing wormlike or cylindrical micelles. But if we replace the salt and add decanol as cosurfactant we get perfectly developed and ordered bilayers. We have not been able to stabilize bilayers where the aggregate only is made up of CTAB. The bilayers are stable in a certain fraction of a decanol cosurfactant due to a competition between alcohol aggregation due to the formation of hydrogen bonds and the electrostatic alcohol-CTAB interactions. After this preliminary work on the behaviour of CTAB and decanol/ CTAB aggregates in solution, we studied their assembly behaviour when deposited on gold surfacce. In our simulations we identified the formation of water channels that allows the diffusion of gold ions froms the solution to the gold surface for particular combinations of the exposed gold surface and the morphology of the surfactant aggregates on top of then. Our results are in very good agreement with experiments, and they have allowed to understand the underlying microscopic mechanism of two recently proposed methods for synthesis of gold nanorods. For it we made the study with the aggregates of CTAB, CTAB + salt and CTAB + decanol, placing them on the gold to study the formation of water channels and the availability on each gold surface of the gold ions responsible of growth of nanorods. These results are surprisingly consistent with the experiments and have helped to understand and optimize the two methods of gold nanorods synthesis with the best aspect ratio and polidispersity up to the date.

Bibliography

[1] P. S. Pershan and M. Schlossman, *Liquid Surfaces and Interfaces: Synchrotron X-ray Methods*. Cambridge: Cambridge University Press, 2012.

[2] M. Allen and D. Tildesley, *Computer Simulation of Liquids*. Oxford: Clarendon Press, 1987.

[3] D. Frenkel and B. Smit, *Understanding Molecular Simulation*. San Diego: Academic Press, second ed., 2002.

[4] L. G. MacDowell, J. Benet, and N. A. Katcho, "Capillary fluctuations and film-height-dependent surface tension of an adsorbed liquid film," *Phys. Rev. Lett.*, vol. 111, p. 047802, Jul 2013.

[5] J. Benet, L. G. MacDowell, and E. Sanz, "Computer simulation study of surface wave dynamics at the crystal–melt interface," *J. Chem. Phys.*, vol. 141, p. 034701, 2014.

[6] J. Benet, L. G. MacDowell, and E. Sanz, "A study of the ice-water interface using the tip4p/2005 water model," *Phys. Chem. Chem. Phys.*, vol. 16, pp. 22159–22166, 2014.

[7] C. Herring, "Some theorems on the free energies of crystal surfaces," *Phys. Rev.*, vol. 82, pp. 87–93, Apr 1951.

[8] W. K. Burton, N. Cabrera, and F. C. Frank, "The growth of crystals and the equilibrium structure of their surfaces," *Phyl. Trans. R. Soc. Lond. A*, vol. 243, pp. 299–358, 1951.

[9] C. Rottman and M. Wortis, "Equilibrium crystal shapes for lattice models with nearest-and next-nearest-neighbor interactions," *Phys. Rev. B*, vol. 29, pp. 328–339, Jan 1984.

[10] J. D. Weeks, W. van Saarloos, D. Bedeaux, and E. Blokhuis, "Consistency of capillary wave theory in three dimensions: Divergence of the interface width and agreement with density functional theory," *J. Chem. Phys.*, vol. 91, no. 10, pp. 6494–6504, 1989.

[11] E. C. Dreaden, A. M. Alkilany, X. Huang, C. J. Murphy, and M. A. El-Sayed, "The golden age: gold nanoparticles for biomedicine," *Chem. Soc. Rev.*, vol. 41, pp. 2740–2779, 2012.

[12] P. Falagan-Lotsch, E. M. Grzincic, and C. J. Murphy, "New advances in nanotechnology-based diagnosis and therapeutics for breast cancer: An assessment of active-targeting inorganic nanoplatforms," *Bioconjugate Chemistry*, vol. 28, no. 1, pp. 135–152, 2017. PMID: 27973767.

[13] N. R. Jana, L. Gearheart, and C. J. Murphy, "Seed-mediated growth approach for shape-controlled synthesis of spheroidal and rod-like gold nanoparticles using a surfactant template," *Advanced Materials*, vol. 13, no. 18, pp. 1389–1393, 2001.

[14] B. Nikoobakht and M. A. El-Sayed, "Preparation and growth mechanism of gold nanorods using seed-mediated growth method," *Chem. Mater.*, vol. 15, pp. 1957–1962, 2003.

[15] J. D. Padmos, M. L. Personick, Q. Tang, P. N. Duchesne, D.-e. Jiang, C. A. Mirkin, and P. Zhang, "The surface structure of silver-coated gold nanocrystals and its influence on shape control," *Nature Communications*, vol. 6, p. 7664, 2015.

[16] G. González-Rubio, P. Díaz-Núñez, A. Rivera, A. Prada, G. Tardajos, J. González-Izquierdo, L. Bañares, P. Llombart, L. G. MacDowell, M. Alcolea-Palafox, L. M. Liz-Marzán, O. Peña-Rodríguez, and A. Guerrero-Martínez, "Femtosecond laser reshaping yields gold nanorods with ultranarrow surface plasmon resonances," *Science*, vol. 358, pp. 640–644, 2017.

[17] G. González-Rubio, V. Kumar, P. Llombart, P. Díaz-Núñez, E. Bladt, T. Altantzis, S. Bals, O. Peña Rodríguez, E. G. Noya, L. G. MacDowell, A. Guerrero-Martínez, and L. M. Liz-Marzán, "Disconnecting symmetry breaking from seeded growth for the reproducible synthesis of high quality gold nanorods," *ACS Nano*, vol. 0, no. 0, p. null, 0. PMID: 30939242.

Resumen

Introducción

En este proyecto que ha dado forma a la Tesis Doctoral que el candidato presenta, los hábitos de crecimiento cristalino han sido estudiados desde el punto de vista estructural de las interfase hielo–vapor y la interfase oro-CTAB-agua. Desde el punto de vista experimental, puede ser muy complicado las mediciones e interpretación de los hábitos de crecimiento cristalino en interfases solidas complejas.[1, 2, 3] Mediante simulación molecular hemos abordado el estudio de la estructura en la superficie del hielo en coexistencia con una fina capa de agua prefundida sobre la superficie del cristal, en donde, el espesor del líquido evoluciona con la temperatura. La película prefundida puede ser caracterizada en términos de las fluctuaciones de las superficies sólido-líquido y líquido-vapor. La fluctuaciones correlacionadas pueden ser estudiadas usando un modelo del Hamiltoniano interfacial acoplado a través del potencial interfacial. [4, 5, 6] Este potencial tiene en cuenta el espesor de la película líquida en el equilibrio y en gran medida determina las propiedades de la interfase.

Por otra parte, dependiendo de la estructura de la superficie sólida, la temperatura va a originar desorden en las diferentes superficies y ocurre que las propiedades pueden variar anisotrópicamente dependiendo de la superficie de hielo que estemos estudiando. Un ejemplo de anisotropía es la rigidez interfacial de una superficie de hielo orientada en la cara basal y en la cara prismática I. La temperatura produce desorden en la superficie del hielo en las caras basal y prismática, siendo ligeramente mayor en esta última. La superficie sólida presenta ondas capilares cuya amplitud puede diverger cuando la temperatura se aproxima al punto triple del agua. Esta es la definición de una superficie rugosa. En superficies rugosas la amplitud de las fluctuaciones en la altura diverge para vectores de onda pequeños. En la transición de rugosidad y por debajo, las fluctuaciones se mantiene finitas para todas las longitudes de onda. [7, 8, 9, 10]

La transición de rugosidad implica cambios en la formación de islas sobre la superficie. Cuando la superficie es rugosa no se necesita formar un núcleo en forma de isla y por lo tanto no hay que vencer la barrera de nucleación de las islas. Debido a este fenómeno la superficie cristalina crece rápida y linealmente con la saturación.

En la superficie de hielo ocurre la fusión de los planos mas externos dando lugar a la superficie prefundida. Esta fusión de los planos sólidos no se produce de forma gradual con el aumento de la temperatura, encontrando que hay varios planos sólidos que están incompletos en favor de la formación de líquido. Esto es debido precisamente al potencial interfacial. Pongamos a modo de ejemplo que la película líquida es estable en un espesor de una sola capa de moléculas de agua: cuando la temperatura es demasiado baja para la fusión de los planos sólidos, ocurre que el líquido

no se depositará de manera homogénea sobre la superficie y se estabiliza formando islotes con espesor del diámetro de una molécula de agua. Esto implica la formación de terrazas y escalones sobre la superficie del solido.

En relación a la interfase oro-CTAB-agua necesitamos entender su estructura y propiedades para ayudar a optimizar los métodos de síntesis de las nanopartículas de oro. En las últimas décadas se ha producido un aumento de los recursos debido al auge de la nanotecnología y sus aplicaciones en biomedicina, captación de energía o almacenamiento de datos, entre otras. [12]

En esta Tesis Doctoral intentamos explicar la morfología de las nanovarillas de oro sintetizadas a partir del método de semilla. [13, 14, 15] Nuestros colaboradores experimentales han propuesto dos métodos de síntesis para obtener nanovarillas de oro con propiedades ópticas excepcionales.

El primer método consiste en sintetizar nanopartículas de oro y mediante un láser de femtosegundos reformar las nanopartículas en forma de varillas. [16] En el segundo método se generan las nanovarillas separando y controlando los procesos de ruptura de simetría y crecimiento cristalino mediante la difusión selectiva de iones a cada cara.[17] Esto se debe a la presencia de decanol en la solución coloidal. Es posible estabilizar la bicapa de surfactante en ciertas caras de oro y así controlar la difusión.

En la identificación de los mecanismos es donde las simulaciones de dinámica molecular han ayudado a establecer un marco conceptual entre los experimentos y los resultados. Gracias a los cálculos de *ab-initio*, se proponen cargas efectivas para las moléculas de CTAB y decanol. Este modelo de cargas ha sido validado en simulaciones de agregados en solución con diferentes concentraciones de surfactante, sales y decanol.

Objetivos

El objetivo general de este proyecto de tesis es alcanzar un conocimiento profundo sobre la estructura molecular de interfases cristalinas complejas y su efecto en el crecimiento y los hábitos de los cristales resultantes. Dada la ubicuidad del agua, se han escogido para ilustrar estos efectos, dos importantes ejemplos de interfase sólida compleja con presencia de agua que tienen tanto interés científico per se, como una notable relevancia social y/ó tecnológica.

Por un lado, se estudiará el efecto del agua líquida *prefundida* sobre la interfase del hielo con su vapor. Se trata en definitiva de la interfase del hielo que en las cercanías del punto triple es una interfase compleja, en la que el hielo y el vapor están separados por una capa de agua desordenada que puede alcanzar varios nanómetros de espesor. La capa de agua formada tiene una influencia enorme en las propiedades de esta interfase tan importante, cuyo comportamiento determina el hábito de los cristales de hielo presentes en la atmósfera.

Por otro lado, se estudiará la interfase de nanopartículas de oro sumergidas en disoluciones acuosas de surfactantes catiónicos, y en particular, el caso del surfactante bromuro de cetiltrimetilamonio. En este otro sistema complejo, el oro está separado de la fase volumétrica de agua por una capa de surfactante, cuya estructura es decisiva a la hora de determinar la forma y velocidad de crecimiento de las nanopartículas de oro.

Para alcanzar estos dos grandes objetivos generales, los hemos dividido en una serie de objetivos menores que suman meticulosamente este proyecto.

- Estudio de la Interfase del hielo con su vapor.

1. Analizar detalladamente la estructura del agua adsorbida sobre el hielo.
2. Determinar los potenciales interfaciales de agua adsorbida sobre hielo.
3. Determinar coeficientes de acomodamiento y estudiar la dispersión clásica de moléculas de agua sobre la interfase del hielo en función de la presión de nitrógeno.
4. Identificar transiciones de fase superficial en la interfase hielo/agua y determinar su relación con los hábitos cristalinos del hielo en la atmósfera

- La Interfases del oro en disoluciones acuosas de surfactantes.

1. Estudiar el proceso de micelización del surfactante CTAB en función de su concentración en agua.
2. Determinar el diagrama de fases de estructuras micelares en función de la concentración de aditivos tales como alcoholes y sales.
3. Determinar el proceso de micelización del surfactante CTAB sobre superficies de oro.
4. Estudiar el efecto de las estructuras micelares adsorbidas sobre la cinética de crecimiento de nanopartículas por deposición de precursores del oro.
5. Relacionar la estructura de la interfase con el proceso de crecimiento y las formas resultantes de las nanopartículas.

Resultados

A continuación, vamos a comentar brevemente los principales resultados que se obtuvieron en base a los objetivos propuestos anteriormente.

- Papel del nitrógeno en la tasa de crecimiento del hielo en la atmósfera

  El nitrógeno ralentiza el crecimiento del hielo. Por primera vez estudiamos computacionalmente el efecto del nitrogeno en la interfase hielo-vapor. En este estudio determinamos la energía de adsorción del nitrógeno que se muestra acorde a los resultados experimentales. Además conseguimos demostrar que el nitrógeno no ejerce un papel estructural en la superficie del hielo sino que reduce el flujo de llegada de moĺeculas de agua hacia la superficie tal y como muestra el coeficiente de acomodo del hielo en función de la presión.

- Similitudes entre interfase hielo–agua y hielo–vapor

  Nuestro estudio muestra que para el modelo TIP4P/2005 las dos superficies distintas que limitan la película se comportan en longitudes de onda pequeñas como interfaces hielo/agua y agua/vapor independientes y atómicamente rugosas. Para longitudes de onda largas, encontramos que las dos superficies se acoplan y se inhiben las fluctuaciones paralelas a gran escala. Debido a este cambio producido en la superficie, la interfase hielo–vapor se vuelve suave. Los resultados de este trabajo suponen una buena base para el avance del proyecto y podrían ayudar a explicar la compleja estructura de los cristales de hielo.

- Transiciones de fase superficiales en el hielo

  Las formas de crecimiento de los cristales de nieve en la atmósfera son descritas en el diagrama de Nakaya y nos proporcionan la prueba para comprender nuestros resultados. Sin embargo, la física detrás de este cambio en las tasas de crecimiento, y su relación con la estructura de la superficie del equilibrio subyacente sigue siendo completamente desconocida. Aquí mostramos que en el rango de -80 a 0 C, las principales facetas de los cristales de nieve sufren una secuencia de transiciones de fase superficiales alternas que resultan en el aumento anómalo de las energías libres de escalón y el cruce de las tasas de crecimiento de los cristales exactamente como se requiere para explicar el diagrama de Nakaya. Tal y como postularon por primera vez Kuroda y Lacmann, nuestro estudio destaca la importancia de las transiciones de fase de superficie y de la película formada por los planos prefundidos del hielo. Ellos discutieron la dependencia del mecanismo de crecimiento con la temperatura con tres tipos de cinéticas: i) Mecanismo Vapor-quasi Liquid-Solid, ii) Deposición de vapor y iii) Crecimiento a partir de nucleación bidimensional. Aunque inesperadamente, observamos la aparición de una sucesión de transiciones de prerugosidad y suavizado inducidas por el líquido prefundido y que identificamos en un modelo atómico por primera vez. Para la película prefundida encontramos dos transiciones de estratificación que se correlacionan con la suavidad de la superficie. Estos resultados revelan la importancia de la fase superficie desordenada, y la discutimos en modelos conocidos como sólidos sobre sólidos (solid on solid).

- Transiciones estructurales de agregados de CTAB

  Estudiamos los agregados de CTAB para un número de moléculas comprendidas entre 60 y 240. En el caso del agregados de mayor tamaño encontramos que el agregado no es estable y se disgrega. Por otro lado, los agregados con un número mayor a 90 moléculas de CTAB dejan de ser esféricos. Además la presencia de sales favorece la formación de micelas de tipo cilíndricas y la presencia de decanol en un intervalo de concentraciones adecuadas favorecen la formación de bicapas estructuradas como un cristal líquido nemático.

- Adsorción de CTAB sobre el oro

  Cuando simulamos los agregados de CTAB sobre la superficie del oro encontramos la formación de micelas hemiesféricas. En función de la concentración de CTAB encontramos que el tamaño de la micela aumenta sin llegar a formar en ningún caso una bicapa de CTAB perfectamente desarrollada. Encontramos que el canal de agua entre el oro y el CTAB se reduce con el aumento de la adsorción sobre el oro.

- Adsorción de CTAB y decanol sobre el oro

  Al simular el agregado de CTAB con distintas fracciones de decanol encontramos que la formación de las bicapas solo es posible en las caras {110} y {250} del oro. En cambio para las caras {100} y {111} el parámetro de orden nos indica la desestabilización de la bicapa.

- Disponibilidad de iones oro y plata sobre la nanopartícula

  Cuantificamos la disponibilidad de iones para cada tipo de superficie de oro con los agregados adsorbidos y encontramos baja disponibilidad de iones oro en las caras cristalográficas donde

el CTAB y el decanol forman bicapas. Por el contrario, cuando estudiamos la disponibilidad de iones plata no hay selectividad en la función de distribución de probabilidad de los iones con respecto a la distancia de la superficie.

Conclusiones

Al inicio de esta tesis, nos propusimos relacionar mediante simulación molecular los hábitos de crecimiento cristalino con la propiedades de las interfases sólidas complejas. Con esta finalidad hemos estudiado la interfase hielo-vapor y la interfase oro-CTAB-agua.

En el caso del agua, comprobamos que la presión atmosférica ejercida por el gas nitrógeno no ejerce ningún efecto estructural sobre la interfase del hielo, y si un efecto cinético a través del cual se reduce el flujo de llegada de moléculas de agua desde la fase vapor hasta la fase sólida. Como consecuencia, la velocidad de crecimiento experimental de los cristales de hielo se reduce en presencia de nitrógeno. En nuestro estudio mostramos como se reduce significativamente, y para todas las temperaturas, la tasa de pegado de las moléculas de agua con el aumento de presión. A continuación, demostramos cerca del punto triple del agua del modelo TIP4P/2005 que la fina capa de líquido adsorbido sobre el sólido en la cara prismática principal, cuando la longitud de la onda capilar es corta, la interfase tiene el comportamiento de dos superficies independientes (hielo-película) y (película-vapor). No es así cuando la longitud de onda es larga y la superficie se vuelve suave. Más en detalle procedemos a realizar el estudio de las ondas capilares en el agua para el modelo TIP4/PIce. El modelo TIP4P/Ice presenta la temperatura de fusión del hielo en torno a 272 K, lo que nos permite explorar la superficie del hielo en un margen de temperaturas más acorde a la situación experimental. No obstante, en este punto quiero recalcar que durante esta tesis se han realizado numerosas comprobaciones entre el modelo Ice y el 2005, y ambos modelos muestran consenso en el espesor de la película líquida si se escalan con respecto a la temperatura de fusión de cada modelo. El estudio de la interfase se realiza a través del análisis de las ondas capilares y su propagación por las superficies para un intervalo de temperaturas desde 190 K hasta 270 K. Para este estudio se observa que el comportamiento de la energía libre de escalón no es monótono y presenta muy buena concordancia con los resultados experimentales en los copos de nieve. Este comportamiento no monótono se debe a la presencia de distintas transiciones de fase superficiales, de las que destacamos la transición de suavizado.

En relación al segundo bloque de esta tesis doctoral, hemos estudiado la estabilidad de agregados de CTAB en disolución y los cambios producidos en los agregados cuando se adsorben en una pared de oro. En nuestro trabajo encontramos que las micelas son estables hasta un número de agregacion de 150 moléculas de surfactante, y dejan de ser esféricas a partir de 90 moléculas de CTAB. Por otro lado cuando el agregado se encuentra en un disolución con fuerza iónica elevada, las micelas comienzan a elongarse y se estabilizan micelas de tipo gusano o cilíndricas. Pero si sustituimos la sal y añadimos decanol como cosurfactante conseguimos estabilizar bicapas perfectamente desarrolladas y ordenadas. De ninguna forma se han conseguido estabilizar bicapas donde exclusivamente el agregado este formado por CTAB. La formación de las bicapas solo es estable en una determinada fracción de cosurfactante debido a la competencia entre enlaces de hidrógeno agua-alcohol y las interacciones electrostáticas alcohol-CTAB. Este trabajo se realiza con la finalidad de ir un poco más alla y ayudar a comprender los mecanismos de crecimiento de nanopartículas

de oro. Para ello realizamos el estudio con los agregados de CTAB, CTAB + sal y CTAB + decanol, colocándolos sobre el oro para estudiar la formación de canales de agua y la disponibilidad sobre cada superficie de oro de los iones oro responsables del crecimiento de las nanovarillas. Estos resultados concuerdan de manera asombrosas con los experimentos y han ayudado a entender los dos métodos de síntesis de nanovarillas de oro con la mejor relación de aspecto y polidispersidad hasta la fecha.

Bibliografía

[1] P. S. Pershan and M. Schlossman, *Liquid Surfaces and Interfaces: Synchrotron X-ray Methods*. Cambridge: Cambridge University Press, 2012.

[2] M. Allen and D. Tildesley, *Computer Simulation of Liquids*. Oxford: Clarendon Press, 1987.

[3] D. Frenkel and B. Smit, *Understanding Molecular Simulation*. San Diego: Academic Press, second ed., 2002.

[4] L. G. MacDowell, J. Benet, and N. A. Katcho, "Capillary fluctuations and film-height-dependent surface tension of an adsorbed liquid film," *Phys. Rev. Lett.*, vol. 111, p. 047802, Jul 2013.

[5] J. Benet, L. G. MacDowell, and E. Sanz, "Computer simulation study of surface wave dynamics at the crystal–melt interface," *J. Chem. Phys.*, vol. 141, p. 034701, 2014.

[6] J. Benet, L. G. MacDowell, and E. Sanz, "A study of the ice-water interface using the tip4p/2005 water model," *Phys. Chem. Chem. Phys.*, vol. 16, pp. 22159–22166, 2014.

[7] C. Herring, "Some theorems on the free energies of crystal surfaces," *Phys. Rev.*, vol. 82, pp. 87–93, Apr 1951.

[8] W. K. Burton, N. Cabrera, and F. C. Frank, "The growth of crystals and the equilibrium structure of their surfaces," *Phyl. Trans. R. Soc. Lond. A*, vol. 243, pp. 299–358, 1951.

[9] C. Rottman and M. Wortis, "Equilibrium crystal shapes for lattice models with nearest-and next-nearest-neighbor interactions," *Phys. Rev. B*, vol. 29, pp. 328–339, Jan 1984.

[10] J. D. Weeks, W. van Saarloos, D. Bedeaux, and E. Blokhuis, "Consistency of capillary wave theory in three dimensions: Divergence of the interface width and agreement with density functional theory," *J. Chem. Phys.*, vol. 91, no. 10, pp. 6494–6504, 1989.

[11] E. C. Dreaden, A. M. Alkilany, X. Huang, C. J. Murphy, and M. A. El-Sayed, "The golden age: gold nanoparticles for biomedicine," *Chem. Soc. Rev.*, vol. 41, pp. 2740–2779, 2012.

[12] P. Falagan-Lotsch, E. M. Grzincic, and C. J. Murphy, "New advances in nanotechnology-based diagnosis and therapeutics for breast cancer: An assessment of active-targeting inorganic nanoplatforms," *Bioconjugate Chemistry*, vol. 28, no. 1, pp. 135–152, 2017. PMID: 27973767.

[13] N. R. Jana, L. Gearheart, and C. J. Murphy, "Seed-mediated growth approach for shape-controlled synthesis of spheroidal and rod-like gold nanoparticles using a surfactant template," *Advanced Materials*, vol. 13, no. 18, pp. 1389–1393, 2001.

[14] B. Nikoobakht and M. A. El-Sayed, "Preparation and growth mechanism of gold nanorods using seed-mediated growth method," *Chem. Mater.*, vol. 15, pp. 1957–1962, 2003.

[15] J. D. Padmos, M. L. Personick, Q. Tang, P. N. Duchesne, D.-e. Jiang, C. A. Mirkin, and P. Zhang, "The surface structure of silver-coated gold nanocrystals and its influence on shape control," *Nature Communications*, vol. 6, p. 7664, 2015.

[16] G. González-Rubio, P. Díaz-Núñez, A. Rivera, A. Prada, G. Tardajos, J. González-Izquierdo, L. Bañares, P. Llombart, L. G. MacDowell, M. Alcolea-Palafox, L. M. Liz-Marzán, O. Peña-Rodríguez, and A. Guerrero-Martínez, "Femtosecond laser reshaping yields gold nanorods with ultranarrow surface plasmon resonances," *Science*, vol. 358, pp. 640–644, 2017.

[17] G. González-Rubio, V. Kumar, P. Llombart, P. Díaz-Núñez, E. Bladt, T. Altantzis, S. Bals, O. Peña Rodríguez, E. G. Noya, L. G. MacDowell, A. Guerrero-Martínez, and L. M. Liz-Marzán, "Disconnecting symmetry breaking from seeded growth for the reproducible synthesis of high quality gold nanorods," *ACS Nano*, vol. 0, no. 0, p. null, 0. PMID: 30939242.

Capítulo 1
Discusión Integradora

El proyecto de Tesis Doctoral que presento en esta memoria es el reflejo del princpipal trabajo de investigacón que he realizado durante los últimos tres años. Con la finalidad de que los lectores tengan una visión clara del trabajo, se ha dividido la memoria en tres partes: La primera parte (Parte I) recoge el fundamento teórico y la metodología empleada para realizar con éxito el proyecto. La segunda parte (Parte II) contiene la exposición y discusión de los principales resultados que se han obtenido. Por último, la tercera parte (Parte III) recoge las conclusiones mas relevantes en base a los resultados obtenidos.

El tema principal de esta tesis es el estudio de interfases complejas mediante simulación molecular. La finalidad directa consiste en relacionar las propiedades interfaciales con los hábitos de crecimiento cristalino de los copos de nieve y de nanopartículas de oro. En el caso de los copos de nieve, hemos conseguido relacionar los hábitos de crecimiento de los cristalitos de hielo en base a transiciones de fase superficiales. Para el caso de las nanopartículas de oro hemos ayudado a entender los mecanismos subyacentes en dos métodos de síntesis de nanovarillas de oro recientemente publicados. A continuación iremos viendo las conclusiones más relevantes para cada capítulo.

En el capítulo 1, nos enfrentamos al reto de esclarecer la influencia de la adsorción de nitrógeno en el crecimiento cristalino de los copos de nieve en la atmósfera. En 1959 van de Heuvel ilustra la dificultad del problema pero no consigue demostrar la influencia de la composición atmosférica en las tasas de crecimiento de los cristales.

Exactamente 60 años después todavía no hay consenso alguno. Nuestros resultados muestran que los modelos atómicos pueden ofrecer una conclusión clara e inequívoca del papel del nitrógeno, cerrando así un tema que lleva siendo objeto de debate durante tantos años. En el estudio de la interfaz hielo-vapor, la mayor parte de las simulaciones por ordenador clásicas se realiza en vacío, mientras que la mayoría de los experimentos se realizan en una atmósfera de nitrógeno controlada. Sin embargo, el papel del gas nitrógeno en las tasas de crecimiento del hielo y los hábitos de los cristales de hielo sigue siendo en gran medida desconocido y controvertido. En este estudio, proporcionamos por primera vez una caracterización detallada a escala atómica de la superficie de hielo para el modelo TIP4P/Ice en condiciones de presión y temperatura comparables al régimen de formación de las nubes de tipo cirro en la atmósfera. Evaluamos el impacto en la determinación de la estructura y la cinética de la superficie de hielo del gas nitrógeno adsorbido. Nuestro estudio de simulación atomística señala un papel crucial del gas nitrógeno en la determinación de las tasas de crecimiento, ligado fundamentalmente a la limitación de la difusión de agua en fase vapor y reduciendo el flujo de moléculas de agua que llegan a la superficie. Una hipótesis que hasta ahora sólo había sido apoyada por estudios macroscópicos.

Una vez que hemos determinado que el papel del nitróneno no tiene relevancia en la superficie del hielo desde el punto de vista estructural podemos continuar con el estudio de la interfaz hielo-vapor independiente de la presión que ejerce el gas.

En el capítulo 2 demostramos que la existencia de la capa líquida adsorbida de espesor finito que está en coexistencia con el hielo permite que la interfase hielo-película sea suave hasta temperaturas muy próximas al punto triple. En cambio la interfase hielo-agua permanece rugosa. Este estudio teórico y de simulación molecular es una buena herramienta para el estudio de la interfase hielo-vapor ya que podemos observar directamente y a escala atómica la superficie. Por otra parte, comparando la estructura de la interfase compleja hielo-vapor y las interfases hielo-agua y agua-vapor, podemos ver que las dos superficies que hay en la interfase hielo-vapor (superficie hielo-peli'cula y superficie película-vapor) presentan una fuerte correlación estructural con las interfases independientes. Es por tanto que la estructura del líquido de espesor finito sobre la superficie del hielo va a determinar la manera en la que se propagan las ondas capilares.

Para el capítulo 3 encontramos en la superfcie del hielo una secuencia de transiciones de fase superficiales completamente desconocidas (transición de prerugosidad, transición de suavizado). Rommelse y den Nijs en 1987 postularon que el paso de una superfici lisa ordenada (OF) a una superficie suave desordenada pero con fluctuaciones finitas (DOF) está controlada por la transición de prerugosidad. Si la temperatura aumenta y se acerca al punto de fusión la DOF pasa a ser una superficie rugosa para la cual las fluctuaciones divergen. El paso de una superficie suave a una rugosa esta determinada por la transición de rugosidad. En esta tesis se localiza por primera vez, para el hielo, varias transiciones de prerugosidad desde una superficie suave (OF) a una fase plana desordenada (DOF). Además encontramos la transición de suavizado en la que la superficie se vuelve suave (HT-RF). Si fuese posible incrementar la temperatura un par de grados, la superficie HT-RF daria lugar a una superficie rugosa con fluctuaciones infinitas.

Lo más importante es que nuestros resultados confirman el escenario sugerido de un aumento anómalo de la energía libre de escalón en las temperaturas donde hay transiciones de suavizado para las caras basal y prismática respectivamente. Empleando el análisis de las ondas capilares en la superficie del hielo, identificamos una serie de transiciones de fase de superficie, que incluyen, la transición de prerugosidad y la transición de suavizado. Es posible identificar estas transiciones gracias a la elección de un parámetro de orden apropiado. Ninguna de estas fases o las transiciones de fases relacionadas se habían formulado hasta entonces en el hielo, más alla del papel fundamental de Kuroda y Lacmann que postularon que el cruce de las tasas de crecimiento de los cristales se produce a consecuencia de la formación de una fina capa cuasilíquida en la superficie del hielo. Podría establecerse a diferentes temperaturas dependiendo de la faceta cristalina. La secuencia de transiciones entre la cara basal y la cara prismática I se asemeja en gran medida a las transiciones de fase que se encuentran en el diagrama de Nakaya y que determinan el hábito de crecimiento cristalino. Mediante el estudio de las ondas capilares por medio del acoplamiento entre el Hamiltoniano interfacial y modelos de sólidos sobre sólidos hemos calculado por primera vez las energías libres de escalón que muestran cruces para distintintas temperaturas y cumplen las expectativas del escenario que emerge de las contribuciones de Kuroda y Lacmann.

A lo largo del capítulo 4 presentamos un estudio muy detallado sobre la estructura de la capa líquida prefundida sobre la superficie del hielo. Parece que la controversia sobre el espesor de la película líquida comienza a aclararse pero aparecen nuevas observaciones sobre las propiedades de la película prefundida, ya sea a lo largo de la línea de equlibrio sólido-vapor o fuera de la

coexistencia. A lo largo de la línea de sublimación, Sánchez *et al.* combinaron experimentos y simulaciones para determinar a 257 K un transición de estratificación de dos capas e identificar la estructura de la interfase hielo vapor en detalle para el modelo TIP4P/Ice. No obstante, en nuestro trabajo realizamos un estudio mucho más detallado de la interfase hielo-vapor, y determinamos dos transiciones de estratificación continuas para la película prefundida. La presencia de las transciones de estratificación se relfejan en el comportamiento levemente oscilatorio del potencial interfacial.

En los capítulos 1, 2 y 3 se pone de manifiesto la importancia de discretizar la interfase compleja hielo-vapor en dos superficies independientes, una superficie hielo-película y otra superficie película-vapor. Sobre todo es muy interesante ya que en simulaciones para el modelo mW muestran en este rango de temperatura, la superficie de hielo exhibe parches de hielo prefundido cuyos tamaños aumentan continuamente a medida que se incrementa la temperatura. Además se trata de un líquido adsorbido, es importante considerar la interacción entre la estratificación del sólido y la mojabilidad del líquido sobre el sólido. Nosotros racionalizamos los resultados en términos del potencial interfacial, que determina la energá libre del sistema en función del espesor de la película. El comportamiento de las capas del sólido presenta reminiscencias de un comportamiento oscilatorio en el potencial interfacial, dando lugar a transiciones de estratificación continuas, sin divergencia de la longitud de correlación y por lo tanto, no singulares. Curiosamente muy cerca de las temperaturas de las transiciones de estratificación, observamos, en el capítulo anterior, como la superficie sólida experimentaba varias transciones de suavizado. Por lo tanto podemos observar una correlación directa entre las transiciones de estratificación, que vemos en este capítulo, y las fases DOF , que vimos en el capítulo 3, y por lo tanto, las trasiciones de estratificación se producirían cuando desaparecen las terrazas en la superficie del hielo a medida que aumenta la temperatura.

Claramente, se puede apreciar el punto en común que presentan estos 4 primeros capítulos es caracterizar la estructura de la interfase hielo-vapor por simulación molecular para determinar los hábitos de crecimiento de los copos de nieve en la atmósfera. Para ello en el primer capítulo demostramos que la atmósfera inerte de nitrógeno únicamente afectaría al crecimento desde un punto de vista cinético y no estructural. Una vez nos liberamos de la necesidad de emplear la atmósfera de nitrógeno en el estudio estructural, continuamos con la búsqueda, en los siguientes 3 capítulos, de las distintas transiciones de fase superficiales que Kuroda y Lacmann responsabilizaban de los cambios producidos en las tasas de crecimiento del hielo y por los que los hábitos de crecimiento de los copos de nieve se modifica. Está dinámica de crecimiento permite a los copos de nieve adoptar las distintas morfologías que presentan, siendo las más habituales los cristales con formas de plato y columnas.

En el capítulo 5 tratamos de estudiar el autoensamblado controlado de agregados de CTAB con diferentes formas. Determinar sus diferentes propiedades es un requisito esencial para entender y diseñar nuevos mecanismos para el crecimiento de nanopartículas con aplicaciones directas en fotónica y biomedicina. En este capítulo mostramos una secuencia de transiciones estructurales en los agregados de CTAB inducidas por el decanol. En particular observamos la formación de bicapas de CTAB a concentraciones intermedias de decanol. Estos resultados proporcionan un diagrama de fase del agregado donde la excentricidad y morfología cambian en función del decanol a CTAB. Este trabajo ha sido crucial para entender el papel que juega el decanol en la preparación de nanovarillas que son altamente anisotrópicas.

Las simulaciones de cientos de nanosegundos no son siempre suficientes para garantizar el equilibrio termodinámico de los agregados. No obstante, se puede obtener información útil de las

simulaciones a partir de agregados preensamblados, ya que estas simulaciones pueden servir para descartar configuraciones inestables del sistema. Storm et al. comentan en un artículo que las condiciones de equilibrio no se alcanzan en 100 ns de simulación para el CTAB. En mi opinión, el sistema es dinámicamente lento debido a mínimos en la superficie de energía potencial del sistema. Cuando hay un agregado de CTAB en disolución, espontáneamente se forma una doble capa eléctrica de iones bromos inducida por la agregación en la superficie de las cabezas polares del surfactante. La magnitud de la repulsión electrostáticas entre dos micelas es grandes y en la práctica implica que la dinámica de unión de dos agregados de CTAB en disolución sea demasiado lenta y no pueda alcanzarse por simulación en tiempos razonables de cálculo. Es posible obtener resultados equilibrados si se parte de configuraciones iniciales cerca del estado de equilibrio y analizar la estabilidad de los agregados preensamblados. Por otra parte las simulaciones, pueden proporcionar información útil acerca de la estructura de los agregados que a menudo es difícil de obtener experimentalmente.

El capítulo 6 pretende resumir la parte computacional del trabajo del candidato realizado en colaboración con excelentes grupos de investigación, tanto experimentales como teóricos en el estudio de crecimiento de nanopartículas de oro. En la primera parte del capítulo encontramos agregados de CTAB esféricos que crecen en tamaño de manera sistemática con la concentración de CTAB. Cuando la concentración de CTAB es igual a la concentración micelar crítica, nuestros colaboradores obtienen los mejores resultados. En la segunda parte del capítulo relacionamos la difusión de iones de oro precursores con el hábito de crecimiento cristalino de nanopartículas esfericas de oro, para dar lugar a nanovarillas. Este proceso se explica en base a la secuencia de transiciones en los agregados de CTAB y decanol descritos en el capítulo 5.

Podemos ver que estos dos capítulos finales tienen un punto en común muy claro que es determinar la estructura y morfología de los agregados formados por el surfactante más empleado en los métodos de síntesis de nanopartículas metálicas como es el CTAB. En nuestro caso nos centramos en las nanopartículas de oro. Debido a la dificultad que se tienen en los experimentos para poder determinar la estructura de la interfase, la simulación computacional tiene la oportunidad de explicar que ocurre sobre la superficie del oro y con ello ayudar a optimizar los métodos de síntesis.

Los puntos en común en estos 2 capítulos de este segundo bloque son que era necesario disponer, para lás distintas moléculas orgánicas, de un campo de fuerzas para utilizar en las simulaciones, y que ese modelo debía ser validado antes de añadir aditivos a la simulación y confinarlo entre dos paredes de oro. El modelo para la molécula de CTAB es diferente al que emplean Kumar *et al.* en sus simulaciones, en el que la carga es de una unidad y está repartida a partes por igual para cada uno de los 4 grupos vecinos del átomo de nitrógeno (3 CH_3-N-CH_2), y no es realista. De esta forma la carga parcial asociada a la molécula es la que se esperaba para el catión CTA^+. No obstante, el nitrógeno permanece neutro y teniendo en cuenta que es de los elementos más electronegativos de la tabla periódica, nos parecía que el modelo se podía mejorar. En una colaboración, el Dr. Mauricio Alcolea nos proporcionó para la molécula de CTAB y decanol sendos modelos de cargas obtenidos a partir de cálculos *ab-initio*. En este modelo, como era de esperar, se le coloca una carga negativa al átomo de nitrógeno.

Si queremos entender que es lo que ocurre sobre la superficie del oro debemos comprender antes como se comporta el sistema en disolución, los resultados que obtendremos serían representativos del sistema. Para validar el modelo de CTAB simulamos diferentes agregados en disolución y añadimos aditivos al agreagado como son el NaBr y el decanol como cosurfactante y comparamos con los experimentos. Por último, conseguimos identificar transiciones de fase estructurales de los agregados

en el cual se origina la selectividad en la transmisión de calor o de los iones oro para algunas caras de la nanopartícula y que han ayudado a explicar dos métodos de síntesis de nanovarillas de oro recientemente propuestos por nuestro colaboradores expermimentales.

Introducción General

En esta tesis se propone el estudio a escala molecular de interfases sólidas de gran complejidad estructural, en las que las fases volumétricas no están separadas por una sola superficie, sino por una capa intermedia adsorbida. El estudio tradicional de estos sistemas se ha llevado a cabo experimentalmente mediante diversas técnicas de dispersión superficial de ángulo bajo. Desgraciadamente, con frecuencia es imposible resolver de la señal los efectos estrictamente superficiales de los volumétricos, lo que dificulta enormemente el análisis y la interpretación de las señales.[1]

A lo largo de este proyecto vamos a ver el estudio en detalle de las interfases de hielo y oro, con la finalidad de ayudar a esclarecer los mecanismos de crecimiento de los copos de nieve y formación de nanovarillas de oro estabilizados por bromuro de hexadeciltrimetilamonio (CTAB). Conocer los mecanismos de crecimiento es fundamental, en el caso del hielo para ayudar a comprender los fenómenos meteorológicos o el proceso de criopreservación [2, 3, 4, 5, 6] y en el caso de las nanopartículas de oro (AuNP) son ampliamente utilizadas en biomedicina o tratamiento de aguas contaminadas. Comprendiendo la interfase de oro se pueden optimizar los métodos de síntesis. [7, 8]

La mayoría de los fenómenos fisicoquímicos que ocurren a nuestro alrededor se producen en las superficies. Dos ejemplos muy evidentes son la oxidación de un clavo de hierro por la acción del oxígeno con el paso del tiempo y el bronceado veraniego que adquirimos cuando se produce una reacción fotoquímica en la superficie de la piel.

Por definición, una superficie o interfase se corresponde con una zona del espacio que delimita dos fases volumétricas con diferentes propiedades físicas o químicas. Las magnitudes de las propiedades que pueden presentar las interfases dependen de la composición de las mismas que determinan las interacciones intermoleculares. No es lo mismo tener una superficie reactiva capaz de formar enlaces covalente entre las dos fases separadas, como en el caso de la reacción de formación de nailon, que es justo en la interfase donde se produce la polimerización, que una superficie inerte como sería el caso de una superficie de dióxido de carbono en una atmósfera de argón. [9] En este segundo tipo de superficies o interfases, las fuerzas intermoleculares de largo alcance de van der Waals, London, etc. determinan el comportamiento del sistema. Un ejemplo de la intensidad de estas fuerzas se dan en las escamas de los dedos de muchos lagartos. El elevado área de la superficie de los dedos permite un gran número de interacciones con la pared suficientes para compensar su peso y adherirse a las mismas. Los fenómenos de superficie son más intensos a medida que la relación entre el área y el volumen aumenta.

Los tipos de interfases que se conocen varían en función del estado de la materia de las dos fases en contacto. Por lo tanto, que sepamos pueden existir interfases de tipo sólido–sólido, sólido–líquido, sólido–vapor, líquido–líquido y líquido–vapor. No obstante en determinadas condiciones de presión y temperatura, la interfase sólido–vapor se ve modificada por un fenómeno de superficie

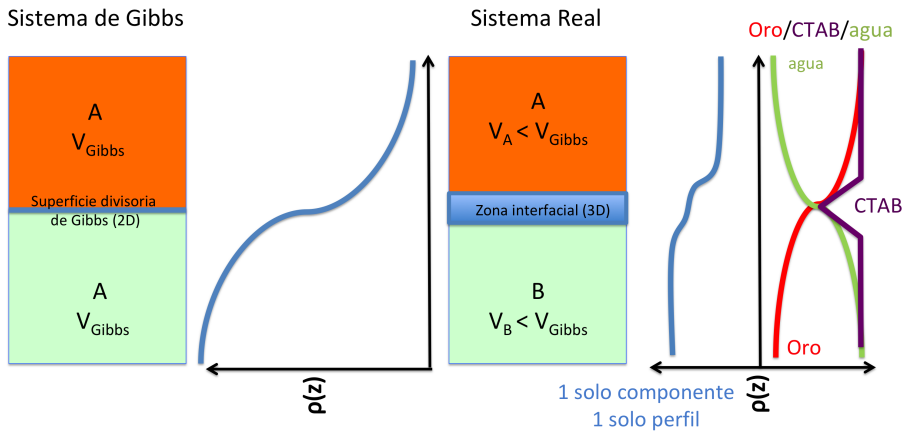

Figura 1.1. Definición de interfase por el criterio de Gibbs y en un sistema real. En las superficies definidas en 2D, es suficiente con determinar el perfil de densidad en la dirección perpendicular a la interfase para determinar las variaciones de una propiedad. Por el contrario, cuando la definición de la interfase se realiza en 3D el análisis requiere extenderse a otra dirección lateral (x o y).

denominado prefundido (*premelting*), que consiste en la fusión de los planos sólidos en contacto con el vapor y la formación sobre la superficie de una película líquida de espesor finito con la temperatura. Este efecto produce una modificación de la interfase sólido–vapor y se forma una interfase compleja sólido–líquido–vapor.

En 1751 se introduce por primera vez el concepto de tensión superficial para un líquido,[10] y en relación a las interfases el primer gran hito fueron los estudios de Young y Laplace en 1805. La ecuación de Young-Laplace relaciona la tensión superficial de un líquido con el ángulo de contacto de un fluido capilar.[11, 12] Actualmente, las interfases se describen como superficies no planas, sino con oscilaciones, que se producen como consecuencia de la agitación térmica y que se propagan como ondas planas. Las ondas planas responsables de las oscilaciones locales se conocen como ondas capilares y permiten la fluctuación de la posición local de la interfase como resultado de la dinámica de la superficie. La amplitud de las ondas capilares estÃ¡n directamente relacionadas en la energía libre interfacial. Por otro lado la energía libre interfacial es la principal barrera energética de los procesos de nucleación y de crecimiento cristalino. Recientemente se han desarrollado varios métodos para determinar la energía libre interfacial como son el método de *semilla*[13], método de integración de molde [14], o el método de fluctuaciones capilares [15, 16] que fue empleado en esta tesis.

Las interfases modulan la variación gradual de las propiedades de dos fases volumétricas en contacto a medida que avanzamos en la dirección perpendicular al plano interfacial. Gibbs en 1878 dio a conocer su modelo de superficies en el cual la interfase presenta un volumen nulo (2D), sentando las bases actuales de la termodinámica de superficies.[17] Más tarde en 1945, Guggenheim[18] desarrolla un modelo de superficies en el que la interfase es una región interfacial tridimensional (3D) que se aproxima más al modelo real (ver figura 1.1).

Empleando la simulación molecular podemos explorar en gran detalle el espacio que abarcan las superficies o interfases. [19, 20] En esta técnica, se parte de un modelo aproximado de potencial

intermolecular para describir el sistema bajo estudio, y se resuelven las ecuaciones del movimiento de las moléculas. Aunque en principio la dinámica está regida por las ecuaciones de la mecánica cuántica, en la práctica a las temperaturas de dos o más centenares de Kelvin, para moléculas de peso molecular medio, la aproximación clásica es suficiente.[21] En tal caso, el problema se reduce al estudio de la dinámica molecular clásica, que se puede describir adecuadamente mediante las ecuaciones de Newton.[22]

A efectos prácticos, la resolución de la dinámica en esta aproximación consiste en la solución de un sistema de ecuaciones diferenciales de segundo grado acopladas, lo que nos proporciona la trayectoria del sistema, es decir, el conjunto de posiciones y velocidades adoptadas por los átomos en función del tiempo.[19, 20]

En esta tesis, estudiamos interfases de gran complejidad, que solo se pueden describir adecuadamente mediante modelos de potencial intermolecular relativamente detallados, a escala atómica. Como resultado, es preciso estudiar el movimiento de entre 20.000 y 8.000.000 átomos, lo que supone unas exigencias computacionales muy significativas.

Por este motivo, es preciso abordar el problema mediante técnicas de computación avanzada, basadas en paradigmas de paralelización. En esta tesis se propone el uso del paquete GROMACS para llevar a cabo las simulaciones, ya que permite el estudio con distintos modos de paralelización para sistemas como los que se requieren en nuestro proyecto.[23]

Los modelos de potencial intermolecular que utilizaremos tienen resolución a escala atómica, y se corresponden con la aproximación de potencial multicentros rígidos no polarizables.[19, 20] En estos modelos, se da cuenta de las interacciones repulsivas y de la atracción dispersiva asociando a cada átomo o grupo de átomos un sitio de interacción de fuerzas centrales tipo Lennard-Jones; mientras que se da cuenta de la polarización permanente de las moléculas mediante sitios adicionales con cargas eléctricas parciales. En esta escala, las distancias y ángulos de enlace se describen cuantitativamente, pero se suponen rígidas. En la literatura, se demuestra que estos modelos son sorprendentemente efectivos a la hora de describir el comportamiento de una gran variedad de sistemas moleculares dominados por interacciones no-covalentes.[24, 25, 26, 27] Como limitación, estos potenciales son no polarizables y no dan cuenta de la reactividad química, lo que es razonable para sistemas suficientemente estables como los estudiados en esta tesis.

Aunque las simulaciones permiten producir una ingente cantidad de datos brutos en forma de trayectorias moleculares, el interés científico del proyecto recae esencialmente en el análisis cuantitativo dirigido a racionalizar las observaciones de los fenómenos producidos en las superficies.

La simulación molecular tuvo su origen en los años cincuenta. Se desarrollaron dos técnicas computacionales que permiten estudiar con precisión el comportamiento de los sistemas modelo utilizando los conceptos básicos de la mecánica estadística. La primera de estas técnicas fue desarrollada por Nicholas Metropolis y los matrimonios de Rosenbluth y Teller, este método se llama Metropolis Monte Carlo. Aparece en 1953 y se basan en números aleatorios y probabilidad. Plantean la idea simple de que los sistemas más estables son los más probables. [28] El otro método de simulación principal fue desarrollado por Berni Alder y Thomas Waingwright, se conoce como Dinámica Molecular (DM). Aparece en 1957 y se basa en resolver las ecuaciones de Newton para el movimiento de todos los átomos en el sistema. [29]

Utilizando la mecánica estadística, podemos calcular promedios temporales relacionando una propiedad física con las posiciones y momentos de los átomos. El colectivo natural de DM es el microcanónico (NVE), en el cual el número de partículas N, el volumen V y la energía total del

sistema E se conservan. Si se desea obtener información del sistema manteniendo constantes otras variables termodinámicas, como son la presión y la temperatura, podemos utilizar barostatos y termostatos respectivamente. Los más empleados habitualmente son los termostatos desarrollados por Bussi–Donadio o el de Andersen y los barostatos de Berendsen, Parrinello-Rahman o Nosé-Hoover.[30, 31, 32, 33, 34] Todos estos algoritmos están implementados y ampliamente testados en paquetes de software como son DL_POLY, LAMMPS o GROMACS, este último fue el paquete empleado en las simulaciones de DM de esta tesis.[35, 36, 23]

El marco conceptual de referencia para nuestro trabajo es la mecánica estadística, que permite relacionar propiedades macroscópicas observables experimentalmente a partir de las trayectorias microscópicas de las simulaciones.[37, 38] En particular, partiendo de modelos simplificados de carácter mesoscópico, es posible relacionar la naturaleza de las fluctuaciones de altura de las superficies involucradas en la interfase con unas pocas propiedades relevantes como son la tensión superficial y el potencial interfacial. De este modo, caracterizamos el comportamiento global de las superficies, que de acuerdo al marco teórico simplificado se pueden dividir entre superficies lisas y rugosas. Los modelos mesoscópicos nos permiten clasificar el comportamiento de las interfases en términos del comportamiento de estas fluctuaciones, lo que a su vez determina la naturaleza del crecimiento cristalino y por ende el hábito de los cristales formados.[39, 40, 41]

De esta discusión se deduce que una de las herramientas metodológicas esenciales para nuestro estudio es un procedimiento sistemático y fiable para caracterizar las superficies de la interfase. En este trabajo utilizaremos un procedimiento empleado ya en trabajos anteriores del grupo de investigación que han funcionado muy bien como forma de caracterizar la interfase y extraer propiedades cuantitativas como la tensión superficial o el potencial interfacial.[42, 43, 44] Mediante un parámetro de orden, es posible distinguir las moléculas pertenecientes a una u otra fase, y la superficie se puede determinar entonces sencillamente mediante la localización de las moléculas presentes en la frontera con las dos fases, que se corresponden justamente con aquellas en las que el parámetro de orden cambia bruscamente.

En 1951 Burton, Cabrera y Frank presentaron un gran avance en la teoría de crecimiento de cristales aplicando métodos de mecánica estadística en el tratamiento de las superficies.[40] En un sólido cristalino los átomos se disponen en una red periódica que se extiende en las tres dimensiones del espacio. Los sólidos pueden crecer mediante la llegada de átomos desde la fase vapor o líquida a posiciones vacías de la red cristalográfica. Este proceso de crecimiento cristalino ocurre cuando la energía libre de los átomos en la fase sólida es menor que en la fase líquida o gaseosa.

Un fenómeno importante en el crecimiento cristalino reside en que si el cristal presenta una superficie perfecta con planos atómicos sin vacantes, la adhesión de un átomo al cristal resulta energéticamente desfavorable debido a la presencia de un número de vecinos inferior respecto a lo que se espera para la fase sólida volumétrica. Cuando esto ocurre, el mecanismo de crecimiento está activado mediante la nucleación de islas sobre la superficie que tienen que adquirir un tamaño crítico para poder crecer y propagarse. Es decir, los átomos que alcanzan la superficie deben poder ser enlazados por un número de vecinos considerable y esto no ocurre en superficies perfectas. La energía libre promedio de los átomos pertenecientes a las islas es mayor en relación a los átomos en la superficie cristalina subyacente, lo que se debe a que los átomos en el borde de la isla tienen menos vecinos. El coste de en la formación del núcleo se reduce a medida que la fracción de los átomos del borde disminuye cuando aumenta el tamaño de la isla. Los posibles defectos o dislocaciones escalonadas proporcionan una base energética para el mecanismo de crecimiento cuando

la saturación de átomos es baja, deteniéndose el crecimiento cuando los escalones se completan, y dando como resultado una superficie suave desde el punto de vista cristalográfico (planos compactos con índices de Miller bajos) y sin sitios activos de unión debido a la falta de escalones.

Cuando el sólido cristalino crece en condiciones de saturación baja, el crecimiento del cristal se produce en espiral y esta controlado por dislocaciones. A medida que aumenta la saturación se favorece la nucleación bidimensional que da como resultado la formación de islas. Al igual que pasa con la nucleación en tres dimensiones, el núcleo debe vencer la barrera de nucleación mientras no tenga un tamaño crítico que le permita crecer sin ningún coste adicional de energía libre. Por lo tanto se dice que este proceso de nucleación es lento y activado por la energía libre interfacial. No obstante, cuando la isla consigue alcanzar el tamaño crítico el crecimiento se produce en los bordes de la isla, se propaga a toda la superficie y genera una superficie perfectamente lisa en que volvemos a necesitar que el proceso de nucleación vuelva a activarse. Frenkel sugiere que el problema de la nucleación y del proceso energéticamente activado se solventa con la rugosidad térmica que presenta la superficie y que genera una alta concentración de escalones e implica un crecimiento continuo La transición de una superficie lisa con fluctuaciones macroscópicas muy próximas a cero, a una superficie rugosa en donde las fluctuaciones divergen se denomina transición de rugosidad y fue propuesta por Burton, Cabrera y Frank. [40] Este cambio de hábito permite un crecimiento sin activar que depende linealmente con la saturación. La primera evidencia experimental en la que se pudo ver la transición de rugosidad fue reportada en 1971 por Pavloska y Nenow. Determinaron la forma de los cristales de difenilo para varias temperaturas y pudieron ver que los cristales se redondean a partir de cierta temperatura cuando aparece la transición de rugosidad y pierden la forma de prisma. [45, 46]

En el primer bloque de esta tesis nos centraremos en la interfase hielo–vapor y como relacionar los hábitos de crecimiento cristalino de los copos de nieve con los fenómenos de superficie que se producen en la interfase hielo–vapor (ver figura 1.2). Estos fenómenos de superficie son la formación de una película prefundida (*prefundido*) y la rugosidad de la superficie sólida (*roughening*). El fenómeno de prefundido fue propuesto por primera vez en las superficies de hielo por Faraday en 1842.[47] Esta película líquida es responsable de la diversión de patinar sobre hielo. Más importante aún, en lo que respecta a los hábitos de los cristales y las formas de crecimiento, la rugosidad de una superficie tiene consecuencias dramáticas en la dinámica, ya que señala un cruce desde un crecimiento nucleado en dos dimensiones a un mecanismo de Knudsen, más rápido y que depende linealmente con la saturación.

Los copos de nieve son cristales con forma de prisma hexagonal. La morfología de los prismas puede ser plana en forma de plato o alargada en forma de columna. Estas geometrías dependen de la temperatura y las condiciones de saturación de vapor de agua en la atmósfera durante el crecimiento del cristal. En el diagrama de Nakaya de la figura 1.3 vemos los diferentes tipos de prismas para cada temperatura y humedad. Nakaya observó que en torno a 0ºC los copos de nieve son de tipo plato hexagonal. Si desciende la temperatura en torno a -5ºC, los copos de nieve que se forman presentan una estructura de prisma columnar. En torno a -10 ºC los copos de nieve vuelven a ser prismas planos. Por último, a unos -20ºC los cristalitos de hielo no presentan selectividad por una u otra morfología y se observan los dos tipos de copos de nieve. Si bien es cierto que la temperatura condiciona la forma de los cristales y su complejidad, también ocurre que el aumento de la saturación condiciona la aparición de las formas dendríticas en el crecimiento, haciendo mucho más complejo todo el proceso. Más adelante vamos a poder detenernos con más detalle la estructura

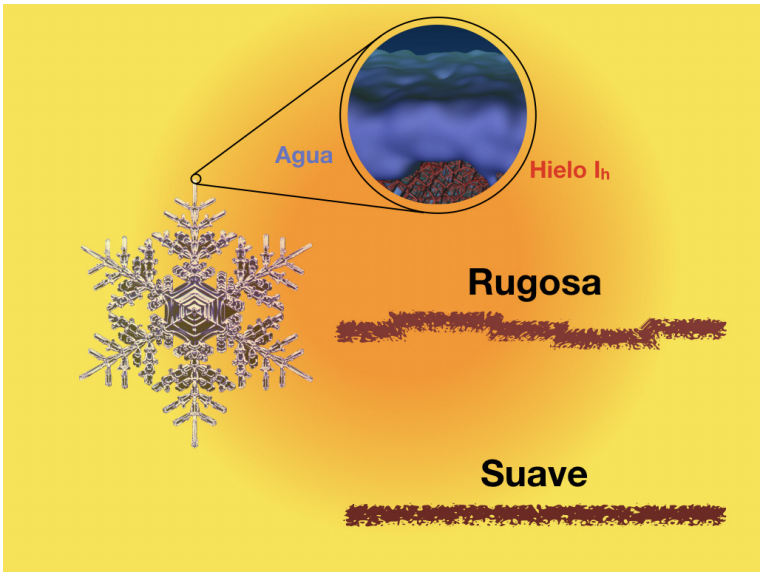

Figura 1.2. Ilustración de los fenómenos de superficie en una interfase hielo–vapor. El cristal de hielo se encuentra en equilibrio con una interfase líquida y una interfase gas. Debajo de la película líquida puede ocurrir que el sólido sea suave o rugoso en función de la amplitud de las fluctuaciones capilares.

cristalográfica del hielo I_h, pero llegados a este punto necesitamos saber dos cosas: en la superficie de un cristal de hielo I_h tenemos dos tipo de facetas cristalográficas, la cara basal y la cara prismática principal (pI). La cara basal como su nombre indica se encuentra en las bases del prisma hexagonal y su crecimiento es responsable de la forma de tipo columna. Por el contrario, la caras pI son las caras laterales del prisma hexagonal y su crecimiento permite que el cristal adopte la forma final de plato.

No obstante el origen de estas formas se pueden explicar en base transiciones de rugosidad y de superficie fundida. Gracias al hallazgo de Burton, Cabrera y Frank, hoy sabemos que una superficie rugosa produce un crecimiento continuo del cristal sin necesidad de dislocaciones o nucleación de islas. La rugosidad en las superficies tiene su origen en la agitación térmica y en las fluctuaciones capilares. La forma intrínseca de propagarse a lo largo de la superficie produce la formación/disgregación constante de escalones. Por lo tanto, la superficie presenta fluctuaciones locales de altura que se propagan por toda la interfase, cuya magnitud se relaciona directamente con la energía libre interfacial. Hoy en día se conoce que la transición de rugosidad esta bien descrita por la transición de fase topológica de Kosterlitz–Thouless. [48, 49] En la transición de Kosterlitz–Thouless se describen vórtices y antivórtices (que se agrupan en pares de manera similar a como ocurre en el caso de la superconductividad de metales con los pares de Cooper) a partir de cierta temperatura crítica. En el caso de superficies los gradientes de altura a lo largo de la superficie son semejantes a los vórtices en la transición de fase de Kosterlitz–Thoules. La temperatura crítica a partir de la cual aparecen vórtices en la superficie se conoce como temperatura de rugosidad, $T_R = 2\tilde{\gamma}_{sl}/b^2$, en donde $\tilde{\gamma}_{sl}$ es la rigidez interfacial de la superficie sólida y b el parámetro de red asociado en la dirección perpendicular a la interfase. [50, 49] Resumiendo, las superficies pueden ser suaves o rugosas dependiendo de si la amplitud de las fluctuaciones capilares que se producen en la interfase son finitas o por el contrario divergen. No obstante, puede aparecer un estado intermedio

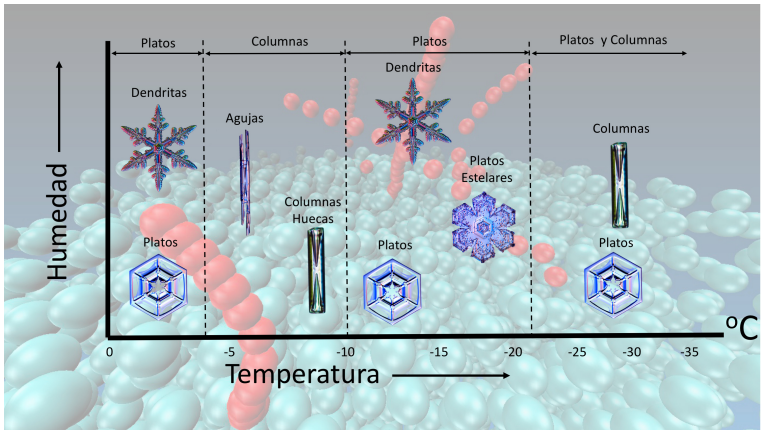

Figura 1.3. Diagrama de Nakaya adaptado. La forma de los copos de nieve depende de las condiciones de presión, temperatura y humedad. Las formas que podemos encontrar varían dependiendo la cara de crecimiento preferente, encontrando cristales planos y cristales columnares. Podríamos decir que cada copo de nieve escribe una historia diferente durante su formación como decía Nakaya en su *h*aiku: ."[El]los nos envían cartas desde el cielo".

conocido como prerugosidad (*p*reroughening). Este estado se caracteriza porque la superficie sólida presenta desorden pero las fluctuaciones de la interfase son finitas. Para diferenciar la transición de rugosidad con respecto a la transición de prerugosidad, podemos imaginar la superficie de un sólido como una pared pintada con gotelé. Para la transición de prerugosidad las gotas tienen un área que ocupan unas pocas moléculas de agua y una altura equivalente a una capa de molecular de agua. Por el contrario, cuando la transición es de rugosidad, el área y la altura de las gotas llega a ser de un número ilimitado de veces la celda unidad de hielo. Mientras que cuando la superficie es lisa no veríamos pintada con gotelé la pared.

Otro fenómeno de superficie interesante en el contexto de transiciones de fases topológicas de orden a desorden es la superficie prefundida (*surface melting*). Un líquido puede ser relativamente fácil enfriarlo por debajo de la temperatura de fusión antes de que se produzca la cristalización. Esto ocurre debido a la necesidad de un núcleo sólido de superar el exceso de energía en la interfase sólido–líquido y que solo puede lograrse mediante un alto grado de subenfriamiento. Este problema puede decirse que es el equivalente tridimensional al de formación de islas en el crecimiento epitaxial. Para un sólido, no es posible sobrecalentarlo por encima del punto de fusión y la razón parece ser porque la fusión de los primeros planos sólidos puede ocurrir de forma espontánea en la superficie del sólido a una temperatura inferior que la de fusión. De manera general cuando se produce el fundido de los planos atómicos superficiales la interfase sólido–vapor se ve modificada formándose una interfase compleja compuesta por una interfase sólido–líquido y otra líquido–vapor. Por supuesto el número de planos sólidos fundidos o el espesor de la capa líquida aumenta más y más a medida que la temperatura se acerca a la temperatura de fusión del sólido. En definitiva, en la transición de rugosidad el desorden se produce en las distintas alturas de las posiciones de red de los átomos en la superficie sólida, y en la superficie fundida lo que se produce es una perdida de orden lateral que finalmente se traduce en una perdida de orden en la dirección perpendicular a la interfase sólido–líquido. Por otra parte, todas nuestras sospechas apuntan a que los hábitos de crecimiento cristalino condicionan las formas de los cristalitos de hielo y dichos hábitos están directamente

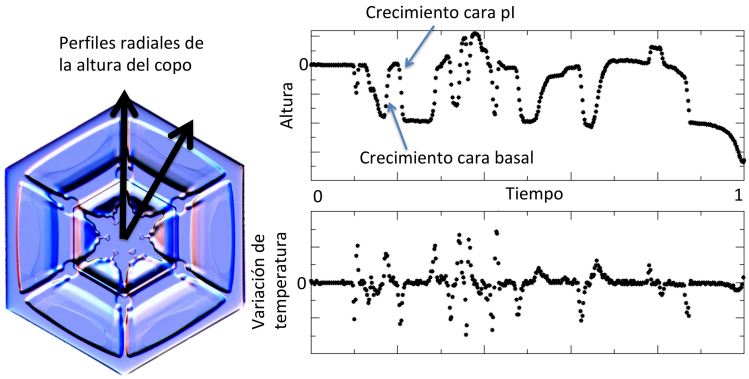

Figura 1.4. Ejemplo de un copo de nieve tipo plato (www.snowcrystals.com). Los hábitos de crecimiento cristalino se regulan con la temperatura y producen variaciones en la forma del cristal. Trazando el perfil radial de alturas podemos obtener el horizonte de un copo de nieve y obtener la secuencia de aumentos de temperatura necesaria para formar este copo de nieve. Las unidades que se muestran son arbitrarias ya que el perfil es obtenido a través de las intensidades de los píxeles de la imagen en función de la distancia, también desconocida, al borde del copo. Supondría un gran reto y enorme avance el hallazgo de los factores para situar la escala de alturas y temperaturas, para con ello, predecir la forma de un copo de nieve a partir de la secuencia temporal de temperaturas.

regulados por las transiciones de fase superficiales.[51, 52] En la figura 1.4 vemos un copo de nieve de tipo plato cuya formación ocurrió según el diagrama de Nakaya bajo condiciones de saturación bajas. Si trazamos el perfil de alturas del cristal utilizando un perfil de intensidad de los píxeles de la foto, obtenemos el perfil de altura del copo de nieve y podemos identificar a cada momento las caras cristalográficas que van creciendo, ya que cuando la altura permanece constante es la cara pI la que crece de manera controlada y su crecimiento se acelera cuando la altura disminuye. Por otra parte, si es la cara basal la que crece la altura del perfil aumenta. Si recordamos el diagrama de Nakaya los cambios de forma de los copos de nieve son resultado de las condiciones en las que se han formado por lo tanto podemos relacionar las variaciones infinitesimales de altura a cada unidad con cada unidad de tiempo y suponer que esos cambios se producen por efecto de la temperatura. La arbitrariedad de las unidades reside en el desconocimiento de cuanto cambia la intensidad de un pixel en función de la altura, ni del tiempo total que tardó el copo de nieve de la figura en alcanzar el tamaño final. No obstante, para explicar de manera cualitativa en esta introducción es suficiente con ver las discontinuidades debidas a los cambios de regímenes en el crecimiento de las caras involucradas. Para este copo de nieve podríamos decir que durante su viaje por las nubes, viendo el perfil y el diferencial del perfil con el progreso del copo de nieve, ha sufrido al menos 17 transiciones de fase superficiales que le confirieron su morfología final.

En relación al otro gran bloque de este proyecto de tesis, trataremos de estudiar e interpretar la interfase compleja oro-CTAB-agua. En las últimas décadas se ha producido un auge en los métodos de síntesis para nanopartículas con gran variedad de formas y tamaños. El aumento de recursos científicos destinados a satisfacer esta demanda reside en el despegue de la nanotecnología y basa su importancia en la diversidad de aplicaciones que presentan las nanopartículas en nuestro día a día. Las aplicaciones más punteras como son la biomedicina, captura y reserva de energía o el

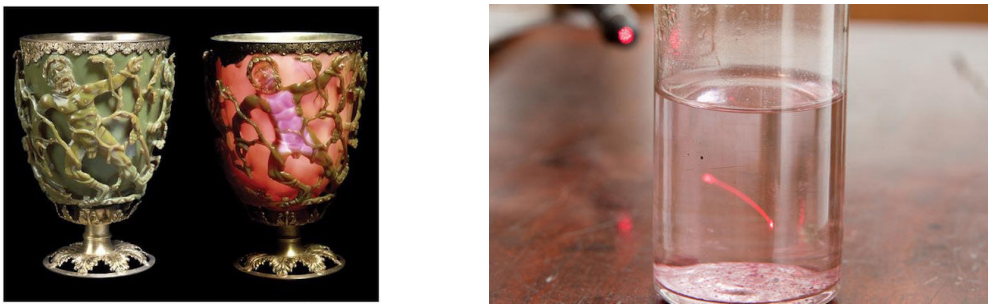

(a) Copa de Licurgo **(b)** Efecto Tyndall

Figura 1.5. (a) Copa de Licurgo (S. IV), Museo Británico. (b) Efecto Tyndall en una disolución coloidad de partículas de oro. Fuente: Paul Wilkinson (The Royal Institution).

almacenamiento de datos, ven en las nanopartículas un potencial hasta hoy en día no imaginado. Otro ejemplo, mucho más antiguo, en las que encontramos nanopartículas en concreto de oro y plata, es la denominada Copa de Licurgo. Datada del siglo IV esta reliquia histórica presenta un cambio de color del material de la copa cuando se cambia el ángulo de exposición a la luz.[53, 54] Este efecto de dicroísmo es debido a la composición del vidrio con el que fue elaborada. Hoy en día sabemos que este fenómeno conocido como efecto Tyndall tiene su origen en las nanopartículas de oro y plata ensambladas en un sistema coloidal (ver figura 1.5).

Faraday en el año 1857 fue el primero que responsabilizó a los coloides de oro del color rojo de la disolución debido a la dispersión de la luz en longitudes de onda que dependen directamente del tamaño del coloide. Otro ejemplo de la dispersión de la luz debido a la interacción con un medio coloidal, es el haz de luz resultante del paso de la radiación a través de un banco de nubes. Este fenómeno se conoce como efecto Tyndall.

Debido al avance de la nanotecnología se han desarrollado multitud de métodos de síntesis de nanopartículas y necesitamos entender con detalle cuales son los fenómenos fisicoquímicos que ocurren durante la síntesis para poder ayudar a optimizar los procesos y como resultado obtener métodos de síntesis de nanopartículas con altos rendimientos que permitan el control de la forma y tamaño, como son esferas, cubos y varillas, estas últimas habitualmente se conocen como *nanorods*. [55, 56, 57, 58, 59]

Para entender los procesos de síntesis necesitamos recurrir a la ciencia de superficies que nos ayuda a entender la interfase resultante. En los principales métodos de síntesis de nanovarillas conocidos, es frecuente el empleo de semillas esféricas de oro. Estas semillas de oro se añaden a un disolución rica en iones oro para que se produzca la deposición de los iones sobre las nanopartículas y con ello el crecimiento de las mismas. En la disolución es muy habitual el empleo de CTAB o alguno de sus derivados halogenados de yodo o cloro. El CTAB es un surfactante catiónico que permite la estabilidad coloidal de las semillas evitando la agregación durante la síntesis, y va a estar adsorbido sobre las superficies de la nanopartícula, creando una interfase compleja (figura 1.6) que ayuda a la regulación del crecimiento. La morfología de los agregados de CTAB resultantes depende de las propiedades intrínsecas de cada superficie de oro.

La anisotropía en la adsorción de CTAB está por lo tanto relacionada con la textura de cada superficie. En el caso del hielo la rugosidad depende de los cambios producidos con la temperatura en los defectos de superficie, y en el caso del oro, nos referimos a la textura como la forma

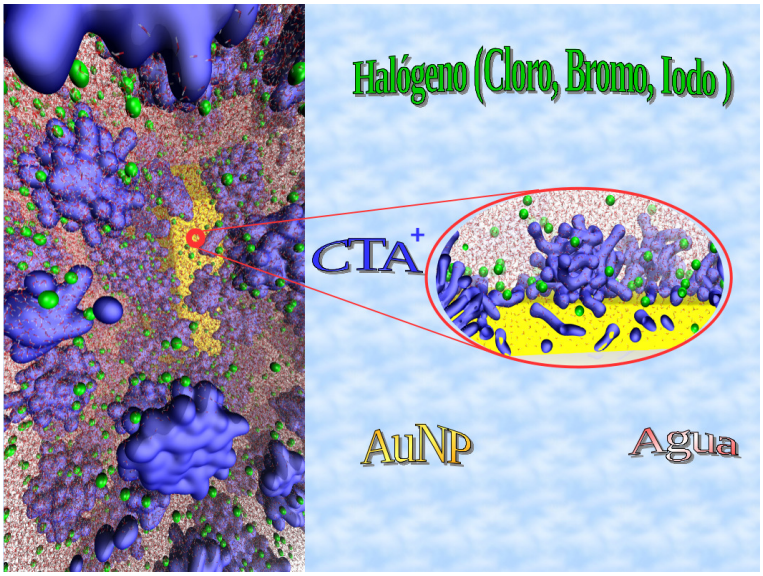

Figura 1.6. Ilustración de una interfase oro-CTAB-agua. El CTAB se deposita sobre las superficies de oro regulando la difusión de iones sobre la superficie y por lo tanto el crecimiento de la nanopartícula.

de compactarse los átomos de oro en cada orientación cristalográfica. Así, superficies de oro con índices de Miller altos {250} presentan superficies más escalonadas que los planos cristalográficos más compactos como el {100} o el {111}. Como siempre, esperamos diferentes barreras en los procesos de nucleación y crecimiento de nanopartículas dependiendo de cada orientación preferente de crecimiento. No obstante, hemos visto que la interfase es un sistema muy complejo con agregados coloidales adsorbidos sobre el oro, y eléctricamente cargados por la existencia de un doble capa eléctrica. Precisamente por esta razón, el proceso de crecimiento de la nanopartícula esta controlado por el CTAB, dirigiendo el tráfico de iones hacia la superficie.

En el proceso de crecimiento de nanopartículas pueden distinguirse dos etapas. La primera etapa consiste en un proceso difusivo de los iones oro desde la disolución hacia la superficie, y la segunda etapa es donde se produce la reacción con la superficie. Es en esta segunda etapa donde tiene un mayor efecto la energía interfacial de cada orientación de oro. No es descabellado suponer que el proceso difusivo es un fenómeno mucho más lento que el tiempo de reacción y por ello consideramos que la barrera difusiva de iones oro es el principal inconveniente para el crecimiento de las semillas. A partir de esta observación se han desarrollado diferentes teorías para el crecimiento de cristales, destacando el mecanismo de LaMer. [60, 61] Este mecanismo se compone de varias etapas, destacando en la cual se encuentra que el proceso de nucleación y el crecimiento tiene lugar bajo el control de la difusión de los iones. En esta tesis veremos que la naturaleza de la capa de CTAB adsorbida sobre el oro permite controlar la velocidad de deposición del oro y por tanto el crecimiento selectivo de una u otra cara del oro.

Bibliografía

[1] P. S. Pershan and M. Schlossman, *Liquid Surfaces and Interfaces: Synchrotron X-ray Methods*. Cambridge: Cambridge University Press, 2012.

[2] X. Y. Liu, E. S. Boek, W. J. Briels, and P. Bennema, "Prediction of crystal growth morphology based on structural analysis of the solid-fluid interface," *Nature*, vol. 374, pp. 342–345, 1995.

[3] I. Sunagawa, ed., *Morphology of Crystals*. Tokyo: Terra Scientific Publishing Company, 1987.

[4] K. G. Libbrecht, "The physics of snow crystals," *Rep. Prog. Phys.*, vol. 68, pp. 855–895, 2005.

[5] Y. Furukawa and J. Wettlaufer, "Snow and ice crystals," *Phys. Today*, vol. 60, pp. 70–71, 2007.

[6] H. R. Pruppacher and J. D. Klett, *Microphysics of Clouds and Precipitation*. Heidelberg: Springer, 2010.

[7] E. C. Dreaden, A. M. Alkilany, X. Huang, C. J. Murphy, and M. A. El-Sayed, "The golden age: gold nanoparticles for biomedicine," *Chem. Soc. Rev.*, vol. 41, pp. 2740–2779, 2012.

[8] P. Falagan-Lotsch, E. M. Grzincic, and C. J. Murphy, "New advances in nanotechnology-based diagnosis and therapeutics for breast cancer: An assessment of active-targeting inorganic nanoplatforms," *Bioconjugate Chemistry*, vol. 28, no. 1, pp. 135–152, 2017. PMID: 27973767.

[9] P. Llombart, *Molecular simulation of argon adsorbed pancakes on solid CO2 surfaces*. 2014.

[10] J. A. von Segner *Comment. Soc. Reg. Götting*, 1751.

[11] T. Young, "An essay on the cohesion of fluids," *Philosophical Transactions of the Royal Society of London*, vol. 95, pp. 65–87, 1805.

[12] P. S. Laplace, *Traité de Méchanique Céleste*, vol. 2, p. 479. Bachelier, Paris, 2nd ed., 1805.

[13] X.-M. Bai and M. Li, "Calculation of solid-liquid interfacial free energy: A classical nucleation theory based approach," *The Journal of Chemical Physics*, vol. 124, no. 12, p. 124707, 2006.

[14] J. R. Espinosa, C. Vega, and E. Sanz, "The mold integration method for the calculation of the crystal-fluid interfacial free energy from simulations," *The Journal of Chemical Physics*, vol. 141, no. 13, p. 134709, 2014.

[15] J. J. Hoyt, M. Asta, and A. Karma, "Method for computing the anisotropy of the solid-liquid interfacial free energy," *Phys. Rev. Lett.*, vol. 86, pp. 5530–5533, Jun 2001.

[16] J. Benet, P. Llombart, E. Sanz, and L. G. MacDowell, "Premelting-induced smoothening of the ice-vapor interface," *Phys. Rev. Lett.*, vol. 117, p. 096101, Aug 2016.

[17] J. W. Gibbs, "On the equilibrium of heterogeneous substances," *Transactions of the Connecticut Academy of Arts and Science*, vol. III, pp. 108–248 and 343–524, 1876-1878.

[18] E. A. Guggenheim, "The principle of corresponding states," *The Journal of Chemical Physics*, vol. 13, no. 7, pp. 253–261, 1945.

[19] M. Allen and D. Tildesley, *Computer Simulation of Liquids*. Oxford: Clarendon Press, 1987.

[20] D. Frenkel and B. Smit, *Understanding Molecular Simulation*. San Diego: Academic Press, second ed., 2002.

[21] E. G. Noya, C. Vega, L. Sese, and R. Ramirez, "Quantum effects on the maximum in density of water as described by the tip4pq/2005 model," *J. Chem. Phys.*, vol. 131, p. 124518, 2009.

[22] D. A. McQuarrie, *Statistical Mechanics*. New York: Harper & Row, 1976.

[23] H. Berendsen, D. van der Spoel, and R. van Drunen, "Gromacs: A message passing parallel molecular dynamics implementation," *Computer Physics Communications*, vol. 91, no. 1 - 3, pp. 43 – 56, 1995.

[24] W. L. Jorgensen, J. Chandrasekhar, J. D. Madura, R. W. Impey, and M. L. Klein, "Comparison of simple potential functions for simulating liquid water," *J. Phys. Chem.*, vol. 79, pp. 926–935, 1983.

[25] W. L. Jorgensen, J. D. Madura, and C. J. Swenson, "Optimized intermolecular potential functions for liquid hydrocarbons," *J. Am. Chem. Soc.*, vol. 106, pp. 6638–6646, 1984.

[26] B. Chen, J. J. Potoff, and I. J. Siepmann *J. Phys. Chem. B*, vol. 105, pp. 3093–3104, 2001.

[27] E. Sanz, C. Vega, J. L. F. Abascal, and L. G. MacDowell, "The phase diagram of water from computer simulation," *Phys. Rev. Lett.*, vol. 92, pp. 255701–1–255701–4, 2004.

[28] N. Metropolis, A. W. Rosenbluth, M. N. Rosenbluth, A. N. Teller, and E. Teller, "Equation of state calculations by fast computing machines," *J. Chem. Phys.*, vol. 21, pp. 1087–1092, 1953.

[29] B. J. Alder and T. E. Wainright, "Phase transition for a hard sphere system," *J. Chem. Phys.*, vol. 27, p. 1208, 1957.

[30] G. Bussi, D. Donadio, and M. Parrinello, "Canonical sampling through velocity rescaling," *J. Chem. Phys.*, vol. 126, no. 1, p. 014101, 2007.

[31] H. C. Andersen, "Molecular dynamics simulations at constant pressure and/or temperature," *The Journal of Chemical Physics*, vol. 72, no. 4, pp. 2384–2393, 1980.

[32] H. J. C. Berendsen, J. P. M. Postma, W. F. van Gunsteren, A. DiNola, and J. R. Haak, "Molecular-dynamics with coupling to an external bath," *J. Chem. Phys.*, vol. 81, p. 3684, 1984.

[33] M. Parrinello and A. Rahman, "Polymorphic transitions in single crystals: A new molecular dynamics method," *J. App. Phys.*, vol. 52, pp. 7182–7190, 1981.

[34] S. Nosé and M. Klein, "Constant pressure molecular dynamics for molecular systems," *Molecular Physics*, vol. 50, no. 5, pp. 1055–1076, 1983.

[35] I. T. Todorov, W. Smith, K. Trachenko, and M. T. Dove, "Dl_poly_3: new dimensions in molecular dynamics simulations via massive parallelism," *J. Mater. Chem.*, vol. 16, pp. 1911–1918, 2006.

[36] S. Plimpton, "Fast parallel algorithms for short-range molecular dynamics," *Journal of Computational Physics*, vol. 117, no. 1, pp. 1 – 19, 1995.

[37] N. Goldenfeld, *Lectures on Phase Transitions and the Renormalization Group*. Reading, Massachusetts: Perseus Books, 1992.

[38] P. M. Chaikin and T. C. Lubensky, *Principles of Condensed Matter Physics*. Cambridge: Cambridge University Press, 1995.

[39] C. Herring, "Some theorems on the free energies of crystal surfaces," *Phys. Rev.*, vol. 82, pp. 87–93, Apr 1951.

[40] W. K. Burton, N. Cabrera, and F. C. Frank, "The growth of crystals and the equilibrium structure of their surfaces," *Phyl. Trans. R. Soc. Lond. A*, vol. 243, pp. 299–358, 1951.

[41] C. Rottman and M. Wortis, "Equilibrium crystal shapes for lattice models with nearest-and next-nearest-neighbor interactions," *Phys. Rev. B*, vol. 29, pp. 328–339, Jan 1984.

[42] L. G. MacDowell, J. Benet, and N. A. Katcho, "Capillary fluctuations and film-height-dependent surface tension of an adsorbed liquid film," *Phys. Rev. Lett.*, vol. 111, p. 047802, Jul 2013.

[43] J. Benet, L. G. MacDowell, and E. Sanz, "Computer simulation study of surface wave dynamics at the crystal–melt interface," *J. Chem. Phys.*, vol. 141, p. 034701, 2014.

[44] J. Benet, L. G. MacDowell, and E. Sanz, "A study of the ice-water interface using the tip4p/2005 water model," *Phys. Chem. Chem. Phys.*, vol. 16, pp. 22159–22166, 2014.

[45] A. Pavlovska and D. Nenow, "Experimental investigation of the surface melting of equilibrium form faces of diphenyl," *Surface Science*, vol. 27, no. 1, pp. 211 – 217, 1971.

[46] D. Nenow, "Surface premelting," *Progress in Crystal Growth and Characterization*, vol. 9, no. 3, pp. 185 – 225, 1984.

[47] "Athenaeum 1181, 640 (1850)„" *The Philosophical Magazine: A Journal of Theoretical Experimental and Applied Physics*, vol. 17, no. 162, 1859.

[48] N. Akutsu and T. Yamamoto, "6 - rough–smooth transition of step and surface," in *Handbook of Crystal Growth (Second Edition)* (T. Nishinaga, ed.), pp. 265–313, Boston: Elsevier, second edition ed., 2015.

[49] P. Noziéres and F. Gallet, "The roughening transition of crystal surfaces. i. static and dynamic renormalization theory, crystal shape and facet grwoth," *J. Phys.(Paris)*, vol. 48, pp. 353–367, 1987.

[50] S. T. Chui and J. D. Weeks, "Dynamics of the roughening transition," *Phys. Rev. Lett.*, vol. 40, pp. 733–736, Mar 1978.

[51] R. Lacmann and I. Stranski, "The growth of snow crystals," *J. Cryst. Growth*, vol. 13–14, no. 0, pp. 236–240, 1972. Third International Conference on Crystal Growth.

[52] T. Kuroda and R. Lacmann, "Growth kinetics of ice from the vapour phase and its growth forms," *J. Cryst. Growth*, vol. 56, no. 1, pp. 189–205, 1982.

[53] H. S. Wagner, F. E. and, L. Stievano, S. Calogero, Q. A. Pankhurst, and K. P. Martinek, "Before striking gold in gold-ruby glass," *Nature*, vol. 407, pp. 691–692, 2000.

[54] W. Cai, U. K. Chettiar, A. V. Kildishev, and V. M. Shalaev, "Optical cloaking with metamaterials," *Nature Photonics*, vol. 1, p. 224, 2007.

[55] N. R. Jana, L. Gearheart, and C. J. Murphy, "Seed-mediated growth approach for shape-controlled synthesis of spheroidal and rod-like gold nanoparticles using a surfactant template," *Advanced Materials*, vol. 13, no. 18, pp. 1389–1393, 2001.

[56] B. Nikoobakht and M. A. El-Sayed, "Preparation and growth mechanism of gold nanorods using seed-mediated growth method," *Chem. Mater.*, vol. 15, pp. 1957–1962, 2003.

[57] J. D. Padmos, M. L. Personick, Q. Tang, P. N. Duchesne, D.-e. Jiang, C. A. Mirkin, and P. Zhang, "The surface structure of silver-coated gold nanocrystals and its influence on shape control," *Nature Communications*, vol. 6, p. 7664, 2015.

[58] G. González-Rubio, P. Díaz-Núñez, A. Rivera, A. Prada, G. Tardajos, J. González-Izquierdo, L. Bañares, P. Llombart, L. G. MacDowell, M. Alcolea-Palafox, L. M. Liz-Marzán, O. Peña-Rodríguez, and A. Guerrero-Martínez, "Femtosecond laser reshaping yields gold nanorods with ultranarrow surface plasmon resonances," *Science*, vol. 358, pp. 640–644, 2017.

[59] G. González-Rubio, V. Kumar, P. Llombart, P. DÃaz-Núñez, E. Bladt, T. Altantzis, S. Bals, O. Peña Rodríguez, E. G. Noya, L. G. MacDowell, A. Guerrero-Martínez, and L. M. Liz-Marzán, "Disconnecting symmetry breaking from seeded growth for the reproducible synthesis of high quality gold nanorods," *ACS Nano*, vol. 0, no. 0, p. null, 0. PMID: 30939242.

[60] V. K. LaMer and R. H. Dinegar, "Theory, production and mechanism of formation of monodispersed hydrosols," *Journal of the American Chemical Society*, vol. 72, no. 11, pp. 4847–4854, 1950.

[61] V. K. L. Mer, "Nucleation in phase transitions.," *Industrial & Engineering Chemistry*, vol. 44, no. 6, pp. 1270–1277, 1952.

Parte I

Fundamento teórico

Capítulo 1
Generación de configuraciones iniciales de hielo I_h

El agua se compone de dos hidrógenos y un oxígeno, dos de los elementos más abundantes en el universo junto al carbono y al helio. Podría parecer entonces que a nivel molecular el agua no presenta demasiadas particularidades. No obstante, cuando hablamos de la presencia de la molécula de agua en la materia condensada se encuentran infinidad de propiedades muy particulares.

La estructura del hielo creó un gran debate durante el primer cuarto del siglo XIX. Se comenzó por estudiar la estructura del hielo I_h, el hielo más común en la naturaleza, al poco tiempo de la aparición de la difracción de rayos X en 1912. [1, 2, 3, 4, 5, 6]

Por el momento se conocen hasta 17 tipos de hielos que se clasifican en hielos con la red de hidrógenos desordenada y los hielos que presentan hidrógenos con posiciones cristalográficas ordenadas. En los hielos con hidrógenos desordenados, los hidrógenos se estructuran siguiendo las reglas de los hielos que fueron postuladas por Bernal y Fowler en 1933. Estas reglas se resumen en que en el hielo, las moléculas de agua están completas y cada átomo de oxígeno se enlaza a dos átomos de hidrógeno. Una molécula de agua está rodeada por otras cuatro moléculas en coordinación tetraédrica, dos moléculas de agua pueden formar un único enlace de hidrógeno entre ellas. La más importante es que según el modelo de Pauling todas las configuraciones de hidrógenos que satisfagan estas condiciones son degeneradas y por lo tanto equiprobables.[7]

En esta tesis se estudia la interfase hielo–vapor y la estructura de las superficies del hielo, por lo que debemos ver en detalle la estructura molecular del hielo (figura 1.1). Dentro de la variedad de hielos que se conocen, principalmente abordaremos en profundidad la estructura del hielo I_h, ya que esta es la fase estable del agua por debajo de su punto de fusión, a presión atmosférica. El hielo I_h presenta un empaquetamiento no compacto con planos atómicos de tipo panal de abeja apilados con una secuencia de apilamiento de planos AB. Dentro de estas secuencias de planos pueden inscribirse hexágonos apilados conformacionalmente en silla o bote. Dependiendo de la orientación cristalográfica expuesta en la superficie tendremos el apilamiento de bicapas formadas por hexágonos silla (Basal), bote (pI) y sin bicapas (pII).[8]

Cristalografía del hielo I_h

En el hielo I_h los átomos de hidrógeno y oxígeno de moléculas vecinas forman una red de enlaces de hidrógeno donde los oxígenos poseen posiciones cristalográficas bien definidas pero la secuencia

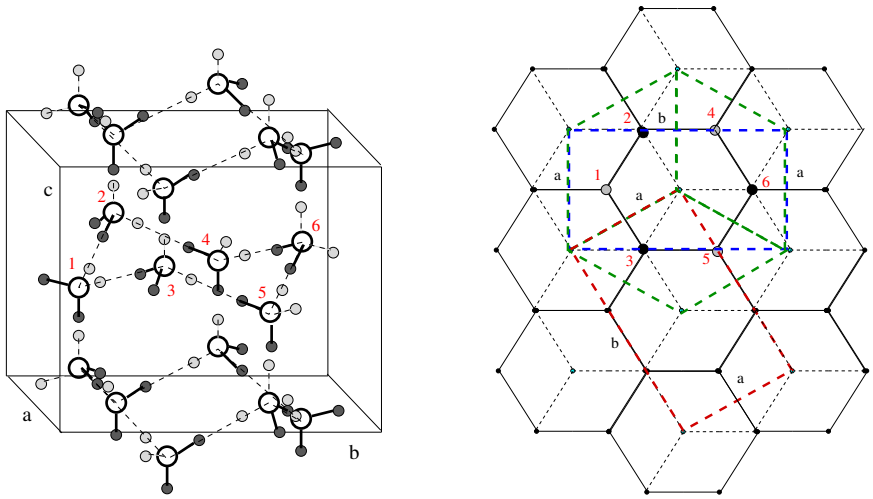

(a) **(b)**

Figura 1.1. (a) Representación de la celda unidad hexagonal del hielo I_h cuyos vectores de red ortogonales son a, $b = \sqrt{3}a$ y c. En círculos blancos y negros se representan los átomos de oxígenos e hidrógenos respectivamente. El hexágono característico que se inscribe dentro de la celda esta formado por dos planos de átomos etiquetados como 1-4-5 y 2-3-6 respectivamente. El otro hexágono se apila formando una imagen especular con el hexágono etiquetado. (b) Vista en planta de una red hexagonal 3D de hielo I_h. Las líneas verdes contienen a la celda unidad hexagonal de lado a, las líneas rojas y azules son celdas ortorrómbicas que pueden inscribirse dentro de la celda hexagonal. Los puntos negros y grises corresponden con las coordenadas que ocupan las moléculas de agua en dos planos contiguos y los puntos azules corresponden a huecos vacíos con ejes de simetría hexagonal.

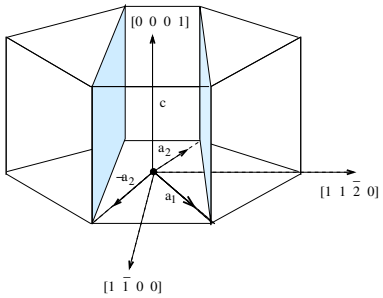

Figura 1.2. Prisma hexagonal resultante en el crecimiento de hielo desde una celda hexagonal. La orientación [0 0 0 1] designa la cara basal. Las orientaciones [1 $\bar{1}$ 0 0] y [1 1 $\bar{2}$ 0] identifican la cara prismática primaria (pI) y prismática secundaria (pII) respectivamente.

de enlaces es aleatoria, de acuerdo a las reglas de los hielos. El crecimiento cristalino de celdas hexagonales de hielo I_h da lugar a la formación de prismas hexagonales, como en los copos de nieve. Dentro de un prisma hexagonal podemos diferenciar dos tipos de caras, unas son las dos bases del prisma con geometría hexagonal y las otras son los seis paralelogramos que forman las caras laterales del prisma. El prisma hexagonal puede dividirse en tres celdas unidad con forma de prisma romboédrico, donde los lados a y b son iguales y $\gamma = 120^o$ como se ve en la figura 1.2. La celdilla unidad hexagonal es el prisma circunscrito por los ejes $\mathbf{a}_1$, $\mathbf{a}_2$ y $\mathbf{c}$. A continuación podemos designar los planos cristalográficos mediante los ejes de un vector perpendicular a cada plano. Una particularidad que poseen las redes hexagonales es la convención de utilizar cuatro en lugar de los tres índices cristalográficos habituales. Podemos definir sobre la base del prisma los vectores $\mathbf{u} = \frac{1}{3}(2\mathbf{a}_1 - \mathbf{a}_2)$, $\mathbf{v} = \frac{1}{3}(2\mathbf{a}_2 - \mathbf{a}_1)$, $\mathbf{t} = \mathbf{v} + \mathbf{u}$ y con ello expresar los vectores $\mathbf{a}_1$ y $\mathbf{a}_2$ en términos de $\mathbf{u}$, $\mathbf{v}$ y $\mathbf{t}$, en la que $\mathbf{a}_1 = \mathbf{u} - \mathbf{t}$ y $\mathbf{a}_2 = \mathbf{v} - \mathbf{t}$.

El siguiente paso consiste en designar las direcciones cristalográficas como [h, k, l, i] donde h es la coordenada del vector $\mathbf{u}$, k la del vector $\mathbf{v}$, l la del vector $\mathbf{t}$ e i la del vector $\mathbf{c}$. De esta manera obtenemos que la dirección perpendicular al plano pI es $\mathbf{a}_1 - \mathbf{a}_2 =$[1 $\bar{1}$ 0 0], la dirección perpendicular al plano pII es $\mathbf{a}_1 + \mathbf{a}_2 =$[1 1 $\bar{2}$ 0] y la dirección perpendicular al plano basal es $\mathbf{c} =$[0 0 0 1].

Llegados a este punto en el que tenemos diferenciadas y nombradas las orientaciones cristalográficas en el prisma hexagonal de hielo, nos vamos a centrar en el estudio de la cara basal, la cara pI y la cara pII. De estas tres caras, solo la basal y la pI son las que aparecen en los bordes del prisma hexagonal y por ello van a ser las responsables de la estructura resultante en el crecimiento de los cristales de hielo en la atmósfera. En el estudio topológico sobre el hielo que se ha realizado en esta tesis, necesitamos conocer en detalle la estructura de cada superficie cristalográfica. Es necesario diferenciar entre direcciones cristalográficas y planos cristalográficos. A lo largo del trabajo veremos referencias a las diferentes direcciones y planos cristalográficos y por ello es necesario pararse detenidamente unos minutos para visualizar en la figura 1.3 las diferentes orientaciones del cristal de hielo.

Anteriormente hemos visto las direcciones cristalográficas responsables del crecimiento de un cristal de hielo I_h. En la figura 1.4 se puede ver la estructura del hielo proyectada sobre los planos perpendiculares a los ejes cristalográficas.

Una vez que hemos visto en detalle la estructura de los planos cristalográficos de interés, el

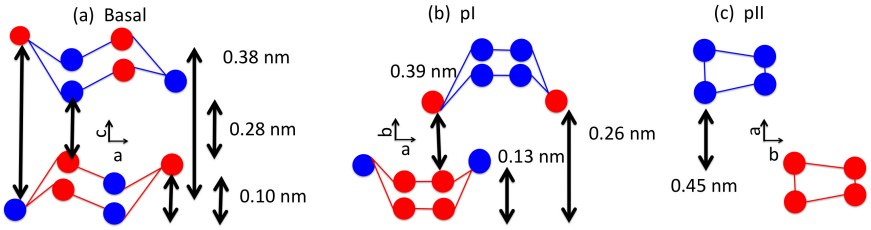

Figura 1.3. Apilamiento de átomos para cada dirección cristalográfica empleadas en las simulaciones. (a) Basal. Los átomos en azul y rojo conforman las 2 bicapas que contienen a los 2 hexágonos. (b) pI. Los átomos en azul y rojo conforman las 2 bicapas que contienen a los 2 hexágonos. (c) Celda unidad empleada en las simulaciones de hielo de la cara pII. En esta cara no hay hexágonos regulares apilados. La dimensión de los parámetros de red son $a = 0{,}90$ nm, $b = 0{,}78$ nm y $c = 0{,}74$ nm.

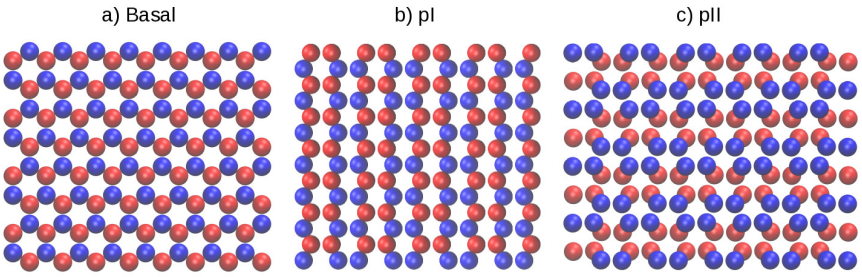

Figura 1.4. Representación en planta de los átomos de oxígeno de la superficie de la cara basal (a), pI (b) y pII (c). Los átomos en color rojo ocupan las posiciones correspondientes al plano A, en color azul los átomos que ocupan el plano B.

Sistema( )[ ] /(h k l i)[h' k' l' i']	( )[ ] / parámetro de red
(Basal)[pII] / (0 0 0 1)[1 1 $\overline{2}$ 0]	(**c**)[**a**]
(pI)[Basal] / (1 $\overline{1}$ 0 0)[0 0 0 1]	(**b**)[**c**]
(pI)[pII] / (1 $\overline{1}$ 0 0)[1 1 $\overline{2}$ 0]	(**b**)[**a**]
(pII)[Basal] / (1 1 $\overline{2}$ 0)[0 0 0 1]	(**a**)[**c**]

Tabla 1.1. Tabla resumen con los parámetros de red que son necesarios para generar las configuraciones iniciales de hielo de acuerdo a las diferentes orientaciones del cristal.

siguiente paso consiste en generar una convención que nos permita distinguir los diferentes sistemas de estudio y, por consiguiente, los diferentes bloques de hielo que vamos a simular en las dinámicas moleculares durante el desarrollo de esta tesis.

Principalmente las dos caras del hielo en contacto con la fase vapor durante el crecimiento de los copos de nieve son la cara basal y la cara pI. En nuestras simulaciones orientamos el cristal de tal forma que la dirección cristalográfica de crecimiento queda localizada a lo largo del eje z. Por consiguiente, cuando hagamos referencia a la cara basal, es el parámetro de red c el que estará paralelo al eje z, y el parámetro de red b para la cara pI.

Generación de configuraciones iniciales

Para generar las configuraciones de hielo, tomamos la celda unidad experimental que contiene las posiciones de los átomos de oxígeno y replicamos el número de celdas unidad necesarias a lo largo de cada dirección a, b y c. Una vez que hemos situado los oxígenos, utilizamos el algoritmo de Rick y Haymet para colocar los hidrógenos de acuerdo con las reglas de Bernal y Fowler. [9, 10] Para estudiar las fluctuaciones con la mayor longitud de onda posible, preparamos una configuración inicial con una geometría de tipo tira o *"slab"*, con el lado de la caja $L_x > L_y$ (consulte la tablas 1.1 con los parámetros de red necesarios para generar las distintas configuraciones de los sistemas estudiados). En consecuencia, para estudiar las fluctuaciones en los sistemas designados como (h k l i) [h' k' l' i'], el plano (h k l i) de la interfaz es perpendicular al eje z, mientras que la dirección [h' k' l' i'] es paralela al eje y. La clasificación arbitraria adoptada es la convencional en estudios de fluctuaciones, (Cara-1)[Cara-2]: [11, 12]

- ( ): Entre paréntesis tenemos la dirección cristalográfica asociada al eje z que es paralela a la amplitud de las ondas capilares.
- [ ]: Entre corchetes encontramos la dirección cristalográfica sobre la que se propaga la onda capilar paralela al eje x.

1. Configuraciones de interfases hielo–vapor

   Estas configuraciones se generan de manera sencilla a partir del bloque de hielo I_h. Para ello, centramos el bloque de hielo en el eje z y añadimos vacío a cada lado de la superficie de hielo aumentando el valor de L_z en la caja de simulación. En la figura 1.5 podemos ver un ejemplo de la configuración inicial que se emplea para el estudio de la interfase hielo–vapor.

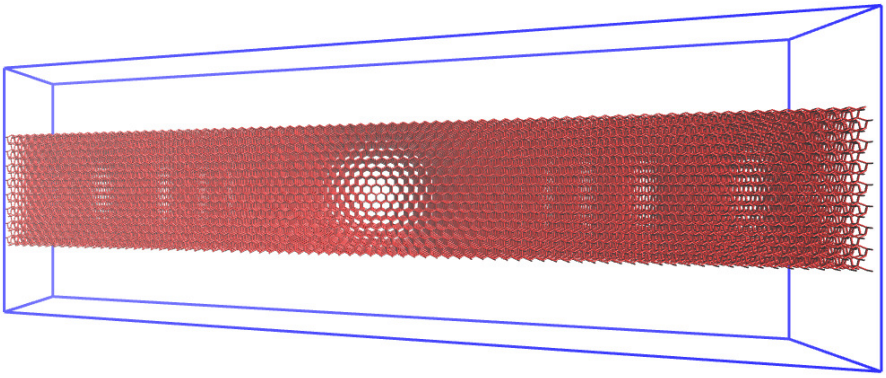

Figura 1.5. Configuración típica empleada en las simulaciones sólido–vapor. En la figura se representa un ejemplo de la interfase (pI)[Basal].

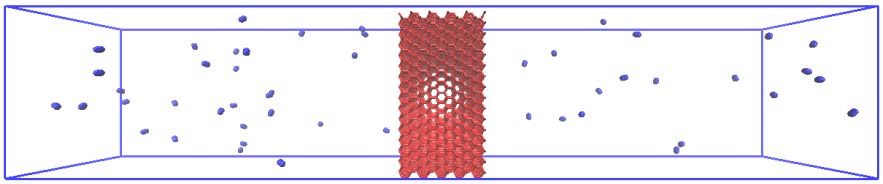

Figura 1.6. Configuración típica empleada en las simulaciones sólido–líquido–nitrógeno.

2. Configuraciones de interfases hielo–vapor–nitrógeno (Utilizadas en el capítulo 2)

   En esta tesis, hemos estudiado también la interfase de hielo–vapor a diferentes presiones, empleando para ello una atmósfera de nitrógeno. La presión del sistema se controla a partir de la densidad de moléculas de nitrógeno en la fase vapor. Para generar estas configuraciones, colocamos las moléculas necesarias de nitrógeno de forma aleatoria en el vacío disponible. En la figura 1.6 podemos ver un ejemplo de una configuración empleada para el estudio de la interfase hielo–vapor–nitrógeno.

3. Configuraciones de interfase líquido–vapor (Utilizadas en el capítulo 2)

   Como en el caso anterior trasladamos el bloque líquido al centro del eje z en la caja de simulación y aumentamos el valor de L_z para crear vacío. Un ejemplo de la configuración inicial empleada puede verse en la figura 1.7.

4. Configuraciones de interfase sólido–líquido

   En este caso la configuración inicial se genera pegando una configuración de un bloque líquido sobre un bloque de hielo. El bloque de hielo se equilibra en NPT para determinar los parámetros laterales adecuados para cada temperatura. Una vez conocemos los valores de red los fijamos y realizamos una simulación en NVT a una temperatura mayor que la de fusión para generar el líquido. Una vez que tenemos el bloque de hielo y el de líquido con los mismos valores laterales perpendiculares al eje z, procedemos a juntarlos y generar la interfase sólido–líquido. Este tipo de configuraciones pueden dar problemas de solapamiento entre las

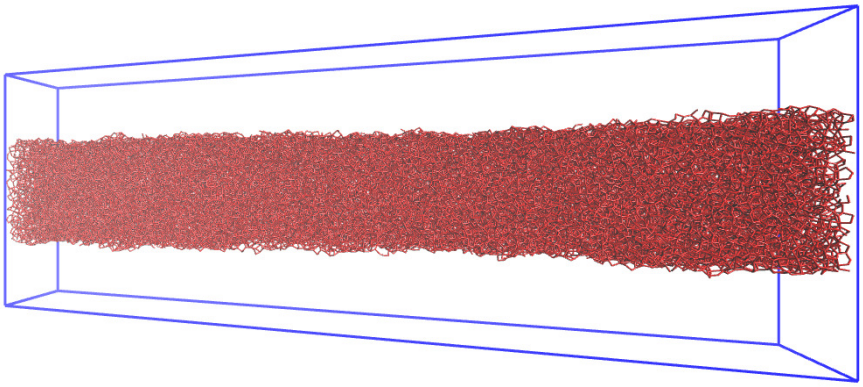

Figura 1.7. Configuración típica empleada en las simulaciones líquido–vapor.

moléculas de agua si el pegado del hielo con el bloque líquido no se realiza de manera correcta. Para ello hay dos alternativas: La primera es la más sencilla y consiste en juntar el sólido y el líquido, ambos equilibrados, dejando entre ellos una distancia suficiente de modo que no se produzcan solapamientos. A continuación, el sistema es equilibrado en Np_zT hasta que tiene lugar la coexistencia directa sólido–líquido y determinamos el lado de la caja perpendicular a la interfase. Un inconveniente de este método puede ocurrir si el sistema tiene un número de moléculas considerable, ya que el proceso de equilibrado puede llegar a resultar bastante lento e ineficiente. La segunda alternativa es colocar el bloque líquido sobre la superficie del hielo y eliminar de la configuración de moléculas de líquidos aquellas moléculas de agua cuya distancia a una molécula del bloque sólido es menor a un diámetro molecular. En la figura 1.8 podemos ver un ejemplo de una configuración empleada para el estudio de la interfase hielo–líquido. Tras mi experiencia, recomiendo esta última forma de proceder para el pegado. Ya que, el hueco que se deja entre las dos fases que se juntan hace que la densidad sea ligeramente menor que la esperada y puede cristalizar el agua que pegamos sobre el sólido.

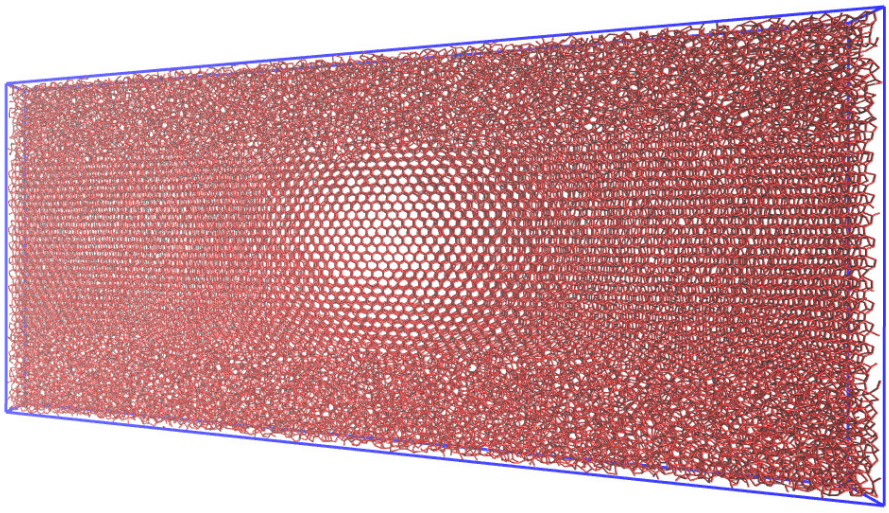

Figura 1.8. Configuración típica empleada en las simulaciones sólido–líquido. En este caso vemos un ejemplo de la interfase (pI)[Basal].

Bibliografía

[1] S. W. H. Bragg, "The crystal structure of ice," *Proceedings of the Physical Society of London*, vol. 34, pp. 98–103, dec 1921.

[2] W. H. Barnes and W. H. Bragg, "The crystal structure of ice between 0c and -183c," *Proceedings of the Royal Society of London. Series A, Containing Papers of a Mathematical and Physical Character*, vol. 125, no. 799, pp. 670–693, 1929.

[3] W. F. Kuhs and M. S. Lehmann, "The structure of the ice ih by neutron diffraction," *The Journal of Physical Chemistry*, vol. 87, no. 21, pp. 4312–4313, 1983.

[4] Kouchi, A., Furukawa, Y., and Kuroda, T., "X-ray diffraction pattern of quasi-liquid layer on ice crystal surface," *J. Phys. Colloques*, vol. 48, pp. C1–675–C1–677, 1987.

[5] V. F. Petrenko and R. W. Whitworth, *Physics of Ice*. Oxford: Oxford University Press, 1999.

[6] E. D. Isaacs, A. Shukla, P. M. Platzman, D. R. Hamann, B. Barbiellini, and C. A. Tulk, "Covalency of the hydrogen bond in ice: A direct x-ray measurement," *Phys. Rev. Lett.*, vol. 82, pp. 600–603, Jan 1999.

[7] J. D. Bernal and R. H. Fowler, "A theory of water and ionic solutions, with particular reference to hydrogen and hydroxyl ions," *J. Chem. Phys.*, vol. 1, pp. 515–548, 1933.

[8] H. Nada and J. P. van der Eerden, "An intermolecular potential model for the simulation of ice and water near the melting point: A six–site model of H2O," *J. Chem. Phys.*, vol. 118, pp. 7401–7413, 2003.

[9] S. W. Rick and A. D. J. Haymet, "Dielectric constant and proton order and disorder in ice Ih: Monte Carlo computer simulations," *J. Chem. Phys.*, vol. 118, pp. 9291–9296, 2003.

[10] L. G. MacDowell and C. Vega, "Dielectric constant of ice ih and ice v: A computer simulation study," *J. Phys. Chem. B*, vol. 114, pp. 6089–6098, 2010.

[11] R. L. Davidchack, J. R. Morris, and B. B. Laird, "The anisotropic hard-sphere crystal-melt interfacial free energy from fluctuations," *J. Chem. Phys.*, vol. 125, no. 9, p. 094710, 2006.

[12] J. Benet, L. G. MacDowell, and E. Sanz, "Computer simulation study of surface wave dynamics at the crystal–melt interface," *J. Chem. Phys.*, vol. 141, p. 034701, 2014.

Capítulo 2
Análisis de la interfase sólido–vapor en el hielo.

Si recordamos, en la introducción vimos que el hielo en equilibrio con el vapor a temperaturas inferiores al punto triple presenta una interfase compleja formada por una interfase sólido–líquido en equilibrio con una interfase líquido–vapor. Este hecho implica que previamente a realizar el análisis topológico de la superficie necesitamos localizar las dos interfases. Para ello necesitamos un parámetro de orden para identificar las moléculas pertenecientes a la fase sólida y las moléculas presentes en la fase líquida. Podemos diferenciar átomos con entornos de coordinación sólido (red ordenada) y líquido (red desordenada) empleando el parámetro de orden local $\bar{q}_6$, propuesto por Lechner y Dellago. Este parámetro adopta valores altos para moléculas de agua con entornos locales ordenados (sólidos) y valores pequeños para entornos locales desordenados (líquidos).[1]

La distribución de $\bar{q}_6$ para el líquido y el sólido solapan ligeramente y no se pueden separar de una manera precisa. Por ello en el líquido obtendremos moléculas etiquetadas como sólido y en el sólido tendremos moléculas sólidas que se van a etiquetar como líquido. Desgraciadamente este error no se puede evitar, pero si minimizar al máximo dentro de lo posible.

Para ello ha sido necesario estimar el valor umbral que separa entornos locales sólidos y líquido ($\bar{q}_6^*$) a cada temperatura que se elige como aquel que minimiza los errores de etiquetado de moléculas sólidas como líquidas y viceversa. En la figura 2.1 representamos los valores umbral obtenidos para todo el intervalo de temperaturas del estudio. Los átomos de oxígeno cuyo valor de $\bar{q}_6$ sea menor que el umbral serán etiquetadas como líquido y el resto como sólidos. En la figura 2.2 vemos un ejemplo del resultado tras aplicar el parámetro de orden $\bar{q}_6$.

Una vez etiquetadas las moléculas que tienen entornos de coordinación sólido, procedemos a buscar el agregado más grande formado por moléculas sólidas. Para ello, consideramos que dos átomos de oxígeno están enlazados y, por lo tanto pertenecen al mismo agregado, si la distancia entre ellos es menor que 3.5 Å .

Método de determinación de superficies

El método de superficies que hemos empleado en esta tesis consiste en buscar sobre cualquier punto aleatorio del bloque de hielo los 4 átomos de oxígeno con mayor o menor valor de z dentro de un área fijada y promediar su posición. En la figura 2.3 vemos una ilustración de este criterio descrito.

1. Localización de la altura local: Dividimos el plano de la interfase en una cuadrícula de puntos y buscamos todos los átomos sólidos que yacen en el interior de un prisma rectangular

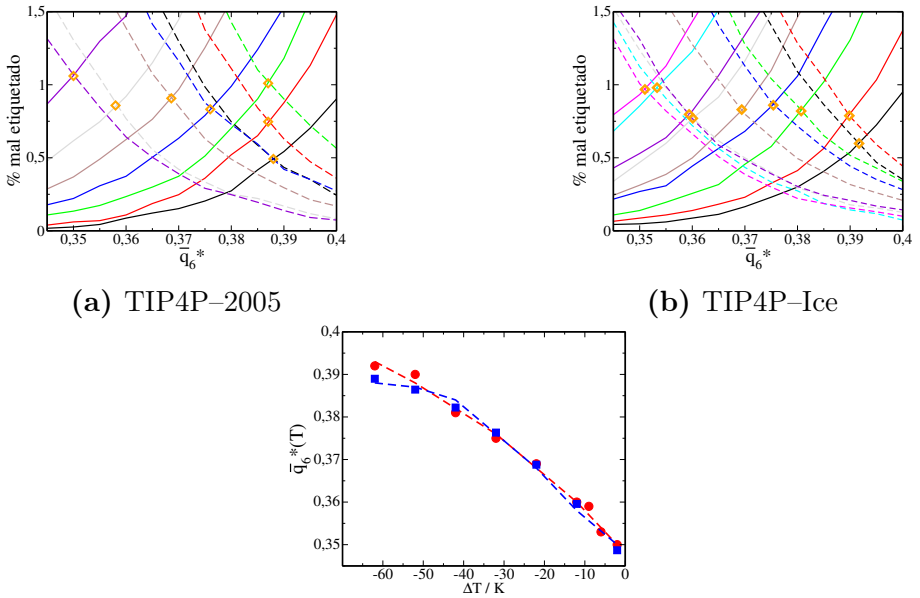

(a) TIP4P–2005 **(b)** TIP4P–Ice

(c)

Figura 2.1. El error en el etiquetado define el valor umbral de $\overline{q}_6^*$ que se define como el valor para el cual el número de moléculas sólidas etiquetadas como líquido, dentro de un sólido volumétrico, y el número de moléculas líquidas etiquetadas como sólido, dentro de un líquido volumétrico, son iguales.[2] (a) TIP4P–2005: Representamos en función del valor umbral $\overline{q}_6^*$ con líneas continuas el % de moléculas líquidas mal etiquetadas y en líneas discontinuas están representados el % de moléculas sólidas mal etiquetadas. En color negro, rojo, verde, azul, marrón, gris y violeta tenemos las temperaturas de 190 K, 200 K, 210 K, 220 K, 230 K, 240 K y 250. En rombos de color naranja los puntos de intersección entre las dos curvas para cada isoterma determina el valor umbral de $\overline{q}_6^*$. (b) TIP4P–Ice: Representamos en función del valor umbral $\overline{q}_6^*$ con líneas continuas el % de moléculas líquidas mal etiquetadas y en líneas discontinuas están representados el % de moléculas sólidas mal etiquetadas. En color negro, rojo, verde, azul, marrón, gris, violeta, cían y magenta tenemos las temperaturas de 210 K, 220 K, 230 K, 240 K, 250 K, 260 K, 263 K, 266 K y 270 K respectivamente. (c) Valores umbral $\overline{q}_6^*$ medidos en relación a la temperatura de fusión para ambos modelos. Los valores umbrales obtenidos son ligeramente corregidos por un ajuste cuadrático: En círculos de color azul representamos $\overline{q}_6^*(T)$ para el modelo TIP4P–2005. En círculos de color negro representamos $\overline{q}_6^*$ para el modelo TIP4P–Ice. En línea roja y azul discontinuas aparecen la funciones de ajuste cuadráticas para cada modelo.
(2005) $\overline{q}_6^*(T) = 0{,}12071 + 0{,}0029952T - 8{,}3333 \cdot 10^{-6}T^2$.
(Ice) $\overline{q}_6^*(T) = 0{,}26266 + 0{,}0016474T - 4{,}8982 \cdot 10^{-6}T^2$.

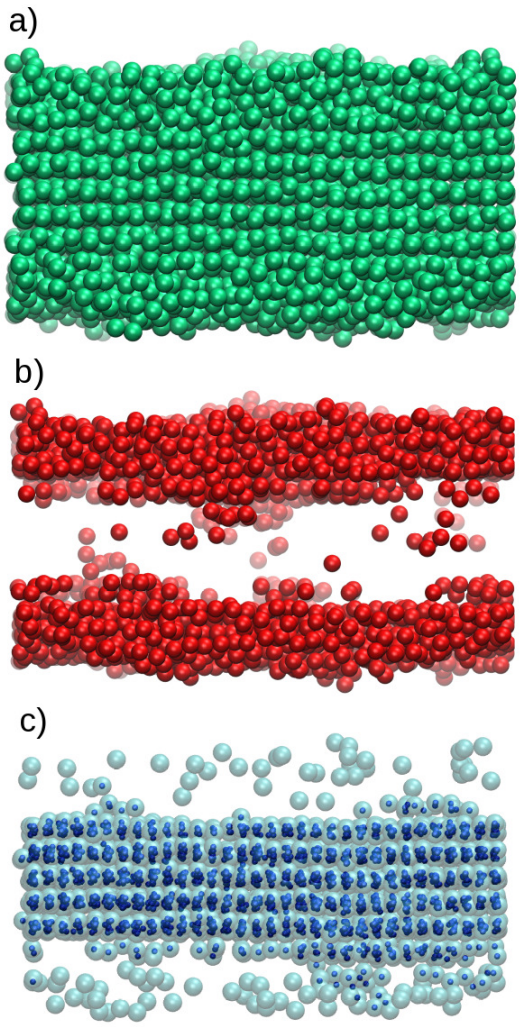

Figura 2.2. (a) Configuración instantánea de una interfase hielo–vapor a 270 K (b) Átomos identificados como líquidos con el parámetro de orden utilizando el valor umbral $\bar{q}_6 = 0{,}350$. (c) Configuración de átomos sólidos tras aplicar el parámetro de orden $\bar{q}_6 = 0{,}350$ (azul claro) y el agregado sólido más grande presente en el sistema (azul oscuro). Los átomos sólidos inmersos en el cluster líquido se ignoran a la hora de determinar la altura del sólido.

centrado en cada nodo de la cuadrícula. La base del prisma rectangular será la base de la celda unidad ortorrómbica de cada orientación del cristal. En el caso del líquido se emplea una base cuadrada de lado 3 diámetros moleculares. La altura de la superficie en ese punto se determina a partir del promedio de la ubicación de los 4 átomos más altos o más bajos. La altura del sólido se determina en el agregado sólido más grande, y la altura del líquido empleando el agregado condensado más grande. De esta forma se garantiza que en ausencia de líquido, la altura determinada en ese punto sea igual a la altura del sólido.

El número de puntos donde hemos evaluado la altura es dos veces el número de celdas unidad replicadas en la dirección x y el número de celdas replicadas a lo largo de la dirección y.

2. Definiciones y promedios: En este punto, vamos a detenernos unos instantes en establecer un conjunto de definiciones para las alturas promedio que hemos empleado en los capítulos 1, 2 y 3 de la parte II (Results): En la figura 2.4 ilustramos las definiciones descritas anteriormente para comodidad del lector.

   - $z_\theta(x) = \frac{1}{N_y^{celdas}} \sum_{i=1}^{N_y^{celdas}} z_\theta(x,y)$: Es la altura local promedio de la interfase a lo largo del eje x y N_y^{celdas} es el número de celdas unidad replicadas en el eje y. El subíndice θ indica la interfase en la que evaluamos la altura (ice: sólido–líquido, film: líquido–vapor).
   - $z_\theta = \frac{1}{N_x^{celdas}} \sum_{i=1}^{2N_x^{celdas}} z_\theta(x)$: Es la altura promedio de la interfase y N_x^{celdas} hace referencia al número de celdas unidad replicadas en el eje x. El subíndice θ indica la interfase en la que evaluamos la altura (ice: sólido–líquido, film: líquido–vapor).
   - $h(x,y) = z_{film}(x,y) - z_{ice}(x,y)$ y $h = z_{film} - z_{ice}$: Es la diferencia de alturas en todos los puntos de la cuadrícula, y la diferencia promedio de las interfase líquida y sólida, respectivamente. h es el espesor promediado sobre todos los puntos de la cuadrícula de la película líquida adsorbida sobre el hielo.
   - $\delta z_\theta(x) = z_\theta(x) - z_\theta$: Es la fluctuación de la altura a lo largo del eje x con respecto a la altura promedio de cada interfase.

Es importante familiarizarse con los conceptos de altura local de la interfase, altura promedio, fluctuación de altura con respecto al plano medio interfacial y el espesor de la película líquida. Ya que esta es la notación del capitulo 3, pero más adelante se empleará en otros capítulos otra notación diferente a estas definiciones.

Método determinación del potencial interfacial, $g(h)$

La energía libre de una película líquida adsorbida sobre un sustrato y con espesor h a la temperatura T se define como:

$$w_T(h) = g(h) - \Delta p(T)h \tag{2.1}$$

En donde $g(h)$ es el potencial interfacial, mientras que Δ es la diferencia de presión entre el líquido y el vapor en equilibrio. En esta expresión, $g(h)$ es una medida de la interacción del sólido con una

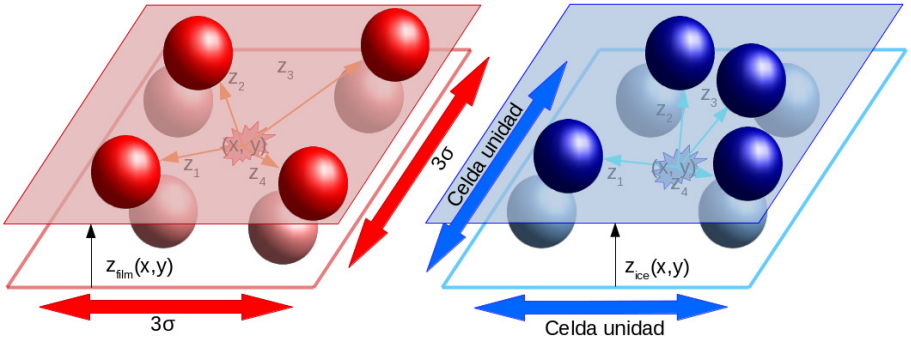

Figura 2.3. Criterio para determinar la altura local de un interfase. A la izquierda de la figura y en color rojo ilustramos el criterio empleado para la determinación de la altura en la interfase líquida. A la derecha de la figura y en color azul podemos ver el método para determinar la altura en el sólido. En ambos casos el método consiste en colocarse en un punto del la cuadrícula ((x, y)) y buscar los 4 átomos (Z_i) más externos para promediarlos y obtener la altura de la interfase ($z_{ice,film}(x, y)$).

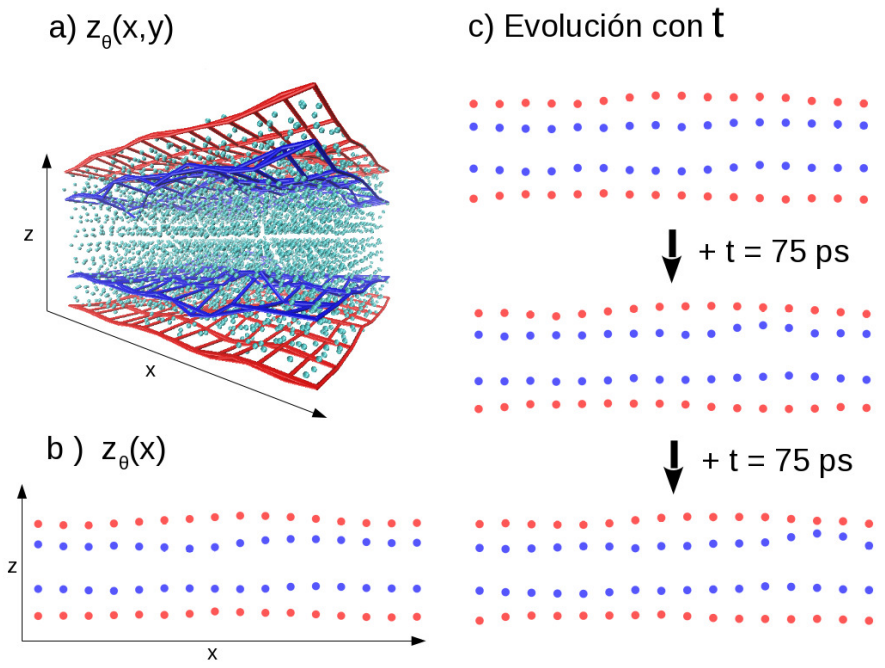

Figura 2.4. (a) Representación de la altura de interfase líquido–vapor y sólido–líquido. En líneas rojas y azules representamos para todos los puntos del mallado la altura de cada nodo evaluado de la rejilla, para la interfase líquido–vapor ($z_{film}(x, y)$) y sólido–líquido (($z_{ice}(x, y)$) respectivamente. (b) Representación de la interfase promediada a lo largo del eje y ($z_\theta(x)$). En puntos rojos el promedio para la interfase líquida y en puntos azules se corresponde con la interfase sólida. (c) Secuencia temporal de la interfase $z_\theta(x)$ obtenida empleando el método de determinación de superficies.

capa de líquido adsorbida sobre su superficie (medida en exceso con respecto a una capa infinita de líquido), mientras $\Delta p(T)h$ es la energía libre del líquido de espesor h medido en exceso sobre la energía del vapor. En la práctica, solo se disponen de datos de espesor a lo largo de la línea de coexistencia hielo–vapor.

Estrictamente, Δp se define como la diferencia de presión entre las fases volumétricas del líquido y del vapor a igual temperatura y potencial químico:

$$\Delta p = p_l(T, \mu) - p_v(T, \mu) \tag{2.2}$$

Para el caso del hielo es posible determinar h a lo largo de la curva de coexistencia hielo–vapor. Tenemos entonces que, $p_v(T, \mu) = p_s(T)$ en donde $p_s(T)$ es la presión de vapor del hielo. Empleando la relación de Gibbs-Duhem a temperatura constante podemos expresar el diferencial de la presión como una función que depende directamente de la densidad, ρ, y el potencial químico, $d\mu$, de esta forma esta relación queda como:

$$dp = \rho d\mu \tag{2.3}$$

Tenemos que esta ecuación es válida tanto para la fase vapor como la fase líquida, de esta forma podemos calcular la variación de presiones de la siguiente manera:

$$d\Delta p = (\rho_l - \rho_v)d\mu \tag{2.4}$$

Si ahora integramos desde la curva de coexistencia líquido-vapor a la curva de coexistencia sólido-líquido, obtenemos:

$$\Delta p = \int_{\mu_{lv}}^{\mu_{sl}} (\rho_l - \rho_v)d\mu \tag{2.5}$$

donde μ_{lv} y μ_{sl} son los potenciales químicos de coexistencia agua-vapor y hielo-agua, respectivamente, y hemos tenido en cuenta que el potencial químico es el mismo para ambas fases. Una buena aproximación es suponer que $\rho_l >> \rho_v$ y ρ_l y que ρ_v no cambia significativamente con las variaciones de potencial químico, con lo que obtenemos:

$$\Delta p = \rho_l(T)(\mu_{sl} - \mu_{lv}) \tag{2.6}$$

en donde $\rho_{l,c}(T)$ es la densidad de coexistencia del agua en equilibrio con el vapor a la temperatura T. Teniendo en cuenta que por debajo del punto triple el vapor de agua es básicamente un gas ideal, tenemos que $\mu \propto K_B T \ln p$ y por tanto

$$\Delta p = \rho_l(T)k_B T \ln(p_{sv}/p_{lv}) \tag{2.7}$$

en donde p_{sv} y p_{lv} son las presiones de vapor del hielo y el agua respectivamente.

Nos falta por calcular $\ln(p_{sv}/p_{lv})$. Para ello usamos la ecuación de Clausius-Clapeyron en su formulación en la que uno de las fases es gas:

$$\frac{dp}{p} = \frac{\Delta H}{RT^2}dT \tag{2.8}$$

En este punto podemos tomar ΔH constante e igual a su valor en el punto triple o considerar la dependencia con la temperatura utilizando la capacidad calorífica.

- Si $\Delta H = \Delta H_t$:

  Cuando suponemos ΔH constante, entonces tenemos para el sólido-vapor:

$$\ln(p_{sv}/p_t) = \frac{\Delta H_{sv}}{R}\left(\frac{1}{T_t} - \frac{1}{T}\right) \tag{2.9}$$

  y para el líquido-vapor:

$$\ln(p_{lv}/p_t) = \frac{\Delta H_{lv}}{R}\left(\frac{1}{T_t} - \frac{1}{T}\right) \tag{2.10}$$

  Por lo tanto tenemos que:

$$\ln(p_{sv}/p_{lv}) = \frac{\Delta H_{sl}}{R}\left(\frac{1}{T_t} - \frac{1}{T}\right) \tag{2.11}$$

  Si utilizamos las curvas de Clausius-Clapeyron y sustituimos en la Ec. 2.7, obtenemos inmediatamente:

$$\Delta p = \frac{\Delta H_{sl}}{v_l T_t}(T - T_t) \tag{2.12}$$

  donde ΔH_{sl} es la entalpía de fusión hielo/agua, v_l es el volumen molar del líquido en el punto triple y T_t es la temperatura del punto triple.

- Si $\Delta H = \Delta H_t + \Delta C_p(T - T_t)$:

  Para mejorar la ecuación de Clausius-Clapeyron tenemos en cuenta que los calores latentes de transición varían con la temperatura. Integrando la ecuación de Clausius, obtenemos:

$$\ln(p_{\alpha v}/p_t) = \frac{\Delta H_t - \Delta C_{p,t}}{R}\left[\frac{1}{T_t} - \frac{1}{T}\right] + \frac{\Delta C_{p,t}}{R}\ln T/T_t \tag{2.13}$$

Esta ecuación vale tanto para la presión de vapor del agua como la del hielo. Los subíndices t se corresponden con las propiedades medidas en el punto triple ($T_t = 272$(TIP4P/Ice), $T_t = 252$(TIP4P/2005), $\Delta C_{p,t}$ es la diferencia de capacidad calorífica entre la fase vapor y la fase condensada (α). En la tabla 4.1 podemos ver los valores termodinámicos empleados en el cálculo del potencial interfacial.

Otra posible mejora que se puede realizar en el calculo de Δp es considerar que en la Ec.2.7 la dependencia de la densidad líquida con la temperatura, $\rho_l(T)$.

Una vez calculado Δp podemos entonces calcular $g(h)$. Esta propiedad termodinámica relaciona la energía libre de una película líquida con la respuesta que ejerce la interfase a la interacción con un campo externo. En nuestro caso el campo externo es ejercido por la superficie de hielo y podemos escribir $g(h)$ de la siguiente manera:

$$g(h) = -k_B T \ln P(h)/A + \Delta p h \tag{2.14}$$

en donde $P(h)$ es la probabilidad de encontrar una película líquida de espesor h sobre la superficie sólida.

Si conocemos la función de distribución de probabilidad del espesor, $P(h)$ y la diferencia de presión sólido–vapor para cada temperatura podemos determinar el potencial interfacial.

H_t^{ice} / KJ mol^{-1}	H_t^{lquido} / KJ mol^{-1}	$C_{p,t}^{hielo}$ / J mol^{-1}K^{-1}	$C_{p,t}^{\text{lquido}}$ / J mol^{-1}K^{-1}
-55.77†	-50.92‡	58.13†	99.63‡
-61.03∗	-55.64∗	65.60	107.26

Tabla 2.1. Valores termodinámicos para los modelos de agua utilizados. La temperatura estimada de fusión es de 252 K para el TIP4P–2005 y de 272 K para el TIP4–Ice. [9, 10]
†: [11]. ‡:[12, 13]. ∗: [13]

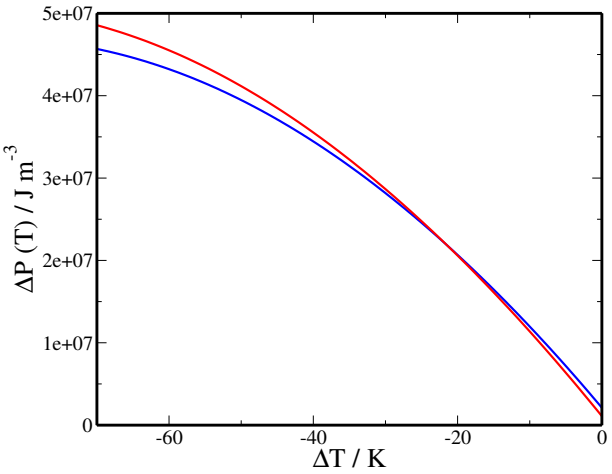

Figura 2.5. Curva de equilibrio sólido–líquido para el modelo TIP4P–2005 (línea roja) y para el modelo TIP4P–Ice (línea azul).

Por otra parte, a partir del potencial interfacial conocemos la presión de ruptura (*disjoining pressure*) que se corresponde con la variación de presión responsable del aumento del espesor del agua líquida adsorbida sobre la superficie del hielo. [3, 4]

$$\Delta p = \Pi(h) = -\frac{dg(h)}{dh} \tag{2.15}$$

Por definición la presión de ruptura tiene relación con la interacción del vapor con el sólido, siendo una propiedad interfacial de exceso con respecto al líquido volumétrico cuando el potencial químico es el de coexistencia.[5, 6, 7, 8]

En la práctica se puede obtener $\Pi(h)$ pod dos métodos.

Método 1

En el método 1 establecemos la condición de equilibrio para el espesor de la película $dw_T(h)/dh = 0$ y de ese modo llegamos a la Ec.2.15. Por tanto, podemos calcular $\Pi(h)$ del siguiente modo:

- Calculamos el espesor promedio de la película adsorbida a las distintas temperaturas.

- A cada espesor, característico de una temperatura, le asociamos su valor $\Pi(h)$ de acuerdo a la ecuación Eq.2.7.

Método 2

Para el método 2 calculamos $g(h)$ siguiendo la Eq.2.14 y mediante la relación que aparece en la Ec.2.15 obtenemos $\Pi(h)$. En las simulaciones solo se muestrea un intervalo limitado de la distribución $P(h)$. Por tanto, se trata de recoger los datos de $g(h)$ juntando los fragmentos obtenidos a las distintas temperaturas. Para que este método funcione, es necesario que los intervalos de muestreo solapen ligeramente unos con otros. Sí ese no fuese el caso, mi recomendación es realizar simulaciones a temperaturas intermedias. Otra precaución a tener en cuenta, es a cada temperatura se deben descartar los valores $P(h)$ en los límites del intervalo muestrado debido a la poca fiabilidad de estos datos.

Método de fluctuaciones capilares

Las fluctuaciones capilares son un fenómeno microscópico relevante en las propiedades macroscópicas de las interfases, ya sean estas líquidas o sólidas. Esta agitación térmica sobre la interfase hace que se produzcan ondas capilares cuya amplitud de onda está directamente relacionado con la energía libre interfacial. La ecuación de Young-Laplace que relaciona la curvatura de una interfase con la tensión superficial falla estrepitosamente cuando la dimensión del problema es de la escala de unos pocos nanómetros.[14]

El hielo por debajo del punto de fusión presenta dos interfase, una interfase hielo–película y otra película–vapor. Cada interfase de manera independiente puede ser descrita en términos de la altura intrínseca al plano medio interfacial. Podemos entonces identificar independientemente una altura intrínseca para la interfase hielo–película ($h_{if}(x)$) y otra para la interfase película–vapor ($h_{fv}(x)$). La Teoría de Ondas Capilares nos proporciona las soluciones para el balance energético de la interfase película–vapor. Para el sólido el balance energético en la interfase hielo-película está ligado a las alturas de la celda unidad del hielo. El modelo de Hamiltoniano sine-Gordon se utiliza frecuentemente en superficies sólidas debido a las oscilaciones energéticas que tienen lugar cuando la altura local del sólido es múltiplo entero del espacio interplanar correspondiente a la dirección perpendicular a la interfase.

- Balance de energía en la interfase película–vapor: De acuerdo a las soluciones que nos proporciona la Teoría de Ondas Capilares, la energía libre $H[h]$ en función de la altura h del perfil líquido viene dada por las soluciones del Modelo del Hamiltoniano Interfacial. [15, 16, 17, 18, 19, 20, 21, 22, 23, 24, 25, 26]

$$H_{l/v} = \int dx[g(h) + \gamma_{lv}\sqrt{1 + (\nabla h)^2}] \tag{2.16}$$

  en donde γ_{lv} es la tensión superficial líquido–vapor. Las interacciones efectivas del sólido con el líquido en equilibrio con la fase gas, son descritas a través del potencial interfacial $g(h)$ en función del espesor de la película líquida. El otro término que aparece en la ec.2.16 tiene en cuenta la penalización energética del crecimiento del área de superficie de la interfase. La tensión superficial implica un gran aporte de energía para aumentar el área de dicha interfase. En esta tesis nos centraremos en el estudio de las ondas capilares y esta ecuación es el punto

de partida para el estudio de fenómenos de superficie. [27, 28, 29, 30, 31, 32]

$$\Delta H_{l/v} = \frac{1}{2}\int dx[g''h^2 + \gamma_{lv}(\nabla h)^2] \tag{2.17}$$

Llegados a este punto, podemos tomar el plano medio interfacial como superficie de referencia para medir la altura de la interfase, h^* y realizar el desarrollo de Taylor de $g(h)$ sobre h^*. El último paso consistiría en expresar las fluctuaciones $h(x) - h^*(x)$ en términos del espacio de Fourier y el vector de onda $\mathbf{q}$, $h(x) = \sum_q h(q)e^{i\mathbf{qx}}$, en donde $\mathbf{q} = 2\pi/\mathbf{x}$.

En realidad, la definición va ligada a las 3 dimensiones del espacio. No obstante las geometrías tipo *"bloque"* empleadas en este trabajo son muy anisotrópicas con el lado de la caja perpendicular a la superficie significativamente más largo que las dos dimensiones perpendiculares a la superficie. Por ello en esta tesis la transformada de Fourier de h unicamente se realiza a lo largo de la dimensión mas larga del bloque de hielo. La solución del Hamiltoniano Interfacial nos proporciona la siguiente expresión para la amplitud de la onda capilar dependiente del vector de onda $\mathbf{q}$:

$$\langle h^2(q)\rangle = \frac{k_B T}{A(g'' + \gamma_{lv}q^2)} \tag{2.18}$$

- Balance de energía en la interfase hielo–película: En nuestra aproximación referida al sólido tenemos en cuenta que este sólido puede presentar escalones sobre la superficie. La altura de los escalones es por lo tanto una función relacionada con el parámetro de red del sólido en la dirección correspondiente (d), según el modelo de sine-Gordon

$$H_{s/l} = \int dx \left[\frac{1}{2}\tilde{\gamma}_{sl}(\nabla h)^2 - u\cos\left(\frac{2\pi}{d}h\right)\right] \tag{2.19}$$

El primer término está gobernado por la rigidez interfacial del sólido ($\tilde{\gamma}_{sl}$), una propiedad muy parecida a la tensión superficial para sistemas fluidos. Una interpretación a la rigidez interfacial que manejaremos será el coste energético de deformar la superficie del sólido. El parámetro u es la energía favorable para aquellas configuraciones en las que la fluctuacion sólidas es un múltiplo del parámetro de red del sólido. Las soluciones de la Ec.2.19 están en concordancia con las soluciones que proporciona la Teoría de Ondas Capilares. A continuación, la expansión del Hamiltoniano en segundo orden nos proporciona las fluctuaciones de la interfase.

$$\Delta H_{s/l} = \frac{1}{2}\int dx \left(\frac{4\pi^2 u}{d^2}h^2 + \tilde{\gamma}_{sl}(\nabla h)^2\right) \tag{2.20}$$

Al igual que para la interfase líquido–vapor la transformada de Fourier se realiza sobre la componente x.

$$\langle h^2(q)\rangle = \frac{k_B T}{A(w + \tilde{\gamma}_{sl}q^2)} \tag{2.21}$$

En realidad γ_{lv} y $\tilde{\gamma}_{sl}$ no son constantes sino que se observa una dependencia con $\mathbf{q}$ que describen las desviaciones del espectro a partir de cierto intervalo de $\mathbf{q}$.[34, 25]. Por lo que vamos a

expresar esa dependencia como $\gamma(q) = \gamma_0 + \kappa q^2$ en donde κ es la penalización de curvar la interfase con una amplitud de onda de $\mathbf{q}$.

Las Ecs. 2.18 y 2.21 son muy similares pero el g'' de la Ec.2.18 corresponde a la segunda derivada del potencial con respecto al espesor del líquido y u se relaciona con la rugosidad (w) a través del parámetro de red (d), siendo $w = \frac{4\pi^2 u}{d^2}$. No obstante para obtener las soluciones a las fluctuaciones de h_{if} y h_{fv} desarrollamos un modelo acoplado. En este modelo g es el responsable del acoplamiento entre los términos de las dos interfases:

$$\Delta H_{s/f/v} = \int dx \left(\tfrac{1}{2}\tilde{\gamma}_{sl}(\nabla h_{if})^2 - u\cos\left(\tfrac{2\pi}{b}h_{if}\right) + g(h_{fv} - h_{if}) + \gamma_{lv}\sqrt{1 + (\nabla h_{fv})^2}\right) \tag{2.22}$$

Como resultado del peso estadístico del Hamiltoniano, $exp(-\Delta H/k_B T)$, obtenemos una distribución de campos gaussianos bivariantes análoga a la distribución de campos encontrados en el acoplamiento bajo gravedad de interfases fluido–fluido. [35, 36, 37] Las soluciones a este modelo de campos gaussianos nos proporciona las ecuaciones que determinan el espectro de fluctuaciones capilares:

$$\begin{aligned}
\langle |h_{if}^2(\mathbf{q})| \rangle &= \frac{k_B T}{A} \frac{g'' + \gamma_{lv} q^2}{[w + g'' + \tilde{\gamma}_{sl} q^2][g'' + \gamma_{lv} q^2] - g''^2} \\
\langle |h_{fv}^2(\mathbf{q})| \rangle &= \frac{k_B T}{A} \frac{w + g'' + \tilde{\gamma}_{sl} q^2}{[w + g'' + \tilde{\gamma}_{sl} q^2][g'' + \gamma_{lv} q^2] - g''^2} \\
\langle h_{if}(\mathbf{q}) h_{fv}^*(\mathbf{q}) \rangle &= \frac{k_B T}{A} \frac{g''}{[w + g'' + \tilde{\gamma}_{sl} q^2][g'' + \gamma_{lv} q^2] - g''^2}
\end{aligned} \tag{2.23}$$

La rugosidad w se puede obtener de forma autoconsistente resolviendo las ecuaciones:

$$w = u k_z^2 \exp\left[-\frac{1}{2} k_z^2 \sum_{\mathbf{q}} \langle |h_{if}^2(\mathbf{q})| \rangle \right] \tag{2.24}$$

Las soluciones que obtenemos para w son importantes para explicar las diferencias que hay en el espectro de fluctuaciones con el espesor de la película líquida. Para un espesor de líquido infinito con $g'' = 0$ obtenemos:

$$w \propto \left(1 + \frac{\tilde{\gamma}_{iw}}{w} q_{max}^2 \right)^{-\tau_{iw}} \tag{2.25}$$

en donde q_{max} es el inverso de la longitud de correlación. Este resultado se corresponde con la solución aproximada del modelo sine-Gordon de Safran.[38] La solución depende fundamentalmente del parámetro $\tau_{iw} = \frac{k_B T k_z^2}{8\pi\tilde{\gamma}_{iw}}$. Para $\tau_{iw} > 1$, la solución es $w = 0$ y la superficie es rugosa, mientras que para $\tau_{iw} < 1$ la solución es finita y la superficie es suave. Por el contrario cuando el espesor de la película es finito, $g'' > 0$ y la situación cambia, siendo las soluciones gobernadas por una ecuación similar:

$$w \propto \left(1 + \frac{\tilde{\gamma}_{iw} + \gamma_{wv}}{w} q_{max}^2 \right)^{-\mu_{if}} \tag{2.26}$$

en la que el nuevo exponente, $\mu_{if} = \frac{\tilde{\gamma}_{iw}}{\tilde{\gamma}_{iw} + \gamma_{wv}} \times \tau_{iw}$, siempre es menor que el exponente τ_{iw}. Podemos entonces decir que para una superficie rugosa de hielo–agua con $\tau_{iw} \geq 1$ tenemos que $\mu_{if} \leq 1$ y

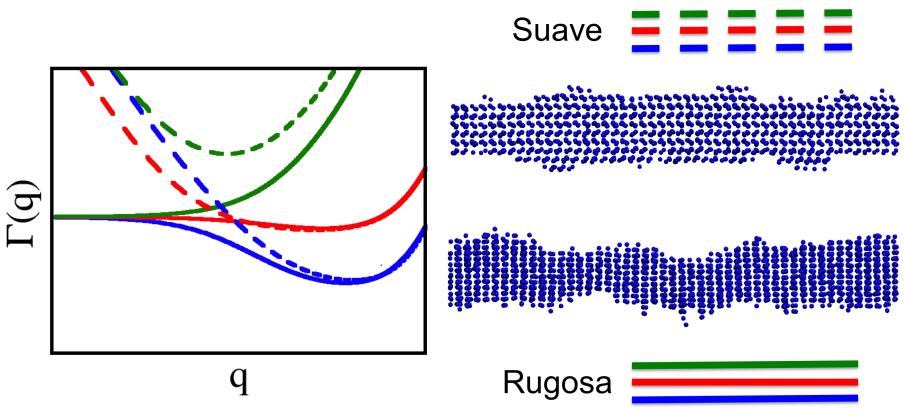

Figura 2.6. Ilustración con los diferentes regímenes de $\Gamma(\mathbf{q})$. En color azul, rojo y verde tenemos representado $\Gamma_{if}(\mathbf{q})$,$\Gamma_{fv}(\mathbf{q})$ y $\Gamma_{iffv}(\mathbf{q})$ respectivamente. En líneas discontinuas representamos la solución del modelo para una interfase suave y en líneas continuas para una superficie rugosa. En la imagen se muestran dos configuraciones que muestran un bloque de hielo con superficie rugosa y otro bloque con superficie lisa.

la superficie correspondiente hielo–película tiende a ser suave aunque la superficie hielo–agua sea rugosa.

Inmediatamente podemos relacionar las amplitudes de las fluctuaciones capilares con la rigidez superficial efectiva:

$$\Gamma_{\alpha-\beta}(\mathbf{q}) = \frac{k_B T}{A} \frac{1}{\langle h_\alpha(\mathbf{q}) h^*_\beta(\mathbf{q})\rangle q^2} \tag{2.27}$$

en donde los subíndices α y β identifican cada superficie if o fv. Destacamos que $\Gamma_{\alpha-\beta}$ se corresponde con la energía libre de superficie y es exactamente la tensión superficial macroscópica de la interfase cuando la superficie es rugosa cuando $\mathbf{q} \to 0$ y $\Gamma(q) = \gamma$.

El comportamiento de las interfases acopladas se rigen por el espectro de fluctuaciones. En la figura 2.6 vemos los diferentes comportamientos de los espectros y en la tabla 2.2 encontramos un resumen de los límites de los diferentes regímenes. Estos comportamientos se discuten ampliamente en los capítulos 2 y 3 de la parte II (Results).

Comparativa con el parámetro de orden local CHILL+

Además del parámetro de orden local propuesto por Lechner y Dellago que se ha utilizado en esta tesis, otro parámetro muy extendido para identificar partículas sólidas en agua es el CHILL+, que es una extension del algoritmo CHILL introducido por Moore et al. [39] Para ello emplea la correlación de orden orientacional de una molécula de agua con los primeros vecinos. El parámetro CHILL+ utiliza el número de enlaces alternados y eclipsados entre moléculas de agua para distinguir hielo cúbico, hielo hexagonal y los hidratos de clatrato en el líquido. Cada uno de los cuatro enlaces agua-agua establecidos en el hielo cúbico se corresponde con enlaces alternados, mientras que cada molécula en el hielo hexagonal (hielo Ih) tiene tres enlaces agua-agua alternados, correspondiente a los enlaces en el plano basal, y un enlace eclipsado, correspondiente al enlace paralelo al eje c.

$\Gamma_{\alpha-\beta}(\mathbf{q})$	$(\xi_{iw}^2+\xi_{wv}^2)q^2 \ll 1$	$\xi_{wv}^2 q^2 \ll 1 \ll \xi_{iw}^2 q^2$	$\xi_{iw}^2 q^2 \ll 1 \ll \xi_{wv}^2 q^2$	$(\xi_{iw}^2+\xi_{wv}^2)q^2 \gg 1$
$\Gamma_{if-if}(\mathbf{q})$	wq^{-2}	$(\tilde{\gamma}_{iw}+\gamma_{wv})$	wq^{-2}	$\tilde{\gamma}_{iw}$
$\Gamma_{fv-fv}(\mathbf{q})$	$\frac{wg''}{w+g''}q^{-2}$	$(\tilde{\gamma}_{iw}+\gamma_{wv})$	γ_{wv}	γ_{wv}
$\Gamma_{if-fv}(\mathbf{q})$	wq^{-2}	$(\tilde{\gamma}_{iw}+\gamma_{wv})$	$\frac{w\gamma_{wv}}{g''}$	$\frac{\tilde{\gamma}_{iw}\gamma_{wv}}{g''}q^2$
Clasificación	Suave y correlacionadas	Rugosa y correlacionadas	Suave y no correlacionadas	Rugosa y no correlacionadas

Tabla 2.2. Tabla resumen con los comportamientos de la rigidez efectiva $\Gamma_{\alpha-\beta}(\mathbf{q})$ en función del vector de onda. Los intervalos se establecen en relación a las diferentes escalas de longitudes de onda para $\xi_{iw}^2 = \tilde{\gamma}_{iw}/w$ y $\xi_{wv}^2 = \gamma_{wv}/g''$. La rugosidad o suavidad determina el comportamiento de la superficie hielo–agua mientras que la correlación se refiere al comportamiento de la superficie agua–vapor en relación a la superficie hielo–agua.

[39, 40] Por el contrario cada molécula de agua en un hidrato forma cuatro enlaces eclipsados con los primeros cuatro vecinos.

En el algoritmo CHILL y su extensión CHILL+ los enlaces alternados y eclipsados se identifican con la correlación del parámetro de orden de enlace orientacional desarrollado sobre la base de los parámetros de orden de enlace de Steinhardt et al. [41, 42] El orden local para l alrededor de cada molécula de agua i se puede cuantificar por un parámetro de orden con enlaces orientacionales. Este parámetro es el vector $q_l(i)$ en donde el número de componentes complejas alrededor de los cuatro primeros vecinos es $2l + 1$.

$$q_{lm}(i) = \frac{1}{4} \sum_{j=1}^{4} Y_{lm}(\widehat{r}_{ij}) \tag{2.28}$$

en donde q_{lm} es el vector complejo basado en armónicos esféricos que proyecta la estructura orientacional de los cuatro vecinos de la molécula. Para diferenciar entre enlaces alternados y eclipsados definimos la correlacion entre la particula i y su vecina j como $c(i, j)$, en donde $c(i, j)$ se calcula como el producto escalar de los vectores normalizados $q_l(i)$ y $q_l(j)$, donde $q_l(i) = \frac{1}{|q_l(i)|} \sum_{m=-l}^{l} q_{lm}(i) q^*_{lm}(i)$

En particular el algoritmo CHILL utiliza la correlación de q_3 para distinguir entre las fases sólidas y el agua líquida. CHILL identifica un enlace alternado cuando $c(i, j) \leq -0{,}8$ y un enlace eclipsado cuando $-0{,}05 \geq c(i, j) \geq -0{,}2$. Para permitir la identificación de clatratos y hielo hexagonal a temperaturas hasta sus puntos de fusión, el intervalo para los enlaces alternados no se ve modificada en el algortimo CHILL+, pero el intervalo para los enlaces eclipsados cambia y se extiende a $0{,}25 \geq c(i, j) \geq -0{,}35$.

Como vemos en las figuras 2.8 y 2.7 hay una discrepancia con el número de moléculas que etiquetan los dos parámetros. De manera general en el CHILL+ se etiquetan menos moléculas como líquidas. No obstante, en el parámetro CHILL+ está diseñado para identificar fases sólidas como los hielos I_c y I_h, clatratos, así como partículas de hielo hexagonal interfacial y clatrato interfacial. El resto de moléculas se asocian a la fase líquida. Básicamente las diferencias surgen porque CHILL+ etiqueta partículas de la interfase como sólidas (las que tienen los enlaces bien formados mientras que Lechner y Dellago toma esas partículas como líquidas). Si vemos las figuras con la evolución temporal de moléculas líquidas etiquetadas con el parámetro de orden de Lechner y Dellago y el CHILL+ se aprecia una enorme correlación entre los dos parámetros. Por tanto, habrá pequeñas diferencias en el espesor de la película líquida como vemos en la figura 2.9. No obstante, las fluctuaciones son las mismas, por lo que, cuando tomemos el origen con respecto al valor medio el valor de las fluctuacion es equivalente y cualquiera de los dos parámetros de orden darían resultados similares. En cualquie caso, hay que destacar que el etiquetado de las partículas justo en la interfase es un problema inherentemente ambiguo, puesto que no existe una definición única de un átoms en la interfase. En mi opinión, al tratarse de una interfase, es menor el número promedio de vecinos que tiene una molécula de agua en la superficie por lo que un buen parámetro de orden debe tener un componente dinámico. Pero esto conlleva, desde el punto de vista computacional, una gran cantidad de recursos en el almacenamiento de trayectorias.

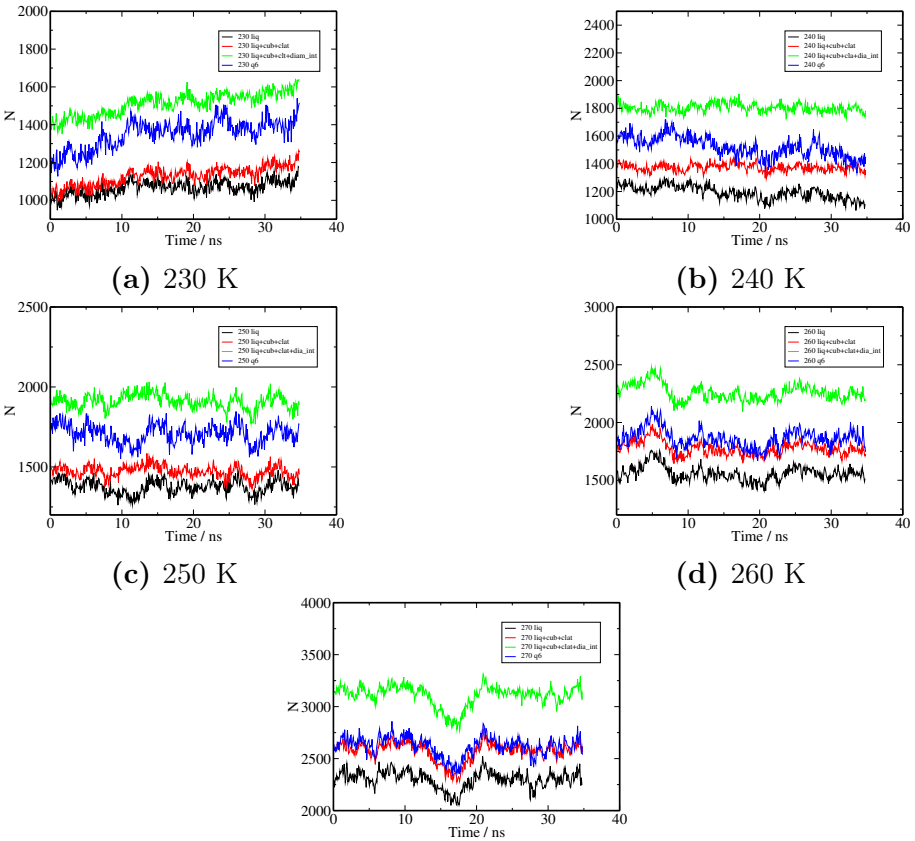

(a) 230 K **(b)** 240 K

(c) 250 K **(d)** 260 K

(e) 270 K

Figura 2.7. Comparativa entre el parámetro de orden CHILL+ y $\bar{q}_6$. En ambos parámetros se emplea el radio de corte de 3.5 Å como criterio de distancias a primeros vecinos.

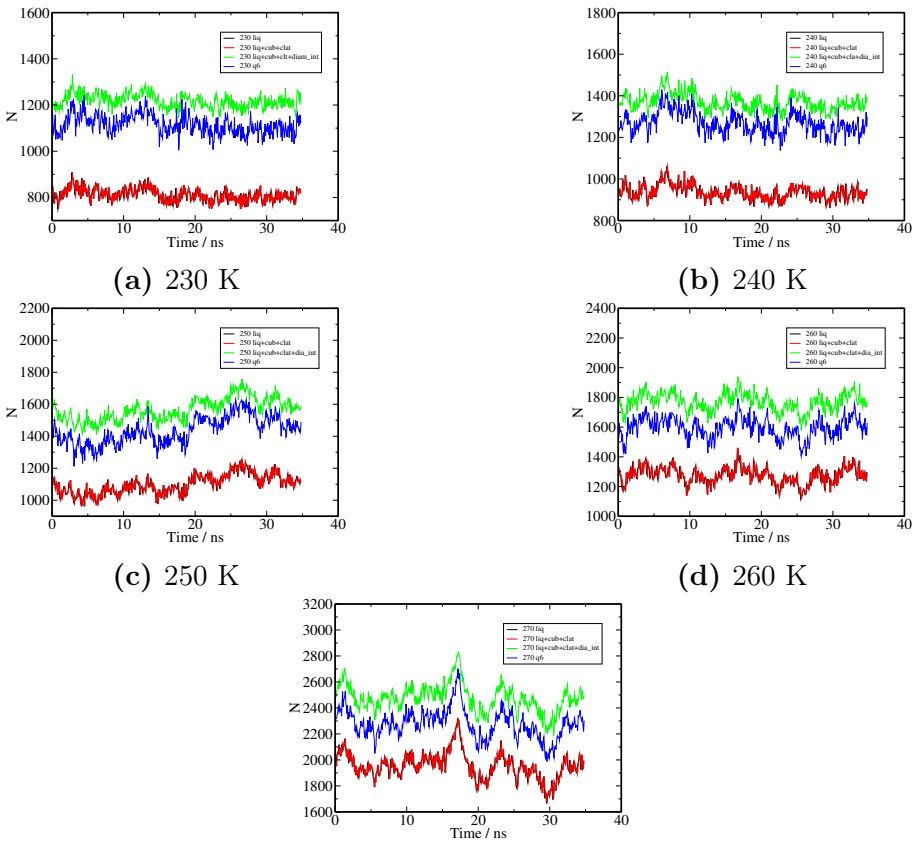

(a) 230 K (b) 240 K

(c) 250 K (d) 260 K

(e) 270 K

Figura 2.8. Comparativa entre el parámetro de orden CHILL+ y $\bar{q}_6$. En ambos parámetros se emplea el radio de corte de 3.5 Å como criterio de distancias a primeros vecinos.

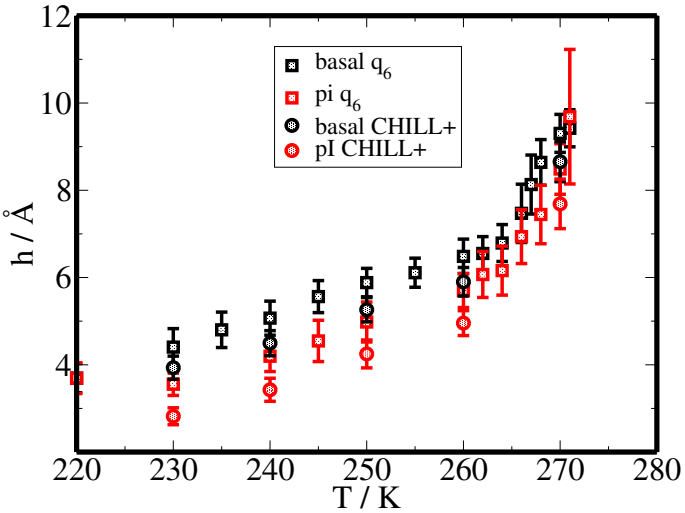

Figura 2.9. Comparativa del espesor de la película líquida empleando las configuraciones sólidas obtenidas mediante el parámetro de orden $\bar{q}_6$ y el CHILL+.[1, 43]

Bibliografía

[1] W. Lechner and C. Dellago, "Accurate determination of crystal structures based on averaged local bond order parameters," *J. Chem. Phys.*, vol. 129, no. 11, p. 114707, 2008.

[2] J. R. Espinosa, C. Vega, and E. Sanz, "Ice/water interfacial free energy for the tip4p, tip4p/2005, tip4p/ice, and mw models as obtained from the mold integration technique," *J. Phys. Chem. C*, vol. 120, no. 15, pp. 8068–8075, 2016.

[3] J. R. Henderson, "Statistical mechanics of the disjoining pressure of a planar film," *Phys. Rev. E*, vol. 72, no. 6, p. 051602, 2005.

[4] J. R. Henderson, "Disjoining pressure of planar adsorbed films," *Euro. Phys. J. ST*, 2011. in this issue.

[5] B. Derjaguin, "Modern state of the investigation of long-range surface forces," *Langmuir*, vol. 3, no. 5, pp. 601–606, 1987.

[6] D. Henderson, *Fundamentals of Inhomogenous Fluids*. New York: Marcel Dekker, 1992.

[7] D. Bhatt, J. Newman, and C. J. Radke, "Molecular simulation of disjoining-pressure isotherms for free liquid, lennard-jones thin films," *J. Phys. Chem. B*, vol. 106, no. 25, pp. 6529–6537, 2002.

[8] L. G. MacDowell, J. Benet, N. A. Katcho, and J. M. G. Palanco, "Disjoining pressure and the film-height-dependent surface tension of thin liquid films: New insight from capillary wave fluctuations," *Adv. Colloid Interface Sci.*, 2013.

[9] J. L. F. Abascal and C. Vega, "A general purpose model for the condensed phases of water: Tip4p/2005," *J. Chem. Phys.*, vol. 123, p. 234505, 2005.

[10] J. L. F. Abascal, E. Sanz, R. G. Fernandez, and C. Vega, "A potential model for the study of ices and amorphous water: Tip4p/ice," *J. Chem. Phys.*, vol. 122, p. 234511, 2005.

[11] E. G. Noya, C. Menduiña, J. L. Aragones, and C. Vega, "Equation of state, thermal expansion coefficient, and isothermal compressibility for ices ih, ii, iii, v, and vi, as obtained from computer simulation," *The Journal of Physical Chemistry C*, vol. 111, no. 43, pp. 15877–15888, 2007.

[12] H. L. Pi, J. L. Aragones, C. Vega, E. G. Noya, J. L. Abascal, M. A. Gonzalez, and C. McBride, "Anomalies in water as obtained from computer simulations of the tip4p/2005 model: density maxima, and density, isothermal compressibility and heat capacity minima," *Molecular Physics*, vol. 107, no. 4-6, pp. 365–374, 2009.

[13] C. Vega, M. M. Conde, C. McBride, J. L. F. Abascal, E. G. Noya, R. Ramirez, and L. M. Sese, "Heat capacity of water: A signature of nuclear quantum effects," *The Journal of Chemical Physics*, vol. 132, no. 4, p. 046101, 2010.

[14] A. Milchev and K. Binder, "Polymer melt droplets adsorbed on a solid wall: A monte carlo simulation," *J. Chem. Phys.*, vol. 114, pp. 8610–8618, 2001.

[15] L. G. MacDowell, J. Benet, N. A. Katcho, and J. M. Palanco, "Disjoining pressure and the film-height-dependent surface tension of thin liquid films: New insight from capillary wave fluctuations," *Adv. Colloid Interface Sci.*, vol. 206, no. 0, pp. 150–171, 2014.

[16] M. Müller and M. Schick, "Structure and nucleation of pores in polymeric bilayers: A Monte Carlo simulation," *J. Chem. Phys.*, vol. 105, pp. 8282–8292, 1996.

[17] M. Müller and L. G. MacDowell, "Interface and surface properties of polymer solutions: Monte Carlo simulations and self-consistent field theory," *Macromolecules*, vol. 33, pp. 3902–3923, 2000.

[18] R. L. Davidchack, J. R. Morris, and B. B. Laird, "The anisotropic hard-sphere crystal-melt interfacial free energy from fluctuations," *J. Chem. Phys.*, vol. 125, no. 9, p. 094710, 2006.

[19] A. O. Parry, C. Rascón, N. R. Bernardino, and J. M. Romero-Enrique, "Derivation of a non–local interfacial hamiltonian for short range wetting: I. double parabola approximation," *J. Phys.: Condens. Matter*, vol. 18, pp. 6433–6451, 2006.

[20] A. O. Parry, C. Rascón, N. R. Bernardino, and J. M. Romero-Enrique, "Derivation of a non–local interfacial hamiltonian for short range wetting: II. general diagramatic structure," *J. Phys.: Condens. Matter*, vol. 19, p. 416105, 2007.

[21] T. Zykova-Tilman, J. Horbach, and K. Binder, "Monte Carlo simulations of the solid–liquid transition in hard spheres and colloid–polymer mixtures," *J. Chem. Phys.*, vol. 133, p. 014705, 2010.

[22] R. E. Rozas and J. Horbach, "Capillary wave analysis of rough solid-liquid interfaces in nickel," *Europhys. Lett*, vol. 93, no. 2, p. 26006, 2011.

[23] J. Benet, P. Llombart, E. Sanz, and L. G. MacDowell, "Premelting-induced smoothening of the ice-vapor interface," *Phys. Rev. Lett.*, vol. 117, p. 096101, Aug 2016.

[24] L. G. MacDowell, P. Llombart, J. Benet, J. G. Palanco, and A. Guerrero-Martinez, "Nanocapillarity and liquid bridge-mediated force between colloidal nanoparticles," *ACS Omega*, vol. 3, no. 1, pp. 112–123, 2018.

[25] J. Benet, P. Llombart, E. Sanz, and L. G. MacDowell, "Structre and fluctuations of the premelted liquid film of ice at the triple point," *Mol. Phys.*, pp. 1–19, 2019.

[26] E. M. Fernández, E. Chacón, P. Tarazona, A. O. Parry, and C. Rascón, "Intrinsic fluid interfaces and nonlocality," *Phys. Rev. Lett.*, vol. 111, p. 096104, Aug 2013.

[27] F. P. Buff, R. A. Lovett, and F. H. Stillinger, "Interfacial density profile for fluids in the critical region," *Phys. Rev. Lett.*, vol. 15, pp. 621–623, Oct 1965.

[28] A. Vrij, "Possible mechanism for the spontaneous rupture of thin, free liquid films," *Discuss. Faraday Soc.*, vol. 42, pp. 23–33, 1966.

[29] D. S. Fisher and D. A. Huse, "Wetting transitions: A functional renormalization-group approach," *Phys. Rev. B*, vol. 32, pp. 247–256, Jul 1985.

[30] H. T. Dobbs and J. O. Indekeu, "Line tension at wetting: Interface displacement model beyond the gradient–squared approximation," *Physica. A*, vol. 201, pp. 457–481, 1993.

[31] C. Bauer and S. Dietrich, "Wetting films on chemically heterogeneous substrates," *Phys. Rev. E*, vol. 60, pp. 6919–6941, 1999.

[32] P. G. de Gennes, F. Brochard-Wyart, and D. Quéré, *Capillarity and Wetting Phenomena*. New York: Springer, 2004.

[33] M. Mecke, J. Winkelmann, and J. Fischer, "Molecular dynamics simulations of the liquid–vapor interface: Binary mixtures of Lennard–Jones fluids," *J. Chem. Phys.*, vol. 110, pp. 1188–1194, 1999.

[34] K. R. Mecke, "Thermal fluctuations of thin liquid films," *J. Phys.: Condens. Matter*, vol. 13, pp. 4615–4636, 2001.

[35] M. Li, A. M. Tikhonov, D. J. Chaiko, and M. L. Schlossman, "Coupled capillary wave fluctuations in thin aqueous films on an aqueous subphase," *Phys. Rev. Lett.*, vol. 86, pp. 5934–5937, Jun 2001.

[36] M. Fukuto, O. Gang, K. J. Alvine, and P. S. Pershan, "Capillary wave fluctuations and intrinsic widths of coupled fluid-fluid interfaces: An x-ray scattering study of a wetting film on bulk liquid," *Phys. Rev. E*, vol. 74, p. 031607, Sep 2006.

[37] P. S. Pershan and M. Schlossman, *Liquid Surfaces and Interfaces: Synchrotron X-ray Methods*. Cambridge: Cambridge University Press, 2012.

[38] S. A. Safran, *Statistical Thermodynamics of Surfaces, Interfaces and Membranes*. Reading: Addison-Wesley, first ed., 1994.

[39] E. B. Moore, E. de la Llave, K. Welke, D. A. Scherlis, and V. Molinero, "Freezing, melting and structure of ice in a hydrophilic nanopore," *Phys. Chem. Chem. Phys.*, vol. 12, pp. 4124–4134, 2010.

[40] I. M. Svishchev and P. G. Kusalik, "Crystallization of liquid water in a molecular dynamics simulation," *Phys. Rev. Lett.*, vol. 73, pp. 975–978, Aug 1994.

[41] P. J. Steinhardt, D. R. Nelson, and M. Ronchetti, "Bond-orientational order in liquids and glasses," *Phys. Rev. B*, vol. 28, pp. 784–805, Jul 1983.

[42] P. ten Wolde and D. RuizMontero, Maria J.and Frenkel, "Numerical calculation of the rate of crystal nucleation in a lennard jones system at moderate undercooling," *The Journal of Chemical Physics*, vol. 104, no. 24, pp. 9932–9947, 1996.

[43] A. H. Nguyen and V. Molinero, "Identification of clathrate hydrates, hexagonal ice, cubic ice, and liquid water in simulations: the chill+ algorithm," *The Journal of Physical Chemistry B*, vol. 119, no. 29, pp. 9369–9376, 2015. PMID: 25389702.

Capítulo 3
Determinación de la presión de equilibrio sólido–líquido.

La determinación de la presión de coexistencia del hielo–agua es fundamental para estudiar la termodinámica de equilibrio a lo largo de la curva de coexistencia sólido–líquido. Habitualmente la metodología empleada para determinar el diagrama de fases consiste en realizar simulaciones de energía libre o coexistencia directa para determinar un punto inicial sobre cada línea de coexistencia, para posteriormente poder realizar la integración termodinámica de tipo Gibbs-Duhem (i.e integrar la ecuación de Clausius-Clapeyron obteniendo así toda la línea de coexistencia) cuando los potenciales químicos de las dos fases son iguales.[1, 2, 3, 4, 5]

Los tiempos de relajación para simulaciones de coexistencia directa en el equilibrio sólido–líquido pueden ser del orden del microsegundo. Esto hace realmente necesario un método eficiente por el cual determinar la presión de equilibrio a cada temperatura. En este capítulo presentamos un método sencillo y rápido para evaluar la presión de coexistencia sólido–líquido. La presión de coexistencia (p_{coex}) sólido–líquido a una temperatura dada se define como aquella presión a la cual coexisten en equilibrio el hielo y el agua. Sabemos que se ha alcanzado el equilibrio cuando el número de moléculas de sólido que pasan a la fase líquida es igual al número de moléculas que cristalizan ($dN_{con} = -dN_{fus}$). El balance de materia del equilibrio puede escribirse de la siguiente manera:

$$N_p = N_{agua} - \frac{dN_{con}}{dt} + N_{hielo} + \frac{dN_{fus}}{dt} \tag{3.1}$$

en donde N_p es el número de moléculas totales a la presión p y dN_i/dt es la tasa de cristalización y fusión de moléculas de agua. En una transición de fases sólido–líquido ocurre un cambio de volumen del sistema. Este incremento de volumen en el caso de la cristalización del hielo tiene lugar debido a una menor densidad de la fase sólida. La transición de fase sólido–líquido sigue una dinámica de crecimiento de primer orden que depende linealmente de la presión. El sistema cristaliza o funde a una velocidad constante y proporcional a la diferencia de potencial químico de ambas fases. Esto se debe a que en este proceso de crecimiento interviene la superficie rugosa del sólido, si la superficie fuese lisa la dinámica de crecimiento o fusión del cristal coincidiría con la de un proceso energéticamente activado por la diferencia de potencial químico. [6, 7, 8, 9, 10] Por lo tanto, podemos relacionar a temperatura constante las variaciones de volumen producidas cuando el hielo está en contacto con el agua y determinar la presión de coexistencia sólido–líquido.

$$\frac{dV(p)}{dt} = k(p_{coex} - p) \tag{3.2}$$

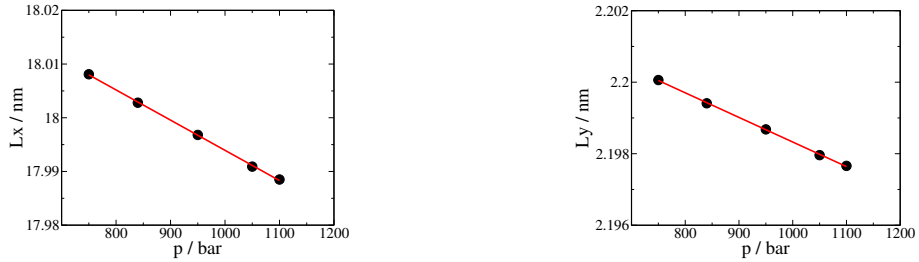

(a) **(b)**

Figura 3.1. Valores laterales de la caja de simulación (Lx, Ly) en función de la presión a la temperatura de 242K para el modelo TIP4P2005.
(a) $Lx = 18{,}05(nm) - 5{,}5624 \cdot 10^{-5}(nm\ bar^{-1})p(bar)$
(b) $Lx = 2{,}205(nm) - 6{,}8770 \cdot 10^{-6}(nm\ bar^{-1})p(bar)$

en donde k es una costante a cada temperatura que indica cuanto cambia el volumen del sistema con la variación de la presión y p_{coex} es la presión de coexistencia de las dos fases para cada isoterma. Podemos representar el volumen del sistema en función de la presión y ajustar a una línea recta para determinar el valor de k. Atendiendo a la dependencia de V en función de p, tenemos que V va disminuyendo con el aumento de la presión ya que el aumento de presión favorece la fusión del hielo en agua, por lo que $dV(p)/dt$ se vuelve negativo y la presión de coexistencia se corresponde con el valor de presión al cual $dV(p = p_{coex})/dt = 0$.

Queremos determinar la presión de coexistencia de un sistema sólido–líquido para realizar una simulación de equilibrio y analizar las fluctuaciones capilares en la interfase hielo–agua (capítulo **2**). Para ello vamos a realizar simulaciones de dinámica molecular en el colectivo NP_zT. De esta forma conseguimos evitar la imposición de una tensión superficial asociada al aumento del área en el plano de la interfase. Este tipo de simulaciones nos permiten variar exclusivamente el volumen del sistema variando la longitud de uno de los lados de la caja de simulación. El único problema que encontramos es que no conocemos las dimensiones de los parámetros de red del plano de la interfase y hay que determinarlos. Para solucionarlo realizamos varias simulaciones de un sólido volumétrico en el colectivo NPT a la temperatura deseada y en un intervalo de presiones determinadas. De esta forma fijamos los parámetros de red correspondientes a la presión y temperatura deseadas para poder evaluar los cambios de volumen del sistema asociados a la variación del eje z. La figura 3.1 muestra los valores de red obtenidos en el plano xy a cada presión.

Una vez conocidos los valores de red que se mantienen constantes durante la simulación NP_zT, realizamos tandas de simulaciones a diferentes presiones en las que vamos a seguir la evolución con el tiempo del volumen de la caja de simulación. Esta variación de volumen se relaciona con la velocidad de crecimiento cristalino. Integrando la ecuación Ec. 3.2 obtenemos:

$$V(p,t) = V_o + k(p_{coex} - p)t \tag{3.3}$$

Representando $V(p,t)$ frente a t y ajustando a una línea recta obtenemos la pendiente $dV(p)/dt = a$. Podemos ver en la figura 3.2 como cambia el volumen con todas las presiones intentadas y realizar el ajuste lineal para determinar a. De esta forma podemos representar a en función del tiempo y ajustar a una línea recta. Por último, interpolamos en la recta el valor $dV(p)/dt = 0$ y obtenemos la presión de coexistencia tal y como indica la Ec. 3.2.

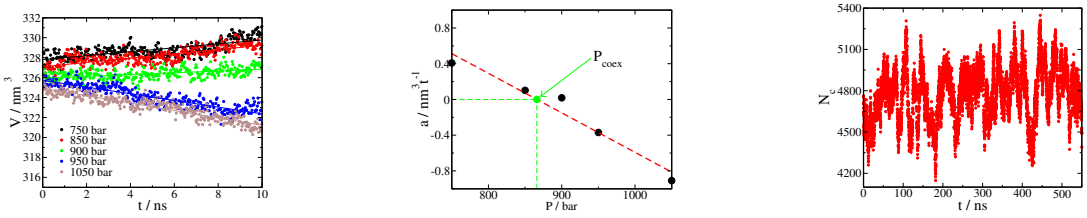

(a) **(b)** **(c)**

Figura 3.2. (a) Evolución del volumen del sistema con el tiempo de simulación. (b) Representación de la pendiente $a = \frac{\partial V}{\partial t}$
$\frac{\partial V}{\partial t} = 3{,}88(nm^3t^{-1}) - 0{,}0044(nm^3t^{-1})p(bar^{-1})$
(c) Evolución del número de moléculas sólidas en una simulación NVT a 242 K para el sistema sólido–líquido rescalado a los valores de red de equilibrio a presión de 882 bar.

Bibliografía

[1] D. Frenkel and A. J. C. Ladd, "New Monte Carlo method to compute the free energy of arbitrary solids. Application to the FCC and HCP phases of hard spheres," *J. Chem. Phys.*, vol. 81, pp. 3188–3193, 1984.

[2] D. A. Kofke, "Direct evaluation of phase coexistence by molecular simulation via integration along the saturation line," *J. Chem. Phys.*, vol. 98, pp. 4149–4162, 1993.

[3] R. García Fernández, J. L. F. Abascal, and C. Vega, "The melting point of ice ih for common water models calculated from direct coexistence of the solid-liquid interface," *The Journal of Chemical Physics*, vol. 124, no. 14, p. 144506, 2006.

[4] M. S. G. Razul and P. G. Kusalik, "Crystal growth investigations of ice/water interfaces from molecular dynamics simulations: Profile functions and average properties," *The Journal of Chemical Physics*, vol. 134, no. 1, p. 014710, 2011.

[5] M. M. Conde, M. A. Gonzalez, J. L. F. Abascal, and C. Vega, "Determining the phase diagram of water from direct coexistence simulations: The phase diagram of the tip4p/2005 model revisited," *The Journal of Chemical Physics*, vol. 139, no. 15, p. 154505, 2013.

[6] J. D. Weeks and G. H. Gilmer, "Dynamics of crystal growth," *Adv. Chem. Phys.*, vol. 40, pp. 157–228, 1979.

[7] C. Jayaprakash, W. F. Saam, and S. Teitel, "Roughening and facet formation in crystals," *Phys. Rev. Lett.*, vol. 50, pp. 2017–2020, Jun 1983.

[8] C. Rottman and M. Wortis, "Equilibrium crystal shapes for lattice models with nearest-and next-nearest-neighbor interactions," *Phys. Rev. B*, vol. 29, pp. 328–339, Jan 1984.

[9] S. A. Safran, *Statistical Thermodynamics of Surfaces, Interfaces and Membranes.* Reading: Addison-Wesley, first ed., 1994.

[10] J. Benet, P. Llombart, E. Sanz, and L. G. MacDowell, "Premelting-induced smoothening of the ice-vapor interface," *Phys. Rev. Lett.*, vol. 117, p. 096101, Aug 2016.

Capítulo 4
Generación de configuraciones iniciales de micelas y bicapas

En el capítulo 6 de esta tesis hemos estudiado micelas de bromuro de hexadeciltrimetilamonio (CTAB) en disolución acuosa y en presencia de diferentes aditivos, así como la adsorción de los agregados coloidales sobre nanopartículas de oro. La complejidad de estos sistemas requiere que para realizar la dinámica molecular sea necesario el uso de configuraciones atómicas para agregados previamente ensamblados como punto de partida. [1] De lo contrario es posible que no se alcance el equilibrio debido a que la formación de los agregados puede ocurrir a tiempos muy grandes (del orden de milisegundos) que no son accesibles mediante simulación [2, 3, 4, 5, 6]

Para realizar una simulación clásica de dinámica molecular, empleamos campos de fuerzas con términos repulsivos que hacen que la energía potencial entre dos partículas aumente de manera muy rápida cuando la separación entre las dos partículas se reduce, haciéndose prácticamente infinito cuando la distancia entre los dos átomos es menor que el diámetro de los átomos (aproximadamente σ en el modelo Lennard-Jones). Como resultado, si inicialmente las partículas se colocan a una distancia menor que el diámetro molecular de otra partícula se producen solapamientos que conducen a fuerzas muy grandes y hacen que el sistema no sea estable bajo el campo de fuerzas empleado. Con el fin de que el sistema sea estable, empleamos el paquete PACKMOL para generar las configuraciones iniciales de los agregados de CTAB. Este paquete permite empaquetar átomos o moléculas de acuerdo a las necesidades de cada sistema. Entre los ejemplos que se destacan hay simples mezclas para sistemas de dos fases, generación de bicapas formadas por lípidos y solvatación de vesículas.[7] Para las simulaciones de dinámica molecular realizadas en esta tesis generamos micelas, bicapas y cilindros que se simulan en disolución o depositados sobre superficies y nanopartículas de oro.

Generación de agregados de CTAB

Para generar los agregados de CTAB insertamos aleatoriamente las moléculas de surfactante dentro de un volumen restringido. Los agregados coloidales que se han generado están formados por moléculas de CTA^+ y CTA^+ más n-decanol. Para las moléculas de CTA^+ y n-decanol proponemos un nuevo modelo de cargas compatible con el campo de fuerzas GROMOS-53a6. En la figura 4.1 podemos ver las cargas parciales obtenidas por cálculos *ab-initio* con correcciones Moller-Plesset de segundo orden para las moléculas en vacío [8, 9, 10] Los contraiones de bromo se modelan mediante

Modelo de CTA^+ y n-decanol

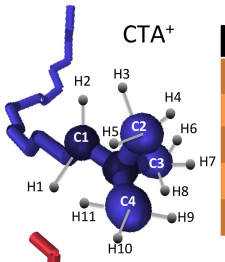

GROUP		CHARGE / eV	
C1,H1,H2	/ CH_2	-0.206,0.248,0.248	/ 0.303
N		-0.359	
C2,H3,H4,H5	/ CH_3	-0.421,0.251,0.251,0.253	/ 0.352
C3,H6,H7,H8	/ CH_3	-0.417,0.251,0.252,0.252	/ 0.352
C4,H9,H10,H11	/ CH_3	-0.420,0.251,0.251,0.253	/ 0.352

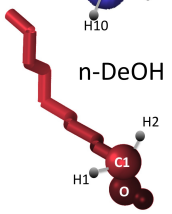

GROUP	CHARGE / eV
C1,H1,H2 / CH_2	-0.027, 0.178, 0.178 / 0.325
O	-0.808
H	0.483

Tabla 4.1. Sup: Molécula de CTA^+ modelada con grupos efectivos CH_3, CH_2 y tabla con las cargas parciales y reducidas para cada grupo.[9, 10] Inf: Molécula de n-decanol (n-DeOH) modelada con grupos efectivos CH_3, CH_2 y tabla con las cargas parciales y reducidas para cada grupo.[10]

un centro de interacción Lennard–Jones y una carga local $(-e)$.

- Generación de micelas y bicapas

  Para generar configuraciones iniciales de sistemas micelares insertamos las moléculas dentro de una esfera de radio igual a la longitud de la molécula de CTAB ($r_{CTA^+} \approx 1{,}7$ nm), aumentando el valor del radio a medida que aumentamos el número de moléculas presentes en el agregado. En la parte superior de la figura 4.1 podemos ver un ejemplo del sistema generado para una micela de 60 moléculas de CTA^+ y 60 iones Br^-. Los iones bromo se colocan en el exterior del agregado en una corona esférica de espesor 1 nm. Para los sistemas preensamblados en forma de bicapa insertamos las moléculas de CTA^+ y el decanol (cuando haya aditivo) en dos capas interconectadas a través de las cadenas alifáticas de las moléculas. El sistema se genera insertando el centro de masas surfactante o del aditivo de forma aleatoria en el plano x, y. El vector cabeza-cola de la molécula insertada se sitúa paralelo al eje z. En la capa superior el sentido del vector es en la dirección $-z$ y $+z$ para la capa inferior.

- Generación de superfices de oro

  La estructura del oro en estado sólido más estable es la que proporciona el empaquetamiento compacto centrado en las cara (fcc). Esta estructura tiene átomos situados en cada una de los vértices de un cubo y en el centro de cada cara. En una celdilla unidad cada átomo de un vértice es compartido entre ocho celdas unidad. Por otra parte, cada uno de los átomos de las caras se comparte con otra celda. Los átomos que forman una red de tipo fcc tienen un número de coordinación igual 12.

  Uno de los objetivos principales en esta tesis es comprender los mecanismos en el crecimiento de nanopartículas de oro, y por qué se establecen direcciones preferentes de crecimiento, dando lugar a una transición en la que las nanopartículas pasan de formar esferas a varillas.

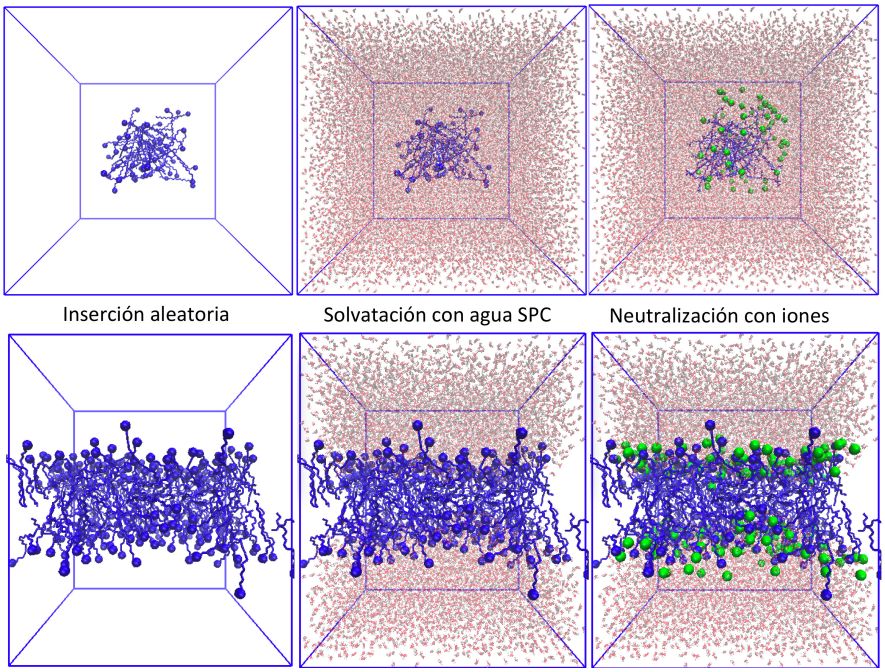

Figura 4.1. Ejemplos de configuraciones iniciales para micelas y bicapas generadas con PACKMOL. En líneas y bolas azules están representados las cadenas y la cabeza de CTA^+ respectivamente. El líneas blancas y rojas las moléculas de agua SPC y en bolas verdes los contraiones Br^- que neutralizan el sistema.

Para explicar este proceso en base al efecto de la interfase CTAB–oro en el crecimiento de las nanovarillas, necesitamos generar las superficies de oro que aparecen con más frecuencia en los procesos de crecimiento resultantes de la síntesis de los mismos. En numerosos estudios las caras del oro que se encuentran para nanopartículas con un tamaño pequeño son las caras {100}, {111}, {110} y {250}. [11]

Para generar las superficies de oro replicamos la celda unidad en las direcciones x e y. Las celdas unidad se construyen con la orientación deseada para cada cara. En la figura 4.2 podemos ver las superficies que se han estudiado en este trabajo.

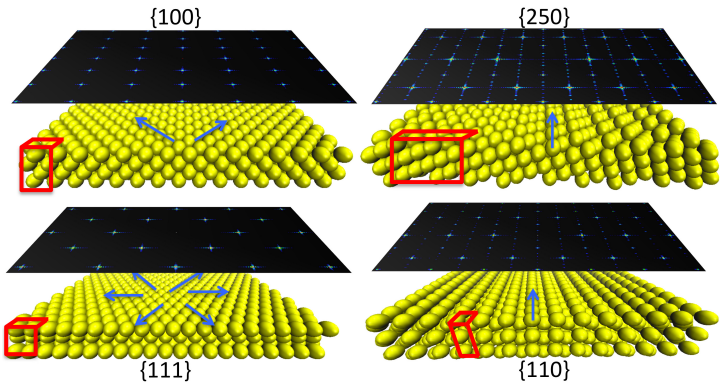

Figura 4.2. Superficies de oro generadas empleando átomos de oro de diámetro $\sigma = 2{,}95$ Å y la red cúbica compacta con $a = 4{,}17$ Å. Remarcamos en rojo la celda unidad correspondiente para cada superficie. Las flechas de color azul indican las direcciones compactas. Sobre cada superficie representamos el factor de estructura bidimensional, $S_{\mathbf{k_x},\mathbf{k_y}}$.

Bibliografía

[1] P. Llombart, L. G. MacDowell, and N. E. G., "Submitted," *Colloids and Surface A*, vol. 0, no. 0, p. null, 0. PMID: 30939242.

[2] Y. Wang, D. S. D. Larsson, and D. van der Spoel, "Encapsulation of myoglobin in a cetyl trimethylammonium bromide micelle in vacuo: A simulation study," *Biochemistry*, vol. 48, pp. 1006–1015, 2009.

[3] M. Jorge, "Structure of cationic surfactant micelles from molecular simulations of self-assembly," *J. of Molec. Structure: THEOCHEM*, vol. 946, no. 1, pp. 88 – 93, 2010. Achievements and Challenges of Computational Chemistry in Portugal.

[4] G. F. Catá, H. C. Rojas, A. P. Gramatges, C. M. Zicovich-Wilson, L. Alvarez, and C. Searle, "Initial structure of cetyltrimethylammonium bromide micelles in acqueous solution from molecular dynamics simulations," *Soft Matt.*, vol. 7, p. 8508, 2011.

[5] S. Storm, S. Jakobtorweihen, I. Smirnova, and A. Z. Panagiotopoulos, "Molecular dinamics simulations of sds and ctab micellization and prediction of partition equilibria with cosmomic," *Langmuir*, vol. 29, p. 11582, 2013.

[6] S. Illa-Tuset, D. C. Malaspina, and J. Faraudo, "Coarse-grained molecular dynamics simulation of interface behaviour and self-assembly of ctab cationic surfactant," *Phys. Chem. Chem. Phys.*, vol. 20, pp. 26422–26430, 2018.

[7] L. Martínez, R. Andrade, E. G. Birgin, and J. M. Martínez, "Packmol: A package for building initial configurations for molecular dynamics simulations," *J. Comp. Chem.*, vol. 30, pp. 2157–2164, 2009.

[8] C. Oostenbrick, A. Villa, A. E. Mark, and W. F. van Gunsteren, "A biomolecular force field based on the free enthalpy of hydration and solvation: the gromos force-field parameter sets 53a5 and 53a6," *J. Comp. Chem.*, vol. 25, pp. 1656–1676, 2004.

[9] G. González-Rubio, P. Díaz-Núñez, A. Rivera, A. Prada, G. Tardajos, J. González-Izquierdo, L. Bañares, P. Llombart, L. G. MacDowell, M. Alcolea-Palafox, L. M. Liz-Marzán, O. Peña-Rodríguez, and A. Guerrero-Martínez, "Femtosecond laser reshaping yields gold nanorods with ultranarrow surface plasmon resonances," *Science*, vol. 358, pp. 640–644, 2017.

[10] G. González-Rubio, V. Kumar, P. Llombart, P. Díaz-Núñez, E. Bladt, T. Altantzis, S. Bals, O. Peña-Rodríguez, E. G. Noya, L. G. MacDowell, A. Guerrero-Martínez, and L. M. Liz-Marzán, "Disconnecting symmetry breaking from seeded growth for reproducible synthesis of high quality gold nanorods," *ACS Nano*, vol. submitted, 2018.

[11] E. Carbó-Argibay, B. Rodríguez-González, S. Gómez-Graña, A. Guerrero-Martínez, I. Pastoriza-Santos, J. Pérez-Juste, and L. M. Liz-Marzán, "The crystalline structure of gold nanorods revisited: Evidence for higher-index lateral facets," *Angewandte Chemie International Edition*, vol. 49, no. 49, pp. 9397–9400, 2010.

Parte II

Results

Chapter 1

Structure and water attachment rates of ice in the atmosphere: role of nitrogen

Pablo Llombart[1,2], *Ramón M. Bergua*[2], *Luis G. MacDowell*[2] *and Eva G. Noya*[1]

(1) Instituto de Química Física Rocasolano, CSIC, Calle Serrano 119, 28006 Madrid, Spain

(2) Departamento de Química Física, Facultad de Ciencias Químicas, Universidad Complutense de Madrid, 28040 Madrid, Spain

Abstract

In this work we perform computer simulations of the ice surface in order to elucidate the role of nitrogen in the crystal growth rates and crystal habits of snow in the atmosphere. In pure water vapor at temperatures typical of ice crystal formation in cirrus clouds, we find that basal and primary prismatic facets exhibit a layer of premelted ice, with thickness in the subnanometer range. For partial pressures of 1 bar, well above the expected values in the troposphere, we find that only small amounts of nitrogen are adsorbed. The adsorption takes place onto the premelted surface, and hardly any nitrogen appears to dissolve within the premelting film. The premelting film thickness does not appear to change either. We quantify the resulting change of the ice/vapor surface tension to be in the hundredth of mN/m and find that the structure of the pristine ice surface is hardly changed in a significant manner. We perform a trajectory analysis of colliding water molecules, and find that the attachment rates from direct ballistic collision are very close to unity irrespective of the nitrogen pressure. Nitrogen is however at sufficient density to deflect a fraction of trajectories with smaller distance than the mean free path. Overall, our results point very clearly to a passive role of nitrogen on surface attachment kinetics, and an influence related essentially to the diffusion limited flow of water vapor across the bulk gas phase.

Introduction

Modeling of radiation processes in clouds is an essential requisite for the prediction of climate change.[1, 2] In the troposphere, ice is a widespread component, as cirrus clouds cover about 30 % of the mid latitudes at any given time.[3] The ice grains that make these cirrus clouds, whether in

mono-crystalline form or as crystal aggregates play a crucial role on the earth's climate.[4, 5, 6, 7, 8] They account for a significant amount of the radiation budget,[4, 5, 6, 7] and concentrate airborne chemicals with an important contribution to the atmosphere's chemistry.[9] However, the underlying microphysics of ice crystallites is a major source of uncertainty for climate change models, while the mechanism for ice growth and surface activity remains poorly understood.[1]

In view of this situation, a great number of recent computer simulation studies seek to characterize the ice surface and shed light onto growth mechanisms.[10, 11, 12, 13, 14, 15, 16, 17, 18] In most such studies, a bulk ice sample is placed either in vacuum or within a saturated water vapor atmosphere, and only rarely is the interaction of atmospheric gases considered explicitly.[19, 20] Of course, acidic gases and polar organic molecules adsorbed on the ice surface are expected to play a crucial impact on atmospheric chemistry.[9, 20] However, their small concentration warrants the study of pristine ice surfaces as an initial starting point.

On the contrary, the two major components of the atmosphere, nitrogen and oxygen, have far less affinity for ice, but are found at concentrations two orders of magnitude larger than saturated water vapor. Although laboratory studies are often performed on a controlled atmosphere of nitrogen gas to avoid possible bias,[21, 22, 23, 24, 25] the fact is that their role on the structure and growth rates remains largely unknown.[20]

A chemical physicist's first guess clearly indicates that an inert gas such as nitrogen should have a very small impact on the properties of the ice surface. Indeed, reported thermodynamic data on surface tension and phase coexistence data for water essentially ignore the role of the surrounding atmosphere. From Henry's constant data,[26] it is expected that the concentration of nitrogen in water at 0 C and one bar is not more than 10^{-3} mol/L, and likely far smaller in ice. Furthermore, adsorption studies of nitrogen on ice consistently yield small BET adsorption energies which are only 2.5 kJ/mol at 77 K.[27, 28, 29] Measurements using other apolar gases such as methane yield similar results.[30, 31]

Intriguingly, laboratory studies of surface structure and crystal growth rates have recurrently reported significant differences between experiments performed on either a controlled nitrogen or pure water vapor atmosphere.[32, 33, 34, 35, 36, 37]

In experiments of ice crystals grown from the vapor, it is well known that the presence of significant amounts of nitrogen gas largely slows down the crystal growth rates.[38, 39] However, it has been usually interpreted that this is not the effect of a significant perturbation of the ice surface, but rather, the effect of diffusion limited growth.[40, 41] This occurs when the slow diffusion rate of water vapor in air is unable to reestablish the depleted ambient vapor density close to the growing ice surface. As a result, the interpretation of growth measurements requires to distinguish the local surface saturation from the asymptotic bulk vapor saturation. In view of the difficulty to accurately estimate the full density field at the crystal, standard experiments aimed at unraveling the *correct* surface attachment kinetics have rather been performed in low pressure chambers with as small nitrogen as possible, under the assumption that nitrogen plays no other role than decreasing the diffusion coefficient of water vapor.[41, 42, 43, 44, 45]

However, some studies on crystal growth, with explicit account of diffusion resistance of air reported that the surface saturation corrected growth rates were strongly influenced by nitrogen, [32, 33, 34] decreasing the surface kinetics selectively on the prismatic facet by factors as large as 1/100 at T=-11 C, and 1/20 at T=-1/20 at -15 C compared to experiments in pure water vapor.[32, 34] In fact, it was claimed that adsorption of nitrogen was essential to explain the anisotropic growth of ice

crystals as described in the Nakaya diagram. Particularly, Beckmann and collaborators postulated a nitrogen poisoning mechanism that is well known in catalysis.[33] Unfortunately, this explanation assumes enthalpies of adsorption ranging from 25 to 40 kJ/mol, which are very much at odds with BET isotherm experiments and ab-initio calculations.[27, 28, 29, 20] On theoretical grounds, another possible role of adsorbed gases is to proliferate in between crystal steps and kinks. This can potentially change the step free energy, and as a result, change significantly the surface roughness and crystal growth rates.[46] However, none of these hypothesis seem to be consistent with later studies of crystal growth habits at reduced pressure, which seem to agree well with results for the standard Nakaya diagram,[47, 41, 44] and exhibit a distinct growth anisotropy,[48, 41, 43, 44, 45] similar to that observed in the presence of air.[49, 50] Furthermore, similar slowing down of growth rates has been confirmed with other inert gases, in support of merely a diffusion limited role on ice growth.[47, 40]

Atmospheric gases have also been postulated to play a significant role in determining the thickness of premelting films of water adsorbed onto the ice surface.[51, 52, 35, 53, 54, 36, 25] Indeed, conflicting results for the equilibrium thickness of premelting films have regularly been found, with thicknesses differing by several orders of magnitude.[55, 56, 57] These discrepancies can be partly reconciled by taking into account that contamination can increase the thickness of the premelting film considerably.[35, 58, 36, 25] An uncontrolled exposure to the atmosphere can easily promote such contamination, and this explains why often crystal samples in air exhibit much larger film thicknesses.[36] However, claims that the thickness of premelting films diverges in the presence of nitrogen,[35] do not seem warranted in view of more recent experiments indicating a finite equilibrium thickness in a controlled nitrogen atmosphere.[21, 22, 23, 24]

In view of this account, it seems clear that the role of adsorbed nitrogen on such significant atmospheric properties as the equilibrium surface structure and the crystal growth rate of ice remains largely unknown and controversial. Certainly, whatever conclusion is made from the current evidence is a result of indirect and hypothetical arguments from macroscopic samples. Computer simulations could be an invaluable tool to shed light into this complex problem, as they can elucidate the microscopic features of the crystal growth mechanism. Indeed, Libbrecht has urged for such a study, in order to clarify some conflicting results on the role of nitrogen in recent crystal growth experiments.[45, 37]

In this work we perform a computer simulation study of the ice surface under a controlled nitrogen atmosphere. In our study we first perform computer simulations of ice in presence of pure water vapor and provide a detailed structural characterization of the ice/vapor interface (section 1.4.1). We then perform additional simulations of ice under nitrogen gas and study the adsorbed layer of nitrogen (section 1.4.2), and its influence on the structural and thermodynamic properties of the ice interface (section 1.4.3). Finally, we present results on the influence of nitrogen gas in water attachment kinetics. (section 1.5). In section 1.6 we summarize and discuss the significance of our results. Overall we find that nitrogen gas does not significantly change the properties of the ice surface, and conclude that crystal growth rate and crystal habit differences observed for ice in nitrogen are related only to the complex diffusion limited flow of water towards the ice surface.

$Altitude/m$	T/K	$p \cdot 10^{-5}$/ Pa
2750	270	0.72
4250	260	0.60
5800	250	0.48
7310	240	0.40
8840	230	0.32

Table 1.1. Average atmospheric temperature and pressure as a function of altitude according to the International Standard Atmosphere (ISO 2533:1975)

Methods

All simulations were performed with the simulation package GROMACS[59, 60]. Water and nitrogen were described using rigid, non-polarizable models, TIP4P/Ice [61] for water and TraPPE [62] for nitrogen. TIP4P/Ice was fitted to reproduce the melting temperature of ice Ih, the densities of liquid water and ices II and V, and the stability region of ice III[61], whereas TraPPE was fitted to reproduce the vapor-liquid equilibrium of nitrogen [62]. Simulations were carried out mostly in the NVT ensemble. Temperature was controlled using the Bussi-Donadio-Parrinello velocity-rescale thermostat with a relaxation time of 1 ps[63]. In those simulations carried out in NpT ensemble, the Berendsen barostat was used to achieve the desired pressure. Periodic boundary conditions were applied on the three directions of space. Interactions were truncated at a distance of 9 Å. Standard long range corrections were used for Lennard-Jones, whereas the Particle Mesh Ewald method was used to deal with electrostatic interactions. Equations of movement were integrated using a timestep of 3 fs.

Determination of the equation of state of nitrogen gas

Prior to the simulations of the ice-vapor interface, we carried out a series of simulations aimed at determining the equation of state for nitrogen. This equation is later used to relate the number of adsorbed nitrogen molecules with the corresponding bulk pressure in the ice-vapor system. The simulations covered densities within ρ =0.5-2 $kg \cdot m^{-3}$ and temperatures within T =230-270 K (at 5 K intervals), corresponding to pressures between about 0.30 to 1.1 bars that bracket the expected pressure of the International Standard Atmosphere (c.f. Tab.1.1) . All simulations were carried out in a cubic box of length 21.5 nm, containing between 120 and 420 nitrogen molecules depending on density. Each of these thermodynamic states was simulated during 3 ns averaging every 75 ps for calculate thermal averages. Pressure was estimated as an ensemble average using the virial route[64]. For each isotherm, the pressure as a function of density was fitted to:

$$P(T) = \rho k_B T(1 + B_2(T)\rho) \tag{1.1}$$

where k_B is the Boltzmann constant and $B_2(T)$ is the second virial coefficient. The values of $B_2(T)$ obtained at each temperature were then fitted to the function $B_2(T) = A_0 - A_1 T^{-1}$. Eq. 1.1 together with this fit can be used to predict the pressure of nitrogen for any particular values of density and pressure within the range of simulated densities and pressures.

The equation of state data and the corresponding virial coefficients are collected in detailed form in the supplementary material. The pressure isotherms and fits to the virial coefficients are displayed in Figure 1.1. Whereas the empirical model employed for nitrogen was fitted at far lower temperatures to match coexistence liquid densities, we find a reasonable agreement for the Boyle temperature, which, by extrapolation from our results is $T_B = 296$ K, compared to the reported experimental value of $T_B = 326$ K.[65]

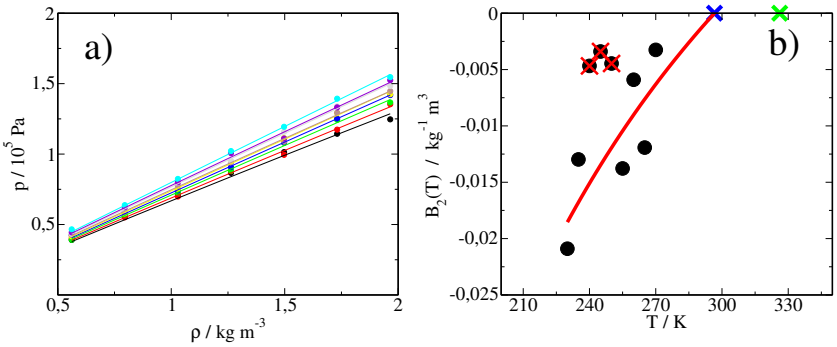

Figure 1.1. (a) Pressure as a function of nitrogen density, with simulation results shown as circles. In order of decreasing slope, studied temperatures are 230 (black), 235 (red), 240 (green), 245 (blue), 250 (yellow), 255 (gray), 260 (brown), 265 (violet) and 270 (cyan) respectively. Fits to Eq. 1.1 for each isotherm are shown as full lines with the same color code. (b) Second Virial Coefficient, $B_2(T)$, as a function of temperature. Black circles correspond to the slopes obtained from the fit to the isotherms, while the red line represents the fit to the function $B2(T) = 0.06402(kg^{-1}m^3) - 18.990(kg^{-1}m^3K)T^{-1}(K^{-1}) = A_0 - A_1T^{-1}$. Symbols with red crosses were not taken into account for the fit. The blue cross is the extrapolated Boyle temperature obtained from the simulated results. The green cross corresponds to the experimental Boyle temperature.[65]

Simulation of the ice-vapor interface in the presence of nitrogen

The ice-vapor interface was built using the following procedure. We start by generating a slab of ice containing $8 \times 8 \times 5$ unit cells. At each temperature, the bulk solid is simulated during 6 ns in the NpT ensemble and $p = 1$ bar. The simulation cell is then rescaled to its equilibrium value, and placed inside a larger elongated cell along the direction z, perpendicular to the interface. A number of nitrogen molecules are then ramdonly inserted in the vacuum region of the box. Simulation boxes typically had a lateral size $L_x = 7$ nm and $L_y = 6$ nm. The perpendicular size was set to $L_z = 15$ nm for pure ice under water vapor and $L_z = 39$ nm for ice in a nitrogen atmosphere. For the latter simulations, the gas phase was formed with 15 to 50 nitrogen molecules. Detailed information about system size and dimensions are provided in the supplemental material.

The system is evolved in the NVT ensemble during 15 ns to allow the premelting layer to equilibrate. Averages are taken over the next 35 ns, saving configurations every 75 ps. The density profile of the vapor phase established mainly by nitrogen molecules is measured, and this data is used to infer the ambient pressure from Eq. (1.1). Amounts of nitrogen are selected such that, for each temperature, the pressure ranges from the expected value for the International Standard Atmosphere (c.f. Tab.1.1) to a pressure somewhat above 1 bar.

In the simulations, the ice slabs in vacuum develop a thin layer of disordered quasi-liquid like molecules. The properties of this layer are best characterized by defining ice-liquid and liquid-vapor surfaces that sandwich the premelting layer.[66, 67] The thickness of the liquid layer formed on the surface of ice can be determined from the average distance between the surfaces.

In order to locate them, we need first of all to establish a criterium to distinguish between solid and liquid water molecules. For that purpose we used the local averaged order parameter, $\bar{q}_6$, proposed by Lechner and Dellago [68]. This order parameter adopts different values depending on the local environment of the water molecule. Solid molecules adopt large values of $\bar{q}_6$, whereas molecules in liquid environments exhibit low values of $\bar{q}_6$, with only a small region of overlap between the distribution of solid and liquid environments. The threshold value of $\bar{q}_6$ used to discriminate between solid and liquid particles is obtained by plotting the distribution of $\bar{q}_6$ for molecules in bulk solid and bulk liquid environments, and finding the limiting value of $\bar{q}_6$ that leads to minimum mislabeling, as described in Ref. [69]. The threshold values obtained at each temperature are provided in Fig. 1.2. A sample configuration in which $\bar{q}_6$ was used to label the particles as solid or liquid is also shown in Fig. 1.2. Once that water molecules have been identified as solid or liquid, the largest cluster is searched using a cluster analysis algorithm, in which two water molecules are considered to be nearest neighbors if the distance between their oxygen atoms is smaller than 3.5 Å.

The outermost layer of oxygen atoms on this cluster corresponds to water-like molecules. To locate the liquid-vapor surface at a point (x, y) on the plane of the interface, $h_{wv}(x, y)$ we search for all liquid like atoms within a rectangular area of $3\sigma \times 3\sigma$, and define the surface height as the average value of the four outermost atoms. Having found the liquid-vapor surface at that point, we then locate the solid-like atoms within a rectangular unit-cell plane about (x, y). The four outermost solid-like atoms within that area determine the solid-liquid surface location, $h_{iw}(x, y)$. The choice of four atoms is dictated by the properties of the unit cell, which exhibits exactly four surface atoms in the low temperature structure.

A local liquid-layer thickness at point (x, y) can be calculated as

$$\delta h(x, y) = |h_{iw}(x, y) - h_{wv}(x, y)| \tag{1.2}$$

The average thickness is determined by averaging the local heights over a mesh with twice as many points as unit cells on the surface.

Further information about the structure of the ice-liquid and liquid-vapor interfaces can be obtained from the density profiles measured along the direction perpendicular to the interface (i.e. along z):

$$\rho_\alpha(z) = \frac{N_\alpha(z)}{L_x L_y \Delta z} \tag{1.3}$$

where α denotes either solid-like or liquid-like molecules, and $N_\alpha(z)$ is the number of molecules of that type in a slice of simulation box centered at z and of width Δz.

Besides analyzing the density profile as a function of the absolute z-coordinate measured with respect to a fixed reference system, we also evaluated the density profiles as a function of the local distance to either the ice-liquid or liquid-vapor surfaces:

$$z^*_{i,\alpha} = z_i - h_\alpha(x, y) \tag{1.4}$$

where $\alpha = iw, wv$ stands here for either ice-water or water-vapor surfaces. Note that adopting a local definition of the distance to the interface, the slice over which the number of water molecules

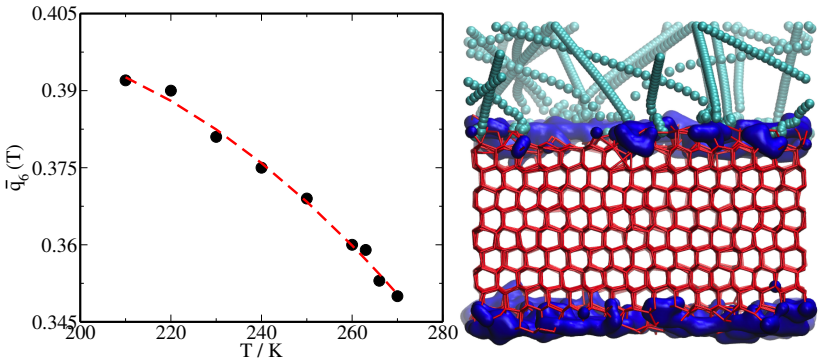

Figure 1.2. Left: Limiting values of $\bar{q}_6$ used to discriminate liquid from solid particles as a function of temperature. These values were obtained using the mislabeling criterium described by Espinosa *et al.* [69]. This limit values can be accurately fitted to a quadratic polynomial function: $\bar{q}_6(T) = 0.26266 + 0.0016474T - 4.8982 \cdot 10^{-6}T^2$. Right: Atomistic view of the ice-vapor interface at T=230 K and of the trajectory of 20 water molecules that are shot to the ice surface. Water molecules identified with $\bar{q}_6$ as solid are shown as red sticks, and liquid molecules as dark blue spheres. The trajectories followed by the molecules are depicted as cyan spheres.

is counted is no longer planar, as in the usual calculation of the density profile. This is illustrated for positions measured relative to the ice-water surface in Figure 1.3.

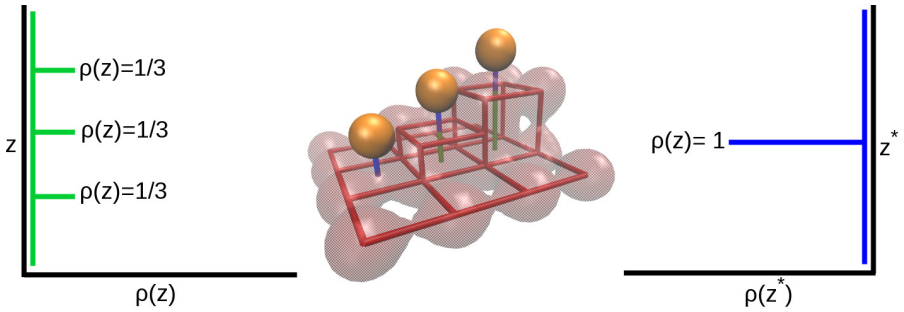

Figure 1.3. Schematic illustration of the difference in the density profiles as a function of absolute z coordinates (measured with respect to the simulation box reference frame) or as a function of the z^* coordinate measured with respect to the local height of the ice-liquid interface. Pink faded spheres represent solid molecules, and orange spheres liquid molecules. The red grid shows the local ice-liquid interface. The three orange molecules are assigned to three different bins when measured in absolute values of z (left scale), whereas to only one single bin when measured with respect to the local solid height (right scale).

The amount of nitrogen adsorbed on the ice surface at each thermodynamic state was quantified by measuring the surface excess or Gibbs adsorption:

$$\Gamma_{N_2} = (n_{N_2} - \rho_{N_2} V_{N_2})/A \tag{1.5}$$

where n_{N_2} is the total number of nitrogen molecules within the simulation box, ρ_{N2} is the bulk density of nitrogen, V_{N_2} the volume of the vapor phase, and A the area of the system in a plane parallel to the interface. Relative to the ice/vapor interface, the volume of the vapor phase is

determined for an equimolar dividing surface as $V_{N_2} = A(L_z - H)$, where H is the thickness of the ice slab, $H = N_w/(A\rho_{ice})$ and N_w is the total number of water molecules in the condensed phase. The change of the surface tension, γ, as a consequence of a change of the pressure induced by nitrogen is accounted for by the Gibbs equation:[70]

$$d\gamma = -\Gamma_{N_2} RT \frac{dp}{p} \tag{1.6}$$

where R is the gas constant, T is temperature and p is the partial pressure of nitrogen. At the low pressures considered in this study, the nitrogen surface excess increases linearly with pressure $\Gamma_{N_2} = ap$, and the slope a can be adjusted to the simulation data. Substitution of this expression into Eq. 1.7, yields:

$$\Delta\gamma = -\Gamma_{N_2} RT = -aRTp \tag{1.7}$$

Estimation of water attachment rates

Finally, we performed a last set of simulations aimed at measuring the attachment rate of water vapor to the ice surface. For this purpose, we performed the following experiment. A total of 400 water molecules were shot against 20 different thermal configurations of ice. Each water molecule shot was initially placed at a distance of 2 nm from the ice surface and assigned a velocity randomly chosen from the corresponding Boltzmann distribution, with the initial z component directed to the interface. The simulations were carried out in the microcanonical ensemble to avoid kinetic energy dissipation before and after the collision. We used a time step of 0.6 fs in these simulations to ensure energy conservation. Using the initial velocity we estimate the time required for the water molecule to reach the surface in a ballistic trajectory, and allow the simulation to proceed for twice as much time. At the end of the simulation we perform a cluster analysis over all molecules and determine whether the colliding molecule is attached to the condensed phase or not. From the ensemble of trajectories, we can estimate the attachment rate (α), which is defined as the ratio between the water molecules that are incorporated into the ice surface after the impact (N_{ads}) and the total number of water molecules that are shot against the ice surface (N_{total}): $\alpha = N_{ads}/N_{total}$. Notice that in this way we are measuring a direct attachment rate, not including the net rate due to evaporation events. These measurements were carried out at three different temperatures, $T =$ 230, 260 and 270 K and at two nitrogen partial pressures, namely, zero and a 1 bar.

Results

In this section we present results for the structure and attachment kinetics of ice in the presence of nitrogen. Our study covers a temperature range between 230 K to 270 K, which spans most of the relevant temperature of ice crystal growth in the atmosphere as described in the Nakaya diagram. For the pressure, we have chosen conditions pertaining to the International Standard Atmosphere at those temperatures (c.f. 1.1). This corresponds to pressures well above typical values in cirrus clouds, and therefore provide an upper limit for the influence of nitrogen on the ice surface. The detailed conditions studied in our simulations as well as the collected results may be found in Table 1.2.

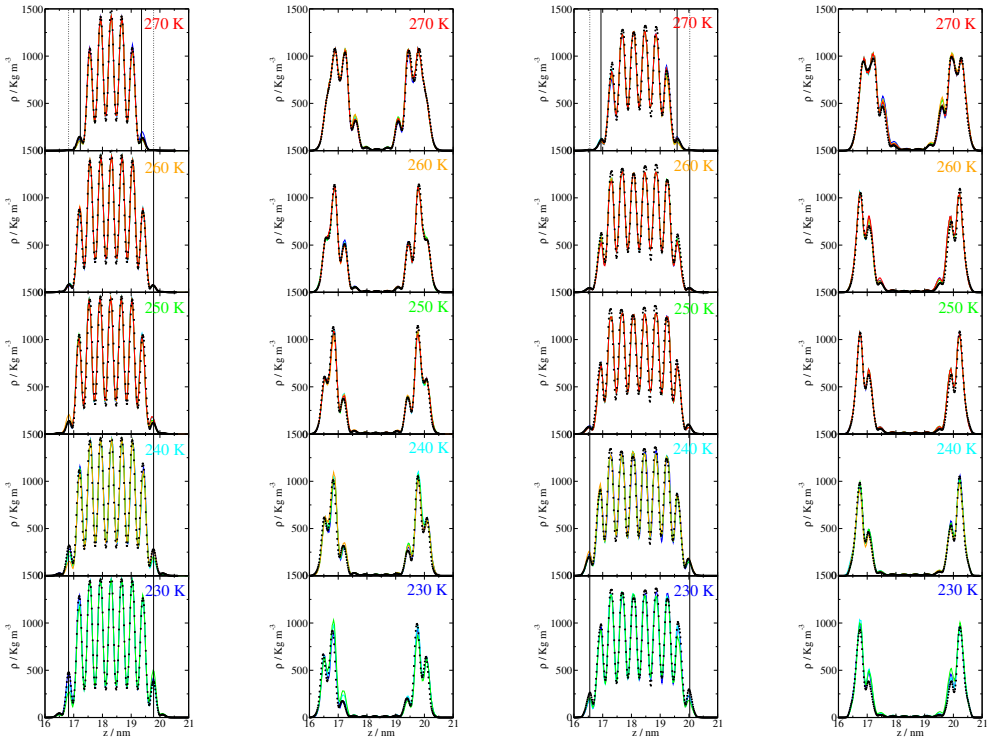

(a) Basal **(b)** Basal **(c)** pI **(d)** pI

Figure 1.4. Density profiles of water as a function of temperature and nitrogen pressure for basal (left) and primary prismatic (right) planes. Columns (a,c) correspond to density profiles of solid like molecules, while columns (b,d) correspond to density profiles of liquid like molecules. Black circles correspond to density profiles in pure water-vapor (zero nitrogen pressure), while colored lines stand for density profiles with cold to warm colors in order of increasing nitrogen pressure, with specific values of pressure as described in table 1.2. For the density profile of solid like molecules, the full vertical line indicates the outermost interfacial bilayer. Notice how the location of this bilayer moves one lattice spacing towards the bulk phase at T=270 K.

Structure of the pristine ice/vapor interface

A priori, the study of the ice/vapor interface is complicated by the presence of a thin layer of disordered ice, which grows as the temperature rises along the ice/vapor sublimation line.[55, 57] Depending on the community, this layer is known as a premelting film or quasi-liquid layer. Here we will stick to the standard terminology of wetting and adsorption physics, and denote the growing adsorbed layer as a premelting film.

Because of the complex structure of this interface, it is convenient to label surface molecules in terms of a suitable order parameter that can distinguish between water-like or disordered molecules and solid-like or ordered molecules.[68] This allows us to give a detailed account of the complex ice/vapor interface with reference to two simpler ice/water and water/vapor surfaces, and to plot separate solid-like and liquid-like density profiles of water molecules.[66, 67]

Figure 1.4 shows the density of solid-like and liquid-like molecules as a function of the perpendicular distance to the interface for both basal and pI facets in a temperature interval between

230 to 270 K. At low temperature (230 K), the solid-like density profile (1.4.a and 1.4.c) reveals an ordered crystalline solid with high density peaks that correspond to complete bilayers within the bulk of the crystal (five for the basal facet and six for the pI facet in our simulation setup). Each such bilayer contains the molecules of full stacked hexagonal rings of ordered ice.[21, 22, 23, 24, 57] As we move away from the bulk solid towards the vapor phase, we find a decay of the solid-like density profile. The interface consists of two partially formed bilayers of intermediate and small density. The outermost bilayer is indicated in the plot with a black vertical line.

As temperature increases towards the melting point, the height of the interfacial bilayers decreases smoothly up to 260 K. However, in the range between 260 K and 270 K, one full bulk like solid bilayer per interface melts into the premelting film. A similar bilayer melting has been observed previously for the TIP4P/ice model that is consistent with Sum Frequency Generation experiments, albeit at a somewhat lower temperature of about 250 K.[71, 57] The difference with previous simulations lies in the improved density representation, which reveals the bilayer melting process more clearly.

Interestingly, the structure of the solid like density profile at the interface remains qualitatively similar along the full temperature range studied, even after the first full bilayer melting (i.e., remains composed of two partial bilayers with intermediate and small densities). This process of melting can be observed also with the complementary density profiles of liquid-like molecules depicted in 1.4.b and 1.4.d. In the range between 230 K and 260 K the profiles reveal an adsorbed film of water molecules which is made from three partial bilayers for the basal face and only two partial bilayers for the pI plane. As temperature rises in this range, the density of the profile increases slightly, but in the range between 260 to 270 K, two of the partial bilayers attain bulk like densities, as found recently for the related TIP4P/2005 model.[66]

The density profiles shown here describe the laterally averaged structure of the ice/vapor interface. A hint on the surface structure in the direction parallel to the interface is given by the partially filled density peaks found in the outermost layer. Their location remains congruent with the lattice spacing, but the height is significantly smaller than that observed in bulk. However, a difference is observed between basal and pI planes. In the former, the small peak is separated from a neighboring peak by a region of depleted density. In the latter, on the contrary, the peak rather appears as a shoulder and hardly exhibits a density minimum separating it from the next peak. This suggests that the outermost region of the ice surface, at least for the basal plane, exhibits interrupted regions of fully formed layers, leading to a stepped surface.[67]

In a forthcoming section, we study the attachment coefficient of water molecules on the ice surface. These are calculated by shooting water molecules against the ice substrate. Here, we exploit this data in order to obtain a scattering profile of the substrate. Merely by calculating the probability $P(z^*)$ to observe an impinging water molecule at a distance z away from the average ice surface location, we find a revealing clue as to significant differences between basal and pI planes. Figure 1.5.a shows plots of $P(z^*)$ obtained from trajectories aimed at an ice substrate equilibrated under pure water vapor. The results show a region of slowly decaying probability at large z that corresponds to close to ballistic trajectories of the water molecules, and then exhibits a high probability region corresponding to the sticking of the water molecules onto the ice substrate. Interestingly, for the basal face we find at the lowest temperature T=230 K a bimodal distribution, indicating that the water vapor molecules shot against the substrate have a choice of two preferred locations. The distance between the two maxima is about 0.25 nm, which corresponds to the

distance between adjacent planes in an ice bilayer (or alternatively, the perpendicular distance between the oxygen molecules of the stacked hexagonal rings). This bimodal structure smoothes at the temperature T=260 K and then eventually disappears at T=270 K. For the pI plane, on the other hand, the distribution is unimodal for all temperatures studied, but clearly broadens as the temperature raises.

This results are clearly supportive of a stepped surface for the instantaneous configurations of basal facets, with stacks of half filled planes of half a bilayer and provide further evidence of the horizontally inhomogeneous distribution on the basal ice surface.[16, 18] The structure of the pI facet on the contrary, does not appear to have this form of surface disorder, and likely builds one full bilayer at a time.

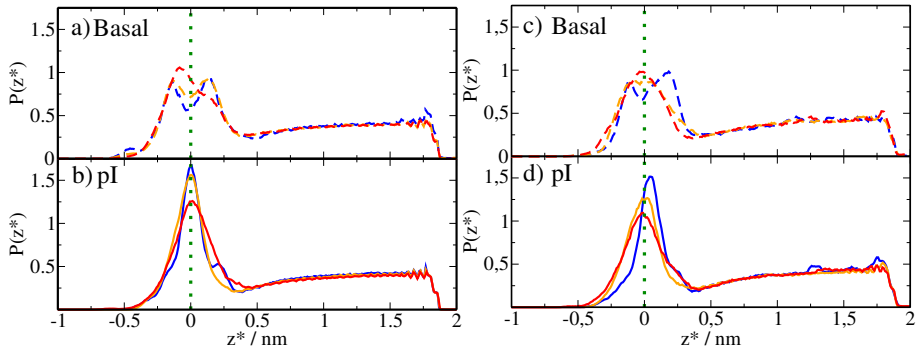

Figure 1.5. Probability $P(z^*)$ of finding impinging water molecules at a distance z for T=230 K (blue), 260 (orange) and 270 (red) at pressures of 0 bar (a,b) and 1 bar (c,d).

Structure of the adsorbed nitrogen layer

Having studied the structure of the pristine ice/vapor interface, we now consider the structure of the adsorbed nitrogen layer on the ice surface. Figure 1.6 shows the density profile of nitrogen molecules as a function of the perpendicular distance to the interface for both basal and pI planes. Results are given for temperature and nitrogen pressure made to match conditions of the International Standard Atmosphere for altitude in the range between 2500 and 9000 m, which correspond to temperatures in the range 230 to 270 K studied above (c.f table 1.1).

In all cases we find a plateau region of constant nitrogen density corresponding to the bulk gas phase, a small but significant adsorption layer at the interface, and a completely depleted central region corresponding to the highly nitrogen insoluble ice phase. Interestingly, the density profiles depicted here suggest a significant difference in the structure of adsorbed nitrogen at the basal and pI planes, with local densities that are roughly between twice (for the basal plane) and four times larger (for the pI plane) than the bulk vapor value. Also, the adsorption profile for the basal plane appears to be about twice as broad than the corresponding profile for the pI plane.

Unfortunately, this 'absolute' density profiles do not quite reveal the position of the adsorption peak relative to the complex ice/vapor interface. Particularly, it does not reveal whether the nitrogen is adsorbed on the premelting layer, or rather, is solubilized within. To study this issue further, we exploit the method of 'intrinsic' surfaces, which allows us to calculate local ice/film, $h_{iw}(\mathbf{x})$ and film/vapor, $h_{wv}(\mathbf{x})$ surfaces for instantaneous configurations during the simulation (c.f.

section 1.3.2). From knowledge of the instantaneous local surfaces, we calculate so called 'intrinsic' density profiles, which are given as (c.f. 1.3):[72, 73]

$$\rho_\alpha(z^*) = \langle \rho(z_i - h_\alpha(x, y)) \rangle \tag{1.8}$$

where α is the surface label corresponding to either wv or iw surfaces.

Figure 1.7 shows the intrinsic density profile of nitrogen molecules as measured relative to the solid/liquid surface. In all cases, for both the basal and pI planes, the nitrogen adsorption peak is located at positive values of z, and reveals essentially zero nitrogen density within the bulk solid phase. Furthermore, the relative position of the adsorption peak moves away from zero as the temperature is raised. This is indicative of the growing premelting layer, which likely carries the adsorbed nitrogen away from the solid phase.

We can check this by plotting the intrinsic density profile of nitrogen molecules measured relative to the water/vapor surface, as shown in Figure 1.7. We find again that the adsorption peak lies always at positive z, outside the premelting layer. The difference is that now its location with respect to the film/vapor surface does not change with temperature. This confirms that the adsorbed nitrogen sticks on the film/vapor surface, and is carried away from the bulk solid as the premelting film grows. Also notice that only occasionally do we find finite nitrogen densities at negative z, whence, only a small fraction of all adsorbed nitrogen is dissolved into the premelting layer. A finite but very small amount of nitrogen may be seen to penetrate the premelting film for the pI plane at the two highest temperatures, but is negligible in most other cases.

A striking feature of the intrinsic density profiles is that the adsorption peaks of both basal and pI planes are now very similar, exhibiting almost equal height and breadth. This means that at a given fixed point on either the water/vapor or ice/water surfaces, the nitrogen density profiles look just the same for both the basal and pI planes. The apparent differences in adsorption suggested by the absolute density profiles of Figure 1.6 is not really given by a distinct interaction of nitrogen with either plane, but rather, by a difference in the structure of the pristine crystal planes. The broader peak observed in the absolute density profiles for the basal plane is rather related to a surface structure with crystal steps and pockets, which can accommodate the nitrogen molecules at different absolute heights, as discussed previously.

Structural and thermodynamic implications of nitrogen adsorption

The study of nitrogen densities seems to indicate a rather passive role of the adsorbed nitrogen, which does hardly dissolve within the premelting film, but rather, remains adsorbed onto the disordered water layer. Furthermore, the surface enrichment is quite moderate, with a local density increase at the ice surface that is only a factor of two greater than the very small bulk gas density at atmospheric pressure.

To shed further light into this issue, we now look at the density of solid-like and liquid-like water molecules in the presence of nitrogen at different pressures (Figure 1.4). The results confirm that nitrogen gas does not result in any significant structural change of the ice/vapor interface. Indeed, neither the density of solid-like, nor the density of liquid-like water molecules seems to change with nitrogen pressure in any significant manner, for nitrogen pressures up to one bar. In fact, the density profiles corresponding to different nitrogen pressures can hardly be distinguished from the result of ice in pure water vapor.

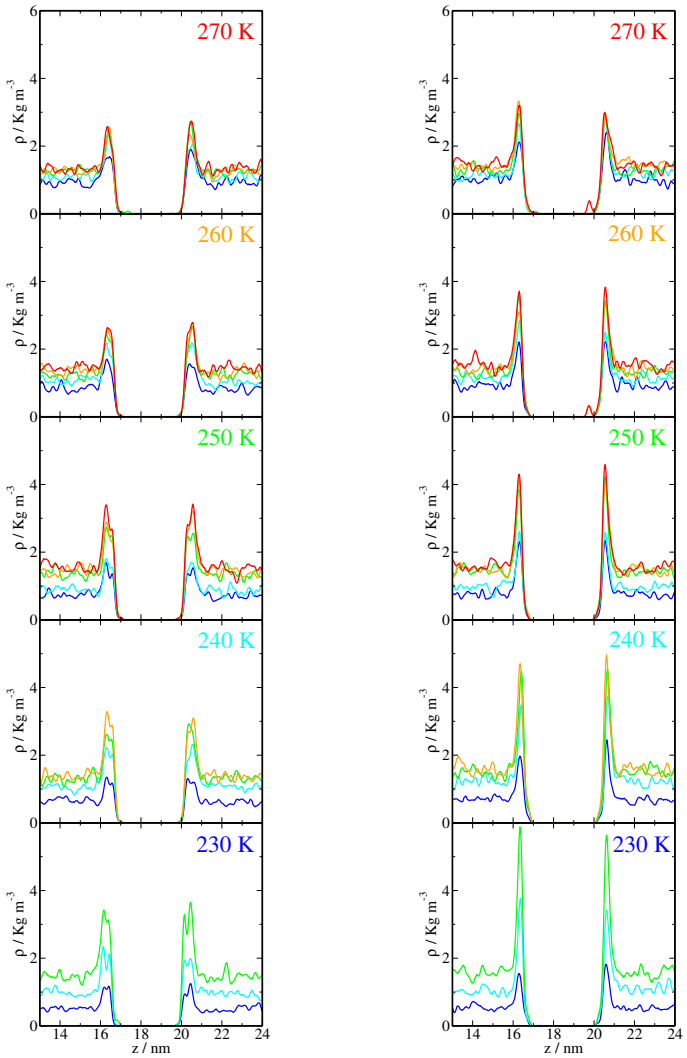

(a) Basal **(b)** pI

Figure 1.6. Density profiles of nitrogen as a function of perpendicular distance to the interface z. For each temperature, density profiles correspond to pressures as indicated in Table 1.2, with pressure increasing in the range from ca. 0.3 to ca. 1 bar from cold to warm colors.

Similarly, the plots of $P(z^*)$, obtained from the distribution of H_2O(g) colliding against the substrate, remain also very similar to those observed in the absence of nitrogen, as shown in Figure 1.5.b. In this case, the distributions do not appear to be identical, but we attribute the small differences mainly to the small amount of equilibrated ice configurations employed in this study, which was just 20, compared to the statistics gathered for the density profiles, which is taken over more than 400 configurations.

As a final illustration of the small role of nitrogen gas on the structure of the ice/vapor interface, we now concentrate on the influence of nitrogen gas on the thickness of the premelting layer, δh, calculated as described in section 1.3.2. Table 1.2 collects the results for all systems studied, while Figure 1.9 shows the premelting layer thickness as a function of nitrogen pressure for

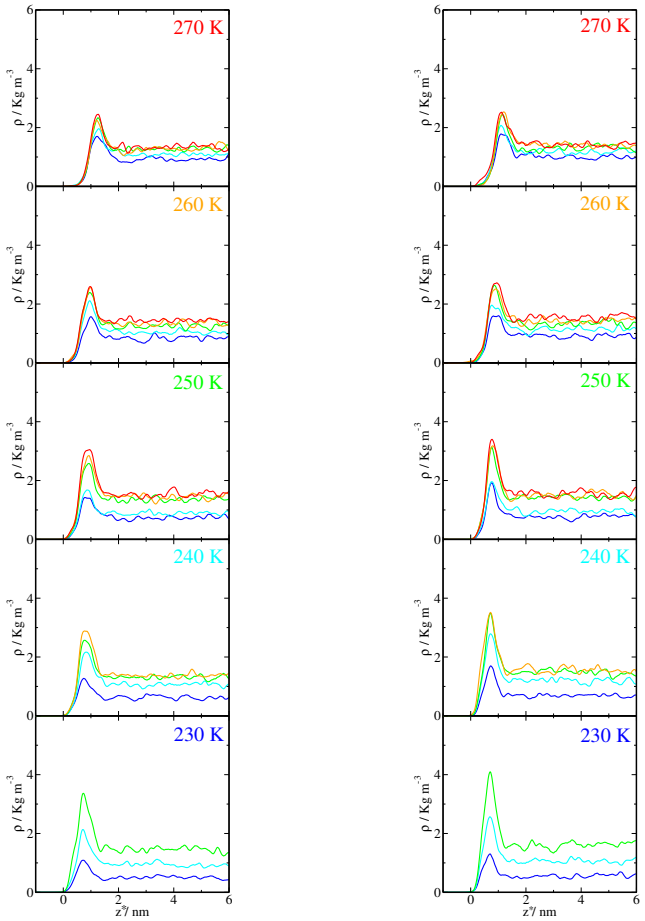

(a) Basal **(b)** pI

Figure 1.7. Density profiles of nitrogen as a function of perpendicular distance to the ice-liquid surface $z - h_{iw}(x, y)$. For each temperature, density profiles correspond to pressures as indicated in Table 1.2, with pressure increasing in the range from ca. 0.3 to ca. 1 bar from cold colors to warm colors.

a set of temperatures in the range between 230 K and 270 K. The results indicate that the premelting layer thickness does not show any significant change with nitrogen pressure, for pressures up to 1 bar, in all the temperature range studied, including the highest temperature of 270 K. Notice that this corresponds to about 2 K less than the melting point of the TIP4P/ice model used here. The results are consistent with recent experiments, which indicate that the premelting film in presence of nitrogen remains in the subnanometer range up to 1 K below melting (similar to results found in pure water vapor, c.f.[36]), but increases very much in the scale of tenths of Kelvin away from the triple point.[25] This seems reasonable, since at such small distances away from the triple point the premelting film could thicken considerably and incorporate nitrogen and other impurities by dissolution. These small perturbations slightly change the intermolecular forces between the film and ice, but very close to the triple point such small changes in the intensity of the intermolecular fores can can significantly shift the equilibrium thickness.[58]

As a summary, the structural analysis suggests that i) the ice/vapor surface essentially behaves as a high-energy inert substrate as regards nitrogen adsorption, with no significant disruption of

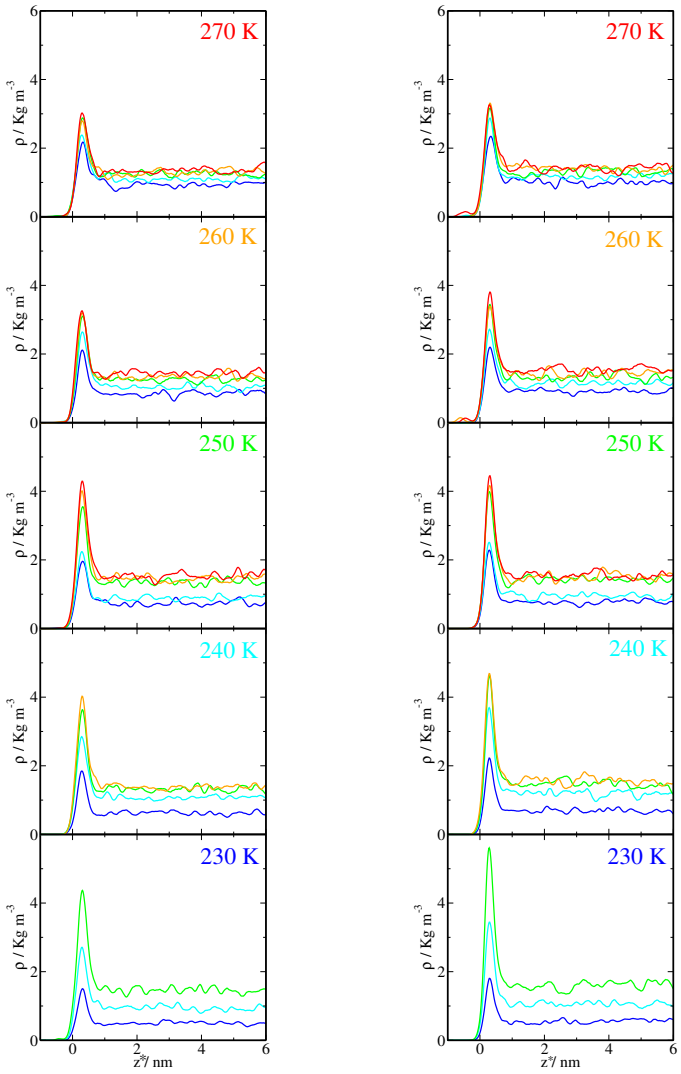

(a) Basal **(b)** pI

Figure 1.8. Density profiles of nitrogen as a function of perpendicular distance to the liquid-vapor surface $z - h_{wv}(x, y)$. For each temperature, density profiles correspond to pressures as indicated in Table 1.2, with pressure increasing in the range from ca. 0.3 to ca. 1 bar from cold colors to warm colors.

the pristine interface and ii) there does not appear to be any apparent difference between the adsorption of nitrogen on basal or pI planes, other than that related with the differences between pristine interfaces under pure water vapor.

In order to quantify these qualitative statements, we now consider the thermodynamic implications of nitrogen adsorption on the ice/vapor interface. Firstly, we calculate the surface adsorption of nitrogen, Γ_{N_2}, as given in terms of adsorbed molecules per unit surface (c.f.Eq. (1.5)).

Fig.1.10.a shows Γ_{N_2} as a function of nitrogen pressure for temperatures in the range 230 to 270 K, for both basal and pI planes. Results obtained in a range of conditions relevant for most practical atmospheric conditions yield adsorptions that are essentially linear in the pressure, and correspond to a simple Henry adsorption law of the form $\Gamma_{N_2} = ap$, wit a, the Henry adsorption

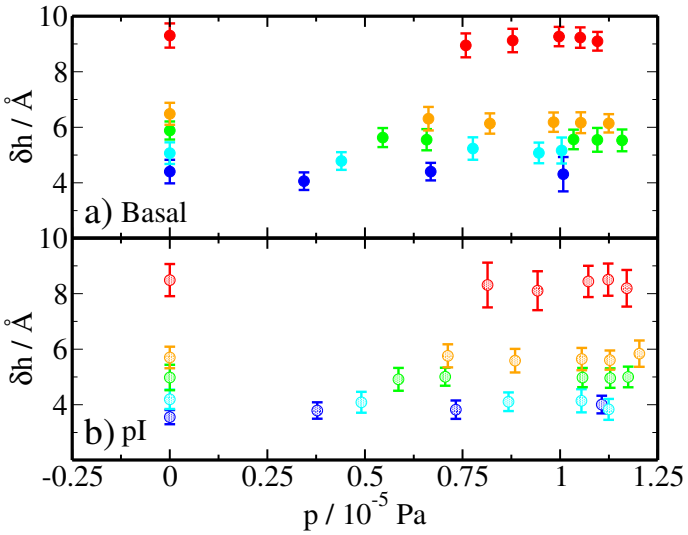

Figure 1.9. Premelting layer thickness, δh, for basal and primary prismatic planes as a function of nitrogen pressure for T=230 K (blue), 240 K (cyan), 250 K (green), 260 K (orange) and 270 K (red).

constant of nitrogen on ice. As regards the temperature dependence, the adsorption increases as temperature is decreased, as reflected by the slope of the adsorption isotherms. Overall, in all the regime of atmospheric conditions explored in this study, we find very small adsorption, and relatively small temperature and pressure dependences. Indeed, reported results for Γ_{N_2} hardly change by a factor of two from the highest to the lowest temperature, while the absolute values lie all in the order of 10^{-2} molecules per nanometer squared, whence, corresponding roughly to a surface concentration of one molecule per lateral area of 30×30 molecular diameters. This adsorption is however not small if we take into account the small solubility of nitrogen gas in water. Indeed, at the triple point the bulk solubility of nitrogen gas in water in terms of mole fractions is only $x_{N_2} \approx 2 \cdot 10^{-5}$.[74, 26] This can be compared with an effective solubility of nitrogen on the premelting film, which we can estimate as $\chi_{N_2} = \Gamma_{N_2} A / N_{H_2O}$, and provides $\chi_{N_2} = 1.133 \cdot 10^{-4}$ and $1.125 \cdot 10^{-4}$ for basal and pI facets. Whence, the premelting film is enriched in nitrogen by an order of magnitude, although, as observed earlier, the nitrogen does not actually dissolve within, but rather, remains adsorbed atop the water/vapor surface.

In order to understand the thermodynamic significance of these results, we now use the adsorption constants to quantify the change in the ice/vapor surface tension resulting from the nitrogen adsorption at the interface. This can be estimated readily from the adsorption isotherms and the Gibbs adsorption equation (c.f. Eq. (1.6)-Eq. (1.7)). The results are shown in Figure 1.10.c, and clearly reveal an extremely small surface activity of nitrogen gas. The change in the ice/vapor surface tension resulting from the nitrogen adsorption is of order -10^{-2}mN/m, which is to be compared with the estimated ice/vapor surface tension, on the order of 100 mN/m.[75, 76] Whence, nitrogen at conditions relevant to atmospheric sciences decreases the ice/vapor surface tension to a negligible extent. The results also reveal an extremely small surface anisotropy of the adsorption process, with only a slightly larger surface activity on the basal plane than on the pI plane.

To further characterize the energetics of nitrogen adsorption on the ice surface, we fit Γ_{N_2}

to the linear law, $\Gamma_{N_2} = ap$, and obtain adsorption constants from the the slope. These Henry's adsorption constants are expected to follow an Arrhenius behavior. This is tested and confirmed in Figure 1.10.c. From the slope of the Arrhenius plots, we find adsorption enthalpies of 7.4 and 6.5 kJ/mol for the basal and pI surfaces, respectively. On the other hand, experimental measurements of nitrogen adsorbed on ice from BET isotherms yield an excess enthalpy of adsorption of about 2.5 kJ/mol at 77 K,[27, 28, 29] as measured relative to nitrogen enthalpy of condensation at 77 K. From phase-change thermodynamic data for nitrogen, we thus find an experimental estimate of adsorption enthalpy of $\Delta H_{ads} = 5.6 + 2.5 = 8.1$ kJ/mol, which is in rather good agreement with the simulation results and far smaller than the the calculated binding energies of water adatoms on ice, wich range from 30 to 70 kJ/mol.[77]

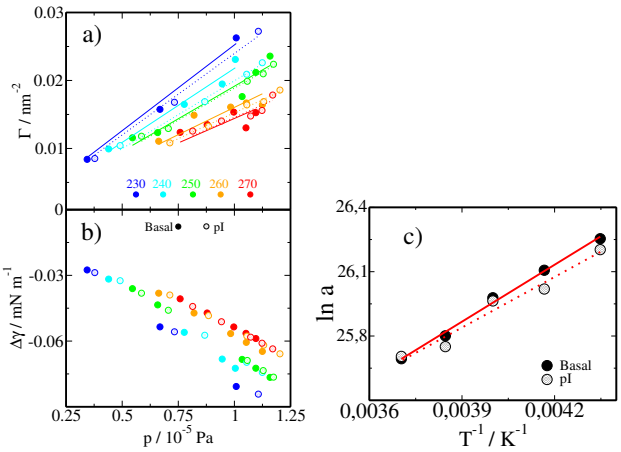

Figure 1.10. Energetics of nitrogen adsorption. (a) Adsorption isotherms as a function of pressure, Γ_{N_2}. (b) Change of the ice/vapor surface tension due to nitrogen adsorption, $\Delta\gamma$, as a function of pressure. (c) Arrhenius plots of Henry adsorption constants, a. Full symbols correspond to data for the basal plane, and empty symbols for the pI plane. Temperature color code as indicated in the legends on the plot.

Surface attachment kinetics

In the previous sections, we have undertaken a study of the structure and thermodynamics of the ice surface in presence of nitrogen. The results reveal an almost negligible surface activity of nitrogen, and only a very small surface anisotropy as regards nitrogen adsorption. Accordingly, the reported influence of nitrogen gas on crystal growth rates must be related to kinetic effects.

In standard applications, the crystal growth rates are reported in terms of the maximum flux of water vapor molecules impinging onto the ice surface, which, from elementary kinetic theory is given as:

$$J_{max} = \frac{1}{4}\langle v\rangle \rho_{H_2O} \tag{1.9}$$

where $\langle v\rangle$ is the thermal average speed of water molecules and ρ_{H_2O} is the water vapor density in the neighborhood of the surface.

In practice, the crystal growth rate depends on the flux of vapor towards the surface, but also on the sublimation rate. Accordingly, the overall growth rate can be expressed as:

$$R = \alpha J_{max} - J_{ev} \tag{1.10}$$

where α is the (microscopic) attachment coefficient, which dictates the probability that a waver molecule in a ballistic trajectory will stick to the ice surface, and J_{ev} is a net flux of sublimation. In view of the difficulties to measure α and J_{ev} separately, the crystal growth rate is usually given experimentally as:

$$R = \alpha_{\text{eff}} J_{max} \tag{1.11}$$

where α_{eff} is now the (macroscopic) accommodation coefficient. This lumps into one single empirical parameter all the complicated surface kinetics, including the adsorption probability of impinging water molecules, the thermal equilibration and surface diffusion into the premelting film, the accommodation of a water-like molecule into the crystal lattice, and the decrease of the crystal growth rate due to sublimation events.[78, 79, 17]

A great number of experiments aimed at calculating α_{eff} in atmospheric conditions have been performed, but unfortunately, results seem to depend considerably on experimental details and data analysis.[78, 80, 45, 81, 82] Most reported results vary between $\alpha_{exp} = 0.1$ to $\alpha_{exp} = 1$, but occasionally provide coefficients well smaller than 0.1, leaving a great room for improvement.[83]

One major source of discrepancy is related to the proper measurement of the net flux of impinging molecules. The reason is that this result is reliable only when the vapor density ρ_{H_2O} is that of water vapor molecules at a distance from the surface in the order of the mean free path. Because most experiments are performed at ambient pressure, and necessitate an inert carrier gas to ensure thermal equilibrium, the macroscopic flow of water vapor is not related to ballistic trajectories implied in Eq. (1.9), but rather, is a slow random walk process. When the rate of attachment of water molecules into the surface is of the order of the rate of diffusion or larger, the density becomes considerably depleted at the neighborhood of the ice surface, and the calculation of J_{max} is then a complicated diffusion limited process. Disentangling this diffusion process from the attachment kinetics on the ice surface has revealed to be rather complicated and ambiguous.

An attractive way to disentangle the impingement rate from gas phase collision events is to carry out explicit computer simulations. In our study, we place water molecules with center of mass and angular velocities selected from a thermal Boltzmann distribution at a distance 2 nm away from an equilibrated ice surface, and shoot the water molecule against the surface, as explained in section 1.3.3. Results for α collected over 400 trajectories and 20 different thermal ice configurations. are shown in Figure 1.11 at zero and one bar for three different temperatures. Detailed statistical information on the trajectories may be found in the supplementary material.

At zero nitrogen pressure, the trajectories sampled are essentially ballistic, because the vapor pressure is extremely small for the TIP4P/ice model (this limitation is shared by most point charge models) and the probability of collisions with evaporated water vapor molecules is negligible for such short trajectories. The results of Figure 1.11 show that this direct microscopic attachment coefficient is almost equal to unity for both the basal and pI surface planes. In fact, for the pI plane all impinging molecules were attached to the ice surface except one, at T=260 K. For the basal plane α is also very close to unity, but five and six water molecules were reflected back at temperatures of T=230 K and T=260 K, respectively. A look at the non-sticking trajectories shows

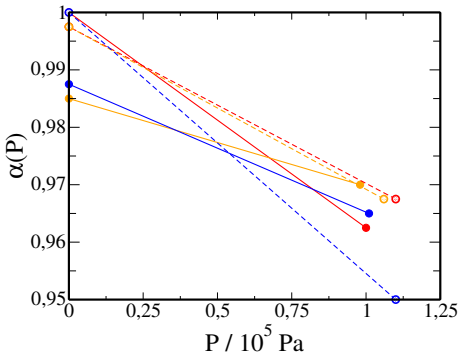

Figure 1.11. Attachment coefficients at three different temperatures measures as a function of nitrogen partial pressure for T=230 K (blue), 260 (orange) and 270 (red). Full symbols correspond to data for the basal plane, and empty symbols for the pI plane.

that in this cases the reflection occurs only for gracing trajectories with a small z-component of the velocity. The molecule then flies at a small distance from the surface and is eventually reflected back by electrostatic repulsion at a distance (rather than in a hard-sphere like collision between molecules at close contact).

At a pressure of one bar, we find that α remains still very close to unity, but has decreased nevertheless significantly from the values at zero pressure. Overall, about 12 to 16 trajectories out of 400 per batch were reflected and did not accommodate into the ice surface. The issue then is whether this decrease in the attachment coefficient is a result of unfavorable surface collisions induced by adsorbed nitrogen molecules, or rather, it is related to repulsive collisions with bulk nitrogen gas. In view of the small amount of unfavorable collisions, we merely performed a one-by-one inspection of the trajectories with visualization software and found that hardly all of the unfavorable trajectories were related to collisions with nitrogen molecules in the gas phase.

The results for attachment coefficients at zero pressure are in full agreement with previous trajectory studies from molecular simulation, which have consistently observed that the fate of vapor water molecules directed towards the ice surface is to stick onto the ice surface,[84, 79, 85] irrespective of the rate of impingement.[13, 14] Our study of trajectories in the presence of nitrogen gas seem to indicate that a similar fate awaits water molecules unless an unfavorable collision with free nitrogen gas molecules occurs. Our results thus clearly favor (microscopic) attachment coefficients of unity, with little evidence of a significant temperature dependence. This is also consistent with some recent experiments for water vapor collision rates on ice.[81]

Why is there then so much scatter in the literature? Clearly, one reason is the difficulty to disentangle pure surface processes from gas phase diffusion processes. However, another large source of discrepancy likely lies in the definition of the accommodation coefficient itself. Here, we have tried to make clear the distinction between the surface attachment kinetics, which refers to the probability of a colliding molecule to stick onto the ice surface (which we term here the attachment coefficient, α), from the effective accommodation coefficient, α_{eff} which accounts for the net balance between global condensation and evaporation kinetics as given in terms of the surface density. Further sources of confusion can arise if α_{eff} is measured in the diffusive regime with a flux J_{max} given in terms of the density at 'large' distances from the sample.[82] We believe the literature does not always clarify which is the actual coefficient that is measured, and this likely

is one reason for the great scatter of experimental results.[83]

Additional support for a (microscopic) attachment coefficient of unity is given by the study of water gas molecules impinging onto supercooled water. At least close to the triple point, where ice is expected to have a premelted liquid layer of nanometer size,[10, 66] the direct impingement of H_2O(g) onto liquid water should not differ significantly, while precisely at the triple point, the effective coefficient should likewise be exactly the same, since then ice and water must have the same evaporation rates. The advantage of experiments performed in water is that the water/vapor interface here is much simpler in structure, so that one does not have to account for the complicated premelting mediated crystal growth mechanisms (c.f., [78, 13, 86]), and only the evaporation flux and diffusion processes needs to be considered. Despite of this somewhat simpler situation, attachment coefficients on liquid water are also difficult to measure and experiments exhibit a large scatter. However, by studying the uptake of a flux of deuterated water it is possible to disentangle the attachment rates from the evaporative flux, and the results obtained this way do seem to support a value of $\alpha = 1$,[87] in agreement with other recent experiments and computer simulations for attachment dynamics on liquid water.[88, 89]

Conclusions

In this work we have carried out a detailed characterization of the ice surface in a controlled atmosphere of nitrogen gas. Results have been obtained at conditions found in the International Standard Atmosphere in a range of altitudes between 2750 to 9000 m. This covers the relevant temperature range between 270 to 230 K expected for ice crystal growth in the atmosphere, and a pressure range between 0.5 and 1 bar well in the upper limit of relevant pressure for cirrus cloud formation. Surprisingly, very little previous effort seems to have been devoted to elucidate the role of nitrogen gas on the properties of the ice surface and crystal growth rates at a microscopic level, despite efforts highlighting the lack of understanding on this issue.[1, 37]

From our study, we find i) the adsorbed amount of nitrogen gas on the ice surface is very small, corresponding to ca. one nitrogen molecule per 100 nm^2. ii) nitrogen adsorbs essentially onto the premelting layer of ice and does hardly dissolve within. iii) The structure of the pristine ice/vapor surface is mediated by a thin liquid film, and does not change in any significant manner by the presence of small amounts of adsorbed nitrogen. iv) The thickness of the premelting layer in the temperature range studied varies between 0.4 to 1 nm, and does not show any significant dependence on nitrogen pressure. v) The adsorption enthalpy of nitrogen on the ice/air interface is approximately 7 kJ/mol, much lower than is required for surface poisoning or step free energy changes to occur. vi) the variation of ice/air surface tension due to nitrogen is in the 10^{-2} mN/m range, and accounts for less than 0.05% of the full surface tension in pure water vapor. vii) Basal and pI surfaces of pristine ice exhibit significant differences. Particularly, the basal surface appears to show a disordered distribution of steps on the surface. However, nitrogen does not appear to shift this anisotropy in any significant manner. viii) Direct attachment rates of water molecules onto the ice surface are very close to unity, and do not seem to change significantly by the presence of small amounts of adsorbed nitrogen. In essence, at temperatures relevant to ice formation and nitrogen pressures well in the upper limit of interest, the ice/vapor interface appears as a high-energy inert substrate for adsorbed nitrogen gas.

In view of these observations, we conclude that nitrogen does not appear to have any significant role on the structural properties of the ice/air interface, and the direct surface attachment kinetics. On the other hand, the density of nitrogen gas at a pressure of 1 bar is sufficient to deflect a small percent of water molecules impinging from a small distance of two nanometers. This highlights the role of nitrogen gas in slowing down the flux of water vapor towards the crystal surface, and indicates that reported differences of crystal growth rate in a nitrogen atmosphere must be essentially related to diffusion limited processes.[32, 33, 34, 37]

Acknowledgment

We gratefully acknowledge funds from the Spanish Agencia Estatal de Investigación under Grant No. FIS2017-89361-C3-2-P.

	Basal					Prismatic I				
T	p	δh	Γ	K	$\Delta\gamma$	p	δh	Γ	a	$\Delta\gamma$
K	$10^{-5}Pa$	Å	nm^{-2}	$10^{-11}m/J$	mN/m	$10^{-5}Pa$	Å	nm^{-2}	$10^{-11}m/J$	mN/m
230	0.34	4.1	0.008	2.52	-0.03	0.37	3.8	0.008	2.39	-0.03
230	0.67	4.4	0.016	2.52	-0.05	0.72	3.8	0.017	2.39	-0.06
230	1.01	4.3	0.026	2.52	-0.08	1.10	4.0	0.027	2.39	-0.08
240	0.44	4.8	0.010	2.18	-0.03	0.49	4.1	0.010	2.00	-0.03
240	0.78	5.2	0.016	2.18	-0.06	0.87	4.1	0.017	2.00	-0.06
240	0.94	5.1	0.019	2.18	-0.07	1.05	4.1	0.021	2.00	-0.07
240	1.00	5.1	0.023	2.18	-0.07	1.12	3.9	0.023	2.00	-0.07
250	0.54	5.6	0.011	1.92	-0.04	0.56	4.9	0.012	1.89	-0.04
250	0.66	5.6	0.012	1.92	-0.04	0.71	5.0	0.013	1.89	-0.05
250	1.03	5.6	0.018	1.92	-0.07	1.05	5.0	0.020	1.89	-0.07
250	1.10	5.5	0.021	1.92	-0.07	1.13	5.0	0.021	1.89	-0.07
250	1.16	5.5	0.024	1.92	-0.08	1.17	5.0	0.022	1.89	-0.08
260	0.66	6.3	0.011	1.60	-0.04	0.71	5.8	0.011	1.52	-0.04
260	0.82	6.1	0.015	1.60	-0.05	0.88	5.6	0.013	1.52	-0.05
260	0.98	6.2	0.016	1.60	-0.06	1.06	5.6	0.016	1.52	-0.06
260	1.05	6.2	0.017	1.60	-0.06	1.13	5.6	0.017	1.52	-0.06
260	1.10	6.2	0.016	1.60	-0.06	1.20	5.8	0.018	1.52	-0.07
270	0.76	8.9	0.012	1.44	-0.04	0.81	8.3	0.012	1.45	-0.04
270	0.88	9.1	0.013	1.44	-0.05	0.94	8.1	0.014	1.45	-0.05
270	1.00	9.3	0.015	1.44	-0.05	1.07	8.4	0.015	1.45	-0.06
270	1.05	9.2	0.013	1.44	-0.06	1.12	8.5	0.016	1.45	-0.06
270	1.10	9.1	0.015	1.44	-0.06	1.17	8.2	0.018	1.45	-0.06

Table 1.2. Summary of systems studied and collected results for premelting thickness, δh, nitrogen adsorption, Γ, Henry adsorption constant, a and change in surface tension, $\Delta\gamma_{iv}$, as a function of temperature and pressure for basal (left) and primary prismatic (right) facets. The color code employed in the table labels defines the color code for the forthcoming figures.

ρ	T	P	ρ	T	P	ρ	T	P	ρ	T	P	ρ	T	P	ρ	T	P	ρ	T	P
	230	0.39		230	0.55		230	0.71		230	0.87		230	1.01		230	1.14		230	1.25
	235	0.40		235	0.55		235	0.70		235	0.88		235	0.99		235	1.17		235	1.35
	240	0.39		240	0.57		240	0.72		240	0.88		240	1.08		240	1.24		240	1.37
	245	0.42		245	0.59		245	0.74		245	0.91		245	1.08		245	1.25		245	1.42
0.56	250	0.42	0.79	250	0.58	1.03	250	0.75	1.26	250	0.94	1.50	250	1.11	1.73	250	1.29	1.96	250	1.42
	255	0.42		255	0.59		255	0.78		255	0.94		255	1.09		255	1.29		255	1.45
	260	0.43		260	0.60		260	0.80		260	0.95		260	1.16		260	1.34		260	1.48
	265	0.44		265	0.62		265	0.80		265	1.00		265	1.11		265	1.33		265	1.52
	270	0.46		270	0.64		270	0.82		270	1.02		270	1.19		270	1.39		270	1.55

Table 1.3. Equation of State for nitrogen. Pressure (P) is expressed in units of 10^5 Pa, temperature (T) in K and density (ρ) in kg m^{-3}.

T	$B_2(T)$
K	$10^3\ kg^{-1}m^3$
270	-3.2
265	-11.9
260	-5.9
255	-13.8
250	-4.5*
245	-3.4*
240	-4.7*
235	-13.0
230	-20.9

Table 1.4. Second virial coefficient B_2 as a function of temperature. * Three out layers were not included in the fit for $B_2(T)$.

Face	*T*	*Lx*	*Ly*	*Lz*	Number of N_2	$\rho^{bulk}_{N_2}$
	K	*nm*	*nm*	*nm*		kgm^{-3}
Basal	270	7.26698	6.29362	15.00000	0	0
				36.85765	46, 44, 42, 37, 32	0.95, 1.10, 1.24, 1.31, 1.37
	260	7.26350	6.29060	15.00000	0	0
				36.85765	49, 46, 43, 36, 29	0.86, 1.06, 1.27, 1.36, 1.46
	250	7.25949	6.28713	15.00000	0	0
				36.85765	53, 50, 47, 30, 25	0.74, 0.89, 1.40, 1.48, 1.56
	240	7.25609	6.28412	15.00000	0	0
				36.88880	48, 45, 37, 21	0.62, 1.09, 1.33, 1.41
	230	7.25229	6.28104	15.00000	0	0
				36.58888	50, 33, 17	0.50, 0.98 1.48
pI	270	7.26707	5.91452	15.00000	0	0
				36.85765	46, 44, 42, 37, 32	1.02, 1.18, 1.34, 1.40, 1.46
	260	7.26329	5.91143	15.00000	0	0
				36.85765	49, 46, 43, 36, 29	0.92, 1.15, 1.37, 1.46, 1.55
	250	7.25957	5.90841	15.00000	0	0
				36.85765	53, 50, 47, 30, 25	0.79, 0.95, 1.42, 1.52, 1.58
	240	7.25604	5.90554	15.00000	0	0
				35.58888	48, 45, 37, 21	0.69, 1.22, 1.48, 1.58
	230	7.25229	5.90249	15.00000	0	0
				35.85765	50, 33, 17	0.55, 1.07, 1.62

Table 1.5. Summary of thermodynamic conditions and system sizes for the simulations of the ice interface in presence of nitrogen.

Facet	T / K	N^{o}N$_2$	N^o not stuck water molecules	N^o deattach water molecules	α
Basal	270	42	14 (14*)	2	0.9650
Basal	270	0	0	0	1.0000
Basal	260	43	12 (9*)	2	0.9700
Basal	260	0	6	1	0.9850
Basal	230	50	14 (11*)	0	0.9650
Basal	230	0	5	0	0.9875
pI	270	42	13 (10*)	2	0.9675
pI	270	0	1	1	0.9975
pI	260	43	13 (11*)	2	0.9675
pI	260	0	1	0	0.9975
pI	230	50	20 (19*)	0	0.9500
pI	230	0	0	0	1.0000

Table 1.6. Summary of number of water molecules that have not stuck to the ice surface. * We have differentiated between water molecules that did not stick due to collision with nitrogen molecules. Accomodation rate for water can be calculated as the ratio between stuck molecules and total molecules thrown against the surface.

Bibliography

[1] T. Bartels-Rausch, "Ten things we need to know about ice and snow," *Nature*, vol. 494, pp. 27–29, 2013.

[2] D. G. Loyola, S. Gimeno García, R. Lutz, A. Argyrouli, F. Romahn, R. J. D. Spurr, M. Pedergnana, A. Doicu, V. Molina García, and O. Schüssler, "The operational cloud retrieval algorithms from tropomi on board sentinel-5 precursor," *Atmospheric Measurement Techniques*, vol. 11, no. 1, pp. 409–427, 2018.

[3] A. J. Baran, "From the single-scattering properties of ice crystals to climate prediction: A way forward," *Atmospheric Research*, vol. 112, pp. 45–69, 2012.

[4] S. G. Warren and R. E. Brandt, "Optical constants of ice from theultraviolet to the microwave: A revised compilation," *J. Geophys. Research*, vol. 113, p. D14220, 2008.

[5] E. Hesse, A. Macke, S. Havemann, A. Baran, Z. Ulanowski, and P. Kaye, "Modelling diffraction by facetted particles," *J. Quantitative Spectroscopy and Radiative Transfer*, vol. 113, no. 5, pp. 342 – 347, 2012.

[6] S. Neshyba, B. Lowen, M. Benning, A. Lawson, and P. M. Rowe, "Roughness metric of prismatic facets of ice," *J. Geophys. Res.: Atmos.*, vol. 118, pp. 3309–3318, 2013.

[7] J. Voigtländer, C. Chou, H. Bieligk, T. Claus, S. Hartmann, P. Herenz, D. N. G. Ritter, and F. S. Z. Ulanowski, "Surface roughness during depositional growth and sublimation of ice crystals," *Atmosph. Chem. Phys.*, vol. 18, pp. 13687–13702, 2018.

[8] E. Järvinen, O. Jourdan, D. Neubauer, B. Yao, C. Liu, M. O. Andreae, U. Lohmann, M. Wendisch, G. M. McFarquhar, T. Leisner, and M. Schnaiter, "Additional global climate cooling by clouds due to ice crystal complexity," *Atmosph. Chem. Phys.*, vol. 18, no. 21, pp. 15767–15781, 2018.

[9] J. P. D. Abbatt, "Interactions of atmospheric trace gases with ice surfaces: Adsorption and reaction," *Chemical Reviews*, vol. 103, no. 12, pp. 4783–4800, 2003. PMID: 14664633.

[10] M. M. Conde, C. Vega, and A. Patrykiejew, "The thickness of a liquid layer on the free surface of ice as obtained from computer simulation," *J. Chem. Phys.*, vol. 129, no. 1, p. 014702, 2008.

[11] A. J. Yang, M. Asta, and B. B. Laird, "Solid–liquid interfacial premelting," *Phys. Rev. Lett.*, vol. 110, p. 096102, 2013.

[12] D. T. Limmer and D. Chandler, "Premelting, fluctuations, and coarse-graining of water-ice interfaces," *J. Chem. Phys.*, vol. 141, p. 18C505, 2014.

[13] S. Neshyba, J. Adams, K. Reed, P. M. Rowe, and I. Gladich, "A quasi-liquid mediated continuum model of faceted ice dynamics," *J. Geophys. Res.: Atmos.*, vol. 121, no. 23, pp. 14,035–14,055, 2016.

[14] A. Hudait and V. Molinero, "What determines the ice polymorph in clouds?," *J. Am. Chem. Soc.*, vol. 138, no. 28, pp. 8958–8967, 2016. PMID: 27355985.

[15] T. Kling, F. Kling, and D. Donadio, "Structure and dynamics of the quasi-liquid layer at the surface of ice from molecular simulations," *The Journal of Physical Chemistry C*, vol. 122, no. 43, pp. 24780–24787, 2018.

[16] I. Pickering, M. Paleico, Y. A. P. Sirkin, D. A. Scherlis, and M. H. Factorovich, "Grand canonical investigation of the quasi liquid layer of ice: Is it liquid?," *J. Phys. Chem. B*, vol. 122, no. 18, pp. 4880–4890, 2018. PMID: 29660281.

[17] A. Mohandesi and P. G. Kusalik, "Probing ice growth from vapor phase: A molecular dynamics simulation approach," *J. Cryst. Growth*, vol. 483, pp. 156 – 163, 2018.

[18] Y. Qiu and V. Molinero, "Why is it so difficult to identify the onset of ice premelting?," *J. Phys. Chem. Lett.*, vol. 9, no. 17, pp. 5179–5182, 2018. PMID: 30149705.

[19] P. Sandler, J. o. Jung, M. M. Szczesniak, and V. Buch, "The complex of n2 with h2o, d2o, and hdo: A combined ab initio and diffusion monte carlo study," *J. Chem. Phys.*, vol. 101, no. 2, pp. 1378–1391, 1994.

[20] C. Girardet and C. Toubin, "Molecular atmospheric pollutant adsorption on ice: a theoretical survey," *Surf. Sci. Rep.*, vol. 44, no. 7, pp. 159 – 238, 2001.

[21] G. Sazaki, S. Zepeda, S. Nakatsubo, M. Yokomine, and Y. Furukawa, "Quasi-liquid layers on ice crystal surfaces are made up of two different phases," *Proc. Nat. Acad. Sci.*, vol. 109, no. 4, pp. 1052–1055, 2012.

[22] H. Asakawa, G. Sazaki, K. Nagashima, S. Nakatsubo, and Y. Furukawa, "Prism and other high-index faces of ice crystals exhibit two types of quasi-liquid layers," *Crystal Growth & Design*, vol. 15, no. 7, pp. 3339–3344, 2015.

[23] H. Asakawa, G. Sazaki, K. Nagashima, S. Nakatsubo, and Y. Furukawa, "Two types of quasi-liquid layers on ice crystals are formed kinetically," *Proc. Nat. Acad. Sci.*, vol. 113, no. 7, pp. 1749–1753, 2016.

[24] K.-i. Murata, H. Asakawa, K. Nagashima, Y. Furukawa, and G. Sazaki, "*In situ* thermodynamic origin of surface melting on ice crystals," *Proc. Nat. Acad. Sci.*, vol. 113, pp. E6741–E6748, 2016.

[25] T. Mitsui and K. Aoki, "Fluctuation spectroscopy of surface melting of ice with and without impurities," *Phys. Rev. E*, vol. 99, p. 010801, Jan 2019.

[26] R. Sander, "Compilation of henry's law constants (version 4.0) for water as solvent," *Atmosph. Chem. Phys.*, vol. 15, no. 8, pp. 4399–4981, 2015.

[27] A. W. Adams, L. M. Dormant, and M. Orem, "Physical adsorption of vapors on ice. i. nitrogen," *J. Colloid. Interface Sci.*, vol. 25, pp. 206–217, 1967.

[28] B. Schmitt, J. Ocampo, and J. Klinger, "Structure and evolution of different ice surfaces at low temperature adsorption studies," *J. Phys. Colloques*, vol. 48, pp. C1–519–C1–525, 1987.

[29] J. T. Hoff, D. Gregor, D. Mackay, F. Wania, and C. Q. Jia, "Measurement of the specific surface area of snow with the nitrogen adsorption technique," *Env. Sci. Tech.*, vol. 32, no. 1, pp. 58–62, 1998.

[30] L. Hanot and F. Dominé, "Evolution of the surface area of a snow layer," *Env. Sci. Tech.*, vol. 33, pp. 4250–4255, 1999.

[31] L. Legagneux, A. Cabanes, and F. Dominë, "Measurement of the specific surface area of 176 snow samples using methane adsorption at 77 k," *J. Geophys. Res.: Atmos.*, vol. 107, no. D17, pp. ACH 5–1–ACH 5–15, 2002.

[32] W. Beckmann, "Interface kinetics of the growth and evaporation of ice single crystals from the vapour phase: Iii. measurements under partial pressures of nitrogen," *J. Cryst. Growth*, vol. 58, no. 2, pp. 443 – 451, 1982.

[33] W. Beckmann, R. Lacmann, and A. Bierfreund, "Growth rates and habits of ice crystals grown from the vapor phase," *J. Phys. Chem.*, vol. 87, no. 21, pp. 4142–4146, 1983.

[34] T. Kuroda and T. Gonda, "Rate determining processes of growth of ice crystals from the vapour phase. part ii: Investigation of surface kinetic processes," *J. Met. Soc. Jap.*, vol. 62, pp. 563–572, 1984.

[35] M. Elbaum, S. G. Lipson, and J. G. Dash, "Optical study of surface melting on ice," *J. Cryst. Growth*, vol. 129, pp. 491–505, 1993.

[36] H. Bluhm, D. F. Ogletree, C. S. Fadley, Z. Hussain, and M. Salmeron, "The premelting of ice studied with photoelectron spectroscopy," *J. Phys.: Condens. Matter*, vol. 14, pp. L227–L233, 2002.

[37] K. G. Libbrecht, "Physical dynamics of ice crystal growth," *Annu.Rev.Mater.Res*, vol. 47, pp. 271–295, 2017.

[38] K. O. L. F. Jayaweera, "Calculations of ice crystal growth," *J. Atmos. Sci.*, vol. 28, pp. 728–736, 1971.

[39] T. Kuroda and T. Gonda, "Rate determining processes of growth of ice crystals from the vapour phase: Part i. theoretical considerations," *J. Met. Soc. Jap.*, vol. 62, pp. 552–561, 1984.

[40] T. Gonda and M. Kombayashi, "Growth of ice crystals in the atmospheres of helium-argon mixture," *J. Met. Soc. Jap.*, vol. 48, pp. 440–450, 1970.

[41] D. Lamb and W. D.Scott, "Linear growth rates of ice crystals grown from the vapor phase," *J. Cryst. Growth*, vol. 12, pp. 21–31, 1972.

[42] W. Beckmann and R. Lacmann, "Interface kinetics of the growth and evaporation of ice single crystals from the vapour phase: Ii. measurements in a pure water vapour environment," *J. Cryst. Growth*, vol. 58, no. 2, pp. 433–442, 1982.

[43] T. Gonda and T. Sei, "The growth mechanism of ice crystals grown in air at a low pressure and their habit change with temperature," *J. Phys. Colloques*, vol. 48, pp. C1–355–C1–359, 1987.

[44] T. Sei and T. Gonda, "The growth mechanism and habit change of ice crystals growing from the vapor phase," *J. Cryst. Growth*, vol. 94, pp. 697–707, 1989.

[45] K. G. Libbrecht and M. E. Rickerby, "Meassurements of surface attachment kinetics for faceted ice crystal growth," *J. Cryst. Growth*, vol. 377, pp. 1–8, 2013.

[46] N. Akutsu, Y. Akutsu, and T. Yamamoto, "Vicinal surface with langmuir adsorption: A decorated restricted solid-on-solid model," *Phys. Rev. B*, vol. 64, p. 085415, Aug 2001.

[47] A. P. V. den Heuvel and B. J. Mason, "Habit of ice crystals grown in hydrogen, carbon dioxide and air at reduced pressure," *Nature*, vol. 184, pp. 519–520, 1959.

[48] D. Lamb and P. V. Hobbs, "Growth rates and habits of ice crystals grown from the vapor phase," *J. Atmos. Sci.*, vol. 28, pp. 1506–1509, 1971.

[49] J. Hallett and B. J. Mason, "The influence of temperature and supersaturation on the habit of ice crystals grown from the vapour," *Proc. R. Soc. Lond. A*, vol. 247, pp. 440–453, 1958.

[50] T. Kobayashi, "On the variation of ice crystal habit with temperature," in *Physics of Snow and Ice: Proceedings* (H. Oura, ed.), Institute of Low Temperature Science, Hokkaido University, 1967, 1967.

[51] M. Elbaum, "Roughening transition observed on the prism facet of ice," *Phys. Rev. Lett.*, vol. 67, pp. 2982–2985, Nov 1991.

[52] M. Elbaum and M. Schick, "Application of the theory of dispersion forces to the surface melting of ice," *Phys. Rev. Lett.*, vol. 66, pp. 1713–1716, 1991.

[53] A. Lied, H. Dosch, and J. H. Bilgram, "Surface melting of ice I_h single crystals revealed by glancing angle x-ray scattering," *Phys. Rev. Lett.*, vol. 72, pp. 3554–3557, 1994.

[54] H. Dosch, A. Lied, and J. H. Bilgram, "Glancing angle x-ray scattering studies of the premelting of ice surfaces," *Surf. Sci.*, vol. 327, pp. 145–164, 1995.

[55] J. G. Dash, A. W. Rempel, and J. S. Wettlaufer, "The physics of premelted ice and its geophysical consequences," *Rev. Mod. Phys.*, vol. 78, pp. 695–741, 2006.

[56] Y. Li and G. A. Somorjai, "Surface premelting of ice," *J. Phys. Chem. C*, vol. 111, no. 27, pp. 9631–9637, 2007.

[57] A. Michaelides and B. Slater, "Melting the ice one layer at a time," *Proc. Nat. Acad. Sci.*, vol. 114, pp. 195–197, 2017.

[58] J. Wettlaufer, "Impurity effects in the premelting of ice," *Phys. Rev. Lett.*, vol. 82, pp. 2516–2519, Mar 1999.

[59] H. Berendsen, D. van der Spoel, and R. van Drunen, "Gromacs: A message passing parallel molecular dynamics implementation," *Comp. Phys. Comm.*, vol. 91, no. 1 - 3, pp. 43 – 56, 1995.

[60] B. Hess, C. Kutzner, D. van der Spoel, and E. Lindahl, "Gromacs 4: Algorithms for highly efficient, load-balanced, and scalable molecular simulation," *J. Chem. Theo. Comp.*, vol. 4, no. 3, pp. 435–447, 2008. PMID: 26620784.

[61] J. L. F. Abascal, E. Sanz, R. G. Fernandez, and C. Vega, "A potential model for the study of ices and amorphous water: Tip4p/ice," *J. Chem. Phys.*, vol. 122, p. 234511, 2005.

[62] J. J. Potoff and J. I. Siepmann, "Vapor-liquid equilibria of mixtures containing alkanes, carbon dioxide, and nitrogen," *AIChE Journal*, vol. 47, no. 7, pp. 1676–1682, 2001.

[63] G. Bussi, D. Donadio, and M. Parrinello, "Canonical sampling through velocity rescaling," *J. Chem. Phys.*, vol. 126, no. 1, p. 014101, 2007.

[64] M. Allen and D. Tildesley, *Computer Simulation of Liquids*. Oxford: Clarendon Press, 1987.

[65] R. Estrada-Torres, G. A. Iglesias-Silva, M. Ramos-Estrada, and K. R. Hall, "Boyle temperatures for pure substances," *Fluid Phase Equilibria*, vol. 258, no. 2, pp. 148 – 154, 2007.

[66] J. Benet, P. Llombart, E. Sanz, and L. G. MacDowell, "Premelting-induced smoothening of the ice-vapor interface," *Phys. Rev. Lett.*, vol. 117, p. 096101, Aug 2016.

[67] J. Benet, P. Llombart, E. Sanz, and L. G. MacDowell, "Structre and fluctuations of the premelted liquid film of ice at the triple point," *Mol. Phys.*, pp. 1–19, 2019.

[68] W. Lechner and C. Dellago, "Accurate determination of crystal structures based on averaged local bond order parameters," *J. Chem. Phys.*, vol. 129, no. 11, p. 114707, 2008.

[69] J. R. Espinosa, C. Vega, and E. Sanz, "Ice-water interfacial free energy for the tip4p, tip4p/2005, tip4p/ice, and mw models as obtained from the mold integration technique," *J. Phys. Chem. C*, vol. 120, no. 15, pp. 8068–8075, 2016.

[70] J. Rowlinson and B. Widom, *Molecular Theory of Capillarity*. Oxford: Clarendon, 1982.

[71] M. A. Sánchez, T. Kling, T. Ishiyama, M.-J. van Zadel, P. J. Bisson, M. Mezger, M. N. Jochum, J. D. Cyran, W. J. Smit, H. J. Bakker, M. J. Shultz, A. Morita, D. Donadio, Y. Nagata, M. Bonn, and E. H. G. Backus, "Experimental and theoretical evidence for bilayer-by-bilayer surface melting of crystalline ice," *Proc. Nat. Acad. Sci.*, vol. 114, no. 2, pp. 227–232, 2017.

[72] M. Jorge, P. Jedlovszky, and M. N. D. S. Cordeiro, "A critical assessment of methods for the intrinsic analysis of liquid interfaces. 1. surface site distributions," *J. Phys. Chem. C*, vol. 114, no. 25, pp. 11169–11179, 2010.

[73] M. Sega, B. Fabian, and P. Jedlovszky, "Layer-by-layer and intrinsic analysis of molecular and thermodynamic properties across soft interfaces," *J. Chem. Phys.*, vol. 143, no. 11, p. 114709, 2015.

[74] R. Battino, T. R. Rettich, and T. Tominaga, "The solubility of nitrogen and air in liquids," *J. Phys. Chem. Ref. Data*, vol. 13, no. 2, pp. 563–600, 1984.

[75] N. H. Fletcher, *The Chemical Physics of Ice*. Cambridge University Press, 1970. Cambridge Books Online.

[76] H. R. Pruppacher and J. D. Klett, *Microphysics of Clouds and Precipitation*. Heidelberg: Springer, 2010.

[77] M. Watkins, D. Pand, E. G. Wang, A. Michaelides, J. VandeVondele, and B. Slater, "Large variation of vacancy formation energies in the surface of crystalline ice," *Nature Materials*, vol. 10, pp. 794–798, 2011.

[78] D. R. Haynes, N. J. Tro, and S. M. George, "Condensation and evaporation of water on ice surfaces," *J. Phys. Chem.*, vol. 96, no. 21, pp. 8502–8509, 1992.

[79] S. Neshyba, E. Nugent, M. Roeselova, and P. Jungwirth, "Molecular dynamics study of ice-vapor interactions via the quasi-liquid layer," *J. Phys. Chem. C*, vol. 113, no. 11, pp. 4597–4604, 2009.

[80] C. Delval and M. J. Rossi, "The kinetics of condensation and evaporation of h2o from pure ice in the range 173-223 k: a quartz crystal microbalance study," *Phys. Chem. Chem. Phys*, vol. 6, pp. 4665–4676, 2004.

[81] J. Skrotzki, P. Connolly, M. Schnaiter, H. Saathoff, O. Möhler, R. Wagner, M. Niemand, V. Ebert, and T. Leisner, "The accommodation coefficient of water molecules on ice-cirrus cloud studies at the aida simulation chamber," *Atmosph. Chem. Phys.*, vol. 13, no. 8, pp. 4451–4466, 2013.

[82] X. Kong, P. Papagiannakopoulos, E. S. Thomson, N. Markovič, and J. B. C. Pettersson, "Water accommodation and desorption kinetics on ice," *J. Phys. Chem. A*, vol. 118, no. 22, pp. 3973–3979, 2014. PMID: 24814567.

[83] IUPAC, "Task group on atmospheric chemical kinetic dataevaluation, http://iupac.pole-ether.fr," tech. rep., IUPAC, 2009.

[84] E. R. Batista, P. Ayotte, A. Bilić, B. D. Kay, and H. Jónsson, "What determines the sticking probability of water molecules on ice?," *Phys. Rev. Lett.*, vol. 95, p. 223201, Nov 2005.

[85] W. Pfalzgraff, S. Neshyba, and M. Roeselova, "Comparative molecular dynamics study of vapor-exposed basal, prismatic, and pyramidal surfaces of ice," *J. Phys. Chem. A*, vol. 115, no. 23, pp. 6184–6193, 2011.

[86] K.-i. Murata, K. Nagashima, and G. Sazaki, "How do ice crystals grow inside quasiliquid layers?," *Phys. Rev. Lett.*, vol. 122, p. 026102, Jan 2019.

[87] Y. Q. Li, P. Davidovits, C. E. Kolb, and D. R. Worsnop, "Mass and thermal accommodation coefficients of h2o(g) on liquid water as a function of temperature," *J. Phys. Chem. A*, vol. 105, no. 47, pp. 10627–10634, 2001.

[88] P. Davidovits, D. R. Worsnop, J. T. Jayne, C. E. Kolb, P. Winkler, A. Vrtala, P. E. Wagner, M. Kulmala, K. E. J. Lehtinen, T. Vesala, and M. Mozurkewich, "Mass accommodation coefficient of water vapor on liquid water," *Geo. Phys. Res. Lett.*, vol. 31, no. 22, 2004.

[89] A. Morita, M. Sugiyama, H. Kameda, S. Koda, and D. R. Hanson, "Mass accommodation coefficient of water: Molecular dynamics simulation and revised analysis of droplet train/flow reactor experiment," *J. Phys. Chem. B*, vol. 108, no. 26, pp. 9111–9120, 2004.

Chapter 2

Premelting induced smoothening of the ice/vapor interface

Jorge Benet[1], *Pablo Llombart*[1], *Eduardo Sanz*[1] *and Luis G. MacDowell*[1]

(1) Departamento de Química Física, Facultad de Ciencias Químicas, Universidad Complutense de Madrid, 28040 Madrid, Spain

Physical Review Letters, ***117***, *096101 (2016)*

Abstract

We perform computer simulations of the quasi-liquid layer of ice formed at the ice/vapor interface close to the ice Ih/liquid/vapor triple point of water. Our study shows that the two distinct surfaces bounding the film behave at small wave-lengths as atomically rough and independent ice/water and water/vapor interfaces. For long wave-lengths, however, the two surfaces couple, large scale parallel fluctuations are inhibited and the ice/vapor interface becomes smooth. Our results could help explaining the complex morphology of ice crystallites.

Nakaya summarized his research on snow flakes in a famous Haiku: "they are letters sent to us from the sky" [1]. Indeed, the habit of ice crystals grown from bulk vapor change from plates, to columns, to plates and yet back to columns as temperature is cooled down below the triple point, with the well known dendritic patterns appearing at sufficiently high super-saturations.[2] Accordingly, the final growth form of a tiny ice crystal conveys detailed information on the atmosphere where it grew.[3]

At a macroscopic level, it is well known that changes in ice crystal habits result from a crossover in the growth rates of the basal and prismatic faces, but exactly what structural transformations occur on the surface to drive this crossover is far from being understood.[4, 1, 2, 5] Kuroda and Lacmann explained the crossover in crystal growth rates as a result of the formation of a thin *quasi-liquid* layer on the ice surface which could set up at different temperatures depending on the crystal facet.[6]

The hypothesis that ice could exhibit a quasi-liquid layer dates back to Faraday, and the formation of such layer on solid surfaces is now well characterized theoretically as a premelting surface phase transition.[7] Experimentally, the advent of modern optical and surface scattering techniques has allowed to gather ample evidence as regards the existence of a premelting liquid film on the surface of ice.[8, 9, 10, 11, 12, 13, 14] Unfortunately, the relatively high vapor pressure of ice makes it very difficult to achieve sizable equilibrium crystals,[2] while the presence of impurities has a very large impact on surface structure.[15, 12] Accordingly, many other relevant properties, such as the premelting temperature, the thickness of the quasi-liquid layer or the presence of surface melting remain a matter of debate.[8]

One particularly important structural property with large impact on crystal growth rates is the surface roughness.[16, 17, 6] Contrary to smooth or singular facets, which have a limited number of defects and serve as basis for most crystal growth models, rough surfaces present diverging height fluctuations which do not differ macroscopically to those found in a fluid interface. As a result, rough crystal planes with correlation lengths that are larger than the crystallite disappear and become round.[18, 19, 20] More importantly, as far as crystal habits and growth forms are concerned, the roughening of a surface has dramatic consequences on the dynamics, as it signals a crossover from a two dimension nucleated growth, to a faster Knudsen mechanism that is linear in the saturation.[17, 6] Unfortunately, this phenomenology has been established only for rather simple interfaces,[17] and the role of a premelting film in the surface roughness is largely unknown.

Here we perform computer simulations of a premelting layer on the primary prismatic facet of the ice/vapor interface. Our study reveals that the structure and fluctuations of the surfaces bounding the quasi-liquid layer at small length-scales are very much like those of atomically rough and independent ice/water and water/vapor interfaces. However, the finite equilibrium thickness of the premelting layer below the triple point drives the long-wavelength structure of the interface from rough to smooth. Our results clarify why the facets of ice crystals remain recognizable up to the triple point, and suggest the formation of a premelting layer could slow down growth kinetics, as required to explain ice crystal growth habits in the atmosphere.[6]

Our study is performed with the TIP4P/2005 model of water, [21] which has been shown to reproduce with remarkable accuracy a large number of bulk and surface properties of (liquid) water and ice.[22] A slab of equilibrated bulk ice with several thousand molecules is placed in contact with vacuum inside a large ortorhombic simulation box, such that an interface of surface area $A = L_x L_y$ is exposed parallel to the xy plane. Surfaces thus prepared exhibit a very large heterogeneity of vacancy energies, with a strong dependence on the proton ordering arrangements.[23] For this reason we prepare our initial samples using a special purpose Monte Carlo algorithm that suitably samples the hydrogen bond network.[24, 25, 26] Averages are then collected using Molecular Dynamics with the Gromacs package for about half a

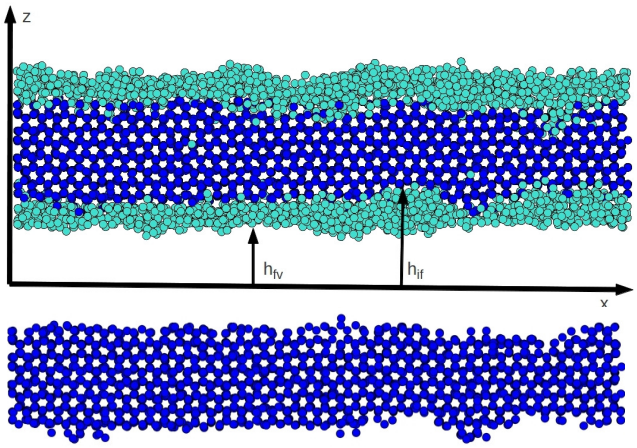

Figure 2.1. Snapshot of the ice/vapor interface during the course of our simulations. Top: A quasi-liquid layer of disordered molecules is clearly seen on top of bulk ice. The order parameter allows us to distinguish between an ice/film and a film/vapor surface. Bottom: Same figure with liquid-like atoms removed.

microsecond,[27, 28, 29, 30, 31, 32, 33, 34, 35] well above the expected relaxation time for the ice/water interface.[36] Performing the simulations along the sublimation line at a temperature $\Delta T = T - T_t$ just 2 K below the triple point temperature, T_t,[37] the first few ice layers melt and form a premelting quasi-liquid layer (Fig.2.1), as noticed earlier.[38, 39, 40, 41] The nature and size of this layer may be quantified using the $\bar{q}_6$ order parameter,[42] which has been optimized to discriminate ice like and water like molecules from a study of molecular correlations up to second nearest neighbors.[43] To get rid of vapor molecules, we identify the premelting layer as the largest cluster of water molecules, and find an average thickness of $\ell = 0.9$ nm, in reasonable agreement with experimental observations,[12, 14] and recent simulations.[38, 39, 40] Here, we attempt to characterize the quasi-liquid film in terms of two fluctuating ice/film (if), and film/vapor (fv) surfaces, which we locate by locally averaging the heights of the outermost solid and liquid molecules of the layer, respectively (Fig.2.1). Comparing our results for the ice/vapor interface with our previous study of the ice/water interface will prove insightful.[44] Since we aim at studying large wavelength fluctuations, we prepare the exposed faces with an elongated geometry, with box side $L_x \gg L_y$. This allows us to identify ice/film, $h_{if}(x)$ and film/vapor $h_{fv}(x)$ surface profiles along the largest axis, x. These film profiles are then Fourier transformed to yield the spectrum of surface fluctuations.[27]

For the purpose of studying the fluctuations of the quasi-liquid layer, it is convenient to define the quantity $\Gamma_{\alpha\beta}(q_x)$, in terms of the thermal averages of Fourier amplitudes $h_{\alpha\beta}$, as:

$$\Gamma_{\alpha\beta}(q_x) = \frac{k_B T}{A \left\langle h_{\alpha\beta}(q_x) h^*_{\alpha\beta}(q_x) \right\rangle q_x^2} \tag{2.1}$$

where k_B is Boltzmann's constant, $q_x = 2\pi n / L_x$, and n is a positive integer. According to Capillary Wave Theory,[45] for a rough interface between bulk phases α and β, the function $\Gamma_{\alpha\beta}(q_x)$ may be identified with a wave-vector dependent stiffness, $\tilde{\gamma}_{\alpha\beta}(q_x)$ whose $q_x \to 0$ limit is the macroscopic stiffness of the interface,[46, 47, 48] corresponding exactly to the surface tension for fluid/fluid interfaces.[49, 50] In the forthcoming exposition we concentrate on the primary prismatic plane (pI) at $\Delta T = -2$ K and study the fluctuations propagated along the basal [Basal] and secondary prismatic [pII] directions.

The results, $\Gamma_{if}(q_x)$ and $\Gamma_{fv}(q_x)$ obtained for the ice/film and film/vapor surface fluctuations of the premelting layer on the primary prismatic plane, either along [Basal] or [pII] orientations agree very nicely

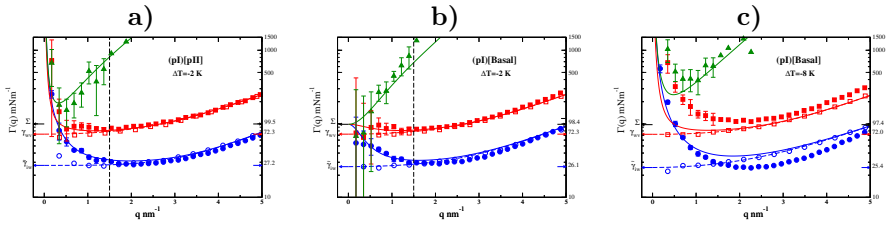

Figure 2.2. Fluctuations of the premelting film on the primary prismatic plane. The plot displays effective wave-vector dependent stiffness, $\Gamma(q_x)$ in log scale for (pI)[pII] at $\Delta T = -2$ K (**a**); and (pI)[Basal] at $\Delta T = -2$ K (**b**) and $\Delta T = -8$ K (**c**). Results for the the quasi-liquid layer are shown with filled symbols, with $\Gamma_{if}(q_x)$ for the ice/film (blue circles) and $\Gamma_{fv}(q_x)$ for the film/vapor surfaces (red squares). The open symbols are results for the ice/water (blue circles) and water/vapor (red squares) interfaces, which are fitted to $\Gamma(q_x) = \gamma + \kappa q_x^2 + \epsilon q_x^4$ (dashed lines) for the purpose of extrapolation (c.f. Ref.[44] and [27]). The colored arrows indicate extrapolation to $q_x = 0$, which provides the ice/water stiffness $\tilde{\gamma}_{iw}$ and the water/vapor surface tension, γ_{wv}, respectively. The black arrow points to $\Sigma = \tilde{\gamma}_{iw} + \gamma_{wv}$, where the effective stiffness of the quasi-liquid film would converge were the interface rough. The dashed vertical line indicates approximately the regime of q_x where the quasi-liquid surfaces cease to behave independently. The green triangles indicate results for the coupled fluctuations of the ice/film and film/vapor surfaces, $\Gamma_{iffv}(q_x)$. Full lines are results from a fit to the model of Eq. (3.2).

with those obtained for the corresponding ice/water, $\Gamma_{\rm iw}(q_x)$, and water/vapor, $\Gamma_{\rm wv}(q_x)$, interfaces down to q_x^* 1.5 nm^{-1} (Fig.2.2.a-b). This implies that for a quasi-liquid layer hardly one nanometer thick, the ice/film and film/vapor surfaces at this length-scales fluctuate independently, with fluctuations that can hardly be distinguished from those found at the rough interfaces of bulk water. Interestingly, at $q_x \approx q_x^*$, $\Gamma_{\rm iw}(q_x)$ and $\Gamma_{\rm wv}(q_x)$ are already close to their $q_x \to 0$ limit, and are therefore close to the corresponding macroscopic stiffness coefficients.

The striking resemblance between the surface fluctuations of the quasi-liquid layer and bulk water for $q_x > q_x^*$ can be understood in terms of the density profiles shown in Fig.2.3 for the primary prismatic plane (with similar results found for the basal and secondary prismatic planes, c.f. Ref.[27]). Indeed, the density profile of solid-like molecules from the ice/vapor interface (full-red) almost matches that observed at the ice/water interface (dashed-indigo). Similarly, the profile of liquid-like molecules of the quasi-liquid layer at the ice/vapor interface (full-blue) is very similar to that at the ice/water interface (dashed-green) until the very end of the premelting film, where it obviously drops to the values expected for the bulk vapor density.

Below q_x^*, the fluctuating surfaces start noticing the finite thickness of the quasi-liquid layer, as implied by the departure of $\Gamma_{if}(q_x)$ and $\Gamma_{fv}(q_x)$ from the ice/water and water/vapor behavior. For the fluctuations in the (pI)[pII] direction, a sharp rise of $\Gamma(q_x)$ for both the ice/film and film/vapor surfaces suggest a divergence as $q_x \to 0$, and indicate the onset of a completely different regime, with finite correlations at infinite wavelengths and an effective infinite stiffness coefficient (Fig.2.2.a). For the fluctuations in the (pI)[Basal] direction, on the contrary, $\Gamma(q_x)$ rises above the values expected for the ice/water and water/vapor interfaces, but seems to attain a finite asymptotic limit for $q_x \to 0$ (Fig.2.2.b). These conflicting results for the (pI) interface at $\Delta T = -2$ K indicate the proximity of a *roughening transition*, where the interface depins from the underlying bulk solid. Roughening is a Kosterlitz-Thoules transition of infinite order.[20] Not unexpectedly, the error bars observed for $\Gamma(q_x)$ are extremely large, and sub-averages may be collected which appear consistent with either a rough or a smooth interface. By simulating the same interfaces just 6 K below, we find that $\Gamma(q_x)$ also becomes divergent for the (pI)[Basal] direction, confirm-

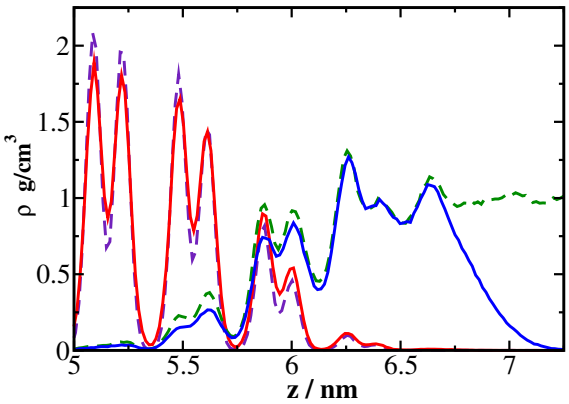

Figure 2.3. Structure of the ice/vapor (full lines) and ice/liquid (dashed lines) interfaces of the primary prismatic plane along the perpendicular direction. The density of solid-like molecules is shown in full-red for the solid/vapor interface and in dashed-indigo for the solid/liquid interface. The density of liquid-like molecules is shown in full-blue for the solid/vapor interface and in dashed-green for the solid/liquid interface.

ing the smoothening of the interface just a few Kelvin below the triple point (as expected the divergence remains for (pI)[pII] direction, c.f. Ref.[27]). This result is consistent with the rounding of edges between prismatic facets observed in simulations of ice micro-crytallites.[40]

The observation of a roughening transition at about $\Delta T = -2$ K is somewhat puzzling. Given the similarity between the structure of the quasi-liquid layer and bulk water at short length scales, why are the long wavelength fluctuations so different? Here we show how the finite thickness of the premelting film can change completely the low wave-vector response of the ice/film and film/vapor surfaces even under the assumption that the corresponding stiffness coefficients are exactly those of rough ice/water and water/vapor interfaces, respectively.

To see this, we consider the sine-Gordon model of the solid/liquid interface,[20, 45] and assume that the free energy of the ice/film layer is given solely in terms of parameters akin to the ice/water interface:

$$H_{if} = \int d\mathbf{x} \left(\frac{1}{2} \tilde{\gamma}_{iw} (\nabla h_{if})^2 - u \cos(k_z h_{if}) \right) \tag{2.2}$$

where $\tilde{\gamma}_{iw}$ is the interface stiffness, $k_z = \frac{2\pi}{b}$ and b is the inter-plane spacing. In this model, the square gradient term penalizes the departure of the ice/film layer from planarity, while the cosine term favors by an amount u those configurations where $h_{if}(\mathbf{x})$ is a multiple of the lattice spacing. For the film/vapor surface, we consider that the free energy is described by capillary wave theory, with departures from planarity penalized by the water/vapor surface tension, γ_{wv}:[51]

$$H_{fv} = \int d\mathbf{x} \left(\frac{1}{2} \gamma_{wv} (\nabla h_{fv})^2 + g(\Delta h) \right) \tag{2.3}$$

For an inert substrate, $g(\Delta h)$ is the interface potential, which dictates the free energy of a planar premelting film of height Δh.[52] In our model, it plays the crucial role of coupling the film/vapor fluctuations to the ice/film surface, since $\Delta h = h_{fv} - h_{if}$.

To solve for this coupled Capillary Wave + sine-Gordon model approximately, we extend a variational theory for the sine-Gordon model due to Safran.[45] The solution yields the Fourier modes of surface fluctuations, as follows:[27]

$$\begin{aligned}
\langle|h_{if}^2(q_x)|\rangle &= \frac{k_BT}{A}\frac{g'' + \gamma_{wv}q_x^2}{wg'' + (g''\Sigma + w\gamma_{wv})q_x^2 + \gamma^2 q_x^4} \\
\langle|h_{fv}^2(q_x)|\rangle &= \frac{k_BT}{A}\frac{w + g'' + \tilde{\gamma}_{iw}q_x^2}{wg'' + (g''\Sigma + w\gamma_{wv})q_x^2 + \gamma^2 q_x^4} \\
\langle h_{if}(q_x)h_{fv}^*(q_x)\rangle &= \frac{k_BT}{A}\frac{g''}{wg'' + (g''\Sigma + w\gamma_{wv})q_x^2 + \gamma^2 q_x^4}
\end{aligned} \tag{2.4}$$

where g'' is the second derivative of the interface potential with respect to the layer thickness, $\Sigma = \tilde{\gamma}_{iw} + \gamma_{wv}$, $\gamma^2 = \tilde{\gamma}_{iw}\gamma_{wv}$, while w is a roughness parameter that needs to be solved self-consistently:

$$w = uk_z^2 e^{-\frac{1}{2}k_z^2 \sum_{\mathbf{q}}\langle|h_{if}^2(\mathbf{q})|\rangle} \tag{2.5}$$

Notice that the sum over wave-vectors confers to w a dependence on the surface geometry.[27]

The above result nicely rationalizes our observations. At large wave-vectors, $q \to \infty$, the system is *atomically rough*, i.e. $\Gamma_{if}(q_x) \to \tilde{\gamma}_{iw}$ and $\Gamma_{fv}(q_x) \to \gamma_{wv}$, whence the ice/film and film/vapor surfaces behave as rough ice/water and water/vapor interfaces as observed in Fig.2.2 (a and b).

Furthermore, the fluctuations are then fully independent. This can be seen by considering the cross correlations, $\langle h_{if}(q_x)h_{fv}^*(q_x)\rangle$, which in this limit fall to zero. Defining the related function $\Gamma_{iffv}(q_x) = k_BT/A\langle h_{if}(q_x)h_{fv}^*(q_x)\rangle q_x^2$, consistent with Eq. (2.1), we find indeed that our simulation results for $\Gamma_{iffv}(q_x)$ diverge at large q (see Fig.2.2). This regime of large wave-vectors is consistent with observations by Limmer and Chandler, who measured a stiffness coefficient from the ice/film fluctuations in reasonable agreement with results for the ice/liquid interface in their simulations.[41] In the limit of small wave-vectors, $q_x \to 0$, however, we get qualitatively different behaviors depending on the roughness parameter (c.f. Fig.6 Ref.[27]). On the one hand, if $w = 0$, the fluctuations diverge, and both surfaces behave as rough interfaces with stiffness Σ, (i.e. $\Gamma_{if}(0) = \Gamma_{fv}(0) = \Gamma_{iffv}(0) = \Sigma$). On the other hand, if $w \neq 0$, the fluctuations remain finite as $q \to 0$, whence $\Gamma_{\alpha\beta}(q_x)$ diverges as q_x^{-2}, indicating a smooth interface. Despite the atomic roughness at small length-scales, the smoothening of the surface has dramatic consequences, since both the crystal shape and crystal growth rate is dictated by $\Gamma_{if}(\mathbf{q} \to 0)$.[17, 18, 19, 45]

In our simulations at $\Delta T = -2$ K, we observe, for the (pI)[Basal] direction, a behavior consistent with $w = 0$, corresponding to a rough interface (Fig.2.2.b). For (pI)[pII] direction, on the contrary, we clearly observe for the smallest wave-vector accessible that $\Gamma_{fv}(q_x)$ has largely exceeded Σ, while $\Gamma_{iffv}(q_x)$ attains a minimum well above Σ, and then exhibits a strong divergence, as predicted by our model for a smooth interface (Fig.2.2.a). This 'roughness anisotropy' is consistent with Eq. (2.5), which indicates that the roughening temperature for our (pI)[pII] system could be higher than that of the (pI)[Basal] system by a factor ≈ 1.01 given by the ratio of the ice/vapor stiffness coefficients (Σ).[27]

The qualitative statements that result from our model may be made quantitative and extended to large wave-vectors provided we replace $\tilde{\gamma}_{iw}$ and γ_{wv} in Eq. (3.2) by the phenomenological wavevector dependent coefficients $\tilde{\gamma}_{iw}(q_x)$, and $\gamma_{wv}(q_x)$ obtained from the simulations of the ice/water and water/vapor interfaces. A least square fit to the Fourier amplitudes of (pI) at $\Delta T = -2$ K, yields $g'' \approx 8 \cdot 10^{15}$ J/m^4 for both directions, while the roughness parameter is $w = 0$ for the (pI)[Basal] direction and $w = 3.3 \cdot 10^{15}$ J/m^4 for the (pI)[pII] direction, indicative of the proximity of a roughening transition. At $\Delta T = -8$ K, the fit for both directions is consistent with $g'' \approx 12 \cdot 10^{15}$ J/m^4 and $w \approx 8 \cdot 10^{15}$ J/m^4, corresponding to a smooth interface.

But how can the surface of the ice/film interface become smooth for small wave-vectors while the small wavelength structure remains essentially equal to that of a film of infinite depth? This question can

be answered by solving for the self-consistent condition, Eq. (2.5), with the help of Eq. (3.2). The result gives w as the root of a transcendental equation.[27] For a film of infinite height, with $g'' = 0$, we obtain:

$$w \propto \left(1 + \frac{\tilde{\gamma}_{iw}}{w}\, q_{max}^2\right)^{-\tau_{iw}} \tag{2.6}$$

where q_{max} is an upper wave-vector cutoff for the fluctuations. The above result corresponds to the approximate solution of the sine-Gordon model due to Safran.[45] The resulting transcendental equation depends essentially on one parameter $\tau_{iw} = \frac{k_B T k_z^2}{8\pi\tilde{\gamma}_{iw}}$. For $\tau_{iw} > 1$, the root is $w = 0$, and the surface is rough, while for $\tau_{iw} < 1$, the root is finite, and the surface is smooth. For films of finite depth, $g'' > 0$, and the situation changes. The roots are still governed by an equation similar to the above result:

$$w \propto \left(1 + \frac{\Sigma}{w}\, q_{max}^2\right)^{-\mu_{if}} \tag{2.7}$$

but now the exponent is $\mu_{if} = \frac{\tilde{\gamma}_{iw}}{\Sigma} \cdot \tau_{iw}$, which is always smaller than τ_{iw}.[27] Whence, for a rough ice/water surface with τ_{iw} close but greater than unity, μ_{if} will be well smaller than unity, and the corresponding ice/film surface will become smooth, even though the ice/water surface is rough. Surprisingly, the exponent dictating the transition does not depend on the thickness of the layer, as long as g'' is finite. Only the precise value of w is dictated by the premelting thickness.[27]

Our theoretical approach explains our simulation results and is consistent with experimental observations. The roughening transition of the prismatic plane has been measured for ice crystals in water[53] and vapor[9, 54]. It is found that from $\Delta T \approx -16$ K up to the triple point, the ice/water interface is rough, while, due to the limited width of the quasi-liquid layer, the ice/film surface remains smooth up to $\Delta T \approx -4$ to -2 K, as suggested in our simulations. In fact, in the atmosphere ice crystals exhibit faceted prismatic faces up to 0 C, even at very low saturation.[2] Since smooth surfaces have a slow activated dynamics, our results suggest it is the formation of the quasi-liquid layer what could actually slow down the crystal growth rates and provide a mechanism for the change of crystal habits, as hypothesized by Kuroda and Lacmann [6].

In summary, we have shown that close to the triple point a quasi-liquid layer of premelting ice on the primary prismatic face behaves as two independent ice/water and water/vapor surfaces at small wavelengths, but becomes smooth at long wavelengths. Our results may help rationalize the role of the premelting layer in the morphology of ice crystals.

Acknowledgments

E. Sanz and J. Benet acknowledge financial support from the EU grant 322326-COSAAC-FP7-PEOPLE-2012-CIG and from a Spanish grant Ramon y Cajal. L.G. MacDowell acknowledges financial support from project MAT-2014-59678-R (Ministerio de Economia y Competitividad).

J.B. and P.L. contributed equally to this work.

Supplemental Material

This file contains supplementary information on simulations details, additional results for (pI)[pII], (Basal)[pII] and (pII)[Basal] systems and the solution for the coupled Capillary Wave + sine-Gordon model described in the paper.

Methods and simulation

Simulations

Our study is performed with the TIP4P/2005 model of water [21]. A slab of bulk ice is first prepared from scratch using the algorithm of Buch et al.[24] to sample a hydrogen bond network consistent with the ice rules. This initial configuration is then equilibrated with a Monte Carlo simulation that samples over closed hydrogen bond loops using a cluster algorithm by Rick and Haymet.[25, 26] It then undergoes an isotropic NpT simulation in order to obtain the equilibrium lattice parameters at coexistence. The equilibrated ice sample is placed in contact with vacuum inside a large ortorhombic simulation box, such that an interface of surface area $A = L_x L_y$ is exposed parallel to the xy plane. For production runs, we performed NVT Molecular Dynamics simulations with the Gromacs package at temperatures $\Delta T = T - T_t$ of -2 and -8 K, with $T_t = 250$ K the estimated triple point temperature of the model.[37] We use the Bussi-Donadio-Parrinello thermostat.[28] Lennard-Jones interactions are truncated at $R_c = 0.85$ nm, and electrostatic interactions are evaluated using Ewald summations.

The surface waves on a crystal depend on the crystal plane that is exposed, as well as on the direction of propagation. We use the conventional terminology (**u**)[**n**] to designate such fluctuations,[47, 36] where **u** is a vector perpendicular to the exposed plane, while **n** is a vector perpendicular to **u** and the direction of propagation. The vectors **u** and **n** are designated by the Miller-Bravais indices {h,k,l,i} of the hexagonal symmetry group corresponding to ordinary ice (Ih). For the sake of brevity, we designate sets of equivalent indices corresponding to a given plane or direction as 'Basal', for $\{0001\}$, 'pI' for $\{10\bar{1}0\}$ and 'pII' for $\{2\bar{1}\bar{1}0\}$.

In order to study fluctuations with the largest possible wave-length we prepare the exposed faces with an elongated geometry, with box side $L_x > L_y$ (see Table 2.1 for a description of system size and simulation conditions). This allows us to identify ice/film, $h_{if}(x)$ and film/vapor $h_{fv}(x)$ surface profiles along the largest axis, x (see Fig.1 of paper). Accordingly, for fluctuations designated as (hkli)[h'k'l'i'], the plane (hkli) of the interface is perpendicular to the z axis, while the direction [h'k'l'i'] is parallel to the y axis. For ice/vapor systems, we considered a very large lateral size $L_x \approx 36$ nm. On the other hand ice/water interfaces were studied using $L_x \approx 18$ nm.

We choose the crystal orientation such that the primary prismatic plane is exposed (pI). Configurations were prepared with the long direction along either the basal [Basal] or secondary prismatic orientations [pII]. This allows us to measure long wavelength fluctuations, which are denoted as (pI)[Basal] and (pI)[pII], for fluctuations on the (pI) plane along the [Basal] and [pII] directions, respectively. Less detailed results for (Basal)[pII] and (pII)[Basal] geometries with $L_x \approx 18$ nm are also reported in this document (see below).

To simulate ice/water interfaces, we use the configurations prepared for the ice/vapor interface. We then equilibrate a slab of liquid water with equal lateral dimensions than the solid. Both phases are brought together, and molecules of the liquid phase less than one molecular diameter apart are removed. The compound system is then equilibrated in an Np_zT simulation with the barostat along the perpendicular

Interphase	plane	direction	T/K	t/ns	n	L_x/nm	L_y/nm	L_z/nm
i/v	(pI)	[Basal]	248.6	624	8328	36.1163	2.2062	19.0000
i/v	(pI)	[Basal]	242.7	517	6909	36.1013	2.2052	19.0000
i/v	(pI)	[pII]	248.9	483	5700	36.7309	1.8034	19.0000
i/v	(pI)	[pII]	242.4	429	5600	36.7190	1.8028	19.0000
i/w	(pI)	[Basal]	242.2	563	7500	18.0009	2.1991	8.2517
w/v	-	-	242.1	431	5400	18.0059	2.2063	12.0000
i/w	(pI)	[pII]	242.3	529	7060	18.3087	1.7978	8.3431
i/v	(Basal)	[pII]	248.8	1268	10870	18.7696	1.8039	9.3319
i/w	(Basal)	[pII]	248.1	715	9533	18.7696	1.8039	9.3319
i/v	(pII)	[Basal]	248.3	257	3426	18.0577	2.2045	9.5000
i/w	(pII)	[Basal]	248.7	603	8036	18.0134	2.1991	8.0808

Table 2.1. Table with detailed description of the simulations performed in this work. For each system studied we describe the interface arrangement, temperature, T, length of simulations, t and size of simulation box L_x, L_y, L_z. All simulations are performed at coexistence.

direction to the interface only.[36, 44] For the liquid-vapor interface, it suffices to equilibrate a liquid slab under periodic boundary conditions. The slab is then placed in vacuum and a liquid-vapor interface equilibrates gradually.

Location of the interface

Liquid like and solid like molecules are distinguished using the $\bar{q}_6$ order parameter by Lechner and Dellago [42], which has been optimized to discriminate ice like and water like molecules from a study of molecular correlations up to second nearest neighbors. For the TIP4/2005 model in the range of temperatures studied we chose a threshold value of $\bar{q}_6 = 0.347$ to discriminate between liquid like and solid like molecules.

To define the film/vapor surface, we define a grid on the xy plane. For each bin on the grid, the position of the interface is determined as an average of the 4 outermost liquid-like molecules contained within a distance $x = 1/2 \cdot \Delta_x$ and $y = 1/2 \cdot \Delta_y$, with $\Delta_x = 0.91$ nm and $\Delta_y = 1/2 \cdot L_y$. A similar procedure is used to evaluate the ice/film surface, with the position of the surface determined from the outermost solid-like molecules. The corresponding surfaces are averaged along the y direction to obtain $h_{if}(x)$ and $h_{fv}(x)$. These film profiles are then Fourier transformed to yield the spectrum of surface fluctuations.

The spectrum of the ice/film fluctuations is compared in Fig.2 of the paper with corresponding fluctuations for the ice/liquid interface at the same temperature. For $\Delta T = -2$ K, we employed results obtained previously by ourselves.[44] For $\Delta T = -8$ K, we performed new simulations (see Table 2.1). Having equilibrated the ice/water interface as explained above, the spectrum of fluctuations is calculated exactly as described for the ice/film surface. The solid and liquid bulk phases that were merged to prepare the interface were previously equilibrated at the coexistence pressure of $p = 882$ bar. Similarly, the spectrum for the water/vapor interface is calculated as for the film/vapor interface.

During the course of the simulations, the center of the solid slab fluctuates and blurs the density profile. To avoid this, we collect density profiles for short periods of 37.5 ns. This also helps eliminate capillary wave roughening. Further details of the procedure may be found in Ref.[36, 44].

Summary of results for the (pI) plane.

Here we collect all results of $\Gamma(q)$ for the (pI) plane. At $\Delta T = -2$ K, (pI)[Basal] appears rough, and (pI)[pII] appears smooth. At $\Delta T = -8$ K, both sets of fluctuations are consistent with a smooth interface, as can be seen from the divergence of $\Gamma(q)$ in the limit $q \to 0$ (Fig.2.4). For $\Delta T = -8$ K, however, the coexistence

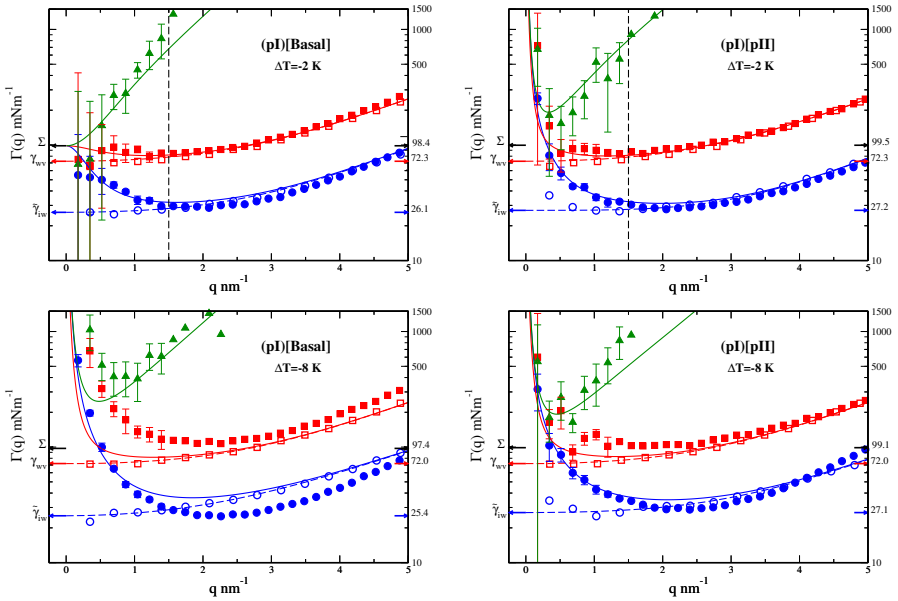

Figure 2.4. Fluctuations of the premelting film for the primary prismatic plane at $\Delta T = -2$ K (top) and $\Delta T = -8$ K (bottom). The plot displays wave-vector dependent stiffness, $\Gamma(q)$ in log scale. Left column corresponds to (pI)[Basal], right column to (pI)[pII].

pressure of the ice/water interface is now about 900 MPa, and the short wave-length fluctuations of the ice/vapor interface differ considerably from the ice/liquid and liquid/vapor results. Note that the presence of atomic roughness at a small lengthscale within a smooth surface is consistent with a pre-roughening scenario suggested by Rommelse and den Nijs.[29]

Results for the basal and secondary prismatic planes

We have also studied the fluctuations on the (Basal) and (pII) planes for $\Delta T = -2$ K and the small system sizes (see Table.2.1). The results seem consistent with the properties of ice mycrocristallites (see Fig.2.5).

The (Basal) plane exhibits a divergence of $\Gamma(q)$ consistent with a smooth interface. A best fit to the model of Eq.4 provides $w = 6.5$ and $g'' = 6.0 \cdot 10^{15}$ J/m^4, while a constrained fit with $w = 0$ yields $g'' = 12 \cdot 10^{15}$ J/m^4 and squared deviations that are one order of magnitude larger.

For the (pII) plane we studied the spectrum along (pII)[Basal] and results are suggestive of a rough interface, with $\Gamma(q)$ apparently converging to Σ. Unconstrained fits to the model of Eq.4 yield unphysical results, with a negative w. A constrained fit with $w = 0$ provides $g'' = 3.6 \cdot 10^{15}$ J/m^4.

As for the (pI) plane, the fluctuations of ice/film and film/vapor surfaces are very well described by results from independent ice/water and water/vapor interfaces. We checked that also the local interfacial structure of the premelting film as described by the density profiles is similar to the independent interfaces, as is seen in Fig.2.6.

Fitting procedure

Fitting of $\Gamma(q)$ to the model of Eq.4 is difficult, because Γ_{iffv} is typically orders of magnitude larger than $\Gamma_{if}(q)$ and $\Gamma_{fv}(q)$. For this reason we find it more convenient to fit the results to $1/\Gamma(q)$. In this

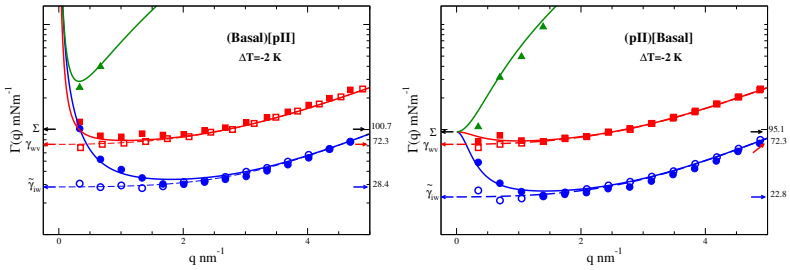

Figure 2.5. Fluctuations of the premelting film for basal and secondary prismatic plane. The plot displays $\Gamma(q)$ in log scale for (Basal)[pII] (left) and (pII)[Basal] arrangements, respectively, for temperature $\Delta T = -2$ K. All symbols as in Fig.2 of the paper.

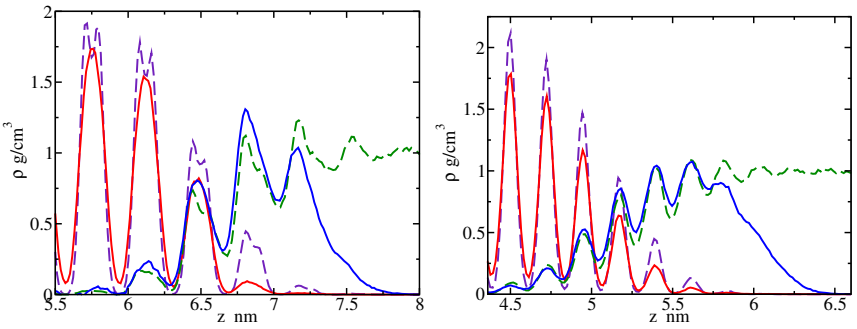

Figure 2.6. Density profiles of solid like (dashed line) and liquid like (full line) ice/vapor (full lines) and ice/liquid (dashed lines) interfaces as a function of perpendicular distance z at $\Delta T = -2$ K. From left to right results are shown for the (Basal) and (pII) planes. Rest of captions as in Fig.3 of paper.

representation all the results are of similar order of magnitude. Fits were performed by simultaneously adjusting results for $\Gamma_{if}(q)^{-1}$, $\Gamma_{fv}(q)^{-1}$ and $\Gamma_{iffv}(q)^{-1}$ with equal weights, from the lowest wave-vector up to $q \approx 4.5$ nm^{-1}. For rough interfaces the $\Gamma(q)^{-1}$ attain a constant value, and for smooth interfaces they vanish as $q \to 0$.

System size effects

Since the decision as to whether a surface remains rough or smooth requires to study the $q \to 0$ limit, it is important to assess whether the simulations are subject to system size effects. In Fig.2.7, we compare $\Gamma(q)$ as obtained for the ice/vapor interface for two different system sizes. The first system size is that reported in the paper, with a long side L_x of about 36 nm. The second is one with equal dimensions for L_y and L_z, but the long side L_x half as large. For the (pI)[pII] system, the figure shows no significant system size dependence (though the large system allows for twice as large density of wave-vectors). For the (pI)[Basal] system, again the agreement between large and small systems is very good, up to the lowest wave-vector. In this case we find the largest system exhibits rough behavior, while the small one suggests a smooth interface. We believe this discrepancy is not a system size effect, but rather, a consequence of the neighborhood of the roughening transition and the difficulty to control the temperature within an interval of about 0.5 K.

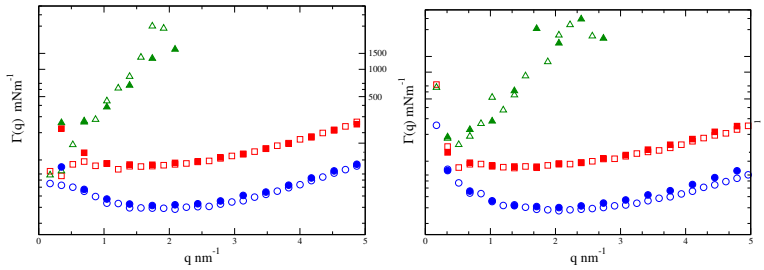

Figure 2.7. System size dependence of $\Gamma(q)$ of the ice/vapor interface for the (pI)[Basal] (left) and (pI)[pII] (right) systems studied in this work. Results for the large system with $L_x \approx 36$ nm are shown with empty symbols, and those for the small system with $L_x = 18$ nm are shown with filled symbols.

Solution of the coupled Capillary-Wave + sine-Gordon model

Model and variational solution

Consider a thin film sandwiched between a solid and a vapor phase. The state of the film is described in terms of a solid/film profile, $h_{if}(x)$, and a film/vapor profile, $h_{fv}(x)$, which we denote for short as $h_1(x)$ and $h_2(x)$, respectively. The solid/film interface is described with the sine-Gordon model,[20] and the film/vapor interface with the Capillary Wave Hamiltonian in quadratic approximation.[51] Our coupled Hamiltonian for the quasi-liquid film is:

$$H_f = \int dx \left\{ \frac{1}{2}\tilde{\gamma}_{iw}(\nabla h_1)^2 - u\cos(k_z h_1) + \frac{1}{2}\gamma_{wv}(\nabla h_2)^2 + \frac{1}{2}g''(h_2 - h_1)^2 \right\} \tag{2.8}$$

where $\tilde{\gamma}_{iw}$ is the stiffness of the ice/water interface, u is a phenomenological coefficient dictating the pining of the ice/film surface to discrete lattice spacings, $k_z = 2\pi/b$, with b the inter-plane spacing in the direction perpendicular to the interface. γ_{wv} is the liquid/vapor surface tension, and g'' is the second derivative of the interface potential with respect to film thickness. Here it serves as a spring constant for the harmonic fluctuations of the film thickness.[52]

We seek solution of the partition function in terms of the Fourier modes of both surfaces $h_\alpha(\mathbf{q})$ (α=1 or 2). Recognizing that the second order approximation of the above result is quadratic in the surface modes, we consider a reference Hamiltonian of independent harmonic oscillators with Gaussian statistics:

$$H_0 = \frac{1}{2}\sum_{\mathbf{q}} \mathbf{h}(\mathbf{q})\mathbf{G}^{-1}(\mathbf{q})\mathbf{h}(\mathbf{q}) \tag{2.9}$$

where $\mathbf{h}(\mathbf{q}) = (h_1(\mathbf{q}), h_2(\mathbf{q}))$ and $\mathbf{G}^{-1}$ is the covariance matrix:

$$\mathbf{G}^{-1}(\mathbf{q}) = \begin{pmatrix} \sigma_{11}^2(\mathbf{q}) & \sigma_{12}^2(\mathbf{q}) \\ \sigma_{21}^2(\mathbf{q}) & \sigma_{22}^2(\mathbf{q}) \end{pmatrix} \tag{2.10}$$

with matrix components: $\sigma_{11}^2(\mathbf{q}) = \langle h_1(\mathbf{q})h_1^*(\mathbf{q})\rangle$, $\sigma_{22}^2(\mathbf{q}) = \langle h_2(\mathbf{q})h_2^*(\mathbf{q})\rangle$, $\sigma_{12}^2(\mathbf{q}) = \langle h_1(\mathbf{q})h_2^*(\mathbf{q})\rangle$ and $\sigma_{21}^2(\mathbf{q}) = \langle h_2(\mathbf{q})h_1^*(\mathbf{q})\rangle$.

The partition function of the reference Hamiltonian is:[30]

$$Z_0 = \int \prod_{\mathbf{q}} d\mathbf{h}(\mathbf{q}) e^{-\frac{1}{2}\beta \sum_{\mathbf{q}} \mathbf{h}(\mathbf{q})\,\mathbf{G}^{-1}(\mathbf{q})\,\mathbf{h}(\mathbf{q})} \tag{2.11}$$

while the free energy is:

$$F_0 = \frac{1}{2} k_B T \sum_{\mathbf{q}} \ln \frac{\det \mathbf{G}^{-1}(\mathbf{q})}{(2\pi k_B T)^2} \tag{2.12}$$

This result can be expressed explicitly in terms of the elements of the covariance matrix:

$$F_0 = -\frac{1}{2} k_B T \sum_{\mathbf{q}} \ln \left[(2\pi k_B T)^2 (\sigma_{11}^2(\mathbf{q}) \sigma_{22}^2(\mathbf{q}) - \sigma_{12}^4(\mathbf{q})) \right] \tag{2.13}$$

Next, we assess the free energy contribution from H_f by performing an average over the Gaussian statistics of the reference oscillators, $F_f = \langle H_f \rangle_0$, with the result:

$$F_f = \frac{1}{2} A \sum_{\mathbf{q}} \left\{ [g'' + \tilde{\gamma}_{iw} q^2] \sigma_{11}^2(q) + [g'' + \gamma_{wv} q^2] \sigma_{22}^2(q) - 2 g'' \sigma_{12}^2(q) - u e^{-\frac{1}{2} k_z^2 \sum_{\mathbf{q}} \sigma_{11}^2(q)} \right\} \tag{2.14}$$

where q is the norm of $\mathbf{q}$. Notice we have taken into account that the Gaussian average of $\cos(k_z h_1(x))$ is $\exp(-\frac{1}{2} k_z^2 \langle h_1^2(x) \rangle)$, and further used Parseval's theorem to transform averages of $h_1^2(x)$ and $h_2^2(x)$ into averages of their Fourier components.

The total free energy is $F_0 + F_f$, and we obtain a solution in closed form by seeking for the variational parameters $\sigma_{11}^2(q)$, $\sigma_{22}^2(q)$ and $\sigma_{12}^2(q)$. The result of this minimization yields:

$$\begin{aligned}
\sigma_{11}^2(q) &= \frac{k_B T}{A} \frac{g'' + \gamma_{wv} q^2}{[w + g'' + \tilde{\gamma}_{iw} q^2][g'' + \gamma_{wv} q^2] - g''^2} \\
\sigma_{22}^2(q) &= \frac{k_B T}{A} \frac{w + g'' + \tilde{\gamma}_{iw} q^2}{[w + g'' + \tilde{\gamma}_{iw} q^2][g'' + \gamma_{wv} q^2] - g''^2} \\
\sigma_{12}^2(q) &= \frac{k_B T}{A} \frac{g''}{[w + g'' + \tilde{\gamma}_{iw} q^2][g'' + \gamma_{wv} q^2] - g''^2}
\end{aligned} \tag{2.15}$$

where the roughness parameter w is

$$w = u k_z^2 e^{-\frac{1}{2} k_z \sum_q \sigma_{11}^2(q)} \tag{2.16}$$

To solve for this self consistent condition, we ignore surface anisotropy, which is small for ice (see next section), and approximate:

$$\sum_{\mathbf{q}} \sigma_{11}^2(q) = \frac{k_B T}{2\pi} \int_0^{q_{max}} q dq \frac{g'' + \gamma_{wv} q^2}{w g'' + (g'' \Sigma + w \gamma_{wv}) q^2 + \gamma^2 q^4} \tag{2.17}$$

where q_{max} is an ultra-violet cut–off and we have introduced $\Sigma = \tilde{\gamma}_{iw} + \gamma_{wv}$ and $\gamma^2 = \tilde{\gamma}_{iw} \gamma_{wv}$ for short.

This integral may be solved in real space along the lines indicated in Ref.[31], with the result:

$$\sum_q \sigma_{11}^2(q) = C \ln(1 + \frac{pr}{w g''} q_{max}^2) + D \ln(1 + \frac{\gamma^2}{pr} q_{max}^2) \tag{2.18}$$

where:

$$p = g'' \Sigma + w \gamma_{wv} \tag{2.19}$$

$$r = \frac{p + (p^2 - 4 w g'' \gamma^2)^{1/2}}{2p} \tag{2.20}$$

$$C = \frac{k_B T}{4\pi} \frac{g'' r p - g'' \gamma_{wv} w}{r^2 p^2 - w g'' \gamma^2} \tag{2.21}$$

$$D = \frac{k_B T}{4\pi} \frac{pr}{\gamma^2} \frac{\gamma_{wv} r p - g'' \gamma^2}{r^2 p^2 - w g'' \gamma^2} \tag{2.22}$$

For H_2O, where $\gamma_{wv} > \tilde{\gamma}_{iw}$ at the triple point, r is always positive and real.

As we shall see, the outcome of the self consistent condition is mainly dictated by the behavior of Eq. (2.18) at small w, whence, we assume $p^2 >> 4wg''\gamma^2$, so that expanding the square root in Eq. (2.20) to zero order, the coefficients C and D simplify to:

$$C = \frac{k_B T}{4\pi} \frac{g''^2 \Sigma}{(g''\Sigma + w\gamma_{wv})^2} \tag{2.23}$$

and

$$D = \frac{k_B T}{4\pi} \frac{\gamma_{wv}}{\tilde{\gamma}_{iw}} \frac{g'' + w}{g''\Sigma + w\gamma_{wv}} \tag{2.24}$$

By use of Eq. (2.16), Eq. (2.18) and Eq.2.23-2.24, we obtain the self-consistent condition in closed form as:

$$w = u k_z^2 \left(1 + \frac{g''\Sigma + w\gamma_{wv}}{w g''} q_{max}^2\right)^{-\mu} \cdot \left(1 + \frac{\gamma^2}{g''\Sigma + w\gamma_{wv}} q_{max}^2\right)^{-\tau} \tag{2.25}$$

where $\mu = \frac{1}{2} k_z^2 C$ and $\tau = \frac{1}{2} k_z^2 D$.

In order to understand the significance of this result, let us first consider the case of the ice/water interface (film of infinite thickness), such that $g'' \equiv 0$. In that case, $\mu \equiv 0$, and we get:

$$w = u k_z^2 \left(1 + \frac{\tilde{\gamma}_{iw}}{w} q_{max}^2\right)^{-\tau_{iw}} \tag{2.26}$$

with $\tau_{iw} = \frac{\pi k_B T}{2\tilde{\gamma}_{iw} b^2}$. It follows that w is the real root of the auxiliary equation $x = y(x)$, with

$$y(x) = \left(1 + \frac{a}{x}\right)^{-\tau_{iw}} \tag{2.27}$$

and a a constant. i.e., w is given by the intersection of a straight line of unit slope with the auxiliary function $y(x)$. This function goes through the origin with positive slope, then bends and eventually becomes constant. For $\tau_{iw} < 1$, $y(x)$ meets the origin with infinite slope, and must therefore cross the straight line of unit slope at finite x. If, on the other hand, $\tau_{iw} > 1$, $y(x)$ meets the origin with zero slope and there is only one root at $x = 0$ (see Fig.2.8). Whence, we encounter a roughening transition from a smooth surface (finite w) to a rough surface ($w = 0$) at $\tau_{iw} = 1$.[45] This corresponds exactly to the roughening transition of the sine-Gordon model.[20]

Let us now consider the general case of an ice surface covered by a quasi-liquid film of finite depth, with finite g''. The solutions for w are now given by Eq. (2.25), which, in the limit $w \ll g''$ becomes:

$$w = u k_z^2 \left(1 + \frac{\Sigma}{w} q_{max}^2\right)^{-\mu_{if}} \cdot \left(1 + \frac{\gamma^2}{g''\Sigma} q_{max}^2\right)^{-\tau_{if}} \tag{2.28}$$

where $\mu_{if} = \frac{\tilde{\gamma}_{iw}}{\Sigma} \cdot \tau_{iw}$ and $\tau_{if} = \frac{\gamma_{wv}}{\Sigma} \cdot \tau_{iw}$. This result shows the dramatic consequences of pining the liquid film on the ice surface. Particularly, the second parenthesis of the right hand side, which drives the roughening transition for the case $g'' \equiv 0$, is now a constant. On the other hand, the first parenthesis, which was unity in that case, becomes responsible for driving the roughening transition. In fact, it takes

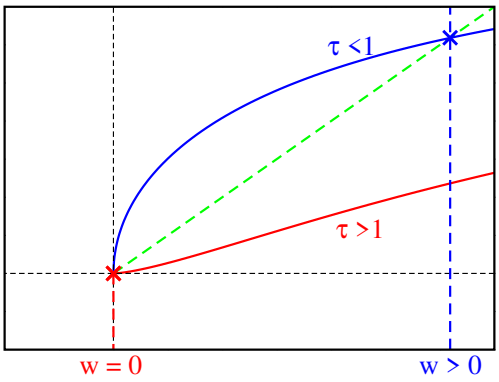

Figure 2.8. Sketch of the solution of $w \propto y(w)$ dictating the roughness of a solid/liquid interface. The green line is a straight line of unit slope. Blue and red lines correspond to y(w) (Eq. (2.27)) for $\tau > 1$ and $\tau < 1$, respectively. The equilibrium roughnes w is given by the intersection of either curve with the straight green line. For $\tau > 1$, only one root at $w = 0$ exists (rough interface). For $\tau < 1$, an additional route $w > 0$ is found (smooth interface).

exactly the same form as Eq. (2.26), albeit, with a completely different exponent, which differs from τ_{iw} by a factor $\tilde{\gamma}_{iw}/\Sigma$. For our model, this is about 1/3 at the triple point. The implication is that under conditions where the ice/water surface has become rough, with $\tau_{iw} \geq 1$, we expect that μ_{if} will be largely below unity. Hence, the coupling of the film/vapor interface to the ice/film surface via g'' drives the rough ice/water interface into a smooth surface. In practice, the effect is significant for large g''. For finite but small g'', the root occurs extremely close to $w = 0$, and the smoothening is then only apparent at very large length-scales. Our results are consistent with previous studies showing the sensitivity of roughening to monolayer surface adsorption.[32]

Roughening anisotropy

Ordinary ice has hexagonal symmetry and is therefore not strictly isotropic. Particularly, for the ice/water interface at $\Delta T = -2$ K, the (pI) crystal plane has slightly different principal stiffness coefficients for the [Basal] (call it x) and [pII] (call it y) directions (i.e., $\tilde{\gamma}_{iw}(x) = 26.14$ mN/m and $\tilde{\gamma}_{iw}(y) = 27.18$ mn/m, respectively). To account for this anisotropy, the Hamiltonian of Eq. (2.8) should be replaced by:

$$H_f = \int dx \left\{ \frac{1}{2}\tilde{\gamma}_{iw}(x)\partial h_1 x^2 + \frac{1}{2}\tilde{\gamma}_{iw}(y)\partial h_1 y^2 - u\cos(k_z h_1) + \frac{1}{2}\gamma_{wv}(\nabla h_2)^2 + \frac{1}{2}g''(h_2 - h_1)^2 \right\} \tag{2.29}$$

The solution of this Hamiltonian in Fourier modes is exactly as for the isotropic case, provided one replaces $\tilde{\gamma}_{iw}q^2$ by $\tilde{\gamma}_{iw}(x)q_x^2 + \tilde{\gamma}_{iw}(y)q_y^2$.[33] Particularly, the result for σ_{11}^2 in Eq. (3.2) should be replaced by:

$$\sigma_{11}^2(\mathbf{q}) = \frac{k_B T}{A} \frac{g'' + \gamma_{wv}q^2}{[w + g'' + \tilde{\gamma}_{iw}(x)q_x^2 + \tilde{\gamma}_{iw}(y)q_y^2][g'' + \gamma_{wv}q^2] - g''^2} \tag{2.30}$$

For large but finite surfaces of circular or square shape the sum $\sum_{\mathbf{q}} \sigma_{11}^2(\mathbf{q})$ required to measure w in Eq. (2.16) is effectively performed from a low wave-vector $\mathbf{q} = (\frac{2\pi}{L}, \frac{2\pi}{L}) \to (0, 0)$, and the anisotropy of the stiffness coefficients is inconsequential.[34]

In our systems, however, we study surfaces that are very thin in one direction and large in the other. Accordingly, the large wave-length modes in the short direction are cut-off and the lower cut-off

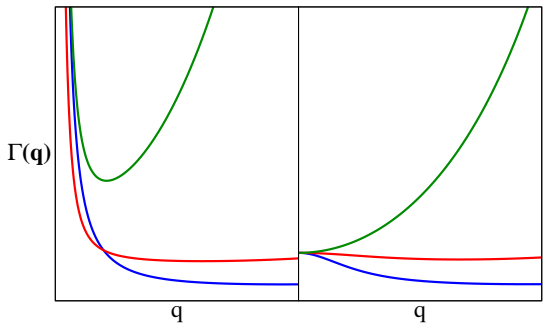

Figure 2.9. Results for $\Gamma(q)$ as obtained from the model of Eq. (3.2) for the ice/film (blue), film/vapor (red) and coupled fluctuations of the ice/film and film/vapor surfaces (green). Left: Behavior expected for a smooth interface, with finite g'' and w. Right: Behavior expected for a rough interface, with finite g'' but $w = 0$.

is anisotropic, since now $\mathbf{q} = (\frac{2\pi}{L_x}, \frac{2\pi}{L_y})$ and $L_x \neq L_y$. Whence, for the (pI)[Basal] direction we have an effective lower cut-off at $\mathbf{q} = (0, \frac{2\pi}{L_y})$, while in the (pI)[pII] direction the lower-cutoff is $\mathbf{q} = (\frac{2\pi}{L_x}, 0)$. As a result, the sum $\sum_{\mathbf{q}} \sigma_{11}^2(\mathbf{q})$ now depends on the system geometry. Accordingly, the self-consistent condition for the roughness parameter, Eq. (2.16), also becomes anisotropic.

The effect is weak, however, because the anisotropy in the stiffness coefficient is small. Indeed, for the crystal/melt interface of NaCl we have checked previously that for systems well above the roughening transition, the results for an elongated system are fully equivalent to those of a square interface.[35]

In our case the problem is more subtle, because we are close to the roughening transition. Unfortunately, this effect cannot be described analytically, because the integral of Eq. (2.30) can be solved in circular coordinates, but not in rectangular coordinates as required here.[34]

Nevertheless, assuming we can obtain the root of w using the exponent μ_{if} for the isotropic case by merely replacing $\Sigma = \gamma_{lv} + \tilde{\gamma}_{iw}$ with the corresponding anisotropic stiffness, we find the exponent for roughening in the (pI)[Basal] direction is $\approx (72 + 27)/(72 + 26) = 1.01$ times larger than that for the (pI)[pII] direction, whence, the (pI)[Basal] system may become effectively rough at a temperature where (pI)[pII] remains smooth, as observed in our simulations.

Asymptotic behavior of the surface fluctuations

The behavior of the surface Fourier modes adopts distinct behavior in the limit $q \to 0$, depending on whether g'' and w are null or finite (Fig.2.9).

This allows to tell whether the surface is rough ($w = 0$) or smooth $w > 0$ from the behavior of the spectrum of fluctuations.

Defining:

$$\begin{aligned} \Gamma_{if}(q) &= \frac{k_B T}{A\langle h_{if}(q) h_{if}^*(q)\rangle q^2} \\ \Gamma_{fv}(q) &= \frac{k_B T}{A\langle h_{fv}(q) h_{fv}^*(q)\rangle q^2} \\ \Gamma_{iffv}(q) &= \frac{k_B T}{A\langle h_{if}(q) h_{fv}^*(q)\rangle q^2} \end{aligned} \tag{2.31}$$

we find, from Eq. (3.2):

Limit of $q \to \infty$.

For sufficiently large q, both surfaces of the quasi-liquid layer behave like rough and independent ice/water and water/vapor interfaces:

$$\begin{array}{rcl} \Gamma_{if}(q) & \to & \tilde{\gamma}_{iw} \\ \Gamma_{fv}(q) & \to & \gamma_{wv} \\ \Gamma_{iffv}(q) & \to & \frac{q^2}{g''} \end{array} \tag{2.32}$$

Limit of $q \to 0$.

In the limit of small q, the behavior is distinctly different depending on whether the ice/vapor interface is smooth ($w > 0$) or rough ($w = 0$):

Smooth interface ($w > 0$).

For a smooth interface, the fluctuations remain finite at zero wave-vector, and the $\Gamma_{\alpha\beta}$ diverge.

$$\begin{array}{rcl} \Gamma_{if}(q) & \to & \frac{w}{q^2} \\ \Gamma_{fv}(q) & \to & \frac{wg''}{(g''+w)q^2} \\ \Gamma_{iffv}(q) & \to & \frac{w}{q^2} \end{array} \tag{2.33}$$

Rough interface ($w = 0$).

For a rough interface, the fluctuations diverge and the interface behaves globally as a rough surface with stiffness $\Sigma = \tilde{\gamma}_{iw} + \gamma_{wv}$.

$$\begin{array}{rcl} \Gamma_{if}(q) & \to & \Sigma \\ \Gamma_{fv}(q) & \to & \Sigma \\ \Gamma_{iffv}(q) & \to & \Sigma \end{array} \tag{2.34}$$

Notice that the latter behavior is also observed for a smooth interface in the range of wave-vectors $g''w \ll g''\Sigma q^2 \ll \gamma^2 q^4$ provided $w \ll g''$. Therefore, for very small w it is required to attain a regime of very small q to discriminate between a rough and a smooth surface.

Bibliography

[1] I. Sunagawa, ed., *Morphology of Crystals*. Tokyo: Terra Scientific Publishing Company, 1987.

[2] K. G. Libbrecht, "The physics of snow crystals," *Rep. Prog. Phys.*, vol. 68, pp. 855–895, 2005.

[3] H. R. Pruppacher and J. D. Klett, *Microphysics of Clouds and Precipitation*. Heidelberg: Springer, 2010.

[4] X. Y. Liu, E. S. Boek, W. J. Briels, and P. Bennema, "Prediction of crystal growth morphology based on structural analysis of the solid-fluid interface," *Nature*, vol. 374, pp. 342–345, 1995.

[5] Y. Furukawa and J. Wettlaufer, "Snow and ice crystals," *Phys. Today*, vol. 60, pp. 70–71, 2007.

[6] T. Kuroda and R. Lacmann, "Growth kinetics of ice from the vapour phase and its growth forms," *J. Cryst. Growth*, vol. 56, no. 1, pp. 189–205, 1982.

[7] R. Lipowsky, "Critical surface phenomena at first-order bulk transitions," *Phys. Rev. Lett.*, vol. 49, pp. 1575–1578, 1982.

[8] J. G. Dash, A. W. Rempel, and J. S. Wettlaufer, "The physics of premelted ice and its geophysical consequences," *Rev. Mod. Phys.*, vol. 78, pp. 695–741, 2006.

[9] M. Elbaum, "Roughening transition observed on the prism facet of ice," *Phys. Rev. Lett.*, vol. 67, pp. 2982–2985, Nov 1991.

[10] A. Lied, H. Dosch, and J. H. Bilgram, "Surface melting of ice I_h single crystals revealed by glancing angle x-ray scattering," *Phys. Rev. Lett.*, vol. 72, pp. 3554–3557, 1994.

[11] H. Dosch, A. Lied, and J. H. Bilgram, "Glancing angle x-ray scattering studies of the premelting of ice surfaces," *Surf. Sci.*, vol. 327, pp. 145–164, 1995.

[12] H. Bluhm, D. F. Ogletree, C. S. Fadley, Z. Hussain, and M. Salmeron, "The premelting of ice studied with photoelectron spectroscopy," *J. Phys.: Condens. Matter*, vol. 14, pp. L227–L233, 2002.

[13] G. Sazaki, S. Zepeda, S. Nakatsubo, M. Yokomine, and Y. Furukawa, "Quasi-liquid layers on ice crystal surfaces are made up of two different phases," *Proc. Nat. Acad. Sci.*, vol. 109, no. 4, pp. 1052–1055, 2012.

[14] K.-i. Murata, H. Asakawa, K. Nagashima, Y. Furukawa, and G. Sazaki, "*In situ* determination of surface tension-to-shear viscosity ratio for quasiliquid layers on ice crystal surfaces," *Phys. Rev. Lett.*, vol. 115, p. 256103, Dec 2015.

[15] J. Wettlaufer, "Impurity effects in the premelting of ice," *Phys. Rev. Lett.*, vol. 82, pp. 2516–2519, Mar 1999.

[16] W. K. Burton, N. Cabrera, and F. C. Frank, "The growth of crystals and the equilibrium structure of their surfaces," *Phyl. Trans. R. Soc. Lond. A*, vol. 243, pp. 299–358, 1951.

[17] J. D. Weeks and G. H. Gilmer, "Dynamics of crystal growth," *Adv. Chem. Phys.*, vol. 40, pp. 157–228, 1979.

[18] C. Jayaprakash, W. F. Saam, and S. Teitel, "Roughening and facet formation in crystals," *Phys. Rev. Lett.*, vol. 50, pp. 2017–2020, Jun 1983.

[19] C. Rottman and M. Wortis, "Equilibrium crystal shapes for lattice models with nearest-and next-nearest-neighbor interactions," *Phys. Rev. B*, vol. 29, pp. 328–339, Jan 1984.

[20] P. M. Chaikin and T. C. Lubensky, *Principles of Condensed Matter Physics*. Cambridge: Cambridge University Press, 1995.

[21] J. L. F. Abascal and C. Vega, "A general purpose model for the condensed phases of water: Tip4p/2005," *J. Chem. Phys.*, vol. 123, p. 234505, 2005.

[22] C. Vega and J. L. F. Abascal, "Simulating water with rigid non-polarizable models: a general perspective," *Phys. Chem. Chem. Phys.*, vol. 13, pp. 19663–19688, 2011.

[23] M. Watkins, D. Pand, E. G. Wang, A. Michaelides, J. VandeVondele, and B. Slater, "Large variation of vacancy formation energies in the surface of crystalline ice," *Nature Materials*, vol. 10, pp. 794–798, 2011.

[24] V. Buch, P. Sandler, and J. Sadlej, "Simulations of H_2O solid, liquid and clusters, with an emphasis on ferroelectric ordering transition in hexagonal ice," *J. Phys. Chem. B*, vol. 102, pp. 8641–8653, 1998.

[25] S. W. Rick and A. D. J. Haymet, "Dielectric constant and proton order and disorder in ice Ih: Monte Carlo computer simulations," *J. Chem. Phys.*, vol. 118, pp. 9291–9296, 2003.

[26] L. G. MacDowell and C. Vega, "Dielectric constant of ice ih and ice v: A computer simulation study," *J. Phys. Chem. B*, vol. 114, pp. 6089–6098, 2010.

[27] "See supplemental material for the model and simulation details and theory, which includes Refs.[28-35]."

[28] G. Bussi, D. Donadio, and M. Parrinello, "Canonical sampling through velocity rescaling," *J. Chem. Phys.*, vol. 126, no. 1, p. 014101, 2007.

[29] K. Rommelse and M. den Nijs, "Preroughening transitions in surfaces," *Phys. Rev. Lett.*, vol. 59, pp. 2578–2581, Nov 1987.

[30] N. Goldenfeld, *Lectures on Phase Transitions and the Renormalization Group*. Reading, Massachusetts: Perseus Books, 1992.

[31] L. G. MacDowell, "Capillary wave theory of adsorbed liquid films and the structure of the liquid-vapor interface," *[cond-mat.soft]*, p. ArXiv:1512.04777, 2015.

[32] N. Akutsu, Y. Akutsu, and T. Yamamoto, "Vicinal surface with langmuir adsorption: A decorated restricted solid-on-solid model," *Phys. Rev. B*, vol. 64, p. 085415, Aug 2001.

[33] D. S. Fisher and J. D. Weeks, "Shape of crystals at low temperatures: Absence of quantum roughening," *Phys. Rev. Lett.*, vol. 50, pp. 1077–1080, Apr 1983.

[34] N. Akutsu and T. Yamamoto, "6 - rough–smooth transition of step and surface," in *Handbook of Crystal Growth (Second Edition)* (T. Nishinaga, ed.), pp. 265–313, Boston: Elsevier, second edition ed., 2015.

[35] J. Benet, L. G. MacDowell, and E. Sanz, "Interfacial free energy of the nacl crystal-melt interface from capillary wave fluctuations," *J. Chem. Phys.*, vol. 142, no. 13, 2015.

[36] J. Benet, L. G. MacDowell, and E. Sanz, "Computer simulation study of surface wave dynamics at the crystal–melt interface," *J. Chem. Phys.*, vol. 141, p. 034701, 2014.

[37] D. Rozmanov and P. G. Kusalik, "Temperature dependence of crystal growth of hexagonal ice (ih)," *Phys. Chem. Chem. Phys*, vol. 13, pp. 15501–15511, 2011.

[38] M. M. Conde, C. Vega, and A. Patrykiejew, "The thickness of a liquid layer on the free surface of ice as obtained from computer simulation," *J. Chem. Phys.*, vol. 129, no. 1, pp. –, 2008.

[39] C. L. Bishop, D. Pan, L. M. Liu, G. A. Tribello, A. Michaelides, E. G. Wang, and B. Slater, "On thin ice: surface order and disorder during pre-melting," *Faraday Discuss.*, vol. 141, pp. 277–292, 2009.

[40] D. Pan, L.-M. Liu, B. Slater, A. Michaelides, and E. Wang, "Melting the ice: On the relation between temerature and size for nanoscale ice crystals," *ACS nano*, vol. 5, pp. 4562–4569, 2011.

[41] D. T. Limmer and D. Chandler, "Premelting, fluctuations, and coarse-graining of water-ice interfaces," *J. Chem. Phys.*, vol. 141, p. 18C505, 2014.

[42] W. Lechner and C. Dellago, "Accurate determination of crystal structures based on averaged local bond order parameters," *J. Chem. Phys.*, vol. 129, no. 11, p. 114707, 2008.

[43] E. Sanz, C. Vega, J. R. Espinosa, R. Caballero-Bernal, J. L. F. Abascal, and C. Valeriani, "Homogeneous ice nucleation at moderate supercooling from molecular simulation," *J. Am. Chem. Soc.*, vol. 135, no. 40, pp. 15008–15017, 2013. PMID: 24010583.

[44] J. Benet, L. G. MacDowell, and E. Sanz, "A study of the ice-water interface using the tip4p/2005 water model," *Phys. Chem. Chem. Phys.*, vol. 16, pp. 22159–22166, 2014.

[45] S. A. Safran, *Statistical Thermodynamics of Surfaces, Interfaces and Membranes.* Reading: Addison-Wesley, first ed., 1994.

[46] J. J. Hoyt, M. Asta, and A. Karma, "Method for computing the anisotropy of the solid-liquid interfacial free energy," *Phys. Rev. Lett.*, vol. 86, pp. 5530–5533, Jun 2001.

[47] R. L. Davidchack, J. R. Morris, and B. B. Laird, "The anisotropic hard-sphere crystal-melt interfacial free energy from fluctuations," *J. Chem. Phys.*, vol. 125, no. 9, p. 094710, 2006.

[48] A. Härtel, M. Oettel, R. E. Rozas, S. U. Egelhaaf, J. Horbach, and H. Löwen, "Tension and stiffness of the hard sphere crystal-fluid interface," *Phys. Rev. Lett.*, vol. 108, p. 226101, May 2012.

[49] M. Müller and M. Schick, "Structure and nucleation of pores in polymeric bilayers: A Monte Carlo simulation," *J. Chem. Phys.*, vol. 105, pp. 8282–8292, 1996.

[50] E. Chacon and P. Tarazona, "Characterization of the intrinsic density profiles for liquid surfaces," *J. Phys.: Condens. Matter*, vol. 17, pp. S3493–S3498, 2005.

[51] D. Nelson, T. Piran, and S. Weinberg, *Statistical Mechanics of Membranes and Surfaces.* Word Scientific, Singapore, 2004.

[52] S. Dietrich, "Wetting phenomena," in *Phase Transitions and Critical Phenomena* (C. Domb and J. L. Lebowitz, eds.), vol. 12, pp. 1–89, New York: Academic, 1988.

[53] M. Maruyama, "Roughening transition of prism faces of ice crystals grown from melt under pressure," *J. Cryst. Growth*, vol. 275, no. 3-4, pp. 598–605, 2005.

[54] H. Asakawa, G. Sazaki, K. Nagashima, S. Nakatsubo, and Y. Furukawa, "Prism and other high-index faces of ice crystals exhibit two types of quasi-liquid layers," *Crystal Growth & Design*, vol. 15, no. 7, pp. 3339–3344, 2015.

Chapter 3

Surface phase transitions and the growth habits of snow crystals in the atmosphere

Pablo Llombart[1,2], *Eva G. Noya*[1] *and Luis G. MacDowell*[2]

(1) Instituto de Química Física Rocasolano, CSIC, Calle Serrano 119, 28006 Madrid, Spain

(2) Departamento de Química Física, Facultad de Ciencias Químicas, Universidad Complutense de Madrid, 28040 Madrid, Spain

Abstract

With climate modeling predicting a raise of at least 2 degrees by year 2100 [1], the fate of ice has become a serious concern.[2] Amazingly, despite ice ubiquity both in large masses on the poles and as tiny crystals in the atmosphere, we do not understand how ice actually grows (or melts).[3] The growth forms of snow crystals in the atmosphere described in the Nakaya diagram provide us with a stringent test for our understanding [4, 5, 6]. At low vapor saturation, ice crystallites are found as simple hexagonal prisms, but their shape changes from plates, to columns to plates and yet back to columns as temperature is cooled down below 0 C.[7, 8] Experiments have allowed to correlate empirically these shape transitions with a crossover of crystal growth rates,[9, 10, 11, 12] and phenomenological models allow to predict crystal shapes with great detail.[13, 14, 15] However, the physics behind this change in growth rates, and its relation with the underlying equilibrium surface structure remains completely unknown.[7, 16] Here we show that in the range from -80 to 0 C, the main facets of snow crystals undergo a sequence of alternating structural surface phase transitions that result in the anomalous increase of step free energies and the crossover of crystal growth rates exactly as required to explain the Nakaya diagram (Fig.3.1). As first postulated by Kuroda and Lacmann on purely speculative grounds,[17] our study highlights the significance of conjectured surface phase transitions and ice's premelting film.[18] However, unexpectedly, we observe the occurrence of a succession of premelting induced preroughening and smoothening transitions that we identify on an atomic model for the first time.[19] Our results reveal the significance of the largely unknown disordered flat phase discussed in simple SOS models as a key to the understanding of growth and sublimation of snow.[20] We expect that the proper characterization of a new surface phase on ice will prove essential for the understanding of ice growth in the atmosphere, ice sublimation in planetology and ice melting on earth.

Initial efforts, mainly aimed at the determination of ice's premelting film thickness have now shifted their emphasis on the crucial role of the heterogeneous in plane structure.[21, 22] However, the identification

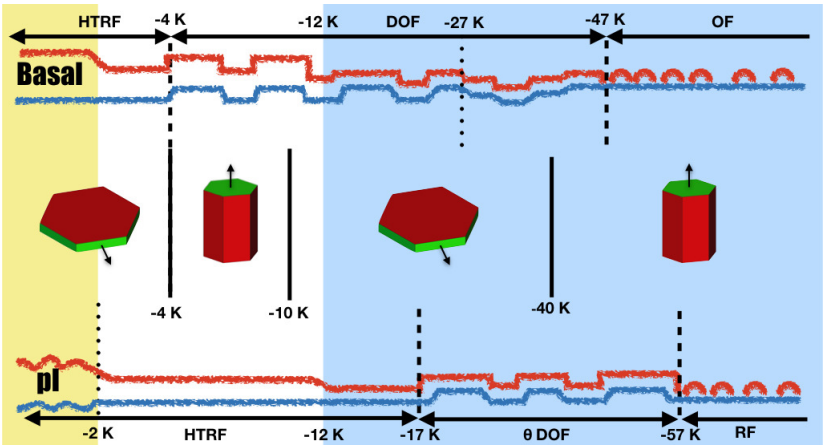

Figure 3.1. Growth of ice crystals at low supersaturation. Middle panel: As temperature decreases, the habit of hexagonal ice prisms grown in the atmosphere change sharply from plate like to columnar at ca. -4 C, from columnar to plate like at -10 C and somewhat less sharply from platelike to columnar at -40 C.[7, 8] The facet which grows faster as indicated by the arrows, dictates the prevalence of plates or columns. The change of crystal habits result from a crossover in the growth rates of the basal (red) and prismatic (green) facets. Top and bottom: Sketch of surface structural evolution with temperature as found in our work. Blue lines represent the i/f surface, and red lines represent the f/v surface. The basal surface (top row) is a High Temperature Reconstructed Flat phase from $\Delta T = 0$ to -4 K. It becomes a Disordered Flat Phase in the range between ca. -4 K to -47 K and is transformed into an Ordered Flat phase at lower temperatures. In this phase, surface disorder resulting form patches of liquid-like molecules remains. The prismatic surface (bottom row) is a High Temperature Reconstructed Flat phase all the way from 0 K to -17 C, but is very close to the roughening transition at $\Delta T > -2$ K in our model. In the range from -17 K to -57 K it is a Disordered Flat Phase and becomes an Ordered Flat phase below -57 K. At the transition from DOF like to HT-RF phases, step free energies increase anomalously and result in the crossover of crystal growth rates. The shaded areas illustrate the temperature range where melting of full bilayers has been accomplished. Blue, less than one full bilayer; white, less than two full bilayers; yellow, more than two full bilayers.

of possible surface phase transitions, and their conjectured relation with crystal growth rates is far from established.[16] In our recent computer simulation studies, we have emphasized the need to describe the ice/vapor interface in terms of two different fluctuating surfaces, separating the quasi-liquid film from the bulk solid and vapor phases, respectively.[23, 24, 25, 16] Averaging the position of the outermost solid and liquid-like atoms of the premelting layer, we are able to identify distinct ice/film, $z_{\rm if}(\mathbf{r})$ and film/vapor $z_{\rm fv}(\mathbf{r})$ surfaces, which separate the premelting film from the bulk solid and vapor, respectively (see Methods and Extended Data Fig.3.5). This allows us to characterize the structure of the ice surface and to reveal the interplay between perpendicular and horizontal correlations with a detail that is not achievable by present day experimental techniques.

In our study, we perform large scale computer simulations of the TIP4P/ice point charge model of water,[26] on elongated rectangular surfaces meant to characterize large wave-length correlations along one direction. A bulk ice sample is placed in vacuum at temperatures below the model's triple point, $T_t = 272$ K. After a few nanoseconds, the surface spontaneously develops a layer of quasi-liquid disordered molecules that can be readily distinguished from the underlying bulk crystal network (Fig.3.2-b, Extended Data Fig.3.7). The average thickness of this layer grows from about 3 Åat $\Delta T = T - T_t = -82$ K to

9 Åat $\Delta T = -2$ K with little measurable anisotropy (Exteded Data Fig. 3.6).[27] However, as recently observed for the basal plane in the mW model,[21, 22] this thin disordered layer is laterally inhomogeneous up to about $\Delta T = -9$ K. Our study reveals that the heterogeneity is also found, to a similar extent on the prismatic plane, with little qualitative differences (Fig. 3.3-b and Extended Data Fig.3.8).

We quantify the surface fluctuations along the long direction, x, by studying deviations of the local surface position, $\delta z_\alpha(x)$, about the average surface, $\delta z_\alpha(x) = z_\alpha(x) - \overline{z}_\alpha$. This analysis is essential to reveal differences between basal and prismatic planes and allows us to identify a number of phase transitions along the sublimation line which cannot possibly be inferred from visual inspection of the snapshots (Fig 3.2-a, 3.3-a and Extended Data Fig.3.9, Fig.3.10).

At low temperature ($\Delta T = -82$ K), the basal plane consists of a relatively ordered flat solid surface (OF), as revealed by a singly peaked, close to Gaussian distribution of both i/f and f/v surface fluctuations (Fig.3.2-a and Extended Data Fig.3.9-a). From the snapshots (Fig.3.2-b), the solid surface is formed mainly of an oxygen-unreconstructed stack of chair hexagons.[28, 29, 30] Patches of disordered liquid-like molecules are found, and often show a tendency to sit on interstitial positions at the center of the primary hexagonal mesh (as in the so called Honeycomb Fletcher phase).[28] The distribution remains uni-modal up to $\Delta T = -52$ K, but somewhat broadens, revealing a large increase of disorder in this temperature interval which is consistent with observations of Sum Frequency Generation Spectroscopy.[31, 32] At $\Delta T = -42$ K, however, the distribution of δz_{fv} developes a distinct trimodal character, which is also observable on the δz_{if} distribution at higher resolutions (Extended Data Fig.3.9-b), but has been washed out upon lateral averaging along the y direction. A main peak is centered at the mean surface position, and two other peaks appear to the left and right, likely as a result of large binding energy heterogeneities of ice molecules in the first two bilayers.[33] The central peak of the trimodal distribution for δz_{fv} gradually fades away into a bimodal, which persists up to $\Delta T = -6$ K. In a narrow range between -9 K to -6 K, the distributions of δz_{fv} and δz_{if} are both fully bimodal and congruent. Finally, at the temperature of -2 K, the bimodal collapses sharply into one single uni-modal distribution.

From our analysis, the outer f/v surface of the premelting film exhibits a bimodal distribution centered at the mean surface location all the way from -22 K to -6 K. The onset of bimodality very much correlates with the vanishing of the (pp-polarized) dangling OH bond stretch observed in SFG experiments.[31] The separation between peaks in the bimodal is approximately 3.1 Å, somewhat smaller that the expected bilayer distance of $c/2 = 3.65$ Å. Furthermore, the bimodal evolves after the appearance at low temperature of a trimodal distribution with a main peak centered at the mean surface position, as if ice melting resulted in the formation of water-like molecules at half integer lattice positions (Extended Data Fig.3.9-a,b).

A strongly disordered phase consisting of a smooth surface with large scale step proliferation has been documented in the literature for Solid on Solid models (SOS) and is known as a disordered flat phase (DOF).[20] Exactly as sugested by the extended SOS model, we observe that the low temperature smooth flat phase transforms into a locally rough interface at a preroughening transition, T_{pr}.[20] However, contrary to the usual scenario, at high temperature the DOF phase does not undergo roughening, but rather, transforms across an apparently first order surface phase transition into a new flat phase at a *smoothening temperature*, T_s. This transition has not been previously reported but is consistent with existing surface phase diagrams for the SOS model.[34, 35, 36] Following the notation of SOS literature, we call this a High Temperature Reconstructed Flat phase (HT-RF).

As expected for the preroughening scenario, the transition to a DOF phase is strongly correlated with the growth of a premelting film in a loosely layer wise fashion.[37, 36, 19] Clearly, we observe that the stabilization of the bimodal DOF phase at $\Delta T = -22$ K results after the full formation of a second layer of premelted ice, as revealed by the mean location of premelting layer fluctuations in Fig.3.2-d (Extended Data 3.9-c). The transition from DOF into the HT-RF phase is also accompanied by the formation of a

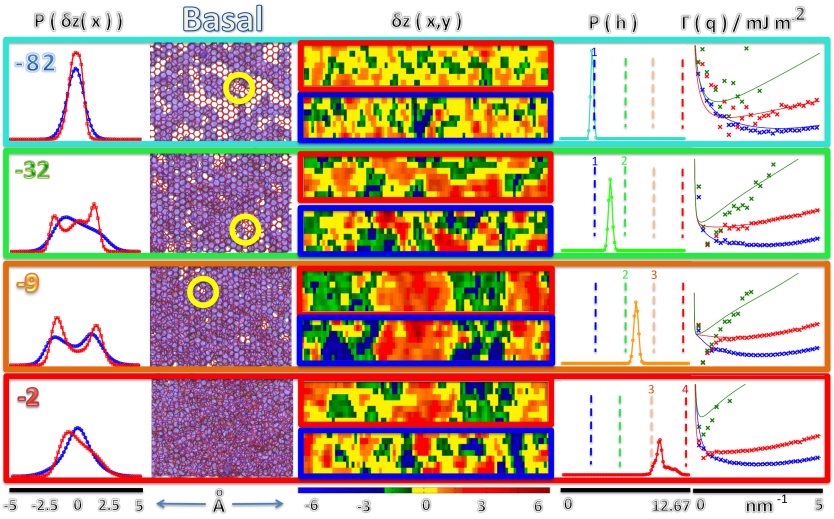

Figure 3.2. Surface fluctuations on the basal facet. a) Probability distribution of i/f (blue) and f/v (red) surface fluctuations, as measured by the deviations of the interface position along x about the average surface. Results are shown for different temperatures as shown in the legend (See S2a). b) Snapshots of the basal surface at the same four temperatures. Red lines show the connected hydrogen bond network of all solid-like and liquid-like water molecules. The violet patches represent disordered liquid-like molecules. At low temperature the surface is mainly a regular hexagonal honeycomb, with a few patches of liquid-like molecules siting on interstitial positions (as indicated by the yellow circles). The extent of filled interstitial positions increases as the premelting layer extends on the surface. c) Plot showing a snapshot of local surface height fluctuations $\delta z_{\mathrm{if}}(\mathbf{r})$ (bottom, blue frame) and $\delta z_{\mathrm{fv}}(\mathbf{r})$ (top, red frame) on the basal ice face. Notice the emergence of large scale correlated patches for the DOF phase in the temperature range $\Delta T = -32$ to -9 K). See movie M1 in Extended data section. The patches disappear at high temperature as the surface flattens again. d) Distribution of average film thickness, h, as temperature increases. Dashed vertical lines represent full layers in units of the molecular diameter. d) Wave-vector dependent stiffness coefficients, as obtained from the inverse surface structure factor for i/f correlations (blue), f/v correlations (red) and crossed i/f -f/v correlations (green). Crosses are results from simulation, full lines are fit to the SG+CW model. The results show that all surfaces are smooth, as indicated by the $q \to 0$ divergence of $\Gamma(q_x)$. Notice the sharp minimum appearing at intermediate length scales in the temperature range $\Delta T = -32$ K to -9 K where the DOF phase is present.

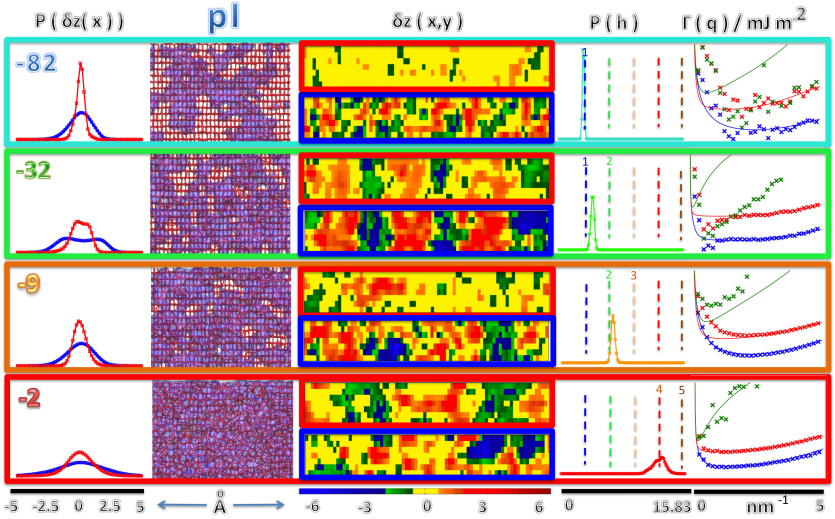

Figure 3.3. Surface fluctuations on the prismatic facet. Content displayed as in Fig.3.2. a) A bimodal distribution in this facet is only visible at temperature $\Delta T = -32$ K. b) Here the snapshots show the characteristic rectangular mesh of the prismatic facet. At low temperature the liquid-like molecules form patches on the solid surface as in the basal face. c) Emergence of large correlated domains signal a DOF phase that is clearly visible at $\Delta T = -32$ K that vanishes at significantly lower temperatures than for the basal facet. d) Notice the transition of premelting layer thickness across integer multiples of the molecular diameter occurs for the prismatic facet at the same temperature as for the basal facet. e) Likewise, the sharp minimum of the stiffness coefficient is visible only at and below $\Delta T = -32$ K.

full third premelted layer, as revealed by the shift in the premelting layer thickness from $\Delta T = -9$ to -2 K (Fig.3.2-d).

The DOF phase is not only characterized by step proliferation and strong local disorder. Also, the steps are highly correlated, and depending on the nature of the DOF phase, can exhibit diverging (finite) parallel correlations at a second (first) order preroughening transition.[34, 35, 36] We explore this with a plot of the local surface height $\delta z_{\rm if}(\mathbf{r})$ fluctuations (Fig.3.2-c), Extended Data Fig. 3.11-a). At low temperature, the i/f surface exhibits small amplitude up and down domains, with small correlation lengths. At $\Delta T = -9$ K, were the DOF phase is fully formed, we observe very large up and down domains of about 9 nm in length, that remain correlated over the full simulation box, as is visible both in the figure and in the accompannyng movie (Extended Data, movie M1-a). Our results are consistent with glancing angle x-ray experiments which reported the appearence of a large surface correlation length in the nanometer range, and the sharp dissaparence of the long range correlations close to the triple point.[23]

The nature of this correlations can be quantified from the wave-vector dependent surface structure factor. Plots of the related effective stiffness, $\Gamma_{\alpha\beta}(q_x) = \frac{k_B T}{A\langle z_\alpha(q_x) z_\beta(q_x)}$ are shown in Fig.3.2-e (Extended Data Fig. 3.9-d). The results confirm that both at the preroughening and at the smoothening transition, the parallel correlations remain finite at $q_x \to 0$, as can be inferred from the strong divergence of the effective stiffness coefficients. Everywhere in the region were a DOF phase is present, however, the strongly correlated up and down domains are detectable as a sharp and deep minimum of the stiffness coefficients. A full theoretical description of this strong enhancement of large but finite correlations seems difficult. However, we can definitively observe in our results how the location of the sharp minima at intermediate wave-vectors decreases as the size of the correlated domains in Fig.3.2-c increase (Extended Data, Fig 3.11-a).

The study of surface fluctuations on the prismatic facet is signficantly different (Fig.3.3). A low temperature flat phase, which preserves the expected low temperature rectangular mesh is observed at $\Delta T = -82$ K. At this temperature, the distribution of both $z_{\rm if}(x)$ and $z_{\rm fv}(x)$ are unimodal (with much more complex structure revealed on the finer grained distributions with resolution over $\mathbf{r}$, see Extended Data Fig.3.10-b), but become gradually broader and skewed to the left as temperature is increased (Fig.3.3-a). At $\Delta T = -32$ K, the distribution becomes symmetric and exhibits two very small shoulders before skewing to the right. From $\Delta T = -12$ K to $\Delta T = -2$ K, the distribution becomes again completely unimodal and Gaussian like, but has broadened abruptly at $\Delta T = -2$ K, signaling the approach of a roughening transition.[38] Although the order parameter is not sharp enough to reveal a strong bimodality, there appear a large proliferation of steps in the range between -62 K to -22 K with distributions that seem to resemble a θDOF phase (similar to the DOF phase, but with a continuous change of the step coverage.[39]) The transition from a DOF phase to a new high temperature reconstructed flat phase (HT-RF) is visible in the surface maps (Fig 3.3-c), where large scale domains appear to end at -32 K. This is also visible in the surface structure factors depicted in Fig.3.3-e, which reveal again diverging stiffness coefficients at $q_x \to 0$ (whence, flat phase), and the complete dissapearence of the sharp minimum beyond this temperature (whence, loss of long range surface order). The transformation of the surface structure across the θDOF phase is also accompanied with continuous increase of the premelting film (Fig.3.3-d), but the transition from two to three layers and beyond appear to occur almost at the same temperature as in the basal facet. On the contrary, the transition from the θDOF phase to the HT-RF phases is distinctly different at the basal (ca. $T_s = -4$ K) and the prismatic (ca. $T_s = -27$ K) facets. Interestingly, these two temperatures, together with the full completion of a second bilayer at $T_l = -12$ C are in very close agreement with the crystal habit changes observed in the Nakaya diagram.

We find that on average, both for the basal and the prismatic facets, $z_{\rm fv}(\mathbf{r})$ follows broadly the corrugation imposed by the $z_{\rm if}(\mathbf{r})$, and the fluctuations of premelted film thickness appear as a broad

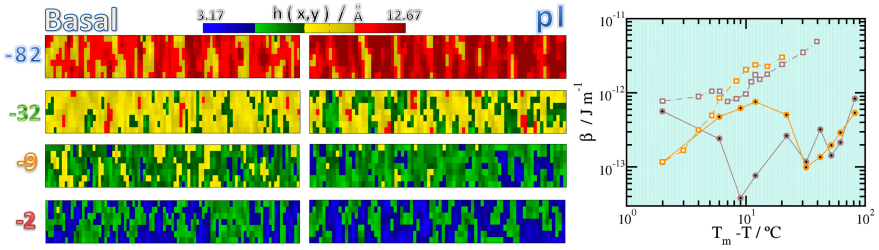

Figure 3.4. Fluctuations of premelting thickness and step free energies Figures a) and b) show a surface of instantaneous premelting thickness, $h(\mathbf{r})$ for basal (a) and prismatic (b) surfaces. Temperatures are indicated. Notice the absence of large correlated domains at all temperatures, in marked contrast with the $\delta z_{\rm if}(\mathbf{r})$ and $\delta z_{\rm fv}(\mathbf{r})$ surfaces shown in Fig.3.2 and Fig.3.3. c) Step free energies as obtained from a fit of the mean field SG+CW model to the regular (Gaussian) part of the stiffness coefficients in Fig.3.2-e,3.3-e. Results are compared to experimental data (empty symbols with dashed lines).[11] The step free energies from the fit (filled symbols and full lines) exhibit a crossover at ca. -5 K, a minimum for the basal (marroon) facet at ca. -9 K and the maximum for the prismatic (orange) facet at ca. -10 K, very much as the experimental data.

unimodal distribution, with no sign of bimodality or diverging correlation lengths (Fig.3.2-d and Fig.3.3-d). Accordingly, there are apparently no layering transitions along the sublimation line, at least in the thermodynamic sense. This is very clearly observed in the surface plot of of film thickness fluctuations (see movies M1-c and M2-c) and is consistent with SFG experiments and preliminary indications for the mW model (Extended Data Fig.3.11-c and 3.12-c).[40, 22]

The significance of DOF phases has been well documented.[20, 41, 42, 36, 19] The step proliferation is akin to a strong reduction of the step free energy, and the sharp decrease of the threshold for linear growth.[41, 42] It is therefore expected that, as temperature raises across the smoothening transition from a DOF to a HT-RF phase, the crystal growth rates will decrease anomalously.

We provide a quantitative test of this expectation using a model of coupled capillary wave and sine Gordon Hamiltonians discussed recently (SG-CW).[24, 25] The capillary wave Hamiltonian describes the f/v surface fluctuations, while the likelihood of step proliferation in the underlying i/f surface is described with a sine Gordon Hamiltonian. Both models are coupled with an interface potential that sets the equilibrium film thickness as the difference between $z_{\rm fv}(\mathbf{r})$ and $z_{\rm if}(\mathbf{r})$. The model can be fit to the regular (Gaussian) part of the surface stiffness, (Fig.3.2-e,3.3-e) and provides phenomenological coefficients for the surface tension and the step free energy, β. The non-monotonous behavior observed for β resembles the behavior measured experimentally for terrace spreading rates [10, 12], and is qualitatively very similar to step free energies obtained from growth measurements on snow crystals (Fig 3.4).[11] Most importantly, our results confirm the suggested scenario of anomalous increase of β exactly at the smoothening transitions of basal and prismatic facets, respectively.

In summary, we identify a series of sequential surface phase transitions on the surface of ice, including, most notably, a newly reported smoothening transition which leads to the anomalous increase of step free energies. Our results provide an explanation for the observed crystal habit crossover of snowflakes (Fig.3.1) and pave the way for a first principles description of ice crystal growth and sublimation rates in the atmosphere.

Methods

Force field

Our study is performed with the TIP4P/Ice model of water [26]. This model was purposely designed to best describe the properties of ice. It predicts a melting point of T=272 K, in excellent agreement with experiment, and reproduces the most relevant surface properties at this temperature, such as liquid-vapor surface tension (γ_{lv} = 82 mN/m calculated by ourselves, compared with γ_{lv} = 75.7 mN/m from experiment),), and solid-liquid surface tension (γ_{sl} = 29.8 mN/m from Ref.[43] compared with recommended results γ_{sl} = 28 mN/m by Pruppacher and Klett [44]). The precise location of the surface phase transitions observed here could somewhat change with the molecular model employed, but we expect the generic features to be quite generally observed for other accurate intermolecular potentials.

Initial configurations

Initial configurations are prepared from a perfect unit cell in pseudoorthorombic arrangement, consisting of two layers of hexagonal rings perpendicular to the hexagonal **c** axis and a total of 16 water molecules. For the basal interface, we arrange a stack of $46 \times 8 \times 8$ cells of 47,104 molecules, with the long direction, x, aligned along the **b** axis of the pseudoorthorombic cell, corresponding to the so called (basal)[pII] surface arrangement described by Davidchack and used in our previous work.[45, 46, 47, 24, 25, 48]

For the pI interface, the simulation box is prepared from a stack of $40 \times 8 \times 8$ unit cells of N=40,960 molecules, with the long direction, x, aligned along the **a** axis. This corresponds to the (basal)[pII] arrangement in our recent work. For each such arrangement, we prepare an independent hydrogen bond network as described in [49]. After forming the ice slab, we perform NpT simulations of the bulk solid at the desired temperature in order to obtain equilibrated unit cell dimensions. The solid is then scaled to the average equilibrium cell value, placed in vacuum, and equilibrated again in the NVT ensemble under periodic boundary conditions.

Computation details

Large scale simulations are carried out on the Mare Nostrum IV facility at Barcelona Supercomputing center from the Spanish National Supercomputing Network. Classical Molecular Dynamics simulations are performed with the GROMACS package.[50, 51] Trajectories are evolved with the velocity-verlet algorithm. Both the Lennard-Jones and Coulomb interactions are truncated at 0.9 nm. The electrostatic interactions are calculated using the Particle Mesh Ewald method. Simulations are thermostated with the velocity rescale algorithm,[52] and the Berendsen barostat when required.[53] A relaxation time of 2 ps is used for both the thermostat and barostat. The timestep employed is 0.003 ps. The simulations proceed over 0.9 μs, with a long equilibration time of 225 ns and 675 ns for the production stage.

Surface analysis

Prior to determining the i/f and f/v surfaces, we label water molecules as either solid or liquid-like, using the $\bar{q}_6$ parameter.[54] Water like molecules are those with a $\bar{q}_6$ parameter below a threshold $\bar{q}_6^*(T)$. In order to determine the threshold, we simulate the probability distribution of $\bar{q}_6$ at a number of temperatures in either bulk solid or liquid water. The threshold value $\bar{q}_6^*(T)$ is determined such that the number of mislabeled liquid molecules on the solid phase is equal to the number of mislabeled solid molecules on the

liquid phase. A cluster analysis is performed to determine which molecules pertain to the condensed phase. Water molecules with oxygen atoms at a distance less than 3.5 Å belong to the same cluster. The i/f surface is determined from the positions of solid-like atoms in the largest solid cluster. We use the heights of of the four topmost (or bottommost) solid atoms of the upper (lower) interface. At a given point $\mathbf{r}$ on the plane of the interface, we find all the solid like atoms lying within a rectangular prism centered at $\mathbf{r}$. The base of the prism is taken to be that of the pseudoorthorombic unit cell of corresponding orientation. The surface height $z_{\rm if}(\mathbf{r})$ at that point is determined from the average location of the four uppermost solid like atoms. At the same point, the liquid surface for the upper (lower) interface is determined by averaging the position of the uppermost (bottom-most) for liquid-like molecules of the cluster of condensed molecules lying within a rectangular area of $3\sigma \times 3\sigma$ Lennard-Jones molecular diameters. The surfaces $z_{\rm if}(\mathbf{r})$ and $z_{\rm fv}(\mathbf{r})$ are determined over points on a grid on the plane of the interface. The grid has twice as many points as unit cells along the x direction, and just as many points as unit cells along the y direction. We perform the surface analysis from the set $\{z_{\rm if}(\mathbf{r})\}$ and $\{z_{\rm fv}(\mathbf{r})\}$ of points on the grid.[24] The instantaneous average position of the i/f surface, $\overline{z_{\rm if}}$ is determined as the lateral average of $\{z_{\rm if}(\mathbf{r})\}$ over all points on the grid. From this value, we obtain $\delta z_{\rm if}(\mathbf{r}) = z_{\rm if}(\mathbf{r}) - \overline{z_{\rm if}}$. The laterally averaged fluctuations $\delta z_{\rm if}(x)$ are obtained from $\delta z_{\rm if}(\mathbf{r})$ upon averaging along points y. $\delta z_{\rm fv}(\mathbf{r})$ and $\delta z_{\rm fv}(x)$ are obtained likewise. Fourier transforms of $\delta z_{\rm if}(x)$ and $\delta z_{\rm fv}(x)$ are obtained by summing $\delta z_\alpha(x) e^{-iq_x x}$ over all points along x. Instantaneous local film heights are obtained as $h(\mathbf{r}) = z_{\rm if}(\mathbf{r}) - z_{\rm fv}(\mathbf{r})$. The instantaneous average film thickness is obtained from the mean of $h(\mathbf{r})$ over the points of the grid.

SG-CW model and fit

We describe the coupled i/f and f/v surface fluctuations with an extended Sine Gordon model for the i/f surface and the Capillary Wave model for the f/v surface.[38, 55] The two terms are coupled via the interface potential, $g(h)$, with the premelting film thickness given by $h(\mathbf{r}) = z_{\rm fv}(\mathbf{r}) - z_{\rm if}(\mathbf{r})$. The full Hamiltonian is given by:

$$H = \int d\mathbf{r} \left[\frac{\tilde{\gamma}_{iw}}{2} (\nabla z_{\rm if})^2 + \frac{\gamma_{wv}}{2} (\nabla z_{\rm fv})^2 + \gamma_{iv} \nabla z_{\rm if} \cdot \nabla z_{\rm fv} - u \cos(q_z z_{\rm if}) + g(z_{\rm fv} - z_{\rm if}) \right] \tag{3.1}$$

where $\tilde{\gamma}_{iw}$ is the bare stiffness coefficient, γ_{wv} is the water-vapor surface tension, γ_{iv} dictates the coupling of surface deformations, u accounts for the cost of moving the surface $z_{\rm if}$ away from integer lattice spacing, $g(h)$ is the interface potential dictating the equilibrium film thickness, and q_z is the wave-vector for a wavelength equal to the lattice spacing. This Hamiltonian can be expanded to quadratic order in deviations away from the mean surface positions $\overline{z_{\rm if}}$ and $\overline{z_{\rm fv}}$, and yields for the thermally averaged surface fluctuations:[24]

$$\begin{aligned}
\langle |z_{\rm if}^2(\mathbf{q})| \rangle &= \frac{k_B T}{A} \frac{g'' + \gamma_{wv} q^2}{[\upsilon + g'' + \tilde{\gamma}_{iw} q^2][g'' + \gamma_{wv} q^2] - [g'' + \Delta g'' - \gamma_{iv} q^2]^2} \\
\langle |z_{\rm fv}^2(\mathbf{q})| \rangle &= \frac{k_B T}{A} \frac{\upsilon + g'' + \tilde{\gamma}_{iw} q^2}{[\upsilon + g'' + \tilde{\gamma}_{iw} q^2][g'' + \gamma_{wv} q^2] - [g'' + \Delta g'' - \gamma_{iv} q^2]^2} \\
\langle z_{\rm if}(\mathbf{q}) z_{\rm fv}^*(\mathbf{q}) \rangle &= \frac{k_B T}{A} \frac{g'' + \Delta g'' - \gamma_{iv} q^2}{[\upsilon + g'' + \tilde{\gamma}_{iw} q^2][g'' + \gamma_{wv} q^2] - [g'' + \Delta g'' - \gamma_{iv} q^2]^2}
\end{aligned} \tag{3.2}$$

where g'' is the second derivative of the interface potential at the equilibrium film thickness, $\Delta g''$ accounts for enhanced coupled compression-expansion of the film thickness, and $\upsilon = q_z^2 u$. In practice, in order to avoid under-determined fits to limited data, we set $\Delta g''$ and γ_{iv} to zero. This model for the spectrum of surface fluctuations has small and large wave-vector regimes. At large wave-vectors, the spectrum of fluctuations depends only on the stiffness and surface tension coefficients, $\tilde{\gamma}_{iw}$ and γ_{wv} respectively.[25] As

in extended capillary wave Hamiltonians, these are modeled as even polynomials of q to order 4. Once $\tilde{\gamma}_{iw}$ and γ_{wv} are known, we fit the remaining parameters g'' and υ to match simultaneously the low wave-vector regime of $q^2\langle z_{\mathrm{if}}(q)z_{\mathrm{if}}(q)\rangle$, $q^2\langle z_{\mathrm{fv}}(q)z_{\mathrm{fv}}(q)\rangle$ and $q^2\langle z_{\mathrm{if}}(q)z_{\mathrm{fv}}(q)\rangle$ as obtained from simulations. The step free energy for the uncoupled Sine Gordon model can be obtained from the parameters $\tilde{\gamma}_{iw}$ and υ as $\beta = (8/q_z^2)(\gamma_{iw}\upsilon)^{1/2}$,[56] which we use as an estimate for the step free energy of the ice/vapor interface in Fig.3.4.

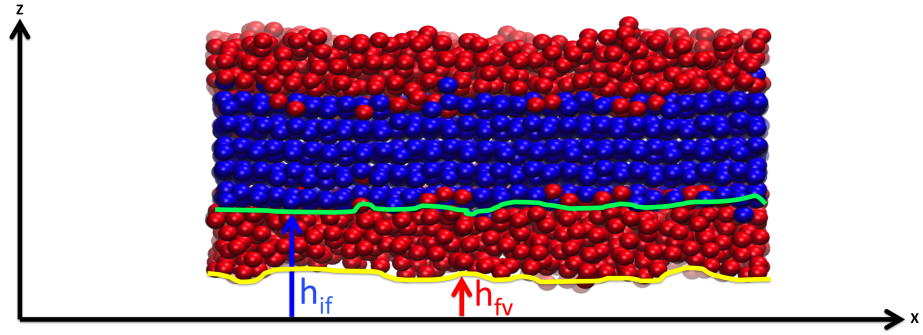

Figure 3.5. Extended Figure: Characterization of the premelting layer. Snapshot of a bulk ice slab in equilibrium with pure water vapor. After placing a slab of perfect ice in vacuum, a premelting layer of disordered water molecules is formed spontaneously in a few nanoseconds. Using a suitable order parameter it is possible to label liquid-like from solid-like molecules. The state of the premelting film may be described in terms of two different surfaces, z_{if} and z_{fv}, separating the film from bulk solid and vapor phases, respectively.

Extended Data

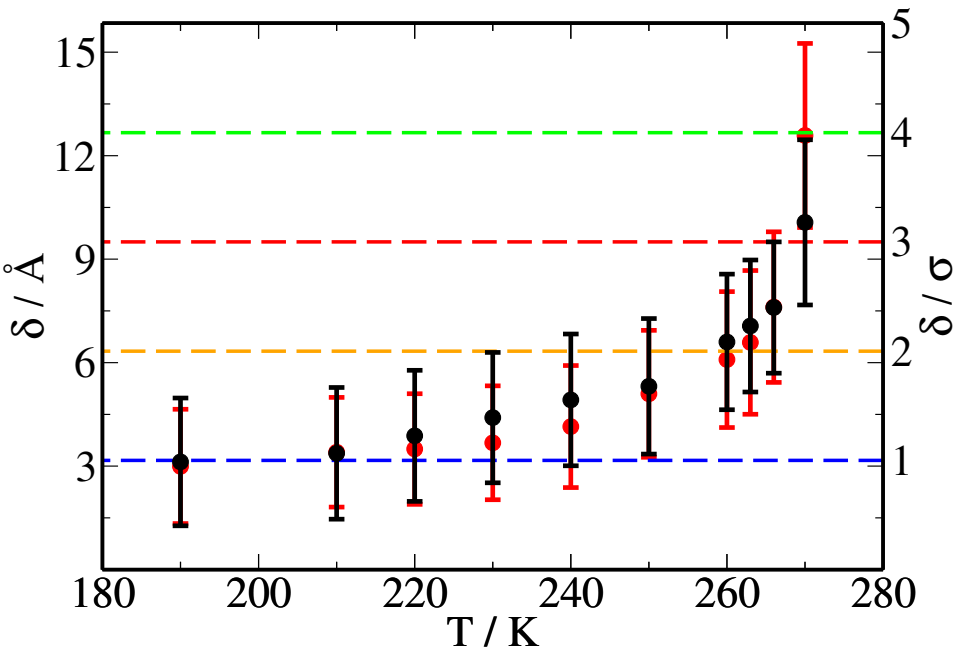

Figure 3.6. Extended Figure: Premelting film thickness as a function of temperature for basal and prismatic faces. Figure shows the thermally averaged film thickness h of the basal (black) and prismatic (red) planes. Dashed lines indicate multiples of the molecular diameter as measured in units of the Lennard-Jones σ parameter. The thickness of the prismatic plane remains only slightly below that of the basal plane up to 270 K, were the prismatic plane premelts by almost one full bilayer more

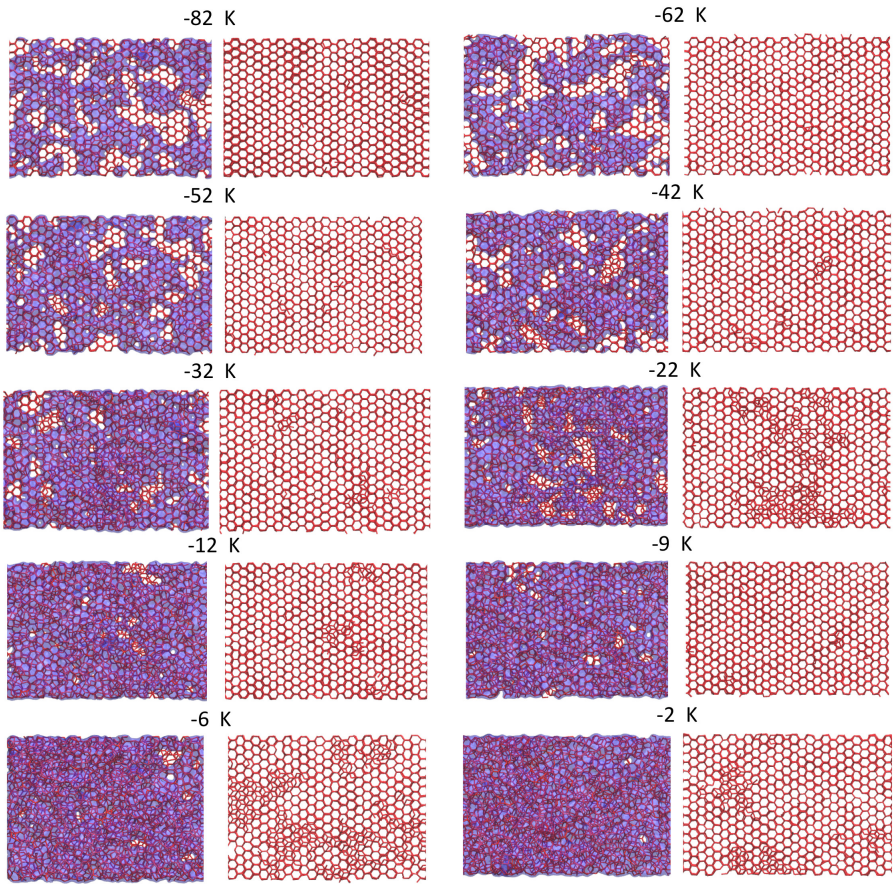

Figure 3.7. Extended Figure: Evolution of surface structure with temperature on the basal face. The first and third columns show the position of all atoms in the cluster of condensed molecules (solid-like or liquid-like), projected onto the x-y plane. The red wire-frame joins atoms separated by less than 3.5 Å, which is the cluster criteria. Liquid-like atoms are further further coloured in violet. The typical hexagonal honeycomb is clearly visible on patches not covered by premelted water-like molecules. Also notice how the premelted molecules often occupy interstitial positions on the center of the hexagonal honeycomb. The second and third columns show only the positions of solid-like atoms, with liquid-like atoms left apart. As far as the position of oxygen atoms, the surface remains unreconstructed in all the temperature domain. Patches of stacking disordered ice appear at temperatures $\Delta T = -22$ and -2 K consistent with the melting of complete solid bilayers.

Acknowledgements

We thank E. Lomba for helpful discussions and J. L. F. Abascal for invaluable support. We acknowledge funds from the Spanish Agencia Estatal de Investigación under Grant No. FIS2017-89361-C3-2-P. This project was made possible thanks to the use of the Mare-Nostrum supercomputer and the technical support provided by Barcelona Supercomputing Center from the Spanish Network of Supercomputing (RES) under grants QCM-2017-2-0008 and QCM-2017-3-0034.

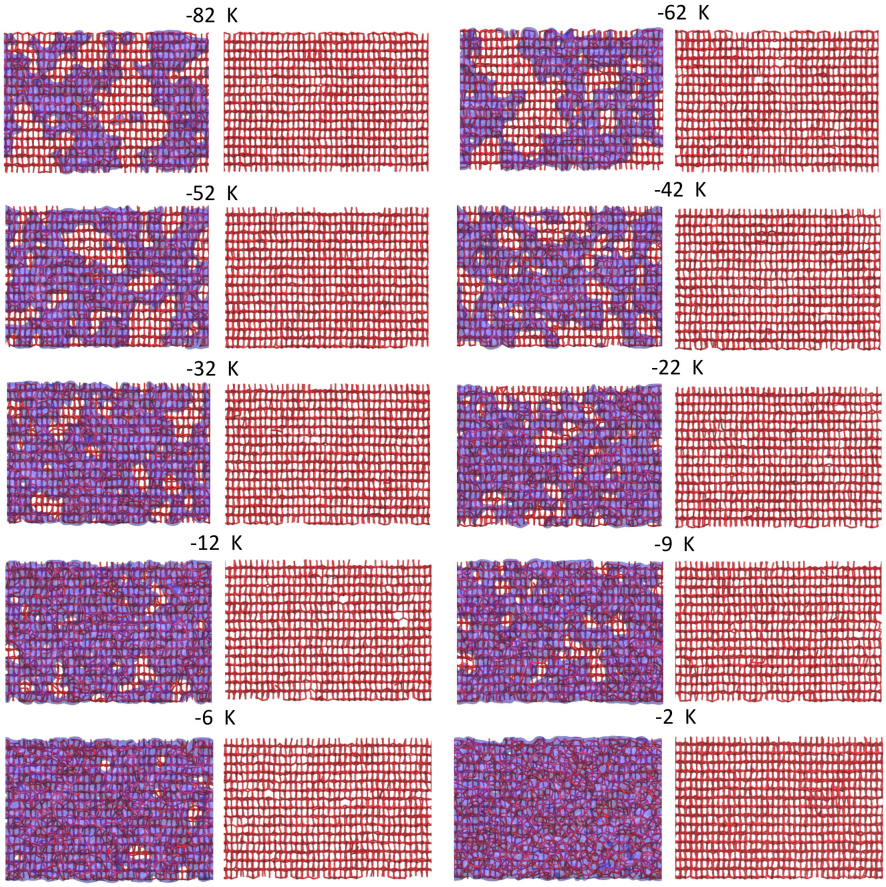

Figure 3.8. Extended Figure: Evolution of surface structure with temperature on the prismatic face. The first and third columns show the position of all atoms in the cluster of condensed molecules (solid-like or liquid-like) projected onto the x-y plane. The red wire-frame joins atoms separated by less than 3.5 Å, which is the cluster criteria. Liquid-like atoms are further coloured in violet. The typical rectangular structure of prismatic faces is clearly visible on patches not covered by premelted water-like molecules. The second and third columns show only the positions of solid-like atoms, with liquid-like atoms left apart. The oxygen framework remains unreconstructed in all the temperature domain.

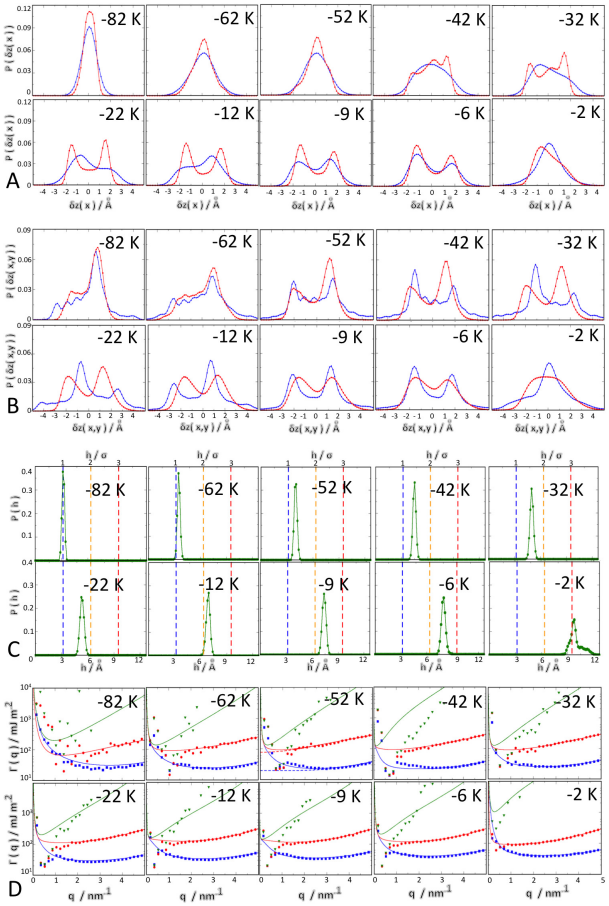

Figure 3.9. Extended Figure: Surface fluctuations on the basal face at all studied temperatures. a) Probability distribution of i/f (blue) and f/v (red) surface fluctuations, as measured by the deviations of the interface position along x about the average surface. b) Same as in a), for the probability distribution of the local height fluctuations $\delta z(\mathbf{r})$. c) Probability distribution of the global premelting layer thickness, h, on the basal face for several temperatures as indicated in the color code. The vertical dashed lines indicate the location of multiples of the layer thickness in units of the molecular diameter (σ parameter of the Lennard-Jones bead in the TIP4P/icemodel). d) Spectrum of fluctuations on the basal face. The figure shows Wave-vector dependent stiffness coefficients, as obtained from the inverse surface structure factor for i/f correlations (blue), f/v correlations (red) and crossed i/f -f/v correlations (green). Symbols are results from simulations. The full lines are a fit to the small wave-vector results to the SG+CW model, using as input results from the large wave-vector fit shown in dashed lines.

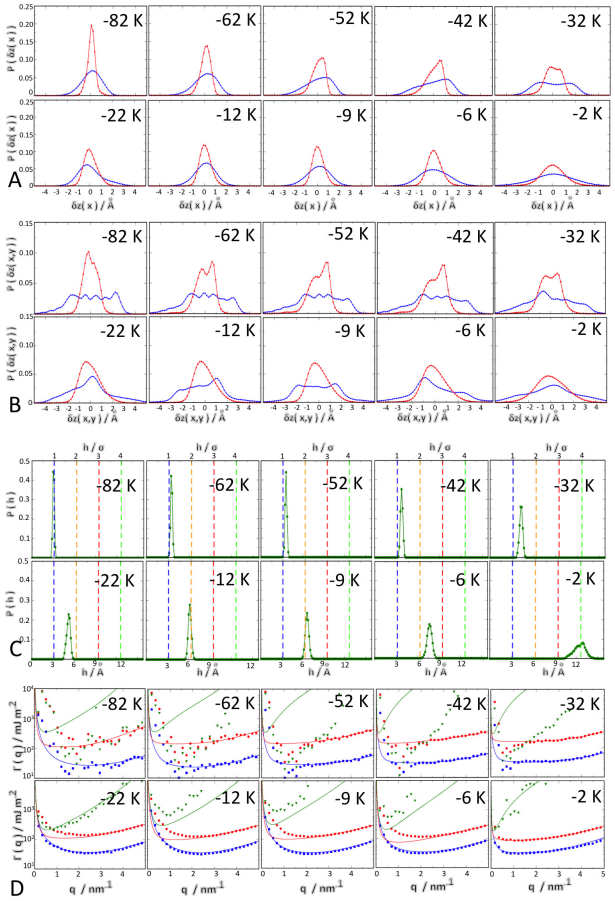

Figure 3.10. Extended Figure: Surface fluctuations on the prismatic face at all studied temperatures. a) Probability distribution of i/f (blue) and f/v (red) surface fluctuations, as measured by the deviations of the interface position along x about the average surface. b) Same as in a), for the probability distribution of the local height fluctuations $\delta z(\mathbf{r})$. c) Probability distribution of the global premelting layer thickness, h, on the basal face for several temperatures as indicated in the color code. The vertical dashed lines indicate the location of multiples of the layer thickness in units of the molecular diameter (σ parameter of the Lennard-Jones bead in the TIP4P/icemodel). d) Spectrum of fluctuations on the basal face. The figure shows Wave-vector dependent stiffness coefficients, as obtained from the inverse surface structure factor for i/f correlations (blue), f/v correlations (red) and crossed i/f -f/v correlations (green). Symbols are results from simulations. The full lines are a fit to the small wave-vector results to the SG+CW model, using as input results from the large wave-vector fit shown in dashed lines.

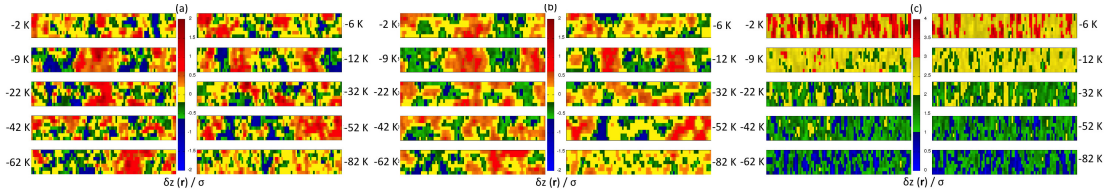

Figure 3.11. Extended Figure: Surface plots of local height fluctuations for the basal face. a) Local height fluctuations $\delta z_{\mathrm{if}}(\mathbf{r})$ of the i/f surface. b) Local height fluctuations $\delta z_{\mathrm{fv}}(\mathbf{r})$ of the f/v surface. At low and high temperatures, the correlation lengths are small and one finds alternated red and blue patches of small size. At intermediate temperatures there appear large red and blue patches indicative of the emergence of large correlations of preferred wave-length. In this regime, comparison of a) and b) shows that the i/f and f/v surfaces are also highly correlated. c) Local fluctuations of film thickness $h(\mathbf{r})$. The correlation length of $\delta h(\mathbf{r})$ remains small at all temperatures as is visible from the small size of alternating patches. The thickening of the films as temperature increases is apparent from the change in color code.

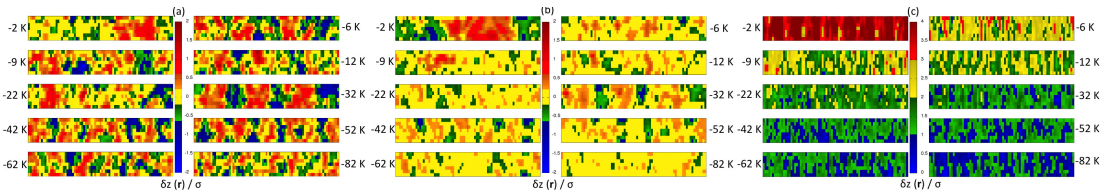

Figure 3.12. Extended Figure: for the prismatic face. a) Local height fluctuations $\delta z_{\mathrm{if}}(\mathbf{r})$ of the i/f surface. At low temperatures the alternation of small blue and red domains is indicative of small correlation lengths. The size of the domains increases significantly at a DOF phase at T=240 K and then decrease again. At the highest temperature, T=270 K, a large correlated domain that spans most of the simulation cell is indicative of the approach to a roughening transition. b) Local height fluctuations $\delta z_{\mathrm{fv}}(\mathbf{r})$ of the f/v surface. The temperature evolution of correlation lenths is similar to that of the i/f , but compared to the basal surface, the amplitude of the fluctuations here is much smaller. c) Local fluctuations of film thickness $h(\mathbf{r})$. As for the basal face, the correlation length of $\delta h(\mathbf{r})$ remains small at all temperatures as is visible from the small size of alternating patches. The thickening of the films as temperature increases is apparent from the change in color code.

Bibliography

[1] A. E. Raftery, A. Zimmer, D. M. W. Frierson, R. Startz, and P. Liu, "Less than 2 c warming by 2100 unlikely," *Nat. Clim. Change*, vol. 7, pp. 637–643, 2017.

[2] T. Bartels-Rausch, "Ten things we need to know about ice and snow," *Nature*, vol. 494, pp. 27–29, 2013.

[3] T. Koop, "When dry air is too humid," *Science*, vol. 314, pp. 1399–1400, 2006.

[4] U. Nakaya, *Snow Crystals: Natural and Artificial*. Harvard University Press, Cambridge, 1954.

[5] J. Hallett and B. J. Mason, "The influence of temperature and supersaturation on the habit of ice crystals grown from the vapour," *Proc. R. Soc. Lond. A*, vol. 247, pp. 440–453, 1958.

[6] A. P. V. den Heuvel and B. J. Mason, "Habit of ice crystals grown in hydrogen, carbon dioxide and air at reduced pressure," *Nature*, vol. 184, pp. 519–520, 1959.

[7] K. G. Libbrecht, "The physics of snow crystals," *Rep. Prog. Phys.*, vol. 68, pp. 855–895, 2005.

[8] M. P. Bailey and J. Hallett, "A comprehensive habit diagram for atmospheric ice crystals: Confirmation from the laboratory, airs ii, and other field studies," *J. Atmos. Sci.*, vol. 66, pp. 2888–2899, 2009.

[9] T. Kobayashi, "On the variation of ice crystal habit with temperature," in *Physics of Snow and Ice: Proceedings* (H. Oura, ed.), Institute of Low Temperature Science, Hokkaido University, 1967, 1967.

[10] T. Sei and T. Gonda, "The growth mechanism and habit change of ice crystals growing from the vapor phase," *J. Cryst. Growth*, vol. 94, pp. 697–707, 1989.

[11] K. G. Libbrecht and M. E. Rickerby, "Meassurements of surface attachment kinetics for faceted ice crystal growth," *J. Cryst. Growth*, vol. 377, pp. 1–8, 2013.

[12] M. Inomata, K.-i. Murata, H. Asakawa, K. Nagashima, S. Nakatsubo, Y. Furukawa, and G. Sazaki, "Temperature dependence of the growth kinetics of elementary spiral steps on ice basal faces grown from water vapor," *Cryst. Growth Des.*, vol. 18, no. 2, pp. 786–793, 2018.

[13] J. Gravner and D. Griffeath, "Modeling snow-crystal growth: A three-dimensional mesoscopic approach," *Phys. Rev. E*, vol. 79, p. 011601, Jan 2009.

[14] J. W. Barrett, H. Garcke, and R. Nürnberg, "Numerical computations of faceted pattern formation in snow crystal growth," *Phys. Rev. E*, vol. 86, p. 011604, Jul 2012.

[15] G. Demange, H. Zapolsy, R. Patte, and M. Brunel, "A phase field model for snow crystal growth in three dimensions," *npj Comp. Mat.*, vol. 3, p. 15, 2017.

[16] P. Ball, "Material witness: Close to the edge," *Nature Mat.*, vol. 15, p. 1060, 2016.

[17] T. Kuroda and R. Lacmann, "Growth kinetics of ice from the vapour phase and its growth forms," *J. Cryst. Growth*, vol. 56, no. 1, pp. 189–205, 1982.

[18] B. Slater and A. Michaelides, "Surface premelting of water on ice," *Nat. Rev. Chem*, vol. 3, pp. 172–188, 2019.

[19] E. A. Jagla, S. Prestipino, and E. Tosatti, "Surface-melting-induced preroughening," *Phys. Rev. Lett.*, vol. 83, pp. 2753–2756, Oct 1999.

[20] K. Rommelse and M. den Nijs, "Preroughening transitions in surfaces," *Phys. Rev. Lett.*, vol. 59, pp. 2578–2581, Nov 1987.

[21] I. Pickering, M. Paleico, Y. A. P. Sirkin, D. A. Scherlis, and M. H. Factorovich, "Grand canonical investigation of the quasi liquid layer of ice: Is it liquid?," *J. Phys. Chem. B*, vol. 122, no. 18, pp. 4880–4890, 2018. PMID: 29660281.

[22] Y. Qiu and V. Molinero, "Why is it so difficult to identify the onset of ice premelting?," *J. Phys. Chem. Lett.*, vol. 9, no. 17, pp. 5179–5182, 2018. PMID: 30149705.

[23] H. Dosch, A. Lied, and J. H. Bilgram, "Glancing angle x-ray scattering studies of the premelting of ice surfaces," *Surf. Sci.*, vol. 327, pp. 145–164, 1995.

[24] J. Benet, P. Llombart, E. Sanz, and L. G. MacDowell, "Premelting-induced smoothening of the ice-vapor interface," *Phys. Rev. Lett.*, vol. 117, p. 096101, Aug 2016.

[25] J. Benet, P. Llombart, E. Sanz, and L. G. MacDowell, "Structre and fluctuations of the premelted liquid film of ice at the triple point," *Mol. Phys.*, pp. 1–19, 2019.

[26] J. L. F. Abascal, E. Sanz, R. G. Fernandez, and C. Vega, "A potential model for the study of ices and amorphous water: Tip4p/ice," *J. Chem. Phys.*, vol. 122, p. 234511, 2005.

[27] M. M. Conde, C. Vega, and A. Patrykiejew, "The thickness of a liquid layer on the free surface of ice as obtained from computer simulation," *J. Chem. Phys.*, vol. 129, no. 1, p. 014702, 2008.

[28] N. H. Fletcher, "Reconstruction of ice crystals at low temperatures," *Phil. Mag. B*, vol. 66, pp. 109–115, 1992.

[29] V. Buch, H. Groenzin, I. Li, M. J. Schultz, and E. Tosatti, "Proton order in the ice crystal surface," *Proc. Nat. Acad. Sci.*, vol. 105, pp. 5969–5974, 2008.

[30] D. Pan, L.-M. Liu, G. A. Tribello, B. Slater, A. Michaelides, and E. Wang, "Surface energy and surface proton order of the ice ih basal and prism surfaces," *J. Phys.: Condens. Matter*, vol. 22, no. 7, p. 074209, 2010.

[31] X. Wei, P. B. Miranda, and Y. R. Shen, "Surface vibrational spectroscopic study of surface melting of ice," *Phys. Rev. Lett.*, vol. 86, pp. 1554–1557, Feb 2001.

[32] W. J. Smit, F. Tang, M. A. Sánchez, E. H. G. Backus, L. Xu, T. Hasegawa, M. Bonn, H. J. Bakker, and Y. Nagata, "Excess hydrogen bond at the ice-vapor interface around 200 k," *Phys. Rev. Lett.*, vol. 119, p. 133003, Sep 2017.

[33] M. Watkins, D. Pand, E. G. Wang, A. Michaelides, J. VandeVondele, and B. Slater, "Large variation of vacancy formation energies in the surface of crystalline ice," *Nature Materials*, vol. 10, pp. 794–798, 2011.

[34] P. J. M. Bastiaansen and H. J. F. Knops, "Roughening and preroughening in the six-vertex model with an extended range of interaction," *Phys. Rev. B*, vol. 53, pp. 126–135, Jan 1996.

[35] G. Santoro, M. Vendruscolo, S. Prestipino, and E. Tosatti, "Disordered flat phase and phase diagram for restricted solid-on-solid models of fcc (110) surfaces," *Phys. Rev. B*, vol. 53, pp. 13169–13186, May 1996.

[36] A. Prasad and P. B. Weichman, "Layering transitions, disordered flat phases, reconstruction, and roughening," *Phys. Rev. B*, vol. 57, pp. 4900–4938, Feb 1998.

[37] P. B. Weichman and A. Prasad, "Zippering and intermeshing: Novel phase diagrams for interfaces and films," *Phys. Rev. Lett.*, vol. 76, pp. 2322–2325, Mar 1996.

[38] J. D. Weeks, "The roughening transition," in *Ordering in Strongly Fluctuating Condensed Matter Systems* (R. T., ed.), pp. 293–317, Plenum, New York, 1980.

[39] P. B. Weichman, P. Day, and D. Goodstein, "Preroughening and reentrant layering transitions on triangular lattice substrates," *Phys. Rev. Lett.*, vol. 74, pp. 418–421, Jan 1995.

[40] W. J. Smit and H. J. Bakker, "The surface of ice is like supercooled liquid water," *Angew. Chem. Int. Ed. Engl.*, vol. 56, no. 49, pp. 15540–15544, 2017.

[41] S. Prestipino, G. Santoro, and E. Tosatti, "Preroughening, diffusion, and growth of a fcc(111) surface," *Phys. Rev. Lett.*, vol. 75, pp. 4468–4471, Dec 1995.

[42] D. L. Woodraska and J. A. Jaszczak, "Roughening and preroughening of diamond-cubic 111 surfaces," *Phys. Rev. Lett.*, vol. 78, pp. 258–261, 1997.

[43] J. R. Espinosa, C. Vega, and E. Sanz, "Ice-water interfacial free energy for the tip4p, tip4p/2005, tip4p/ice, and mw models as obtained from the mold integration technique," *J. Phys. Chem. C*, vol. 120, no. 15, pp. 8068–8075, 2016.

[44] H. R. Pruppacher and J. D. Klett, *Microphysics of Clouds and Precipitation*. Heidelberg: Springer, 2010.

[45] R. L. Davidchack, J. R. Morris, and B. B. Laird, "The anisotropic hard-sphere crystal-melt interfacial free energy from fluctuations," *J. Chem. Phys.*, vol. 125, no. 9, p. 094710, 2006.

[46] J. Benet, L. G. MacDowell, and E. Sanz, "Computer simulation study of surface wave dynamics at the crystal–melt interface," *J. Chem. Phys.*, vol. 141, p. 034701, 2014.

[47] J. Benet, L. G. MacDowell, and E. Sanz, "A study of the ice-water interface using the tip4p/2005 water model," *Phys. Chem. Chem. Phys.*, vol. 16, pp. 22159–22166, 2014.

[48] P. Llombart, R. M. Bergua, E. G. Noya, and L. G. MacDowell, "Structure and water attachment rates of ice in the atmosphere: Role of nitrogen," *Phys. Chem. Chem. Phys*, pp. –, 2019.

[49] V. Buch, P. Sandler, and J. Sadlej, "Simulations of H_2O solid, liquid and clusters, with an emphasis on ferroelectric ordering transition in hexagonal ice," *J. Phys. Chem. B*, vol. 102, pp. 8641–8653, 1998.

[50] H. Berendsen, D. van der Spoel, and R. van Drunen, "Gromacs: A message passing parallel molecular dynamics implementation," *Comp. Phys. Comm.*, vol. 91, no. 1 - 3, pp. 43 – 56, 1995.

[51] B. Hess, C. Kutzner, D. van der Spoel, and E. Lindahl, "Gromacs 4: Algorithms for highly efficient, load-balanced, and scalable molecular simulation," *J. Chem. Theo. Comp.*, vol. 4, no. 3, pp. 435–447, 2008. PMID: 26620784.

[52] G. Bussi, D. Donadio, and M. Parrinello, "Canonical sampling through velocity rescaling," *J. Chem. Phys.*, vol. 126, no. 1, p. 014101, 2007.

[53] M. Allen and D. Tildesley, *Computer Simulation of Liquids.* Oxford: Clarendon Press, second ed., 2017.

[54] W. Lechner and C. Dellago, "Accurate determination of crystal structures based on averaged local bond order parameters," *J. Chem. Phys.*, vol. 129, no. 11, p. 114707, 2008.

[55] K. R. Mecke and S. Dietrich, "Effective hamiltonian for liquid-vapor interfaces," *Phys. Rev. E*, vol. 59, pp. 6766–6784, Jun 1999.

[56] P. Noziéres and F. Gallet, "The roughening transition of crystal surfaces. i. static and dynamic renormalization theory, crystal shape and facet grwoth," *J. Phys.(Paris)*, vol. 48, pp. 353–367, 1987.

Chapter 4

Rounded Layering Transitions on the Surface of Ice

Pablo Llombart[1,2], *Eva G. Noya*[1] *and Luis G. MacDowell*[2]

(1) Instituto de Química Física Rocasolano, CSIC, Calle Serrano 119, 28006 Madrid, Spain
(2) Departamento de Química Física, Facultad de Ciencias Químicas, Universidad Complutense de Madrid, 28040 Madrid, Spain

Abstract

We perform a detailed study of premelting film thickness on the basal and primary prismatic planes of ice for the TIP4P/Ice model. In the range between 210 K and 270 K, the film thickness increases from about 3 Å to about 9 Å for both facets. We employ a novel methodology to calculate the disjoining pressure curves for ice premelting. The disjoining pressure curves can be fit to a model of damped oscillatory decay based on liquid state theory. The results suggest the presence of non-singular continuous layering transitions from about one to two and from two to three water layers. We explore the nature of the transitions by performing a fluctuation analysis. The results suggest that mean field layering transitions are rounded and become continuous due to capillary wave broadening of the interface. We point that true first order layering transitions could persist at low temperature in a pressure range between the metastable line of water/vapor coexistence and the sublimation line.

Introduction

Understanding the properties of the ice surface is of crucial importance in many important phenomena, such as the growth of snowflakes,[1] the freezing and melting rates of ice in the poles,[2] or the scavenging of trace gases on ice particles.[3] A particularly relevant issue regarding the properties of the ice surface is the existence of a quasi-liquid layer of premelted ice,[4] which is expected to have a very important effect on crystal growth rates,[5, 6] adsorption,[3] friction,[7] and many others.[8, 9] But despite its significance, and great progress in the experimental understanding of ice properties,[4, 10, 11, 12, 13, 14, 15, 16, 17] the extent of ice premelting, i.e., onset temperature, if this can be defined at all, as well as the film thickness has been a longstanding matter of debate.[18, 19, 8] After many years of controversial research, however, it is possible to identify a number of recent experimental studies with widely different techniques,[20, 21]

which seem to agree with some of the early studies,[12, 13] and computer simulations,[22] and indicate the premelting layer along the sublimation line remains at subnanometer thickness up to -1°C or less, and then strongly increases. However, the details of the onset temperature (c.f. -4°C,[4] -12°C,[23] -0.1°C,[21]) and precise thickness beyond the onset is likely very much dependent on the extent of adsorbed impurities.[24]

As the controversy regarding the film thickness starts to clarify, new and exciting observations have been made regarding the properties of the premelting film, either along the saturation line [17, 25, 26] or off coexistence. [15, 27] Along the sublimation line, Sanchez *e*t al. used Sum Frequency Generation experiments and found a discontinuous OH frequency jump at 257 K, which they interpreted, with help from computer simulations of the TIP4P/Ice model as the signature of a discrete bilayer melting transition.[17, 19] Surprisingly, a clearly related signature found many years earlier in the *p*pp polarized signal of dangling OH bonds,[11] had received little attention, likely due to the considerable difficulties in interpreting SFG experiments. Despite this evidence, in fact, it has been suggested also based on SFG experiments that bilayer melting starts at a temperature of 250 K, but occurs rather in a continuous fashion, until close to the triple point where the spectral signal can be hardly distinguished from that of bulk water.[16] Interestingly, computer simulations of the mW model show that at about this temperature range, the ice surface exhibits patches of premelted ice, whose size increases continuously as temperature is increased.[28, 25, 26]

Another indication reminiscent of layering occurs in confocal microscopy experiments performed for saturated vapor pressures above the sublimation line, which clearly show the emergence of an apparently discontinuous transition from a thin to a thick liquid layer at sufficient high pressures, with a height increase that appears however considerably larger than the ice lattice spacing.[14, 15, 27] This kind of transition is reminiscent of the so called frustrated complete wetting states, predicted long time ago,[29, 30] and found more recently both in experiments and computer simulations.[31, 32, 33, 34, 35, 36]

These two observations–namely, the appearance of smoothed or discrete discontinuities of the premelting film thickness, both below and above water saturation–suggest that ice's premelting layer could exhibit layering phenomena similar to that studied in past decades in simple model systems.[37, 38, 39, 40, 41, 42, 43]

In the most simplified lattice gas models, one considers the layerwise adsorption of a vapor onto an inert substrate. At sufficiently low temperatures, it is found that the gas adsorption is not continuous, but rather, proceeds by either a finite or infinite number of layering transitions.[37, 38] Details depend on the nature of the adsorbate. For solids below the roughening transition, adsorption proceeds across an infinite number of layering transitions as the pressure increases towards saturation. At sufficiently high temperatures, however, past the roughening temperature of the solid, the interface exhibits thermal capillary waves, and the roughening transitions are smoothed out. One then finds that the lines of layering transitions terminate in layering critical points. However, even for simplified lattice models, the adsorption behavior can become very rich and complicated, with a number of first order, second order, or reentrant transitions.[39, 44]

When one deals with an adsorbed liquid, as modeled by simple spherical potentials, the behavior follows roughly the same trends as those of lattice models. However, it is important also to consider the interplay between layering and wetting.[42] Both phenomena depend considerably on the range of intermolecular forces. For the adsorption of water on ice at small thickness, short range forces dominate, because the long range, algebraically decaying van der Waals forces are very weak, and only take over short range forces for thickness beyond the nanometer. Fortunately, the behavior for systems with short range interactions is fairly well understood.[40, 41, 42, 43] Here, results are best rationalized in terms of an interface potential, $g(h)$, which dictates the free energy of the system as a function of film thickness, h. The layering behavior at the mean field level is revealed as an oscillatory behavior of the interface potential, with one minimum corresponding to discrete states of full layer formation, and maxima to the

instability of partially filled states. The generic mean field behavior is given qualitatively as:

$$g(h\ ) = A_2 e^{-2\kappa h}\ - A_1 e^{-\kappa h}\ \cos(k_z h\ ) \tag{4.1}$$

where A_1 and A_2 are positive coefficients, κ is a bulk correlation length and $k_z \approx 2\pi/d$, with d, a molecular diameter. For small h , the first term dominates, and the interface potential is positive, meaning a propensity to increase the film thickness, which proceeds either continuously for small A_1 or small k_z, or in layerwise fashion, for large A_1 and k_z. Eventually, for sufficiently large h , the second term becomes dominant. The interface potential is then negative, indicating a state of incomplete wetting, and a propensity to attain an equilibrium film thickness in one of the minima. However, if the vapor becomes saturated, a linear term Δph must be added to the interface potential, and then the growth of the liquid film becomes favourable and could proceed downhill discontinuously from one layer to the other.

In a remarkable paper, however, Chernov and Mikheev emphasized the role of capillary waves at the liquid-vapor interface of the adsorbed film.[40, 45] A surface is a two dimensional system where fluctuations are very large. Usually, the surface tension is not sufficiently large to damp large wave-length fluctuations. Accordingly, the interface is rough on a scale that can become significantly larger than the typical layer spacing. The result is that the mean field interface potential is strongly renormalized. Using techniques of Gaussian renormalization,[46] it is possible to write down the renormalized interface potential in a manner analogous to the mean field interface potential, albeit with renormalized coefficients:[40, 45, 43]

$$g_R(h\ ) = A_2 e^{-2\kappa h}\ - A_1 e^{-\kappa_R h}\ \cos(k_{z,R} h\ ) \tag{4.2}$$

The important conclusion is that renormalization drives κ_R larger than 2κ. As a result, the second term is now of shorter range than the first one. For large h then the interface potential becomes positive, and the system is driven to a state of fluctuation dominated complete wetting. The second significant effect of the thermal capillary waves is to renormalize k_z, which, in its renormalized version becomes considerably smaller. Accordingly, the layering transitions proceed by steps of much larger thickness than one molecular diameter. Eventually, at the ice/water/vapor interface, long range forces of negative sign will set in, and will prevent the system to actually reach complete wetting.[47] The interplay between short range and non-renormalizable van der Waals forces of negative sign could be significant, but is unfortunately not at all trivial to work out. Likely, the long range forces provide effectively an infrared cutoff for the divergences, and then the issue is whether κ_R will become larger than 2κ or not. In the latter case, the behavior would remain roughly similar to the mean field scenario, albeit with a renormalized $k_{z,R}$ coefficient; in the former case, the system would also remain at incomplete wetting, but with a very large equilibrium thickness.

The adsorption of water on ice is further complicated by the fact that the substrate is made of the same component as the adsorbate. In this case, the growth of a thick water film on top of ice results in the formation of two interfaces, made of ice/water and water/vapor. When only short range forces operate, the relevant issue is when does the fluctuation dominated wetting transition occur relative to the triple point of the system. Chernov and Mikheev showed that the wetting temperature must alway be higher than the roughening transition of the ice/water interface.[40, 45] Based on experiments, the ice/water interface of the prismatic plane roughens at about -16°C,[48, 49] so that in the absence of van der Waals forces, i.e., water could in principle exhibit a wetting transition on the prism facet before the triple point is attained. On the contrary, for the ice/melt basal face all evidence seems to indicate that there is no roughening transition before the triple point, so that one should therefore not expect wetting of water on the basal plane at the triple point.

In this work we measure the adsorption isotherms of water on ice along the sublimation line, and exploit these data to obtain the disjoining pressure of the premelting films for the first time. The disjoining pressure exhibits incipient traces of instability, but does not show evidence of layering transitions at

undersaturation. Fits to the disjoining pressure as predicted by Eq. (4.2) are consistent with the Chernov and Mikheev scenario of renormalization in a finite system, with κ_R far larger than κ, but not quite as large as 2κ, and no apparent renormalization of k_z. Furthermore, we perform a finite system size analysis. The results corroborate the absence of proper, first order layering transitions, but indicate a continuous transition with origin in the rounding of a mean field first order transition due to capillary waves. We speculate that there exist lines of layering transitions, which terminate at a layering critical point at pressures above the sublimation line. The prolongation of two of these lines of layering transitions beyond the layering critical point cross the sublimation line at T=250 and T=267 K, and explain the rounding of the transition and the seggregation of the premelting film in small lateral domains as observed in experiments and simulations.[10, 28, 25, 26]

Results

Previously, computer simulation evidence for a layering transition of the TIP4P/Ice model on the basal plane has been discussed in terms of the density profile, $\rho(z)$ of water molecules.[17] In a rather coarse temperature range between 250 and 270 K, it was observed that a double peaked structure of the density profile at 250 K, corresponding to a full solid bilayer, transformed into a single peak at 270 K. This was taken for evidence of a bilayer by bilayer melting process, suggestive of a first order layering transition.[17, 19] However, other experimental studies and simulations of the mW model rather suggest a continuous melting process.[16, 26]

A more detailed description of layering phenomena in terms of density profiles can be afforded by identifying liquid-like and solid-like environments with the $\bar{q}_6$ parameter.[50] This allows us to plot the density of liquid like and solid like molecules, and whence, identify the features that are specific to the premelting layer.[51, 52, 53] In a previous paper,[53] we represented the density of solid-like molecules and found that the edge of the profile moved by one full bilayer in the range between 260 and 270 K. This better locates a conjectured layering transition but still is not a sufficiently fine range to discuss the continuous or discontinuous nature of the transition.

In this study we have performed a detailed analysis of the ice surface structure over sixteen different temperatures in the range between 210 and 271 K, including a set of 8 temperatures in the interval between 260 and 271 K.

The density profile of liquid-like molecules for the basal plane can be seen in Figure.4.1-a At low temperatures, the plot shows a prominent outermost peak at about 92 Å, followed by a double peak centered at 90 Å . The distance between the outermost peak and the innermost spike of the double peak is about 3.5 Å , very close to the preferred lattice spacing of the underlying solid. This, together with the bilayer structure of the double peak is suggestive of a rather ordered liquid like environment at low temperature (indeed, by choosing the $\bar{q}_6$ order parameter, liquid-like molecules include undercoordinated molecules with allotropic crystalline environments such as ice Ic, c.f.[54]). As temperature increases, the outermost peak decreases in favor of the second peak, and a new double peak starts growing at about 86 Å . However, the density profiles appear to transform in a rather continuous manner up to about 267 K. At this temperature a qualitative change in the density profiles is observed by the dissapearence of the first minimum of the density profile, which now decays monotonously towards the vapor phase.

Further detailed information on the structure of the premelting layer may be obtained by plotting intrinsic density profiles.[55, 56, 57] These are defined as density profiles measured relative to a locally determined surface. Following previous work, we describe the premelting liquid layer in terms of two bounding surfaces separating the quasi-liquid film from bulk ice and bulk vapor.[51, 52, 53] For points $\mathbf{x}$ along a flat reference plane, we calculate a if surface, $z_{\text{if}}(\mathbf{x})$ from the position of the outermost

solid molecules. Likewise, we calculate a fv surface, $z_{\text{fv}}(\mathbf{x})$ from the position of the outermost liquid-like molecules. An intrinsic density profile relative to the local fv surface can then be determined as the density of atoms at a distance $z - z_{\text{fv}}(\mathbf{x})$. The intrinsic density profiles with respect to fv are shown in Fig.4.1-b. Here we see a large peak centered at $z - z_{\text{fv}}(\mathbf{x}) = -1.2$ Åwhich corresponds to the atoms that define the fv surface. At low temperature, the profile is made of two peaks only, but as temperature increases, two new peaks gradually build up towards the interior of the bulk solid. The profiles change rather gradually again, but now a striking feature is observed in the range between 262 and 267 K. Firstly, similar to what was observed in the absolute profiles of liquid molecule, the outermost minimum and maximum of the profiles disappear across an inflection point at about $z - z_{\text{fv}}(\mathbf{x}) = -2.2$ Å point, and the decay of the density profile towards the vapor phase becomes monotonous as expected for a liquid-vapor interface. Secondly, it is clearly visible at $z - z_{\text{fv}}(\mathbf{x}) = 7.5$ Å that a maximum in the density profile largely increases also in this temperature range. This can be put into a clear context by comparing the maxima found at this location in the range between 240 to 255 K, which increase by far much less than it does in the range 262 and 267 K.

Finally, we explore the intrinsic density profile of liquid-like molecules measured relative to the if surface in Fig.4.1-c. This illustrates the difficulty to locate a layering transition by exploring density profiles. Merely by changing the origin, the density profiles now appear as evolving in a rather continuous fashion. Interestingly, at the highest temperature, the density profile so obtained hardly is distinguished from the profile of a pure solid/liquid interface shown in circles. It appears in this case that there is no hint of discontinuity at 267 K, as evidenced in the previous profiles. But, surprisingly, we notice the appearance of a maximum at about 6.7 Å which occurs across an inflection point in the range between 230 and 235 K.

We now pursue our study by considering the structure of the prismatic plane. Figure 4.1-d shows the density profile of liquid like molecules. Some features of this profile indicate specific differences between basal and prismatic planes, but overall the trend of increasing premelting thickness with temperature can be found in both. The changes between temperatures are again rather gradual up to about 264 K. At this temperature, we find the disappearance of the small maximum at about 93 Å, in the range between 264 and 266 K. Furthermore, looking at $z = 95$ Å, we also find the outermost maximum dissapears in the range between 245 and 250 K. Again, looking at different profiles does not yield always the same information. Intrinsic density profiles measured relative to the fv surface are shown in Fig.4.1-e. Here, we do not find any signature of discontinuity on approaching the triple point, but we do find inflexion points at $z - z_{\text{fv}}(\mathbf{x}) = 0$ and $z - z_{\text{fv}}(\mathbf{x}) = -2.5$ Å in the range between 240 and 250 K. On the contrary, ploting the intrinsic density profile measured relative to the if surface does not show apparent discontinuities at 240 K, but allows to identify again an inflexion point at about $z - z_{\text{if}}(\mathbf{x}) = 6$ Å in the range between 268 and 270 K.

Could the occurrence of inflexion points in the density profiles be the signature of layering transitions? are these continuous or discontinuous? And are they singular? i.e. correspond to a properly defined surface phase transition? Why do such signatures appear in some density profiles but not in others?

In order to clarify the process of bilayer melting further, we need to restort to a more transparent order parameter than the density profiles can afford. Based on the intrinsic if and fv surfaces, we can define an instantaneous local film thickness as $\hat{h}(\mathbf{x}) = z_{\text{fv}}(\mathbf{x}) - z_{\text{if}}(\mathbf{x})$. We exploit this local parameter to calculate the mean film thickness h upon lateral and canonical averaging over the simulation run.

Fig.4.2-a and 4.2-c depicts the results obtained for both the basal and primary planes in the range between 210 and 270 K, for a fine grid of temperatures. The film thickness grows from about one molecular layer at T=210 K, to about three molecular layers at T=270 K. The results show that the thickness of the premelting layer is somewhat larger for the basal plane than the prismatic plane up to about 260 K, corresponding to the melting of one full bilayer, but becomes very similar in thickness and eventually

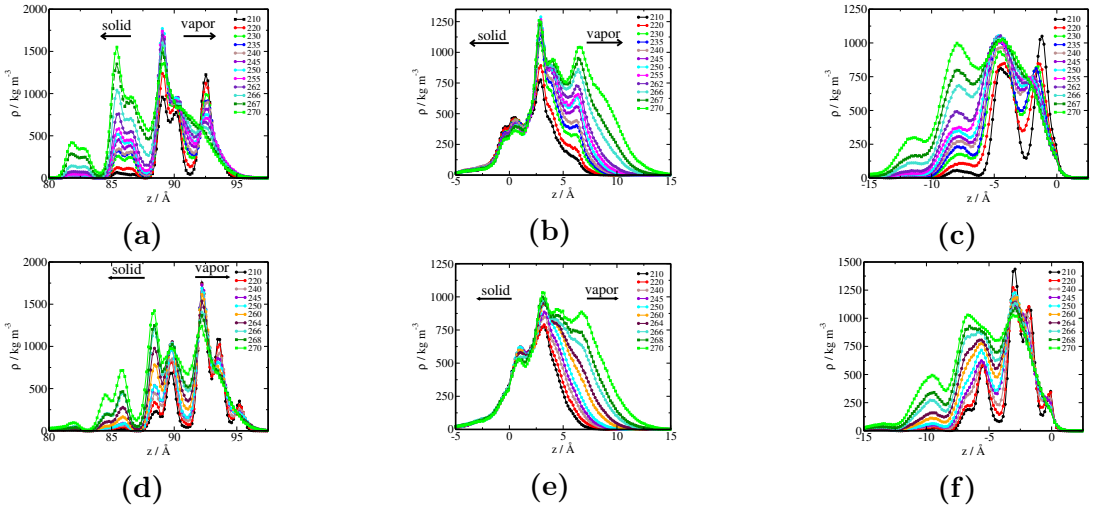

Figure 4.1. Evolution of density profiles as a function of temperature. a) and d) Density profile of liquid like molecules for basal and prismatic I faces, respectively. b) and e) Intrinsec density profiles of liquid molecules measured relative to the fv surface. c) and f) Intrinsec density profiles of liquid molecules calculated with respect to the if surface. Results are shown for selected temperatures to avoid crowding.

becomes thicker as the melting point is approached. In either case, the film thickness appears to grow gradually, with no clear evidence of a first order layering transition. We provide a full thermodynamic characterization by calculating the disjoining pressure, $\Pi(h) = -dg(h)/dh$ of the film, which accounts for the pressure difference between the adsorbed liquid film and the bulk liquid at equal chemical potential, i.e.:[58, 59, 60]

$$\Pi(h) = p_v(\mu, T) - p_l(\mu, T) \tag{4.3}$$

In practice, $\Pi(h)$ is to an adsorbed liquid film as the Laplace pressure to a liquid droplet. Particularly, the vapor pressure of an ideal gas in equilibrium with a film of thickness h is given in a manner analogous to the Kelvin-Laplace equation as $p_v = p_{v,w}e^{-\beta\Pi(h)}$, where $p_{v,w}$ is the saturated vapor pressure over water, and $\beta = 1/k_BT$. An equilibrium film thickness for water adsorbed at the ice/vapor interface can be meaningfully defined only along the sublimation line, where the vapor pressure equals the saturated vapor pressure over ice, $p_{v,i}$. Accordingly, the above equation becomes $p_{v,i} = p_{v,w}e^{-\beta\Pi(h)}$. It follows that using accurate coexistence vapor pressures, and the corresponding equilibrium film thickness $h\ (T)$ along the sublimation line, we can readily determine $\Pi(h)$ (supplemental material). The significance of this result can be hardly overemphasized. By exploiting the data $h\ (T)$, which provides the film thickness at solid/vapor coexistence, we can now determine the film height of the premelting film at arbitrary temperature *and pressure*, by merely solving Eq. (4.3) for h. Therefore, our disjoining pressure curves provide the long sought input required to understand the premelting film properties of ice over the complete thermodynamic phase diagram.[5, 61]

Results for both the basal and prismatic planes are shown in Fig. 4.2-b and 4.2-d. The disjoining pressure curve up to $h = 10$ Å that we are able to measure exhibits a monotonous behavior, with clear indications of overdamped oscillatory decay at positive disjoining pressure. On the contrary, a system exhibiting first order layering transitions exhibits sinusoidal oscillations in mean field, or alternatively, an equal tangent Maxwell construction with a segment of zero slope beyond mean field. Our results do not appear to support this hypothesis. However, by plotting the numerical derivative of the disjoining pressure (inset), we do find indeed traces of enhanced stability at $h = 6$ Å for the basal plane and at $h = 5.4$ Å for

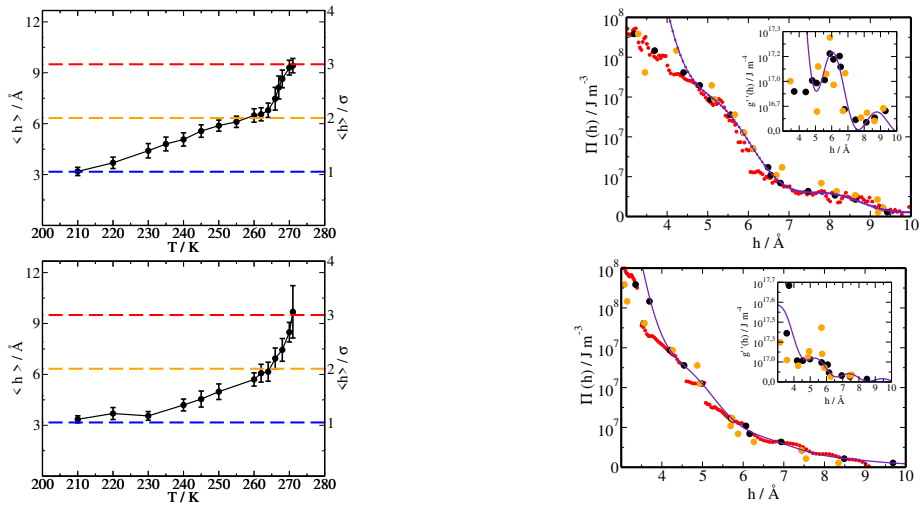

Figure 4.2. Film thickness (left) and disjoining pressure (right) of basal (top) and primary prismatic (bottom) facets. Panels a) and c) show the average film thickness for the $n_x \cdot n_y = 64$ system as a function of temperature for basal and prismatic planes, respectively. The dashed lines indicate film heights in units of the molecular diameter. Panels b) and d) show the disjoining pressure as a function of film height for basal and prismatic I faces, respectively: full symbols, method 1; empty symbols, method 2, as described in chapter 2 of this thesis. The full lines are a fit to Eq. (4.1). Inset shows the surface susceptibilities as obtained from numerical derivation and from analytical derivation of fits.

the prismatic plane. This implies that the system will retain these preferred thickness over a somewhat larger pressure (or temperature) interval than neighbouring film thicknesses, but is not a sufficient criteria for the occurrence of a phase transition. Interestingly, for the basal plane, the disjoining pressure curve obtained for the small system (orange symbols), appears to show a minimum at $h = 7$ Å , and hints to a truly oscillatory contribution in the range between $h = 6$ and $h = 8$ Å. Accordingly, it appears that at mean field level there could be a signature of layering which is washed away upon renormalization to larger lengthscales, as suggested from the study of capillary wave fluctuations.[40, 43]

A fit of the disjoining pressure curves from simulation to the derivative of Eq. (4.2) shows excellent agreement. The parameters of the fit for the basal plane are $\kappa = 0.31\text{Å}^{-1}$, $\kappa_R = 0.43\text{Å}^{-1}$ and $q_{z,R} = 2.36\text{Å}^{-1}$. Alternatively, a fit under the constraint $\kappa_R = \kappa$, provides very similar results, with $\kappa = 0.31\text{Å}^{-1}$ and $q_{z,R} = 2.27\text{Å}^{-1}$. The first set of parameters is consistent with a renormalization of κ_R, but exhibits a q_z parameter expected for mean field, with $q_z = 2\pi/d$, and d very similar to the expected molecular diameter. On the other hand, the second set of parameters is fully consistent with the mean field scenario. On the scale, both fits are essentially equal, the only difference being how $g(h)$ is extrapolated at thicknesses beyond those obtained in our simulations. From the derivative of the disjoining pressure, we estimate a parallel correlation length $\xi = \sqrt{g''/\gamma_{lv}}$ ranging between 8 Åand 50 Åin the range of temperatures studied, whence, far away from a strong fluctuating regime for these thickness. This justifies a small renormalization of the coefficients and the proximity to a mean field scenario. At any rate, we have $2\kappa > \kappa_R$ in both cases, which implies absence of complete wetting at the triple point, and a partial wetting state resulting merely from short range interactions. The derivative of the disjoining pressure from the fits to Eq. (4.2) is consistent with the numerical derivatives, and further suggests enhanced stability at $h = 9$ Å . In practice, the fact that $\kappa_R < 2\kappa$ implies that there is an infinite many number of maxima with enhanced stability as $h \to \infty$, but at such long distances it is expected that the oscillatory behavior will become strongly renormalized.

For the prismatic plane, the fit to the mean field model yields $\kappa = 0.30$ Å^{-1} and $q_z = 3.15$ Å^{-1}. Notice that strictly in mean field, the parameters κ and q_z should be related to the bulk liquid, and should not be related to details of the substrate, so κ appears consistent with this picture, but q_z does not. For the renormalized scenario, the fit provides $\kappa = 0.31$ Å^{-1}, $\kappa_R = 0.90$ Å^{-1} and $q_{z,R} = 3.14$ Å^{-1}. Interestingly, in this case the condition $\kappa_R > 2\kappa$ is fullfilled. Accordingly, in the mean field scenario the prismatic plane is not completely wet by the liquid, but under the fit consistent with renormalization, the bulk liquid wets ice on the prismatic plane. This is indeed consistent with the theory by Chernov and Mikheev, since the roughening temperature of the ice/water interface for the prismatic plane has been measured to lie about -16 ° C,[48, 49] it is possible to have a wetting transition before the triple point is reached. Be as it may, it is expected that for large distances, the short range forces will be suppressed exponentially, and then the algebraically decaying van der Waals forces will take over and dominate the wetting behavior. From Lifshitz theory, it is expected that van der Waals forces at the ice/water/vapor interface will conspire against wetting,[47] and the system will remain also in a state of incomplete wetting. Likely, however, the equilibrium thickness of the prismatic plane very close to the triple point should be considerably thicker than it is for the basal plane.

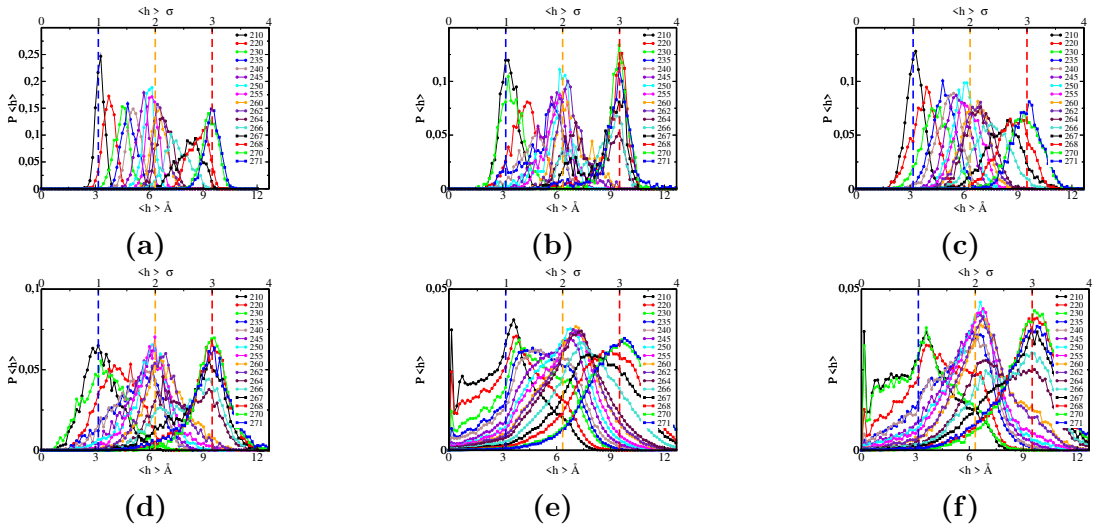

Figure 4.3. System size analysis of thickness distributions on the basal plane. Results are shown for the $n_x \cdot n_y = 64$ (left) and $n_x \cdot n_y = 16$ (right) system. Panels a) and b): probability distribution of the global film thickness, h. c) and d): probability distribution of the partial film thickness $h_{1/4}$. e) and f): probability distribution of the local order parameter $h(\mathbf{x})$. Dashed vertical lines show the film thickness in units of the molecular diameter. Results are shown for temperatures in the range from T=210 K to T=271 K, with color code as indicated on the figure. Results are as displayed in Fig.4.2-a.

In order to clarify whether the layering is consistent with either a continuous or a first order phase transition, we perform a block analysis of the film thickness distributions.[62, 63] To this end, we plot the probability distribution of film thicknesses averaged over lateral areas of increasing size. We consider first h (**x**), which accounts for a lateral size of two unit cells; $h_{1/4}$, which accounts for an average over a quarter of the full system, and h , an average over the full system size. The results, shown for two system sizes is are presented in Fig.4.3 and 4.4.

The analysis appears extremely suggestive of the presence of two rounded layering transitions. Notice that previously, Sum Frequency Generation experiments had revealed the likelihood of one bilayer melting at about 257 K.[17] Here, our analysis reveals clearly the signature of two rounded layering transitions,

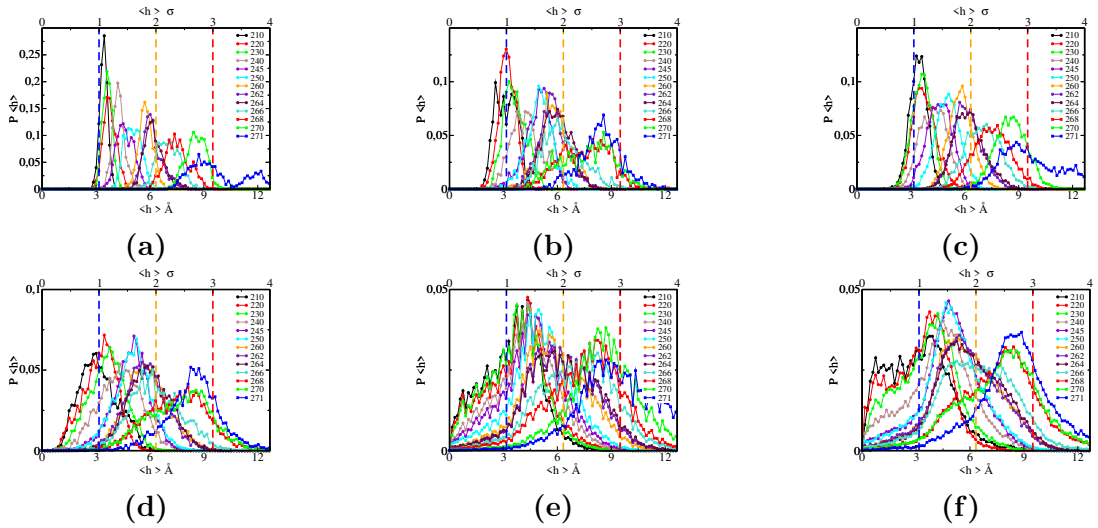

Figure 4.4. System size analysis of thickness distributions on the prismatic plane. Results are as displayed in Fig. 4.2-c.

first, from one to two bilayers, at about T=235 K and other, from two to three bilayers at T=267 K. For the local order parameter h (**x**), we find rather broad distributions, which span as much as 9Å, i.e., ca. 3 molecular diameters. For most temperatures, we find the distributions appear as roughly single gaussians, except for transitions in the range T=235 K to T=240 K, and T=267 K to T=268 K. In these cases, the distributions are considerably flattened at the maximum. This kind of distributions in a small system are indicative of either i) a first order transition rounded by the small system size or ii) a continuous transition that is broadened due to a large correlation length of the same order of the system size. The continuous transition can be either a proper phase transition if the correlation length diverges, or non-singular if the correlation length remains finite. For finite systems, the non-singular scenario can easily be confused with the proper first order or second order phase transition scenaria. This is particularly plausible situation to occur at an interface, as two dimensional systems usually exhibit large fluctuations, and usually have large parallel correlation lengths. The system size analysis is precisely meant to distinguish these three possibilities. In the event of a first order phase transition, broad distributions found in small systems will become bimodal, with two sharp peaks separated by a gap of increasingly smaller probability as system size grows. In a continuous non-singular transition, on the other hand we expect that the distributions will become more strongly gaussian, and the gap between the two preferred thicknesses will be occupied by gaussian distributions. The block analysis performed over distributions of $h_{1/4}$ and h , seem indicative of a continuous transition. All of them sharpen very much and exhibit fluctuations of not more than three molecular diameters for the global order parameter. No signs of bimodality persists in any of the distributions, while the gap between two and three layers is filled with unimodal distributions. Furthermore, the comparison with the distributions from the smaller system size, $n_x \cdot n_y = 16$, indicate that the separation between unimodal distributions becomes less sharp as the system size increases, which is also at odds with expectations for a first order transition.

Results for the primary prismatic plane are shown in Fig.4.4. In this case, again, the distributions reveal the presence of two transitions. One from one to two molecular diameters occurs at about 250 K, somewhat higher than that observed in the basal face. For the transition from two to three layers, on the other hand, it is found in the interval between 267 and 268 K, very much as for the basal face. The analysis of the distributions here is less obvious, because the results appear to be more noisy, but again they are

suggestive of a continuous phase transition with no indications of a diverging length scale. On the other hand, for the highest temperature studied, $T = 271\ K$, our results are suggestive of a first order layering transition. Indeed, here we observe that the distribution of $h_{1/4}$ is a very broad band which becomes bimodal when studied in terms of the global film thickness. However, because of finite system sizes and lack of sufficient data, we remain cautious with respect to this observation.

Conclusions

In this work we have studied the surface thermodynamics of premelting films on the basal and prismatic facets of ice. We have calculated film thicknesses over a fine grid of temperatures in the temperature range from 210 to 270 K. We exploit these data to calculate the disjoining pressure of the films. This allows us to estimate premelting film thicknesses for arbitrary values of temperature and pressure. The disjoining pressure curves exhibit a monotonous behavior, and appears to have rounded oscillations reminiscent of a mean field layering transition washed out by capillary wave fluctuations. The curves can be fit very well to a model of damped oscillatory decay expected from liquid state theory. A system size analysis is performed that seems to confirm the rounding of the mean field layering transitions, at least for film thicknesses in the subnanometer range. Overall, the results could indicate the existence of a line of layering transitions at low temperature that terminates in layering critical points that lie above the sublimation line. The prolongation of the first order layering lines beyond the critical point, as in a Fisher-Widom line, intersect the sublimation line at about 235 and 267 K for the basal plane, where an apparently continuous transition takes place. Interestingly, the first transition occurs very close to the dissaperance of the *p*pp polarized dangling OH stretch of the basal face found by Wei et al. many years ago,[11] while a transition at ca. 267 K correlates with the vanishing of the *s*sp polarized band found by Sanchez *e*t al. recently.[17] At any rate, we clearly find that the bilayer melting previously found in the range between 250 and 270 K for the TIP4P/Ice model actually occurs at 268 K, far away from the transition found for the band center that occurs at 257 K. These results help to understand the apparent microphase separation of premelted patches on the ice surface observed for the mW model recently, which could result from the prolongation of the layering line.[25, 26] For the prismatic plane, we find similar transitions at about 250 and 267 K. However, it seems that in the absence of long range van der Waals forces water could wet the prismatic plane. In practice, because of the presence of the algebraic decay of dispersion forces, we expect the premelting film will eventually stabilise at a large but finite thickness. No experimental data seems available to compare this prediction. The verification of this hypothesis born out by simulations and liquid state theory will hopefully encourage new experiments with confocal microscopy, sum frequency generation and others.[64, 15, 17, 16, 65, 21]

Acknowledgement

We would like to acknowledge Enrique Lomba for helpful discussions and Jose Luis F. Abascal for support. We acknowledge use of the Mare-Nostrum supercomputer and the technical support provided by Barcelona Supercomputing Center from the Spanish Network of Supercomputing (RES) under grants QCM-2017-2-0008 and QCM-2017-3-0034. We also acknowledge funding from Agencia Estatal de Investigación under research grant FIS-89361-C3-2-P.

Supplementary Material

Intrinsic surfaces

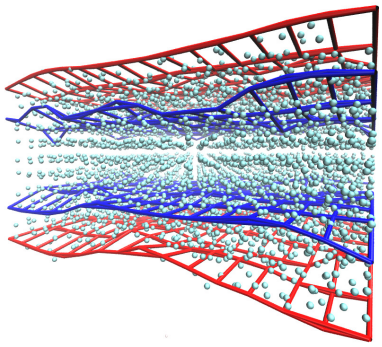

Figure 4.5. Sketch showing the bounding surfaces, if and fv that we employ to characterize the premelting film. The ice/film surface is shown in blue and the film/vapor surface is shown in red.

Determination of the sublimation and condensation lines

H_t^{iv} / kJ mol^{-1}	H_t^{wv} / kJ mol^{-1}	$C_{p,t}^{i}$/ J mol^{-1}K^{-1}	$C_{p,t}^{w}$ / J mol^{-1}K^{-1}
-61.03	-55.64	65.60	107.26

Table 4.1. Thermophysical properties of the TIP4P/Ice model at the triple point $T_t = 272$ K, required for the determination of sublimation and condensation pressures.

From integration of the Clausius-Clapeyron equation, we obtain for the coexistence of condensed phase α with the vapor phase the following vapor pressure:

$$\ln p_{\alpha v}(T)/p_t = \frac{\Delta H_t^{\alpha v} - \Delta C_{p,t}^{\alpha} T_t}{R} [1/T_t - 1/T] + \frac{\Delta C_{p,t}^{\alpha}}{R} \ln T/T_t \tag{4.4}$$

System sizes studied

Film thickness for two different system sizes

Temperature / K	N = 5120, Lx x Ly x Lz / nm	N = 1280, Lx x Ly x Lz / nm
210	7.24541 x 6.27494 x 15.00000	3.62270 x 3.13747 x 15.00000
220	7.24868 x 6.27776 x 15.00000	3.62434 x 3.13888 x 15.00000
230	7.25247 x 6.28104 x 15.00000	3.62623 x 3.14052 x 15.00000
235	7.25427 x 6.28292 x 15.00000	3.62714 x 3.14146 x 15.00000
240	7.25609 x 6.28412 x 15.00000	3.62804 x 3.14206 x 15.00000
245	7.25780 x 6.28587 x 15.00000	3.62890 x 3.14294 x 15.00000
250	7.25949 x 6.28713 x 15.00000	3.62974 x 3.14356 x 15.00000
255	7.26152 x 6.28888 x 15.00000	3.63076 x 3.14444 x 15.00000
260	7.26350 x 6.29060 x 15.00000	3.63175 x 3.14530 x 15.00000
262	7.26419 x 6.29120 x 15.00000	3.63209 x 3.14560 x 15.00000
264	7.26488 x 6.29181 x 15.00000	3.63244 x 3.14590 x 15.00000
266	7.26558 x 6.29241 x 15.00000	3.63270 x 3.14620 x 15.00000
267	7.26586 x 6.29264 x 15.00000	3.63293 x 3.14632 x 15.00000
268	7.26628 x 6.29302 x 15.00000	3.63314 x 3.14651 x 15.00000
270	7.26698 x 6.29362 x 15.00000	3.63349 x 3.14681 x 15.00000
271	7.26731 x 6.29432 x 15.00000	3.63360 x 3.14716 x 15.00000

Table 4.2. Temperature and systems dimensions for basal face. The number of unit cells in x, y and z directions are $N_x = 8$, $N_y = 8$ and $N_z = 5$ for bigger system. Small system has half $N/2$ unit cells in x and y directions and equal number of unit cells along z

Temperature / K	N = 5120, Lx x Ly x Lz / nm	N = 1280, Lx x Ly x Lz / nm
210	7.24528 x 5.89679 x 15.00000	3.62270 x 2.94840 x 15.00000
220	7.24876 x 5.89961 x 15.00000	3.62434 x 2.94980 x 15.00000
230	7.25229 x 5.90249 x 15.00000	3.62623 x 2.95124 x 15.00000
240	7.25604 x 5.90554 x 15.00000	3.62804 x 2.95277 x 15.00000
245	7.25780 x 5.90697 x 15.00000	3.62890 x 2.95348 x 15.00000
250	7.25957 x 5.90841 x 15.00000	3.62974 x 2.95420 x 15.00000
260	7.26329 x 5.91143 x 15.00000	3.63175 x 2.95571 x 15.00000
262	7.26405 x 5.91205 x 15.00000	3.63209 x 2.95602 x 15.00000
264	7.26480 x 5.91267 x 15.00000	3.63244 x 2.95633 x 15.00000
266	7.26556 x 5.91328 x 15.00000	3.63270 x 2.95664 x 15.00000
268	7.26631 x 5.91389 x 15.00000	3.63314 x 2.95694 x 15.00000
270	7.26707 x 5.91452 x 15.00000	3.63349 x 2.95726 x 15.00000
271	7.26729 x 5.91470 x 15.00000	3.63360 x 2.95735 x 15.00000

Table 4.3. Temperature and systems dimensions for prismatic I face. The number of unit cells in x, y and z directions are $N_x = 8$, $N_y = 8$ and $N_z = 5$ for bigger system. Small system has half $N/2$ unit cells in x and y directions and equal number of unit cells along z

Temperature / K	$\langle h \rangle$ / Å$(Area = 1)$	$\langle h \rangle$ / Å$(Area = \frac{1}{4})$
210	3.18	3.29
220	3.69	4.23
230	4.40	3.46
235	4.80	5.10
240	5.07	5.17
245	5.56	5.66
250	5.88	5.90
255	6.11	6.12
260	6.48	6.83
262	6.55	6.69
264	6.79	7.80
266	7.47	8.18
267	8.13	8.63
268	8.63	9.18
270	9.30	9.32
271	9.42	9.19

Table 4.4. Thickness as a function of temperature for the basal face and the two systems simulates.

Temperature / K	$\langle h \rangle$ / Å($Area = 1$)	$\langle h \rangle$ / Å($Area = \frac{1}{4}$)
210	3.35	3.08
220	3.69	3.15
230	3.55	3.60
240	4.20	4.26
245	4.55	4.87
250	4.98	4.94
260	5.70	5.73
262	6.07	5.70
264	6.16	5.88
266	6.94	6.26
268	7.44	7.44
270	8.49	7.55
271	9.69	8.34

Table 4.5. Thickness as a function of temperature for the prismatic I face and the two systems simulated.

Density profiles for solid like molecules

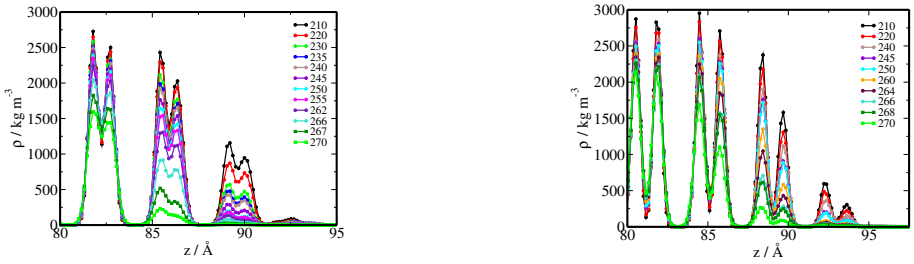

Figure 4.6. Evolution of density profiles for solid like molecules as a function of temperature. a) Basal b) Prismatic I.

Parameters for the fit to the interface potential

face	fit	$A_1/J\,m^{-2}$	$A_2/J\,m^{-2}$	κ/Å	κ_R/Å	$k_{z,R}$/Å	θ/rad
Basal	mf	0.1064	0.00100	0.3085	κ	2.269	10.919
Basal	R	0.1070	0.00161	0.3051	0.429	2.360	10.323
pI	mf	0.0662	0.000148	0.3039	κ	3.149	7.716
pI	R	0.0701	0.00379	0.3103	0.900	3.144	7.796

Table 4.6. Parameters for the fit of simulated disjoining pressures to the model interface potentials of Eq. (4.1) (mf) and Eq. (4.2) for basal and prismatic planes.

Bibliography

[1] K. G. Libbrecht, "Physical dynamics of ice crystal growth," *Annu.Rev.Mater.Res*, vol. 47, pp. 271–295, 2017.

[2] J. G. Dash, A. W. Rempel, and J. S. Wettlaufer, "The physics of premelted ice and its geophysical consequences," *Rev. Mod. Phys.*, vol. 78, pp. 695–741, 2006.

[3] J. P. D. Abbatt, "Interactions of atmospheric trace gases with ice surfaces: Adsorption and reaction," *Chemical Reviews*, vol. 103, no. 12, pp. 4783–4800, 2003. PMID: 14664633.

[4] Y. Furukawa, M. Yamamoto, and T. Kuroda, "Ellipsometric study of the transition layer on the surface of an ice crystal," *J. Cryst. Growth*, vol. 82, no. 4, pp. 665–677, 1987.

[5] T. Kuroda and R. Lacmann, "Growth kinetics of ice from the vapour phase and its growth forms," *J. Cryst. Growth*, vol. 56, no. 1, pp. 189–205, 1982.

[6] T. Kuroda, "Recent developments in theory and experiment of growth kinetics of ice crystals from the vapour phase and their growth forms," *J. Cryst. Growth*, vol. 65, no. 1–3, pp. 27–35, 1983.

[7] B. Weber, Y. Nagata, S. Ketzetzi, F. Tang, W. J. Smit, H. J. Bakker, E. H. G. Backus, M. Bonn, and D. Bonn, "Molecular insight into the slipperiness of ice," *J. Phys. Chem. Lett.*, vol. 9, no. 11, pp. 2838–2842, 2018. PMID: 29741089.

[8] B. Slater and A. Michaelides, "Surface premelting of water on ice," *Nat. Rev. Chem*, vol. 3, pp. 172–188, 2019.

[9] Y. Nagata, T. Hama, E. H. G. Backus, M. Mezger, D. Bonn, M. Bonn, and G. Sazaki, "The surface of ice under equilibrium and nonequilibrium conditions," *Acc. Chem. Res.*, vol. 52, no. 4, pp. 1006–1015, 2019.

[10] H. Dosch, A. Lied, and J. H. Bilgram, "Disruption of the hydrogen-bonding network at the surface of ih ice near surface premelting," *Surf. Sci.*, vol. 366, pp. 43–50, 1996.

[11] X. Wei, P. B. Miranda, and Y. R. Shen, "Surface vibrational spectroscopic study of surface melting of ice," *Phys. Rev. Lett.*, vol. 86, pp. 1554–1557, Feb 2001.

[12] H. Bluhm, D. F. Ogletree, C. S. Fadley, Z. Hussain, and M. Salmeron, "The premelting of ice studied with photoelectron spectroscopy," *J. Phys.: Condens. Matter*, vol. 14, pp. L227–L233, 2002.

[13] V. Sadtchenko and G. E. Ewing, "Interfacial melting of thin ice films: An infrared study," *J. Chem. Phys.*, vol. 116, no. 11, pp. 4686–4697, 2002.

[14] G. Sazaki, S. Zepeda, S. Nakatsubo, M. Yokomine, and Y. Furukawa, "Quasi-liquid layers on ice crystal surfaces are made up of two different phases," *Proc. Nat. Acad. Sci.*, vol. 109, no. 4, pp. 1052–1055, 2012.

[15] H. Asakawa, G. Sazaki, K. Nagashima, S. Nakatsubo, and Y. Furukawa, "Two types of quasi-liquid layers on ice crystals are formed kinetically," *Proc. Nat. Acad. Sci.*, vol. 113, no. 7, pp. 1749–1753, 2016.

[16] W. J. Smit and H. J. Bakker, "The surface of ice is like supercooled liquid water," *Angew. Chem. Int. Ed. Engl.*, vol. 56, no. 49, pp. 15540–15544, 2017.

[17] M. A. Sánchez, T. Kling, T. Ishiyama, M.-J. van Zadel, P. J. Bisson, M. Mezger, M. N. Jochum, J. D. Cyran, W. J. Smit, H. J. Bakker, M. J. Shultz, A. Morita, D. Donadio, Y. Nagata, M. Bonn, and E. H. G. Backus, "Experimental and theoretical evidence for bilayer-by-bilayer surface melting of crystalline ice," *Proc. Nat. Acad. Sci.*, vol. 114, no. 2, pp. 227–232, 2017.

[18] Z. D. Li and J. Z. Wu, "Potential distribution theorem for the polymer-induced depletion between colloidal particles," *J. Chem. Phys.*, vol. 126, pp. 144904–, 2007.

[19] A. Michaelides and B. Slater, "Melting the ice one layer at a time," *Proc. Nat. Acad. Sci.*, vol. 114, pp. 195–197, 2017.

[20] J. Gelman Constantin, M. M. Gianetti, M. P. Longinotti, and H. R. Corti, "The quasi-liquid layer of ice revisited: the role of temperature gradients and tip chemistry in afm studies," *Atmospheric Chemistry and Physics*, vol. 18, no. 20, pp. 14965–14978, 2018.

[21] T. Mitsui and K. Aoki, "Fluctuation spectroscopy of surface melting of ice with and without impurities," *Phys. Rev. E*, vol. 99, p. 010801, Jan 2019.

[22] M. M. Conde, C. Vega, and A. Patrykiejew, "The thickness of a liquid layer on the free surface of ice as obtained from computer simulation," *J. Chem. Phys.*, vol. 129, no. 1, p. 014702, 2008.

[23] H. Dosch, A. Lied, and J. H. Bilgram, "Glancing angle x-ray scattering studies of the premelting of ice surfaces," *Surf. Sci.*, vol. 327, pp. 145–164, 1995.

[24] J. Wettlaufer, "Impurity effects in the premelting of ice," *Phys. Rev. Lett.*, vol. 82, pp. 2516–2519, Mar 1999.

[25] I. Pickering, M. Paleico, Y. A. P. Sirkin, D. A. Scherlis, and M. H. Factorovich, "Grand canonical investigation of the quasi liquid layer of ice: Is it liquid?," *J. Phys. Chem. B*, vol. 122, no. 18, pp. 4880–4890, 2018. PMID: 29660281.

[26] Y. Qiu and V. Molinero, "Why is it so difficult to identify the onset of ice premelting?," *J. Phys. Chem. Lett.*, vol. 9, no. 17, pp. 5179–5182, 2018.

[27] K.-i. Murata, K. Nagashima, and G. Sazaki, "How do ice crystals grow inside quasiliquid layers?," *Phys. Rev. Lett.*, vol. 122, p. 026102, Jan 2019.

[28] A. Hudait and M. T. A. V. Molinero, "Sink or swim: Ions and organics at the ice-air interface," *J. Am. Chem. Soc.*, vol. 139, pp. 10095–10103, 2017.

[29] I. E. Dzyaloshinskii, E. M. Lifshitz, and L. P. Pitaevskii, "General theory of van der waals forces," *Soviet Physics Uspekhi*, vol. 4, no. 2, p. 153, 1961.

[30] P. G. de Gennes, "Wetting: statics and dynamics," *Rev. Mod. Phys.*, vol. 57, pp. 827–863, Jul 1985.

[31] N. Shahidzadeh, D. Bonn, K. Ragil, D. Broseta, and J. Meunier, "Sequence of two wetting transitions induced by tuning the hamaker constant," *Phys. Rev. Lett.*, vol. 80, pp. 3992–3995, 1998.

[32] J. O. Indekeu, K. Ragil, D. Bonn, D. Broseta, and J. Meunier, "Wetting of alkanes on water from a cahn-type theory: Effects of long-range forces," *J. Stat. Phys.*, vol. 95, pp. 1009–1043, 1999.

[33] M. Müller and L. G. MacDowell, "Wetting of a short chain fluid on a brush: First order and critical wetting transitions," *Europhys. Lett*, vol. 55, pp. 221–227, 2001.

[34] M. Müller, L. G. MacDowell, P. Virnau, and K. Binder, "Interface properties and bubble nucleation in compressible mixtures containing polymers," *J. Chem. Phys.*, vol. 117, pp. 5480–5496, 2002.

[35] L. G. MacDowell and M. Müller, "Observation of autophobic dewetting on polymer brushes from computer simulation," *J. Phys.: Condens. Matter*, vol. 17, pp. S3523–S3528, 2005.

[36] L. G. MacDowell and M. Müller, "Adsorption of polymers on a brush: Tuning the order of the wetting transition," *J. Chem. Phys.*, vol. 124, p. 084907, 2006.

[37] J. D. Weeks, "Variational theory of multilayer solid adsorption," *Phys. Rev. B*, vol. 26, pp. 3998–4000, 1982.

[38] D. A. Huse, "Renormalization-group analysis of layering transitions in solid films," *Phys. Rev. B*, vol. 30, pp. 1371–1376, Aug 1984.

[39] A. Patrykiejew, D. Landau, and K. Binder, "Lattice gas models for multilayer adsorption: variation of phase diagrams with the strength of the substrate potential," *Surface Science*, vol. 238, no. 1, pp. 317 – 329, 1990.

[40] A. A. Chernov and L. V. Mikheev, "Wetting of solid surfaces by a structured simple liquid: Effect of fluctuations," *Phys. Rev. Lett.*, vol. 60, pp. 2488–2491, Jun 1988.

[41] P. C. Ball and R. Evans, "Structure and adsorption at gas-solid interfaces: Layering transitions from a continuum theory," *J. Chem. Phys.*, vol. 89, no. 7, pp. 4412–4423, 1988.

[42] R. Evans, "Density functionals in the theory of nonuniform fluids," in *Fundamentals of Inhomogenous Fluids* (D. Henderson, ed.), ch. 3, pp. 85–175, New York: Marcel Dekker, 1992.

[43] J. R. Henderson, "Wetting phenomena and the decay of correlations at fluid interfaces," *Phys. Rev. E*, vol. 50, pp. 4836–4846, Dec 1994.

[44] P. B. Weichman, P. Day, and D. Goodstein, "Preroughening and reentrant layering transitions on triangular lattice substrates," *Phys. Rev. Lett.*, vol. 74, pp. 418–421, Jan 1995.

[45] A. A. Chernov and L. V. Mikheev, "Wetting and surface melting: Capillary fluctuations vs. layerwise short-range order," *Physica. A*, vol. 157, pp. 1042–1058, 1989.

[46] J. D. Weeks, "Statics and dynamics of the roughening transition: A self-consistent calculation," in *Ordering in Strongly Fluctuating Condensed Matter Systems* (R. T., ed.), pp. 319–324, Plenum, New York, 1980.

[47] M. Elbaum and M. Schick, "Application of the theory of dispersion forces to the surface melting of ice," *Phys. Rev. Lett.*, vol. 66, pp. 1713–1716, 1991.

[48] M. Maruyama, T. Nishida, and T. Sawada, "Crystal shape of high-pressure ice ih in water and roughening transition of the (10-10) plane," *The Journal of Physical Chemistry B*, vol. 101, no. 32, pp. 6151–6153, 1997.

[49] M. Maruyama, "Roughening transition of prism faces of ice crystals grown from melt under pressure," *J. Cryst. Growth*, vol. 275, no. 3-4, pp. 598–605, 2005.

[50] W. Lechner and C. Dellago, "Accurate determination of crystal structures based on averaged local bond order parameters," *J. Chem. Phys.*, vol. 129, no. 11, p. 114707, 2008.

[51] J. Benet, P. Llombart, E. Sanz, and L. G. MacDowell, "Premelting-induced smoothening of the ice-vapor interface," *Phys. Rev. Lett.*, vol. 117, p. 096101, Aug 2016.

[52] J. Benet, P. Llombart, E. Sanz, and L. G. MacDowell, "Structre and fluctuations of the premelted liquid film of ice at the triple point," *Mol. Phys.*, pp. 1–19, 2019. In press.

[53] P. Llombart, R. M. Bergua, E. G. Noya, and L. G. MacDowell, "Structure and water attachment rates of ice in the atmosphere: Role of nitrogen," *Phys. Chem. Chem. Phys*, pp. –, 2019.

[54] A. H. Nguyen and V. Molinero, "Identification of clathrate hydrates, hexagonal ice, cubic ice, and liquid water in simulations: the chill+ algorithm," *J. Phys. Chem. B*, vol. 119, no. 29, pp. 9369 – 9376, 2014.

[55] E. Chacon and P. Tarazona, "Characterization of the intrinsic density profiles for liquid surfaces," *J. Phys.: Condens. Matter*, vol. 17, pp. S3493–S3498, 2005.

[56] M. Jorge, P. Jedlovszky, and M. N. D. S. Cordeiro, "A critical assessment of methods for the intrinsic analysis of liquid interfaces. 1. surface site distributions," *J. Phys. Chem. C*, vol. 114, no. 25, pp. 11169–11179, 2010.

[57] M. Sega, B. Fabian, and P. Jedlovszky, "Layer-by-layer and intrinsic analysis of molecular and thermodynamic properties across soft interfaces," *J. Chem. Phys.*, vol. 143, no. 11, p. 114709, 2015.

[58] B. Derjaguin, "Modern state of the investigation of long-range surface forces," *Langmuir*, vol. 3, no. 5, pp. 601–606, 1987.

[59] J. R. Henderson, "Statistical mechanics of the disjoining pressure of a planar film," *Phys. Rev. E*, vol. 72, no. 6, p. 051602, 2005.

[60] J. Benet, J. G. Palanco, E. Sanz, and L. G. MacDowell, "Disjoining pressure, healing distance, and film height dependent surface tension of thin wetting films," *J. Phys. Chem. C*, vol. 118, pp. 22079–22089, 2014.

[61] D. Nenow and A. Trayanov, "Thermodynamics of crystal surfaces with quasi-liquid layer," *J. Cryst. Growth*, vol. 79, no. 1, pp. 801–805, 1986.

[62] K. Binder, "Finite size analysis of ising model block distribution functions," *Z. Phys. B*, vol. 43, pp. 119–140, 1981.

[63] D. P. Landau and K. Binder, *A Guide to Monte Carlo Simulations in Statistical Physics*. Cambridge: Cambridge University Press, 2000.

[64] H. Asakawa, G. Sazaki, K. Nagashima, S. Nakatsubo, and Y. Furukawa, "Prism and other high-index faces of ice crystals exhibit two types of quasi-liquid layers," *Crystal Growth & Design*, vol. 15, no. 7, pp. 3339–3344, 2015.

[65] W. J. Smit, F. Tang, M. A. Sánchez, E. H. G. Backus, L. Xu, T. Hasegawa, M. Bonn, H. J. Bakker, and Y. Nagata, "Excess hydrogen bond at the ice-vapor interface around 200 k," *Phys. Rev. Lett.*, vol. 119, p. 133003, Sep 2017.

Chapter 5

Structural transitions and bilayer formation of CTAB aggregates

Pablo Llombart[1,2]*, Mauricio Alcolea-Palafox*[2]*, Luis G. MacDowell*[2] *and Eva G. Noya*[1]

(1) Instituto de Química Física Rocasolano, CSIC, Calle Serrano 119, 28006 Madrid, Spain
(2) Departamento de Química Física, Facultad de Ciencias Químicas, Universidad Complutense de Madrid, 28040 Madrid, Spain

Abstract

Controlled CTAB self-assembly is an essential prerequisite for the formation of gold nanorods with tailored shape and monodispersity. In this paper, we exploit the use of salt concentration and co-surfactant decanol for the preparation of CTAB aggregates with different morphologies. To this end we use a model of CTAB recently developed by ourselves, and perform electronic structure calculations in order to improve current point charge parametrization of decanol. Using molecular dynamics simulations with the new models, we find a sequence of structural transitions of CTAB aggregates induced by salt concentration and added cosurfactant. In pure solutions, CTAB aggregates form spherical micelles with a compact ionic shell and a diffuse double layer that can be qualitatively described with Poisson-Boltzmann theory. Addition of decanol as a cosurfactant induces a sequence of dramatic structural transitions at low surfactant concentration and allows the stabilization of compact ordered bilayers in a well defined range of intermediate decanol/CTAB ratios. At low and high decanol/CTAB ratios spherical micelles are transformed into wormlike cylindrical micelles. At intermeidate decanol/CTAB ratios, fully formed bilayers are observed, with surfactants exhibitting a compact structure with strong positional and orientational order. We discuss how the controlled self-assembly of compact CTAB bilayers at low global CTAB concentration can pave the way for the selective passivation of gold facets and the controlled formation of monodisperse gold nanorods.

Introduction

Cetyltrimethylammonium bromide (CTAB) is a cationic surfactant that is commonly employed as additive in the synthesis of nanoparticles and nanostructured materials, acting either as template[1] or as a colloidal stabilizer and shape directing agent[2]. Our interest on the assembly of CTAB surfactant stems precisely

from their use in the synthesis of gold nanorods by the seeded growth method[2, 3, 4]. In this method 1-2 nm crystalline gold seeds are dispersed in solution and subsequently grown by reduction of gold salts. The morphology of the nanoparticles is often controlled by addition of CTAB surfactant[2], organic additives (such as aromatic[5] or long chain alcohols, e.g. decanol[6]) and silver ions (that act as impurities that likely affect the chemistry at the gold surfaces, and thus their growth[7]), and other parameters, such as pH, temperature and reducing agents[8]. Early studies argued that CTAB could induce anisotropic growth of gold nanoparticles as a consequence of its different binding affinity to different gold crystal facets. Based on diffraction (small angle X-ray and neutron) scattering and transmission electron microscopy experiments it was initially thought that CTAB formed bilayers around gold nanoparticles[9]. Recent computer simulation studies, however, suggest that the gold surface is rather covered by a heterogeneous assembly of micellar aggregates.[10, 11, 4] These studies put forward that it is important to understand the assembly mechanism of CTAB and CTAB/organic cosurfactants on gold surfaces exposing different atomic planes as well as the usefulness of MD simulations for that aim, as often experiments report indirect information that it is difficult to interpret.

The assembly behavior of CTAB in aqueous solution has been extensively studied experimentally.[12, 13, 14, 15, 16] The critical micellar concentration (CMC, the concentration at which micelles start to form and above which all the added surfactant goes to the aggregates) is around 1 mM at room temperature [13, 14, 17], and there are also evidences that CTAB might exhibit a second CMC at a surfactant concentration 0.24 M that separates a slow from a fast growing regime[15]. Experimental information about aggregation number (i.e., the number of surfactant molecules per micelle) is not very consistent due to the difficulties in experimentally accessing this property. Quirion and Magid[16] performed neutron and light scattering experiments and concluded that at the CMC, CTAB micelles are roughly spherical and contain about 100 surfactant molecules, the aggregation number increasing with concentration up to 300 molecules at a 0.3 molal solution. This seems to be a rather general trend of cationic surfactants.[18] They also found that aggregates adopt rod-like shapes already at relatively low concentrations. Törnblom *et al*[19] performed nuclear magnetic resonance experiments and reported aggregation numbers within 100-400 and rod-like shapes for 0.12-0.48 molal CTAB solutions, consistent with previous suggestions.[12] More recent experiments report a lower aggregation number at the CMC, of about 60-68[17]. The addition of bromide salts yields larger aggregation numbers and higher tendency to adopt non-spherical shapes[19, 20, 16, 21, 22, 23]. Organic additives, such as alcohols and weakly polar aromatic molecules, are known to induce morphological transitions in CTAB aggregates[24, 25, 26, 27, 28, 29, 30, 31]. For example, small amounts of long chain alcohols (0.005 to 0.03 M) induce a transition from rod-like to worm-like micelles[25]

Despite the relevance of CTAB, the number of simulations addressing its assembly behavior at atomic scale are relatively scarce[21, 32, 33, 34, 35]. These studies have been often aimed at providing information not easily accessible in experiments, such as the aggregation number[32, 33, 34]. Quite often simulations are performed for pre-assembled aggregates but, due to the high computational cost, cover rather short times (tens of nanoseconds). One notable exception is the work of Storm *et al.*[34] in which simulations were started from the unassembled state and extended over rather long times (100 ns). However, aggregation numbers obtained in this way were rather small compared to experimental data, which indicates that equilibrium might not have been reached. This is not so surprising given that simulations using coarse grained models indicate that even microseconds might not be enough to attain equilibrium in surfactant aggregation simulations[36]. Thus, recent work is starting to focus on the search of reliable coarse-grained models that allow to access such unusually long simulation times[35].

Here we report an extensive study of the structure of CTAB aggregates in aqueous solution as a function of micelle aggregation number. The effects of adding bromide salt and decanol cosurfactant are

also investigated. This work extends our previous study of the adsorption of CTAB micelles on gold.[4, 6] The results provide a complementary picture with valuable information. On one hand, they allow us to assess the reliability of our previous simulations by comparing with available data, and, on the other, they provide access to detailed microscopical description of the structure of the aggregates that is not always easily accessible in the laboratory.

Methods

Simulation details

The assembly behavior of CTAB in aqueous solution was investigated by means of Molecular Dynamics simulations. CTAB is dissociated into CTA^+ and Br^- in solution. Both CTA^+ and decanol were described using the GROMOCS 53a6 force field[37], which consists of a united atom model with Lennard-Jones centers located at each carbon atom of the hydrocarbon chain. CTA^+ carries interaction sites also at the nitrogen and the three methyl groups bound to it, whereas decanol has two additional sites at the oxygen and hydrogen atoms of the hydroxyl group. CTA^+ and decanol heads carry charges. Those charges were estimated from *ab initio* calculations of the isolated molecules (CTA^+ ion and decanol) to second order Moller-Plesset perturbation theory[4]. Charges of CTA^+ anion were already reported in previous work[4], whereas those of decanol are provided in Figure 5.1. Bromide and sodium anions were described using a Lennard-Jones center with a point charge at the center, whereas the SCP model was used for water.

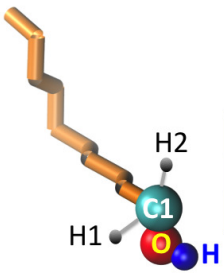

GROUP	CHARGE / eV
C1,H1,H2 / CH_2	-0.027, 0.178, 0.178 / 0.325
O	-0.808
H	0.483

Figure 5.1. Distribution of charges in decanol as obtained from *ab initio* calculations. Carbon and hydrogen atoms forming the CH_2 group are merged in a single interaction site with an effective charge obtained by summing the charges of the three atoms.

All simulations were performed in the NpT ensemble using the package GROMACS[38]. Equations of movement were solved using the velocity-Verlet algorithm with a time step of 3 fs. Temperature was controlled using a velocity scaling thermostat with a relaxation time of 2 ps[39], whereas a Berendsen barostat with a relation of 2 ps was used for pressure coupling[40]. Temperature and pressure were set to ambient conditions, namely, T=298 K and p=1 bar. Periodic boundary conditions were used along the three directions of space.

Firstly we studied the stability of CTAB micelles of different aggregation number. Spherical micelles with sizes between $N_{CTAB} = 60$ to 240 were generated with Packmol[41]. Surfactant molecules were initially placed within a sphere of increasing radius with N_{CTAB} to avoid overlaps (Table 5.1). Each micelle was placed at the center of a simulation box leaving another 3 nm along the three dimensions of space. We expect that this distance is large enough so that interaction between the micelle and its images

N_{CTAB}	N_{H_2O}	R_{init}/nm	$\langle L \rangle$/nm	M (mol/L)
60	32162	2.20	10.07	0.10
75	31967	2.27	10.08	0.12
90	31747	2.39	10.09	0.15
100	31588	2.46	10.08	0.16
120	31318	2.63	10.10	0.19
150	41184	2.86	11.05	0.19
240	39823	3.17	11.07	0.29

Table 5.1. Number of CTAB and water molecules employed in each simulation, as well as the initial radius of the micelles R_{init}. The average edge of the cubic simulation box $\langle L \rangle$ and the CTAB concentration are also given.

is small. These structures were then solvated with water molecules (between 30,000 and 40,000 molecules were needed depending on the number of CTAB molecules) and the appropriate number of counterions (Br^-) to make the system neutral. Bromide ions were randomly placed within a spherical shell of width 0.5 nm around the micelles.

In a second set of simulations the stability of a bilayer was investigated. For that purpose, we started another simulation in which 240 CTAB molecules were arranged forming a double layer of width 2.7 nm with a packing density of 2.70 nm^{-2}, which is close to the maximum packing fraction[10]. As before, a 3 nm wide layer containing 12002 water molecules was placed at each side of the bilayer, in which bromide ions were randomly distributed. Besides the pure aqueous solution, we performed another simulation in 0.25 M NaBr solution (which corresponds to 75 NaBr in our simulations) to study the effect of the ionic strength on the stability of the bilayer. This salt concentration is typically used in the seeded growth of gold nanorods using CTAB as colloidal stabilizers[4]. Given that in the synthesis of gold nanorords CTAB and gold seeds are immersed in a salt solution (which includes gold and silver salts at typical concentrations of ≈0.01 M)[4], besides the pure aqueous solution, we performed another simulation in 0.25 M NaBr solution (which corresponds to 75 NaBr in our simulations) to study the effect of the ionic strength on the stability of the bilayer. Note that this salt concentration is much higher than that typically used in the seeded growth of gold nanorods, but it is chosen so high to prove that an increased ionic strength cannot explain the stabilization of CTAB bilayers.

Finally, we considered the assembly of CTAB in the presence of cosurfactant decanol. The initial configurations were generated by placing 240 CTA^+ chains forming a bilayer and in which a varying number of decanol molecules (up to a maximum of 72) were randomly inserted. The number density of CTA^+ in the pre-assembled bilayer was again 2.70 units nm^{-2} The system was solvated with a 3 nm wide water layer, with the appropriate number of bromide ions to achieve electrostatic neutrality. More details about the simulated systems are provided in Table 5.2. In all the simulations starting from a bilayer, pressure was controlled using anisotropic Parrinello-Rahman barostat.

Prior to the simulations, the initial configurations were minimized using a steep descendent method until the maximum force converged at 1000 kJ mol^{-1} nm^{-1} to avoid atomic overlaps. The first 75 ns were used for equilibration and averages were taken over the last 75 ns of the simulation.

$r_{DeOH/CTAB}$	$\langle L_x \rangle \times \langle L_y \rangle \times \langle L_z \rangle$
0.000	10.544×10.368×4.599
0.042	10.830×10.650×4.389
0.083	9.801×9.637×4.456
0.125	10.701×10.522×4.550
0.133	7.553×7.427×9.016
0.146	7.368×7.511×8.834
0.167	7.741×7.612×8.702
0.200	7.723×7.595×8.696
0.225	7.638×7.511×8.925
0.250	9.265×9.111×6.224
0.300	11.063×10.878×4.363

Table 5.2. Decanol/CTAB ratios studied in this work. In all these simulations, the bilayer contains 240 CTAB surfactants and is solvated with 12002 water molecules. This corresponds to roughly a 0.8 M CTAB concentration. CTAB and decanol molecules were initially placed in a bilayer of width 2.7 nm. The average edges of the box ($\langle L_x \rangle$, $\langle L_y \rangle$ and $\langle L_z \rangle$) at the end of the simulations are also given.

Structural analysis of CTAB aggregates

The structure of the CTAB aggregates was investigated by plotting two-dimensional density maps projected on planes perpendicular to their three principal moments of inertia. For the case of spherical (or nearly spherical) micelles we also calculated their radii from the radius of gyration R_g using the relation[34, 42]

$$R = \sqrt{\frac{5}{3}} R_g \tag{5.1}$$

The radii can also be estimated from the maximum of the density profiles of the CTA^+ heads measured from the center of mass of the micelles[34, 10]. The asphericity was quantified by evaluating the eccentricity ϵ defined as[34, 43]:

$$\epsilon = 1 - \frac{I_{min}}{I_{av}} \tag{5.2}$$

where I_{min} is the lower moment of inertia along the principal axes and I_{av} is the average of the three moments of inertia. The eccentricity is zero for a sphere and tends to unity for a needle-like aggregate.

Finally, in the simulations with cosurfactants, the orientational order of CTA^+ was monitored by evaluating the order parameter S_z that measures the average of the second Lengendre polynomial:

$$S_z = \frac{1}{2} \langle 3 \cos^2 \theta - 1 \rangle \tag{5.3}$$

where angular brackets denote ensemble average, θ is the angle formed by the head to tail vector of each CTAB molecule and the $z-$axis. The parameter S_z adopts a value close to zero for an isotropic phase and one for a completely ordered state.

Modeling of counterion charge distribution with Poisson-Boltzmann equation

Besides studying the shape of the micelles, we also analyzed the charge distribution in the system. The distribution of ions in a solution around a charged impenetrable sphere can be estimated from the Poisson-Boltzmann (PB) equation. The potential $\Psi(r)$ created by a sphere of diameter d and charge Ze at a given distance r can be obtained by solving Poisson electrostatic equation:

$$\nabla^2\Psi(r) = -\frac{4\pi}{\epsilon}\rho(r) \tag{5.4}$$

where $\rho(r)$ is the charge density due to the ionic atmosphere at distance r (the central charge does not contribute to this charge density) and $\epsilon = \epsilon_0\epsilon_r$ is the permittivity of the medium. The charge density is related to the electrostatic potential through the Maxwell-Boltzmann distribution:

$$\rho(r) = zec_0 \exp\left(-\frac{ze\Psi(r)}{k_BT}\right) \tag{5.5}$$

where c_0 is the concentration of counterions with charge ze in the solution at a reference point r_0, k_B is the Boltzmann constant and T is the temperature. Note that in Eq. 5.5 the volume occupied by the counterions is ignored. This approximation is completely justified in this case, as both the size and concentration are small. Combining Eqs. 5.4 and 5.5 it follows:

$$\nabla^2\Psi(r) = -\frac{4\pi ze}{\epsilon}c_0 \exp\left(-\frac{ze\Psi}{k_BT}\right) \tag{5.6}$$

Introducing the reduced potential $y = -\beta e\psi$, and taking into account that bromide counterions carry a unit (negative) charge $z = -1$, this equation can be written as:

$$\nabla^2 y(r) = -4\pi l_B c_0 e^{y(r)} \tag{5.7}$$

where $l_B = e^2\beta/\epsilon$ is the Bjerrum length. Considering that the relative permittivity of SPC liquid water is $\epsilon_r = 65.6(2)$ at room conditions[44], the Bjerrum length is about 8.6 Å for our system. As we are dealing with a system with spherical symmetry, it is convenient to express Eq. 5.7 in spherical coordinates[45]:

$$\nabla^2 y = \frac{d^2y}{dr^2} + \frac{2}{r}\frac{dy}{dr} = -4\pi l_B c_0 e^y \tag{5.8}$$

This is a second order differential equation and, therefore, two boundary conditions are needed. One of these conditions is obtained by imposing charge neutrality at distance R, i.e., the electric field must vanish at that distance:

$$\left.\frac{dy}{dr}\right|_{r=R_c} = 0 \tag{5.9}$$

Here the radius of the confining sphere R_c is chosen approximately equal to half the simulation box. The second boundary condition imposes that the electric field at the micelle surface corresponds to that generated by the micelle total charge Ze:

$$\left.\frac{dy}{dr}\right|_{r=R_m} = \frac{Zl_B}{R_m^2} \tag{5.10}$$

where R_m is the micelle radius. The differential Eq. 5.8, together with the boundary conditions given by Eqs. 5.9 and 5.10, was solved numerically using Mathematica[46].

Once the electrostatic potential is known, the counterion concentration can be obtained by substituting the potential in Eq. 5.5. From there it is also possible to calculate the integrated charge inside an sphere of radius r:

$$Z(r) = Z_0 - \int_{R_m}^{r} \rho(r_1) 4\pi r_1^2 dr_1 \tag{5.11}$$

This function will be compared with that obtained from the simulations to assess the ability of Poisson-Boltzmann theory to describe the charge distribution of the micelles.

Results

Stability and morphology of CTAB aggregates

Let us start by presenting the results for the stability of pre-assembled micelles with a number of CTAB molecules between 60 and 240 (N_{CTAB}=60, 75, 90, 100, 120, 150 and 240). As can be seen in Fig. 5.2, after 150 ns, all micelles remain stable, except for the largest considered size (N_{CTAB}=240), in which the initial pre-assembled aggregate breaks up into two smaller micelles of sizes N_{CTAB}=105 and 135. Specific results for all the considered sizes are provided in the Supplementary Material.

Even though our simulations are rather long (150 ns), it cannot be discarded that the system has not reached equilibrium, i.e., that smaller micelles would also break up if longer simulations were performed. Indeed, there are evidences that indicate that even microseconds might not be enough to reach equilibrium aggregation numbers[36]. Even admitting that our simulations might not have yet converged, the fact that the micelle with 240 surfactants becomes unstable during the 100 ns of the simulation marks an upper limit for the aggregation number for 0.1-0.3 M concentrations. Thus we can conclude that aggregation number is lower than 240 and possibly higher than 150 within this concentration range. Our results are consistent with previous simulations that also showed that CTAB micelles with up to 120 surfactants were stable[33]. Here we demonstrate that these micelles are stable over much longer times and up to a size of at least 150. Note, however, that this value is much higher than that obtained from simulations starting from unassembled surfactant solutions, where aggregations ranging from 23 at 0.1 M CTAB concentration to 110 at 0.73 M were reported [34]. Discrepancies between simulations starting from the assembled and unassembled states are just reflecting the difficulty in attaining equilibrium when simulating surfactant aggregation. Nevertheless, aggregation numbers derived from pre-assembled simulations are much more in line with those reported experimentally, typically 100-180 within this concentration range[16, 19], which suggests that starting from a pre-assembled state seems to be a reasonable approach when equilibration times are higher than the time scales accessible to simulations.

Regarding the shape of the micelles, visual inspection of the trajectories reveals that at lower aggregation numbers micelles are roughly spherical, whereas at higher aggregation number they adopt prolate ellipsoidal shapes (see Fig. 5.2, top panel). Asphericity becomes evident by projecting the density of the CTAB carbon atoms onto the planes perpendicular to the three principal moments of inertia (see bottom panels of Fig. 5.2). Indeed, these plots show that micelles are not perfectly spherical even at the smaller considered size (N_{CTAB}=60). As can be seen in Figure 5.3 and Table 5.3, eccentricity, estimated from Eq. 5.2, remains almost constant up to $N_{CTAB} \approx 100$, exhibiting only a mild increase with size, and grows quite rapidly above this threshold. For example, eccentricity of the N_{CTAB} =150 micelle is about $\epsilon = 0.41 \pm 0.10$ to be compared to $\epsilon = 0.15 \pm 0.02$ at N_{CTAB} =100. From these results it can be concluded that simulations predict a transition from spherical to rod-like aggregates at size N_{CTAB} =100. These results are consistent with experimental evidences that point to spherical micelles at the CMC and to prolate ellipsoidal shapes at similar concentrations to those studied here[16, 19].

The radius of the aggregates was estimated both form the gyration radius (using Eq. 5.1) and from the maximum of the density distribution of the nitrogen atom of the CTA^+ head group (shown in Fig. 5.4, top panel). Both routes give rather consistent results (see Fig. 5.3), differences becoming more evident as size increases. These slight discrepancies are simply reflecting the increasing eccentricity of the aggregates, that make that the nitrogen head atom density distribution more asymmetrical for larger aggregate sizes. Interestingly, micelle radii follow a linear relation with $N_{CTAB}^{1/3}$, which means that even though micelles are not spherical, the spherical approximation can be used to make predictions of the average radius from the value of N_{CTAB}. As can be seen in Fig. 5.3, our values of micelle radii and eccentricity are in good agreement with previous simulation studies[33, 34, 10] and with experimental data[19].

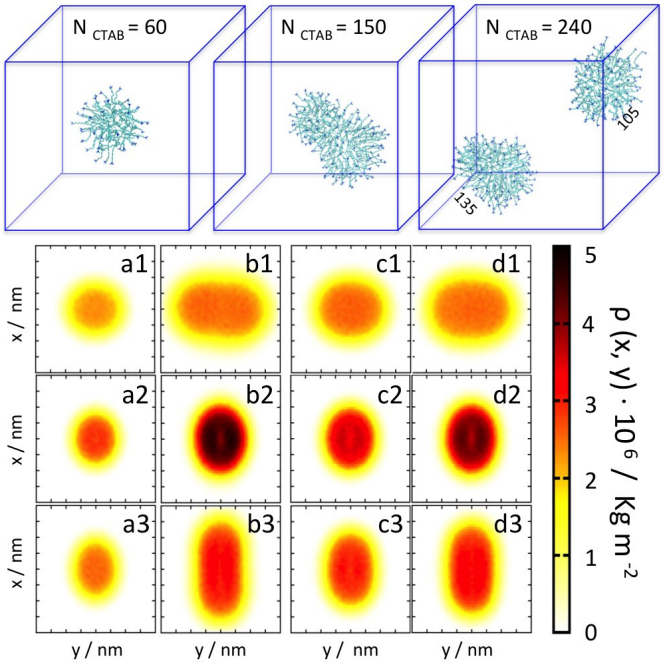

Figure 5.2. Top panels: Final configurations of simulations starting from pre-assembled micelles with N_{CTAB} =60, 150 and 240. In the system with N_{CTAB} =240, the initial aggregate breaks up into two smaller micelles of sizes N_{CTAB} =135 and 105. Bottom panels: Bidimensional atomic density profiles of CTA^+ for N_{CTAB} =60 (a1, a3, a3), N_{CTAB} =150 (b1, b2, b3) and N_{CTAB} =240 (c1,c2,c3 show the profiles for N_{CTAB} =105 and d1, d2, d3 for N_{CTAB} =135) projected on planes perpendicular to the three principal moments of inertia (top, middle and bottom rows show, respectively, the normal planes to I_2, I_1 and I_3, being $I_1 > I_2 > I_3$).

Besides the aggregate morphology, the structure of the bromide ions surrounding CTA^+ micelles was also analyzed. The average distribution of ions as a function of the distance to the micelle center of mass is shown in Fig. 5.4 (central panel). This distribution exhibits two differentiated regimes; a first one at short distances from the micelle surface in which bromide density decreases rapidly and a second regime at long distances in which bromide density decays very slowly. This structure is very similar to that of an electric double layer with a first relatively narrow region (or Stern region) in which contraions are strongly adsorbed onto a charged surface,[32] followed by a second diffuse layer which, due to charge screening effects, is more loosely attracted to it. The first layer extends over about 1.0 nm for the micelle

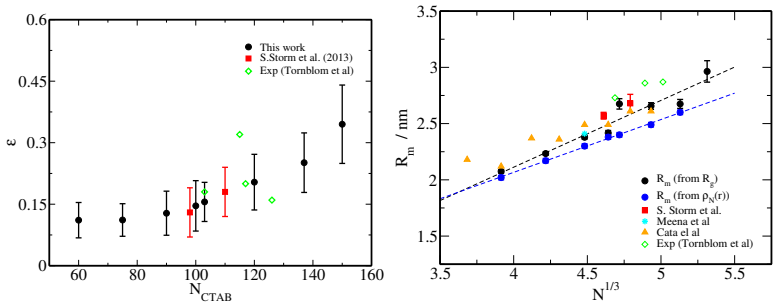

Figure 5.3. Evolution of the eccentricity (top panel) and radius (bottom panel) of micelles as a function of number of CTAB molecules. For comparison data taken from the literature are also shown[34, 33, 10]

.

N_{CTAB}	ε	R_m^1 / nm	R_m^2 / nm
60	0.11 ± 0.04	2.07 ± 0.02	2.02 ± 0.02
75	0.11 ± 0.04	2.23 ± 0.02	2.17 ± 0.02
90	0.13 ± 0.05	2.38 ± 0.02	2.30 ± 0.02
100	0.15 ± 0.06	2.42 ± 0.02	2.38 ± 0.02
105	0.16 ± 0.05	2.68 ± 0.04	2.40 ± 0.02
120	0.20 ± 0.07	2.67 ± 0.03	2.49 ± 0.02
135	0.25 ± 0.07	2.67 ± 0.04	2.60 ± 0.02
150	0.34 ± 0.10	2.96 ± 0.10	–

Table 5.3. Eccentricity and radii of CTAB micelles as a function of the number of CTAB molecules. The radii were evaluated using two different routes: from the gyration radii (R_m^1) and from the maxima in the density distribution of nitrogen atoms (R_m^2).

with $N_{CTA+} = 60$ (i.e., about 3 bromide molecular diameters) and becomes broader for larger micelle sizes, specially for N_{CTA+} =120 and 150. The thickness of this first layer is larger than that expected to form around an spherical particle (for which this layer is of the order of the ion molecular diameter). This is just reflecting the aspherical shape and the softness of the micelle. Indeed, this layer becomes rather wide for micelles with sizes above $N_{CTA+} > 100$, threshold above which the asphericity of micelles increases more rapidly. It is also interesting to note that, for all the considered micelle sizes, the diffuse layer extends over quite long distances. Indeed, as can be seen in Fig. 5.4 (middle panel), the bromide density does not decay to zero at distances equal to half the edge of the simulation box (roughly 5 nm for all simulations). This means that ions in these diffuse layers are the result of the superposition of the diffuse layers generated by the central micelle and by its periodic images.

Given the evident similarity between the measured ion distribution around the micelle and that expected for ions around a charged impenetrable sphere, we decided to estimate the distribution of ions around a hard sphere of diameter approximately equal to that of the micelle by solving Poisson-Boltzmann equation (Eq. 5.8), together with the boundary conditions given by Eqs. 5.9 and 5.10. Besides the radius of the central sphere (which was set to the radius of the micelles given in Table 5.3), we must provide the radius of the confining sphere (i.e. the distance at which electrical neutrality is attained). As mentioned before, in our simulations the counterion density goes to zero at distances longer than half the edge of the simulation box ($L/2$). This situation can be accounted for by setting a radius of the confining sphere larger than $L/2$. This boundary condition barely affects the core counterion shell, but it changes the decay

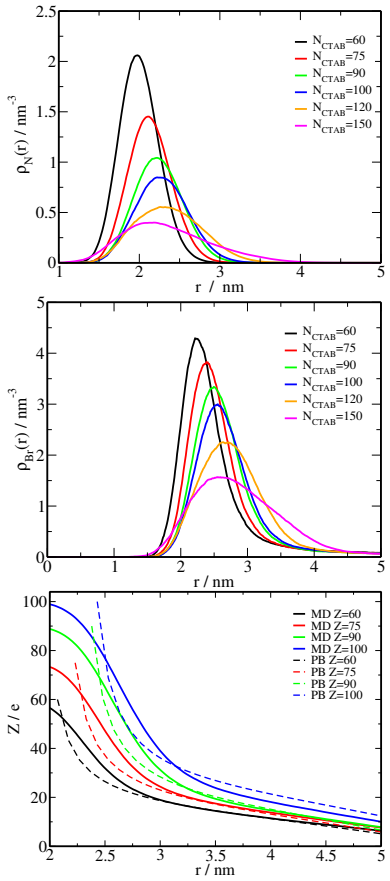

Figure 5.4. Top and middle panels: average number density of nitrogen atoms (top) and bromide ions (middle panel) measured from the center of mass of the CTA^+ micelles. Bottom panel: Charge within a sphere of radius r measured from the center of the micelle as obtained from simulations (solid lines) and from the PB equation solved for an impenetrable sphere of diameter approximately equal to that of the micelles (dashed lines).

slope of the outer diffusive cloud. As a matter of fact, the slope of the diffusive shell is best reproduced for a confining sphere of radius of about 5.7 nm (as compared to $L/2 \approx 5$ nm). In principle, increasing the range of the confining radius is equivalent to imposing that the charge at distance $L/2$ adopts a finite positive value (instead of zero). Once the ion density is known, the integrated charge within a sphere of radius r was calculated using Eq. 5.11. This quantity is compared with that obtained from the simulations. Given that micelles are soft entities, the positive charge of the CTA^+ heads is also distributed over a layer of a certain thickness on the micelle surface. However, we considered here that all the micelle's positive charge was located at its center of the mass, so that this plot shows the evolution of bromide density, regardless of the distribution of the positive charge carried by the surfactant heads. The integrated charge obtained from PB equation and from simulation are compared in Fig.5.4 (bottom panel). As can be seen, the solution of PB equation around an sphere reproduces qualitatively the bromide distribution around the micelles (although results are not obviously quantitative). There is a first regime close to the micelle surface where charge decreases rapidly followed by a second regime at intermediate distances in which the charge decays more slowly. Unsurprisingly, larger deviations between PB and simulations emerge at shorter distances, which is just a consequence of the micelle softness. Intuitively, one might think that increasing

salt concentration (i.e, reducing the Debye screening length) might give rise to a better agreement between the simulated charge distribution and PB equation. However, added salt is known to promote the formation non-spherical micelles[19, 20, 16, 21, 22, 23], which, on the other hand, lead to a poorer performance of PB equation.

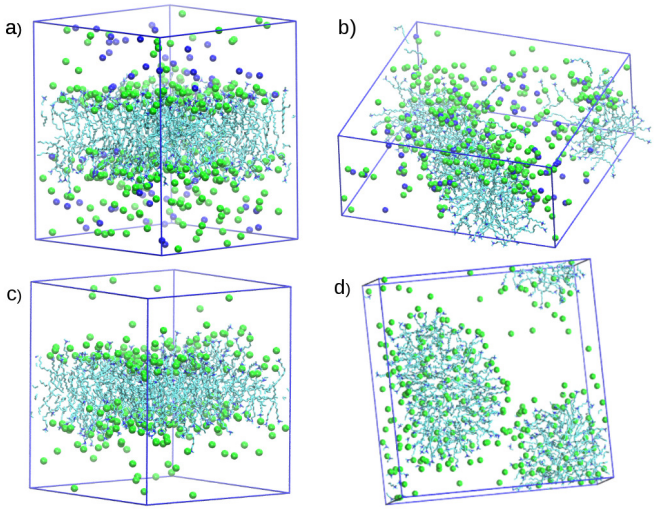

Figure 5.5. Evolution of a CTAB pre-assembled micelle in an 0.25 NaBr aqueous solution (a) and in pure water (c). CTAB bilayer is unstable in both situations evolving to (b) a cylindrical aggregate in the presence of salt and (d) to two micelles of sizes N_{CTAB}=103 and 137 in pure water.

Finally we also studied whether CTAB bilayers become stable at higher CTAB concentration or by addition of bromide salt. For that purpose we started a new set of simulations of a pre-assembled bilayer in water and in a 0.25 M NaBr aqueous solution. CTAB concentration was now about 0.8 M, i.e., more than twice that of the simulations of the pre-assembled micelles (see Table 5.1). As can be seen in Fig. 5.5, bilayers are unstable in both cases, evolving to two micelles of sizes N_{CTAB}=103 and 137 in water and to a cylindrical aggregate in the salt solution. A more detailed analysis of the structures formed are provided in the Supplementary Material. Curiously, CTAB final aggregation state in water is remarkably similar to that obtained starting from a pre-assembled micelle in spite of the rather different CTAB concentrations (different by a factor of two). Thus our simulations suggest that aggregation number does not change much with concentration within this concentration range. The morphological transition from spherical to elongated rod-shaped aggregates by the addition of bromide salts has also been observed experimentally [16, 19].

Stabilization of bilayers by cosurfactant n-decanol

Once we have seen that the bilayer is not stable at CTAB concentrations within the range of 0.2-0.8 M, we checked whether it could be stabilized by adding decanol as cosurfactant. As mentioned before, our motivation stems again from recent experimental studies that show that gold seeds synthesized in the presence of decanol cosurfactant adopt the optimal shape for subsequent growth into monodisperse nanorods, which was explained by the formation of highly ordered bilayers on specific facets of the gold surface[6]. In view of this, an interesting question is whether bilayers can be stabilized by the sole presence of decanol or attachment to specific gold surfaces is also necessary. To investigate the stability of free decanol/CTAB bilayers, we performed simulations of pre-assembled CTAB bilayers with a certain number of decanol molecules

randomly distributed, covering decanol/CTAB ratios between 0 and 0.30. We found that when the ratio of decanol to CTAB molecules ($r_{DeOH/CTAB}$) is lower than about 0.10 the pre-assembled bilayer evolves to percolating worm-like aggregates, that become straighter as the ratio of decanol/CTAB increases. At intermediate decanol ratios ($r_{DeOH/CTAB}$=0.133, 0.146, 0.167, 0.200, and 0.225) bilayers remain stable over the 150 ns of simulations. But if the concentration of decanol is further increased ($r_{DeOH/CTAB}$=0.25 and 0.30), the bilayer becomes again unstable transforming now into nearly straight cylindrical aggregates. The final configurations, as well as density profiles projected on planes perpendicular to the three principal moments of inertia, for three representative cases in these three regimes are depicted in Fig. 5.6. Analysis of all the remaining simulations are collected in the Supplementary Material.

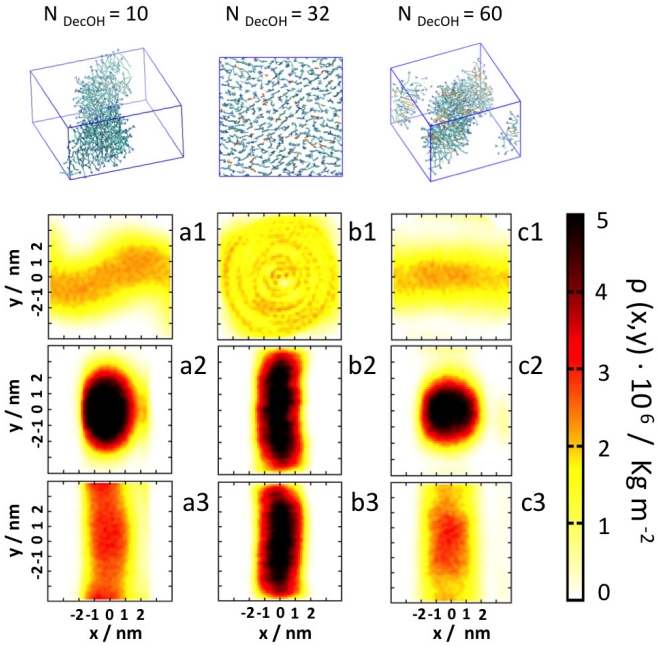

Figure 5.6. Top panels: Final configurations of simulations of pre-assembled CTAB/decanol bilayer of varying decanol concentrations, namely $r_{DeOH/CTAB}$=0.042 (left), 0.133 (middle) and 0.25 (right). Bottom panels: CTAB atomic density profiles projected on planes perpendicular to the principal moments of inertia.

Visual inspection of instantaneous configurations, as well as density maps projected on a plane parallel to the bilayer indicate that CTAB molecules exhibit a large degree of orientational and translational order in a plane parallel to the bilayer. The orientational order of CTA^+ was quantified by measuring the order parameter S_z (Eq. 5.3). Its evolution with the decanol/CTAB ratio is shown in Fig. 5.7 (and in the Supplementary Material). The two structural transitions mentioned above, from worm-like aggregates to bilayers and from bilayers to cylinders are clearly signaled in this graph. S_z adopts values close to zero (meaning that there is not a preferred surfactant orientation) at low and high decanol ratios, when CTA^+ forms worm-like or cylindrical aggregates, and values close to one (indicating that all surfactants are aligned along the same direction) at intermediate decanol/CTAB ratios for which bilayers remain stable. The translational order of CTAB was assessed by plotting the pair correlation distribution of CTA^+ heads (measured from the nitrogen atoms). As can be seen in Fig. 5.8, the radial distribution functions of nitrogen in the bilayers exhibit two sharp peaks at distances coincident with the relative

distances between the first and second peaks of a two-dimensional triangular lattice, whereas the second peak moves to larger distances and becomes broader for worm-like and cylindrical aggregates. This suggests that surfactants are rather tightly packed in the bilayers and forced to arrange locally as in a triangular lattice, with about half of CTA^+ chains pointing upwards and the other half pointing downwards (see Fig. 5.8). Note that although both structural transitions seem rather sharp in Fig. 5.7, this is likely an artifact of the simulations, which are performed in a relatively small system using periodic boundary conditions. In the real system, these transitions are likely to be smoother, finding coexistence between different aggregate morphologies for decanol contents in the neighbourhood of the structural transitions. Interestingly, there are some experimental studies that also report the existence of disc-like micelles similar to the ones observed here in the ternary CTAB/decanol/water system[47]. Our results are also consistent with recent experiments that report a transition from nearly spherical to cylindrical micelles by the addition of small concentrations of decanol (corresponding to $r_{DeOH-CTAB}$ ratios less than 0.1)[25]. Curiously, a recent simulation study of the assembly of octanol/CTAB found that this system forms disc-like micelles with structure similar to decanol/CTAB bilayers, but the transition from cylinders to disc-like micelles occurred at higher alcohol/CTAB concentration than for decanol. However, comparison of our results with those previous studies is not straightforward, as they were both undertaken at much lower CTAB concentrations than those considered in our work.

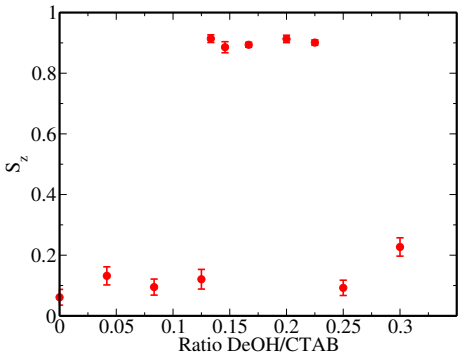

Figure 5.7. Evolution of the orientational order parameter S_z (Eq. 5.3) as a function of decanol/CTAB ratio, $r_{DeOH/CTAB}$.

With the aim of providing a description of the bilayer structure we measured the density profiles of bromide ions, nitrogen (located at the heads of CTAB) and oxygen (located at the hydroxyl group of decanol) as a function of the distance to the plane that bisects the bilayer (Fig. 5.9). As expected, density profiles are symmetric about this plane. From the maxima in the nitrogen distribution (red lines) we estimate that the width of the bilayer is about 2.4 nm, which is significantly less than twice the radius of the smallest studied micelle (about 4 nm). This means that the hydrophobic chains are more tightly bound in a bilayer than in a micelle, due to the favorable packing descrbied above.

Note also that these distributions are quite broad, which is consistent with the fact that bilayers are quite dynamic and exhibit large deviations from the average plane (see Fig. 5.8). This motion translates to the equilibrium properties as a smoothening of the structural features of the pair correlation and density profiles, in a manner similar to the smoothening that occurs by capillary wave dynamics on the surface of other complex interfaces [48, 49, 50, 51]. Bromide ions are located close to the bilayer surface, again showing two distint regimes (blue lines). A strongly adsorbed layer next to the CTA+ cations is observed, followed by a diffusive layer with a slow decay at long distances. Finally, oxygen atoms are burried within the bilayer, exhibiting maxima at a distance of about 0.45 nm from the nitrogen maxima (green lines).

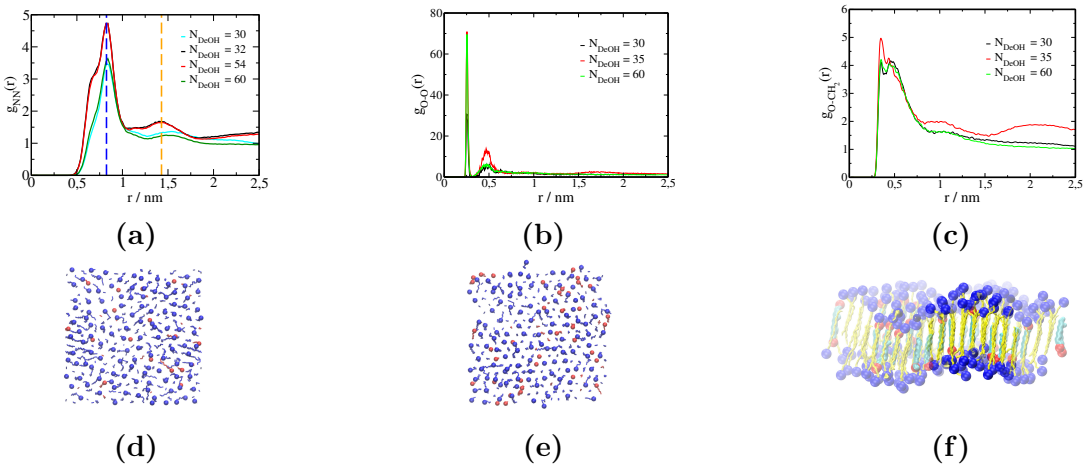

Figure 5.8. Radial distribution functions of (a) CTA^+ heads (measured with nitrogen atoms), (b) decanol oxygen and (c) nitrogen-oxygen, as a function of decanol/CTAB concentration. The vertical dotted lines in (a) mark the relative positions of the first and second peaks of the radial distribution function of a triangular lattice. (d) and (e) Instantaneous configurations of one of the layers in the systems with N_{DeOH}=32 and N_{DeOH}=54. (f) Side view of an instantaneous configuration of the bilayer formed at N_{DeOH} =32. Blue spheres represent the nitrogen atom in CTA^+ head and red spheres are the oxygens in decanol; CTAB chain is shown in yellow whereas that of decanol is shown in cyan.

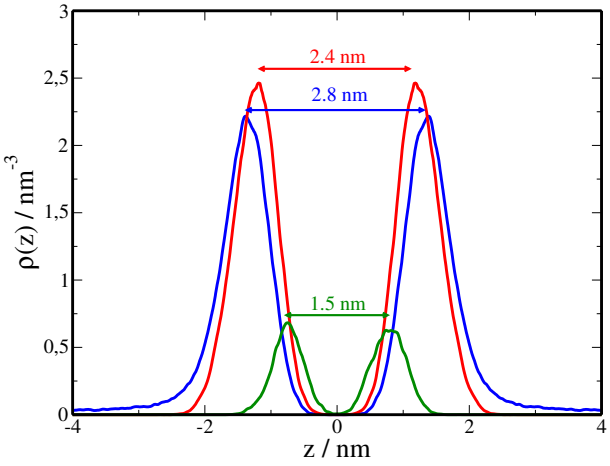

Figure 5.9. Average number density of nitrogen atoms in the ctab head (red), oxygens atoms in decanol (green) and bromide ions (blue) for a bilayer formed at $r_{DeOH/CTAB}$=0.2.

This indicates that oxygen atoms (negatively charged, -0.808e) are likely bound to the methylene bridge at CTA^+ heads (positively charged, +0.303e)[4].

Further information about the role of decanol on the stabilization and destabilization of the bilayer can be obtained by plotting the radial distribution functions between different atomic groups in CTA^+ and decanol (see Fig. 5.8). From these plots, we can conclude that there is some tendency of decanol hydroxyl groups to aggregate through the formation of hydrogen bonds that increases with decanol concentration (this tendency was corroborated by calculating the average number of hydrogen bonds per decanol molecule, which is shown in Fig. 5.10). Interestingly, the second maximum (located at about 0.48-0.50 nm) becomes

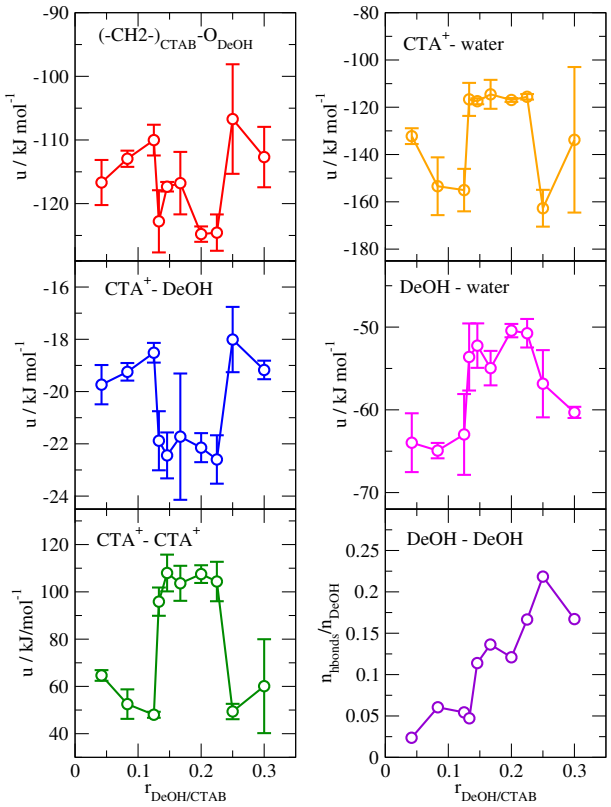

Figure 5.10. Evolution of average interaction energies between selected groups of atoms as a function of $r_{DeOH/CTAB}$. Note that, for the sake of brevity, CTA^+ and DeOH heads (-(CH2-OH) in the case of DeOH and -$(CH_2)N(CH_3)_3$) in the case of CTA^+ are labeled simply as CTA^+ and DeOH. The average number of hydrogen bonds between decanol molecules is also shown in the right lower panel.

more pronounced for those decanol concrentrations for which the bilayer is stable. This second maximum corresponds to the case in which two hydroxyl groups are nearest neighbours in the roughly local triangular environment of the bilayer, but without forming a hydrogen bond. Instead, they are electrostatically bound to the methylene bridge (-CH_2-) of other surrounding CTA^+ heads. The tendency of these two groups to bind through electrostatic interactions is also evident in the oxygen-methylene distribution functions, that exhibits a maximum at 0.35 nm which coincides with the cross oxygen-CH_2 σ Lennard-Jones parameter. Again this maximum is more pronounced in those cases in which the CTAB/decanol system forms bilayers. Analysis of the average interaction energy between the surfactant methylene bridge and decanol oxygen confirms these conclusions. As can be seen in Fig. 5.10 the interaction between those groups is rather strong and becomes stronger in the bilayers. As a consequence, the net interaction between CTA^+ and DeOH heads becomes more attractive, leading to shorter distances between nearest neighbour CTA^+ heads and, thus, to higher repulsions between them. The more efficient packing of CTA^+ heads in the bilayer (compared to the packing in worm and cylindrical micelles) becomes again evident when looking at the interactions between the heads of CTA^+ and DeOH molecules with water, as those interactions weaken in the bilayer. This is simply reflecting that, as CTA^+ heads are more efficiently packed, the area that they expose to the solvent is lower. The same argument explains the weaker decanol-water interactions: a higher packing of the surfactant heads leads to a lower exposure of decanol to water.

In the literature it is common to use the molecular packing parameter to predict the size and shape

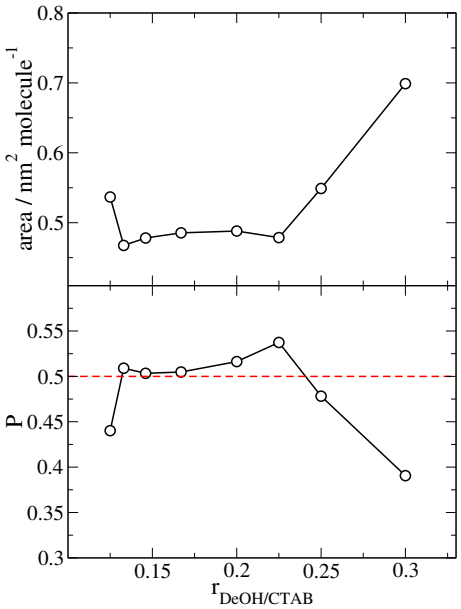

Figure 5.11. Estimates of the effective area per surfactant head (top panel) and of the molecular packing parameter P (bottom panel) as a function of the DeOH/CTA$^+$ ratio. In the lower panel, the dashed red line indicates the crossover from cylindrical to bilayer aggregates according to Israelachvili *et al.*[52]

of surfactant aggregates[52, 53]. The packing parameter, introduced by Israelachvili *et al.*[52], is defined as $P = v_0/(a \times {}_0)$, where v_0 and l_0 are the volume and length of the surfactant tail, and a is the effective area of the head group. The packing parameter adopts different values depending on the aggregates shape: $0 \leq P \leq 1/3$ for spherical micelles, $1/3 \leq P \leq 1/2$ for cylinders and $1/2 \leq P \leq 1$ for bilayers. The effective area of the head group, a, can be estimated from the simulation data: in the case of bilayer from the average edges of the simulation box and in the case of cylinders from its diameter and length (see Fig. 5.11). Clearly the area per head adopts the lower values in the bilayer. The ratio v_0/l_0 is often taken as 0.21 nm^2 for surfactants with a single tail and 0.42 nm^2 for surfactants with a double tail, although it is known that this is an oversimplification that neglects the effect of solvent or the addition of co-surfactants[53]. Given that decanol is buried within the bilayer, with its head bound to the methylene group of CTA$^+$ and its chain parallel to CTA$^+$ tails, the addition of decanol induces an increase of v_0/l_0, similar to the increase observed between surfactants with single and double tails. A very rough estimation of the enhancement of v_0/l_0 as decanol content increases can be obtained by using a linear fit between the values of surfactants with a single tail (which would correspond to $r_{DeOH/CTAB}$=0) and with double tail ($r_{DeOH/CTAB}$=1). As can be seen in Fig. 5.11, the packing parameter obtained with these approximations follows Israelachvili *et al.* predictions: it adopts values $1/3 \leq P \leq 1/2$ for cylindrical and worm like aggregates and values slightly about 0.5 for bilayers.

Putting all the ingredients together, our explanation for the role of decanol in the stabilization and destabilization of CTAB bilayers is as follows. Decanol hydroxyl groups tend to bind to the methylene bridges in CTA$^+$ heads, the decanol chain running parallel to the chains of the surrounding surfactants. As a consequence, CTA$^+$ heads can get closer, but tails have to move slightly appart to leave room for the decanol chain, i.e., decanol induces the alignment of neighbouring surfactant chains. When the concentration of decanol is low, this local straightening of the micelles induces a transition from spherical to cylindrical micelles. However, when the decanol/CTAB ratio is roughly 1/6, every CTAB molecule can have one decanol nearest neighbour (assuming an homogenous distribution of decanol). As a consequence,

it is favourable to form a bilayer, in which all surfactant chains are aligned. If we increase further decanol concentration, at a 1/3 ratio, each alcohol molecule can be surrounded by six surfactant chains. At higher concentrations, necessarily some alcohol molecules have to be nearest neighbours, which leads to a less efficient packing of the CTAB heads on the aggregate surface. However, as hydroxyl groups show a tendency to aggregate through the formation of hydrogen bonds that increases at larger decanol concentrations, the destabilization of the bilayer actually happens before that point. In other words, there is a competition between decanol hydrogen bonds and decanol-CTAB electrostatic interactions, which leads to the destabilization of the bilayers when hydrogen bonds are more likely due to a higher decanol concentration.

Summary and conclusions

In this paper we have investigated the stability and structure of CTAB aggregates with and without cosurfactant *n*-decanol by atomistic molecular dynamics simulations. In absence of decanol, micelles with up to 150 molecules remain stable within 0.1-0.8 M CTAB concentrations. In agreement with experimental evidences[16], we find a structural transition from spherical to prolate ellipsoidal shapes at sizes of about 100 CTAB molecules. Measurements of parameters to characterize the shape of the aggregates, such as the radius and eccentricity, are in good agreement with previous simulation and experimental studies. Interestingly, even though micelles are not spherical, our results suggest that both the average micelle radius and the contraions distribution can be reasonably described using the spherical approximation. Bilayers are unstable in this concentration range, either in presence or absence of added bromide salt. When assembled together with cosurfactant decanol, bilayers remain stable for intermediate decanol/CTAB ratios, $0.13 \leq r_{DeOH/CTAB} \leq 0.225$, transforming into worm-like and cylindrical aggregates at lower and higher decanol/CTAB ratios, respectively.

Even though we are aware that simulations lasting hundred of nanoseconds are not always sufficient to ensure full thermodynamic equilibrium of surfactant aggregates, useful information can be obtained from simulations starting from pre-assembled aggregates. On one hand, these simulations are useful to discard unstable configurations of the system. Large micelles and bilayers are quickly distabilized in the CTAB/water system, and the same occurs with decanol/CTAB bilayers at low and high decanol/CTAB ratios. On the other hand, they can provide useful information about the atomic structure of the aggregates which is often difficult to obtain experimentally.

Our simulations show that decanol/CTAB solutions can aggregate into stable, or at least metastable ordered bilayers. Of course most surfactants do eventually form bilayers at sufficiently high surfactant concentration. However, our results show that the bilayer morphology is achievable by use of cosurfactant decanol at low global CTAB concentrations that are regularly used for the optimal preparation of gold nanoparticles. Furthermore, the ordered nature of this bilayer and the triangular lattice arrangement of CTA+ heads could help understand the selective adosorption of the bilayers on gold facets. Indeed, bilayers are expected to adsorb preferentially on gold facets matching the triangular lattice arrangement.[6] Therefore, decanol appears as an ideal cosurfactant in gold nanorod synthesis, where small variations of decanol/CTAB can be used to tune the shape of the equilibrium solution aggregates and thus to tune as well the aggregate coverage on nanoparticle surface. According to recent studies, the control of surface coverage during preparation of metallic nanoparticles can dramatically improve the synthesis performance of monodisperse gold nanorods with selected aspect-ratio.[4, 6]

Acknowledgment

We would like to thank A. Guerrero-Martínez and G. González-Rubio for attracting our interest in this topic and for many helpful discussions. We gratefully acknowledge funds from the Dirección General de Investigación Científica y Técnica under Grant No. FIS2017-89361-C3-2-P.

Supplementary Material

Calculation of density profiles

In order to describe the shape of micellar aggregates we plot density profiles of the carbon atoms of CTAB molecules.

Firstly we perform a cluster analysis and locate each micelle individually. The criterion adopted to determine the cluster is based on the distance between atoms. All atoms within a cutoff radius of less than 4.2 nm are considered, and therefore they are part of the same cluster.

Once the cluster is located, we seek a local micellar reference frame by calculating the principal axis of inertia. The three dimensional density is then calculated and projected onto planes perpendicular to the three principal axis of inertia.

Moments of inertia.

In order to describe the shape of micellar aggregates within a local reference frame, we calculated the inertia tensor of the micelle based on the mass distribution of carbon atoms.

The inertia tensor of a rigid solid is a symmetric tensor whose tensor components are given by:

$$I_{ij} = I_{ji} = \int_M [\delta_{ij} r^2 - x_i x_j] dM \tag{5.12}$$

x_1,x_2,x_3 are the cartesian coordinates and M is the mass of the atoms that make up the rigid solid.

Diagonalization of the inertia tensor within an arbitrary reference frame provides a set of three eigen-vectors or principal axis of inertia. In terms of these axis, the tensor adopts the simple form:

$$I_{11} = m \sum_{i=1}^{N} (x_2^2 + x_3^2) \tag{5.13}$$

$$I_{22} = m \sum_{i=1}^{N} (x_1^2 + x_3^2) \tag{5.14}$$

$$I_{33} = m \sum_{i=1}^{N} (x_1^2 + x_2^2) \tag{5.15}$$

where we assumed unit mass m for all atoms for convenience.

The components $I_{ii}, i = 1,2,3$ are known as the principal moments of inertia with respect to the axis x_i. In practice, we arrange the axis labels such that $I_1 < I_2 < I_3$ (c.f. Fig.5.12).

Summary of the density profiles of CTAB bilayers with and without additives.

We will extend the results not included in the main document. Specifically, the study of the carbon atom density profiles for micelles and bilayers of CTAB. We can see in detail the morphology of the different aggregates that form the CTAB molecules in different conditions (salt, co-additives).

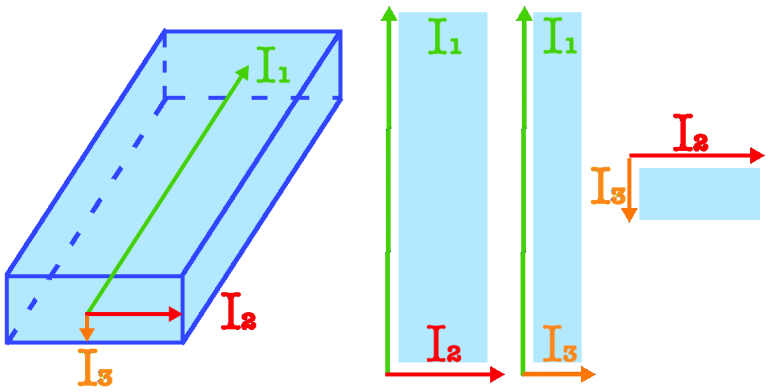

Figure 5.12. Example of the 3 moments of inertia of a rectangular prism, the values of the eigenvectors for each moment of inertia are $I_1 < I_2 < I_3$

Density profiles of the CTAB micelles

Here we show the results of micellar density of simulations starting from pre-assembled micelles of increasing aggregation number.

Density profiles of CTAB bilayers.

Here we show the density profiles for aggregates obtained from simulations with pre-assembled bilayers as initial state.

Density profiles of CTAB bilayer with and without NaBr

Density profiles of CTAB bilayers with differents concentrations of decanol.

Evolution of the order parameter (S_z) with the variation of decanol concentration

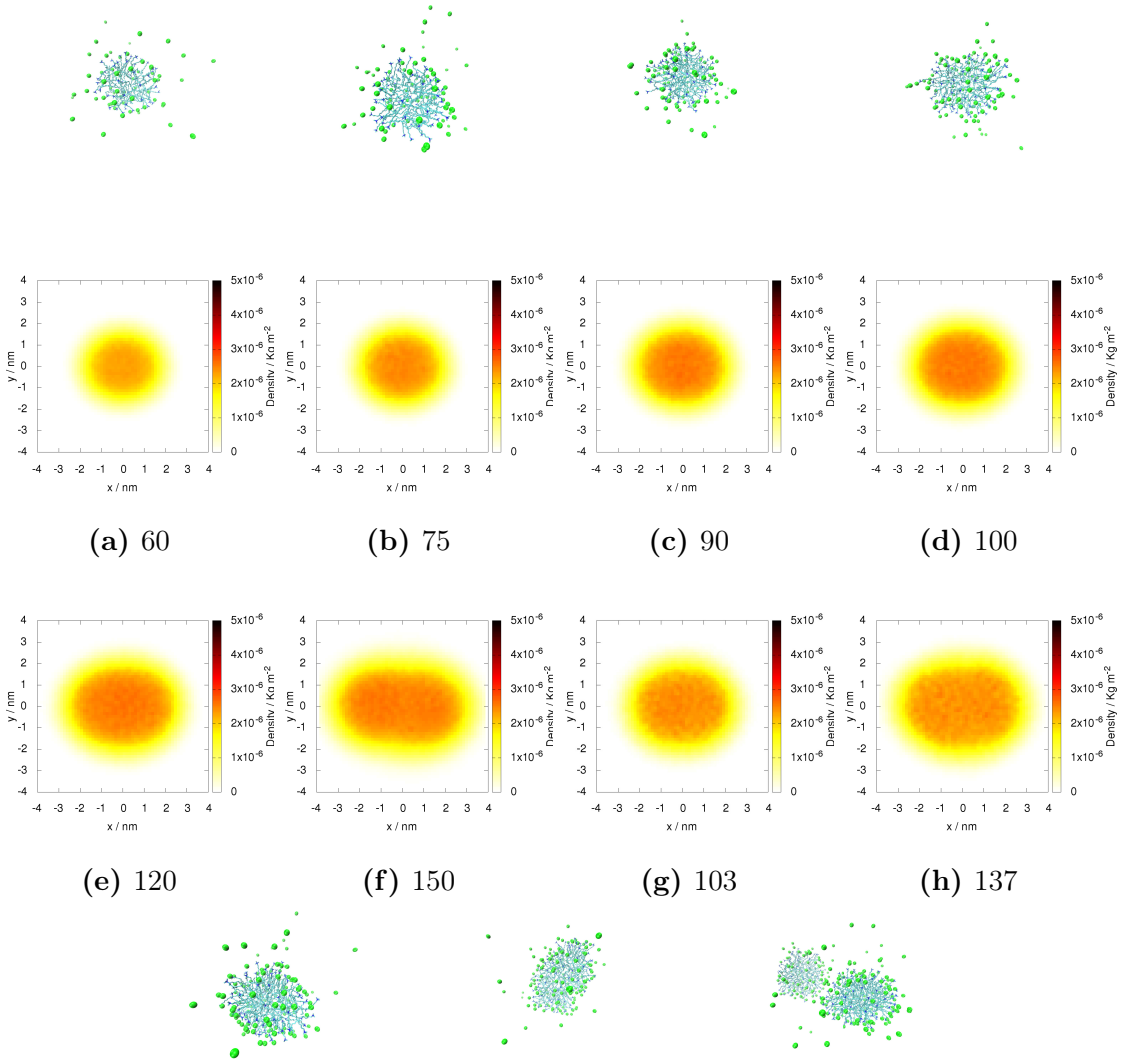

(a) 60 **(b)** 75 **(c)** 90 **(d)** 100

(e) 120 **(f)** 150 **(g)** 103 **(h)** 137

Figure 5.13. Top and bottom rows show final configurations of simulations starting from pre-assembled micelles. The number of CTAB molecules in each micelle can be seen on the labels next to the corresponding figure. The middle rows illustrate bidimensional atomic density profiles of CTA^+, as projected onto the plane perpendicular to x_1. The micelle with $N = 240$ was split into two smaller micelles. Density profiles for each micelle are shown separately (figures g and h).

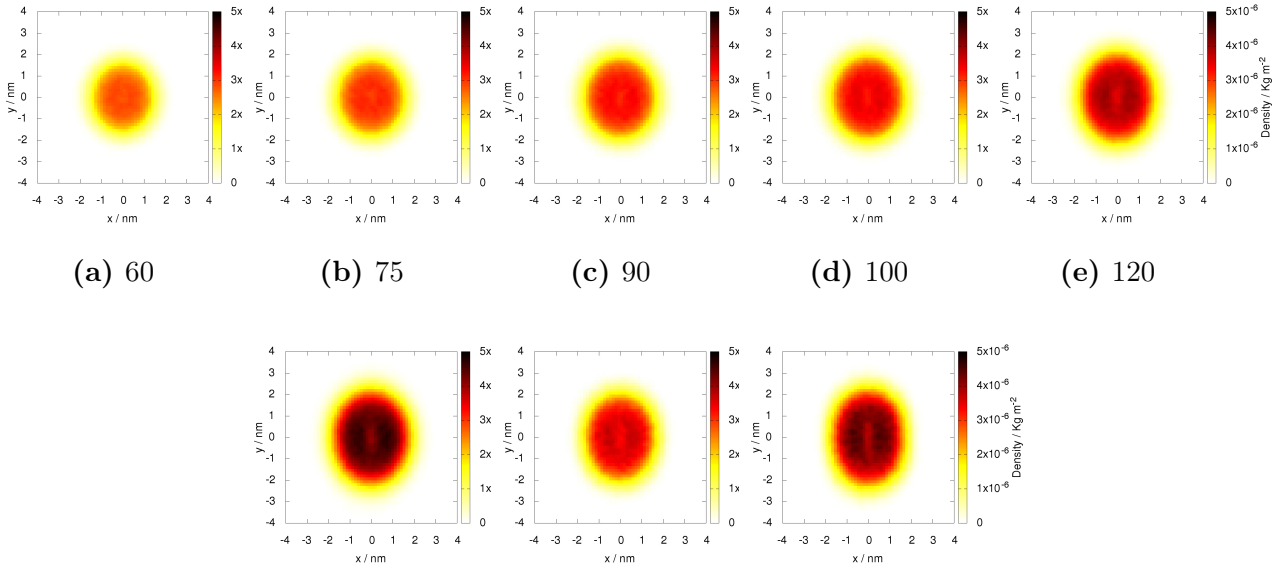

(a) 60 **(b)** 75 **(c)** 90 **(d)** 100 **(e)** 120

(f) 150 **(g)** 103 **(h)** 137

Figure 5.14. Bidimensional atomic density profiles of CTA^+. The number of CTAB molecules in each micelle can be seen on the label of each figure. Density profiles were projected on the plane perpendicular to x_2. The micelle with $N = 240$ was split into smaller micelles. Density profiles for each micelle are shown separately (figures g and h).

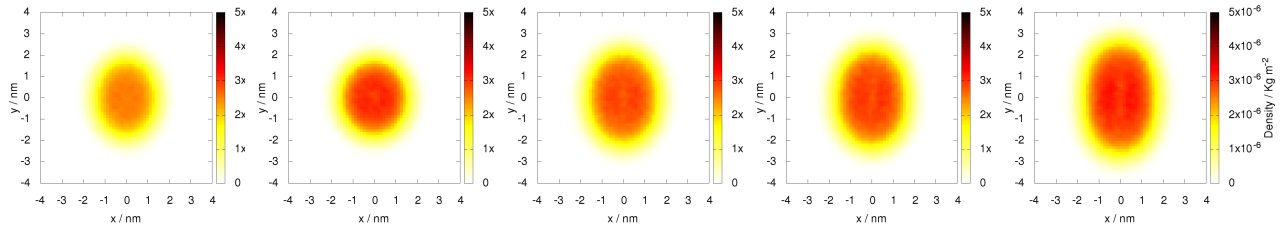

(a) 60 **(b)** 75 **(c)** 90 **(d)** 100 **(e)** 120

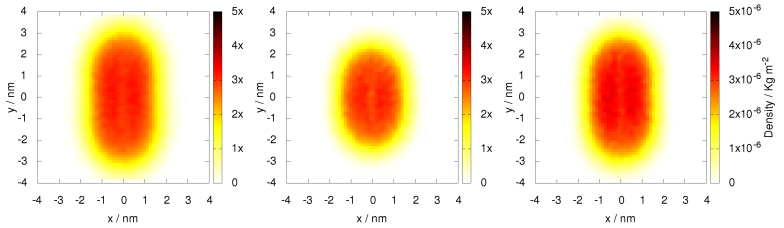

(f) 150 **(g)** 103 **(h)** 137

Figure 5.15. Bidimensional atomic density profiles of CTA^+. The number of CTAB molecules in each micelle can be seen on the label of each figure. Density profiles were projected on the plane perpendicular to x_3. The micelle with $N = 240$ was split into smaller micelles. Density profiles for each micelle are shown separately (figures g and h).

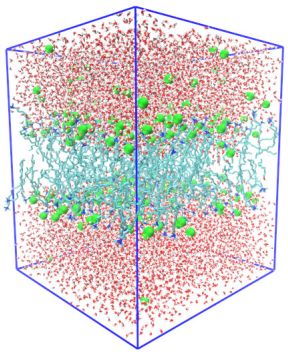

Figure 5.16. Initial configuration used in the bilayer simulations in which we introduce up to 72 decanol molecules. Red/white lines represent water molecules. CTA^+ molecules are depicted as blue lines and decanol molecules as orange lines. Finally green spheres represent the bromine counterions that neutralize the system.

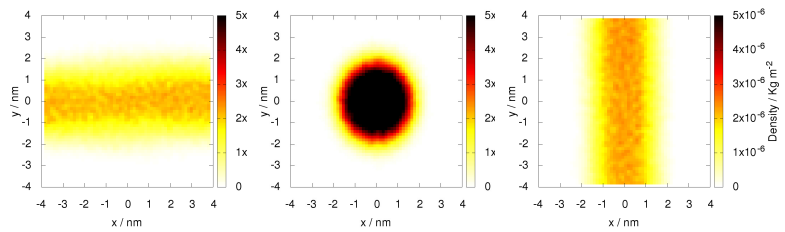

(a) **(b)** **(c)**

Figure 5.17. Bidimensional atomic density profiles of CTA^+ for concentration of NaBr equal to 0.25 M. The CTAB bilayer evolves to a cylindrical aggregate. Density profiles were projected on planes perpendicular to the three principal axis of inertia x_1 (a), x_2 (b) and x_3 (c).

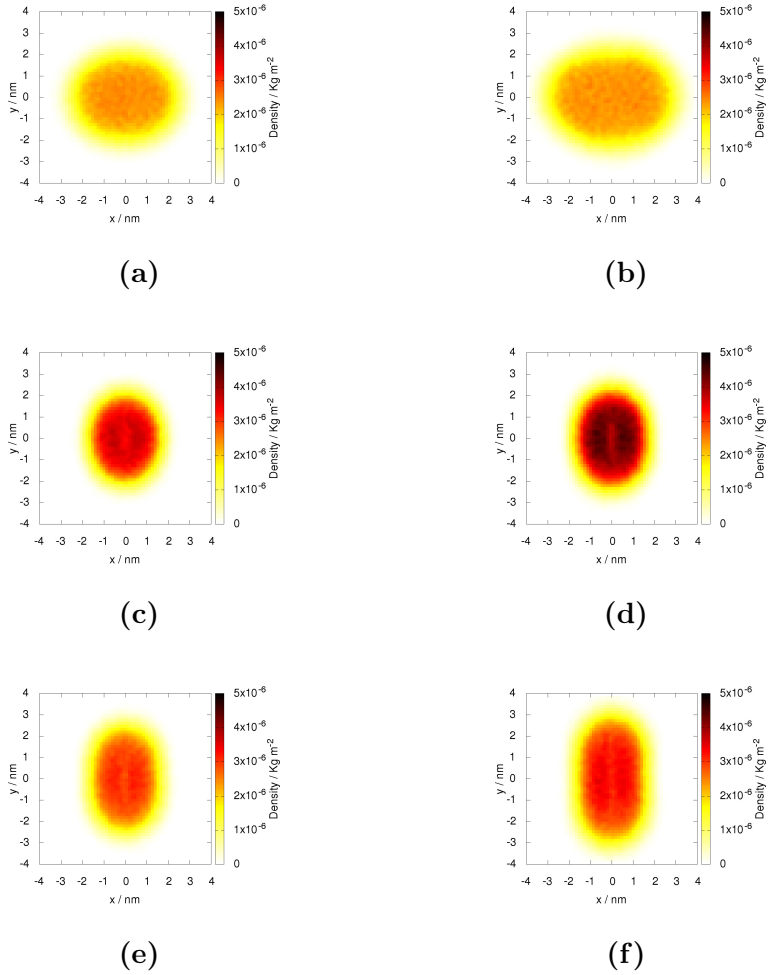

Figure 5.18. Bidimensional atomic density profiles of CTA^+ in absence of salt. The CTAB bilayer disappears in favor of the formation of two micelles, giving rise to the same system as the micelle containing 240 molecules of surfactant. The number of CTAB molecules in each micelle can be seen on the label of each figure. Density profiles were projected on planes perpendicular to the three principal axis of inertia, x_1 (a, b), x_2 (c, d) and x_3 (e, f).

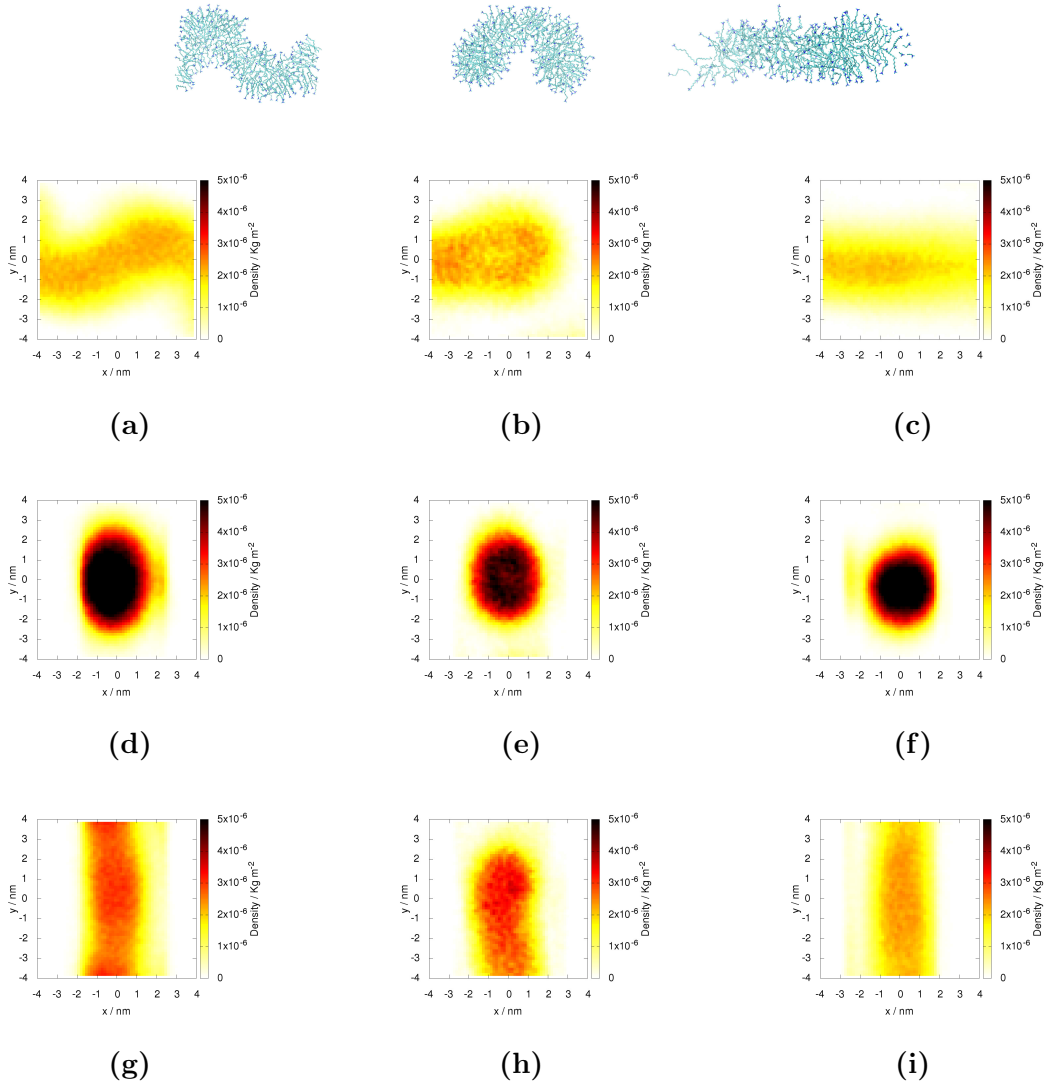

Figure 5.19. Final configurations of simulations starting from pre-assembled bilayers with $N_{DeOH} = 10 - 30$ (top row). Bidimensional atomic density profiles of CTA^+ (bottom rows). The ratios of DeOH/CTAB molecules for each aggregate are 0.042 (a, d, g), 0.083 (b, e, h) and 0.125 (c, f, i). Density profiles were projected on planes perpendicular to the three principal axis of inertia x_1 (a, b, c), x_2 (d, e, f) and x_3 (g , h, i).

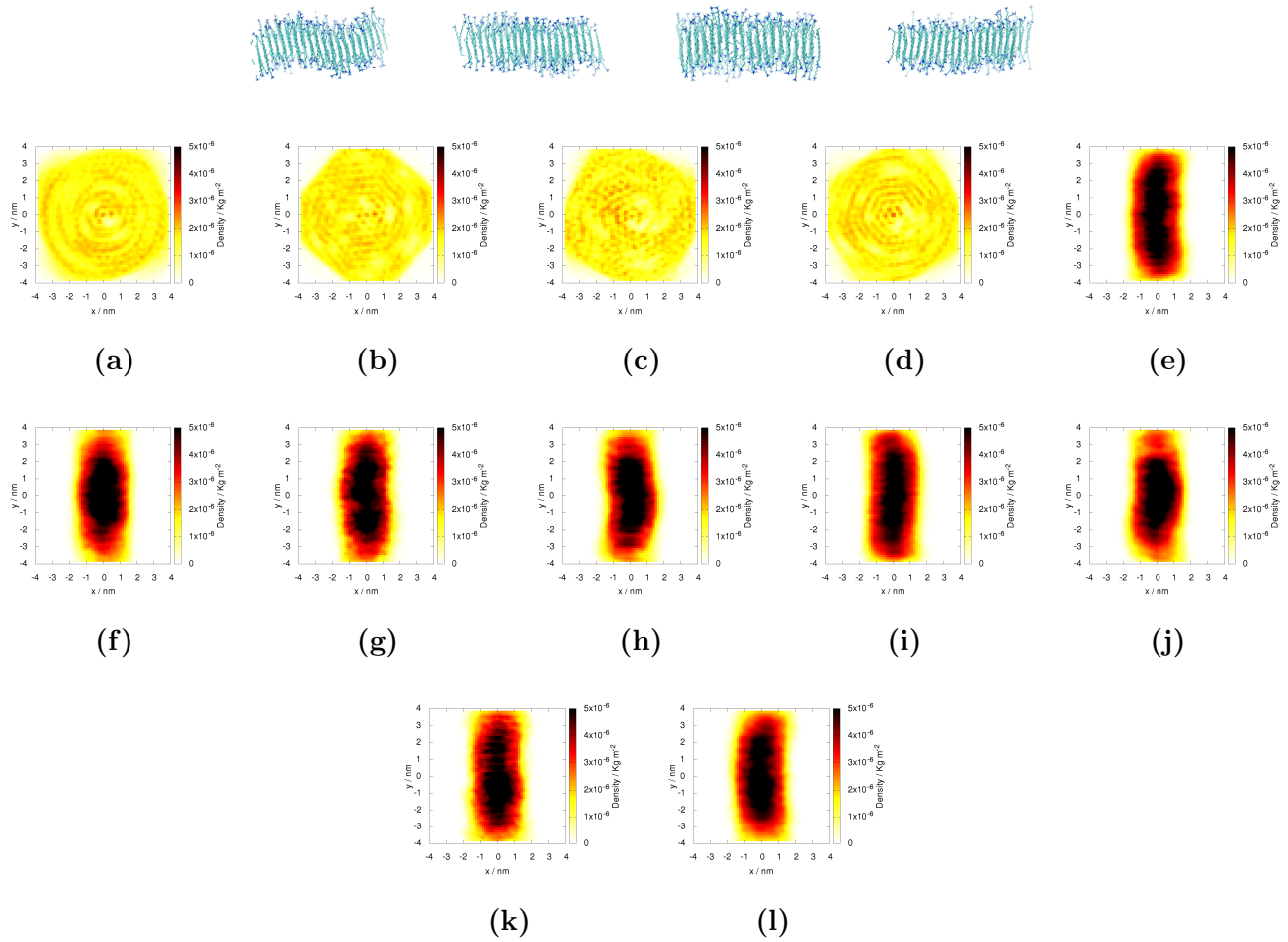

Figure 5.20. Final configurations of simulations starting from pre-assembled bilayers with $N_{DeOH} = 31-40$ (top row). Bidimensional atomic density profiles of CTA^+ (bottom rows). The ratios of DeOH/CTAB molecules for each aggregate are 0.133 (a, e, i), 0.146 (b, f, j), 0.167 (c, g, k) and 0.200 (d, h, l). Density profile were projected on planes perpendicular to the three principal axis of inertia x_1 (a, b, c, d), x_2 (e, f, g, h) and x_3 (i, j, k, l).

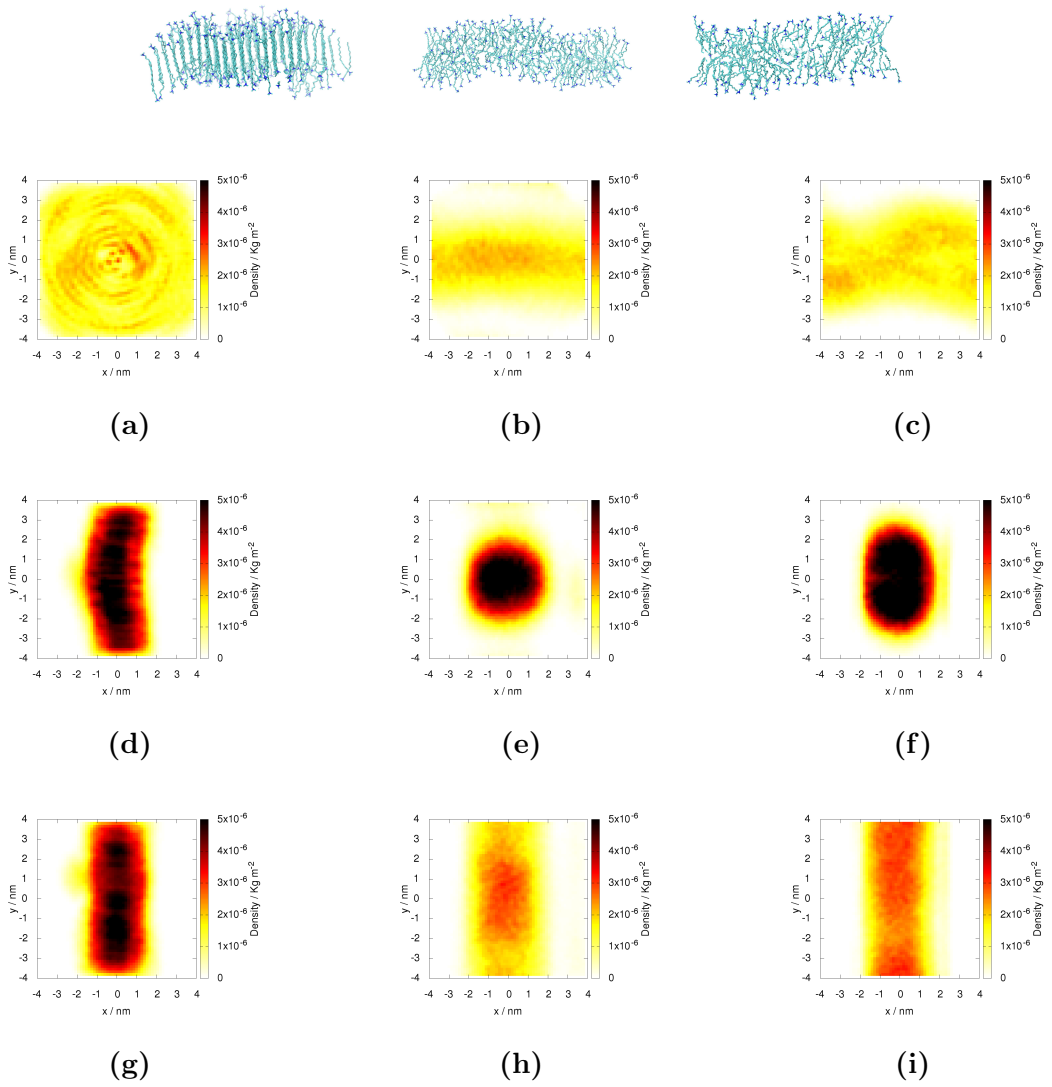

Figure 5.21. Final configurations of simulations starting from pre-assembled bilayers with $N_{DeOH} = 10 - 30$ (top). Bidimensional atomic density profiles of CTA^+ (bottom rows). The ratios of DeOH/CTAB molecules for each aggregate are 0.225 (a, d, g), 0.250 (b, e, h) and 0.300 (c, f, i). Density profile were projected on planes perpendicular to the three principal axis of inertia x_1 (a, b, c), x_2 (d, e, f) and x_3 (g , h, i).

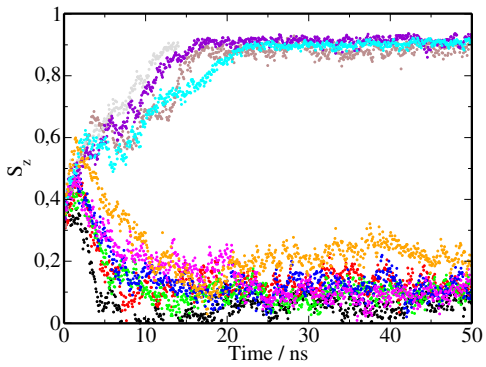

Figure 5.22. Evolution of the order parameter S_z during the progress of the simulation. In black, red, green, blue, brown, grey, purple, cyan, magenta and orange lines show the ratios DeOH/CTAB 0.000, 0.042, 0.083, 0.125, 0.133, 0.146, 0.167, 0.200, 0.250 and 0.300, respectively.

Bibliography

[1] A. Berggren, A. E. Palmqvist, and K. Holmberg, "Surfacant templated mesostructured materials from inorganic silica," *Soft Matt.*, vol. 1, pp. 219–226, 2005.

[2] J. Gao, C. M. Bender, and C. J. Murphy, "Dependence of the gold nanorod aspect ratio on the nature of the directing surfactant in aqueous solution," *Langmuir*, vol. 19, pp. 9065–9070, 2003.

[3] C. J. Murphy, L. B. Thompson, A. M. Alkilany, P. N. Sisco, S. P. Boulos, S. T. Sivapalan, J. A. Yang, D. J. Chernak, and J. Huang, "The many faces of gold nanorods," *J. Chem. Phys. Lett.*, vol. 1, pp. 2867–2875, 2010.

[4] G. González-Rubio, P. Díaz-Núñez, A. Rivera, A. Prada, G. Tardajos, J. González-Izquierdo, L. Bañares, P. Llombart, L. G. MacDowell, M. Alcolea-Palafox, L. M. Liz-Marzán, O. Peña-Rodríguez, and A. Guerrero-Martínez, "Femtosecond laser reshaping yields gold nanorods with ultranarrow surface plasmon resonances," *Science*, vol. 358, pp. 640–644, 2017.

[5] X. Ye, L. Jin, H. Caglayan, J. Chen, G. Xing, C. Zheng, V. Doan-Nguyen, Y. Kang, N. Engheta, C. R. Kagan, and C. B. Murray, "Improved size-tunable synthesis of monodisperse gold nanorods through the use of aromatic additives," *ACS Nano*, vol. 6, pp. 2804–2817, 2012.

[6] G. González-Rubio, V. Kumar, P. Llombart, P. Díaz-Núñez, E. Bladt, T. Altantzis, S. Bals, O. Peña-Rodríguez, E. G. Noya, L. G. MacDowell, A. Guerrero-Martínez, and L. M. Liz-Marzán, "Disconnecting symmetry breaking from seeded growth for reproducible synthesis of high quality gold nanorods," *ACS Nano*, vol. submitted, 2019.

[7] C. J. Murphy, L. B. Thompson, D. J. Chernak, J. A. Yang, S. T. Sivapalan, S. P. Boulos, J. Huang, A. M. Alkilany, and P. N. Sisco, "Gold nanorod crystal growth: From seed-mediated synthesis to nanoscale sculpting," *Current Opinion in Colloid and Interface Science*, vol. 16, pp. 128–134, 2011.

[8] B. Nikoobakht and M. A. El-Sayed, "Preparation and growth mechanism of gold nanorods using seed-mediated growth method," *Chem. Mater.*, vol. 15, pp. 1957–1962, 2003.

[9] S. Gómez-Graña, F. Hubert, F. Testard, A. Guerrero-Martínez, I. Grillo, L. M. Liz-Marzán, and O. Spalla, "Surfactant bilayers on gold nanorods," *Langmuir*, vol. 28, pp. 1453–1459, 2012.

[10] S. K. Meena and M. Sulpizi, "Understanding the microscopic origin of gold nanoparticle anisotropic growth from molecular dynamics simulations," *Langmuir*, vol. 9, p. 14954, 2013.

[11] S. K. Meena and M. Sulpizi, "From gold nanoseeds to nanorods: The microscopic origin of the anisotropic growth," *Angew. Chemie. Int. Ed.*, vol. 55, pp. 11960–11964, 2016.

[12] P. Ekwall, L. Mandell, and P. Solyom, "The aqueous cetyl trimethylammonium bromide solution," *Journal of Colloid and Interface Science*, vol. 35, pp. 519–527, 1971.

[13] J. Mata, D. Varade, and P. Bahadur, "Aggregation behavior of quaternary salt based cationic surfactants," *Thermochim. Acta*, vol. 428, pp. 147–155, 2005.

[14] S. P. Moulik, M. E. Hauqe, P. K. Jana, and A. R. Das, "Micellar porperties of cationic surfacants in pure and mixed states," *J. Phys. Chem.*, vol. 100, pp. 701–708, 1996.

[15] L. M. Bergström, "Second cmc in surfactant micellar systems," *Current Opinion in Colloid and Interface Science*, vol. 2016, pp. 46–50, 2016.

[16] F. Quirion and L. J. Magid, "Growth and counterion binding of cetyltrimethylammonium bromide aggregates at 25c: a neutron and light scattering study," *J. Phys. Chem.*, vol. 90, pp. 5435–5441, 1986.

[17] M. Pisárčik, F. Devínsky, and M. Pupák, "Determination of micelle aggregation numbers of alkyltrimethylammonium bromide and sodium dodecyl sulfate surfactants using time-resolved fluorescence quenching," *Open Chem.*, vol. 13, pp. 922–931, 2015.

[18] A. Jusufi and A. Z. Panagiotopoulos, "Explicit- and implicit-solvent simulations of micellization in surfactant solutions," *Langmuir*, vol. 31, no. 11, pp. 3283–3292, 2015. PMID: 25226280.

[19] M. Törnblom, U. Henriksson, and M. Ginley, "Field dependent ^{2}h nuclear magnetic relaxation study of the aggregation behaviour in micellar solutions of ctab and sds," *J. Phys. Chem.*, vol. 98, pp. 7041–7051, 1994.

[20] T. Imae, R. Kamiya, and S. Ikeda, "Formation of spherical and rod-like micelles of cetyltrimethylammonium bromide in aqueous nabr solutions," *J. Colloid Interface Sci.*, vol. 108, p. 215, 1985.

[21] Y. Wang, D. S. D. Larsson, and D. van der Spoel, "Encapsulation of myoglobin in a cetyl trimethylammonium bromide micelle in vacuo: A simulation study," *Biochemistry*, vol. 48, pp. 1006–1015, 2009.

[22] N. C. Das, H. Cao, H. Kaiser, G. T. Warren, J. R. Gladden, and P. E. Sokol, "Shape and size of highly concentrated micelles in ctab/nasal solutions by small angle neutron scattering (sans)," *Langmuir*, vol. 28, pp. 11962–11968, 2012.

[23] B. Michels and G. Waton, "Effect of pentanol and salt on the fusion-scission kinetics for ctab micelles," *J. Phys. Chem. A*, vol. 107, pp. 1133–1137, 2003.

[24] V. Patel, N. Dharaiya, D. Ray, V. K. Aswal, and P. Bahadur, "ph controlled size/shape in ctab micelles with solubilized polar additives: A viscometry, scattering and spectral evaluation," *Colloids and Surfaces A*, vol. 455, pp. 67–75, 2014.

[25] J. Karayil, S. Kumar, P. A. Hassan, Y. Talmon, and L. Sreejith, "Microstructural transition of aqueous ctab micelles in the presence of long chain alcohols," *RSC Adv.*, vol. 5, pp. 12434–12441, 2015.

[26] T. Schmutzler, T. Schindler, M. Schmiele, M.-S. Appavou, S. L. abd A. Kriele, R. Gilles, and T. Unruh, "The influence of n-hexanol on the morphology and composition of ctab micelles," *Colloids and Surfaces A*, vol. 5, pp. 12434–12441, 2018.

[27] X. Jia, J. Chen, B. Wang, W. Lu, and J. Hao, "Molecular dynamics simulation of shape and structure evolution of preassembled cylindrical cetyltrimethylammonium bromide micells induced by octanol," *Colloids and Surfaces A*, vol. 457, pp. 152–159, 2014.

[28] X. Jia, S. Yu, Y. Ma, X. Li, W. Xu, and J. Liu, "Model of cylindrical micelles with different endcaps," *Journal of Dispersion Science and Technology*, vol. 457, pp. 621–625, 2017.

[29] L. Sreejith, S. Parathakkat, S. M. Nair, S. Kumar, G. Varma, P. A. Hassan, and Y. Talmon, "Octanol-triggered self-assemblues of the ctab/kbr system: a microstructural study," *J. Phys. Chem. B*, vol. 115, pp. 464–470, 2011.

[30] A. B. Cortes, M. Valiente, and E. Rodenas, "Properties of the l and lyotropic phases in ctab/glycerol/water and ctab/glyceraldehyde/water systems," *Langmuir*, vol. 118, pp. 6658–6663, 1999.

[31] A. J. Mills, J. Wilkie, and M. M. Britton, "Nmr and molecular dynamics study of the size, shape and composition of reverse micelles in a cetyltrimethylammonium bromide (ctab)/n-hexane/pentanol/water microemulsion," *J. Phys. Chem. B*, vol. 118, pp. 10767–10775, 2014.

[32] M. Jorge, "Structure of cationic surfactant micelles from molecular simulations of self-assembly," *J. of Molec. Structure: THEOCHEM*, vol. 946, no. 1, pp. 88 – 93, 2010. Achievements and Challenges of Computational Chemistry in Portugal.

[33] G. F. Catá, H. C. Rojas, A. P. Gramatges, C. M. Zicovich-Wilson, L. Alvarez, and C. Searle, "Initial structure of cetyltrimethylammonium bromide micelles in acqueous solution from molecular dynamics simulations," *Soft Matt.*, vol. 7, p. 8508, 2011.

[34] S. Storm, S. Jakobtorweihen, I. Smirnova, and A. Z. Panagiotopoulos, "Molecular dinamics simulations of sds and ctab micellization and prediction of partition equilibria with cosmomic," *Langmuir*, vol. 29, p. 11582, 2013.

[35] S. Illa-Tuset, D. C. Malaspina, and J. Faraudo, "Coarse-grained molecular dynamics simulation of interface behaviour and self-assembly of ctab cationic surfactant," *Phys. Chem. Chem. Phys.*, vol. 20, pp. 26422–26430, 2018.

[36] D. N. LeBard, B. G. Levine, P. Mertmann, S. A. Barr, A. Jusufi, S. Sanders, M. L. Klein, and A. Z. Panagiotopoulos, "Self-assembly of coarse-grained ionic surfactants accelerated by graphics processing units," *Soft Matter*, vol. 8, p. 2385, 2012.

[37] C. Oostenbrick, A. Villa, A. E. Mark, and W. F. van Gunsteren, "A biomolecular force field based on the free enthalpy of hydration and solvation: the gromos force-field parameter sets 53a5 and 53a6," *J. Comp. Chem.*, vol. 25, pp. 1656–1676, 2004.

[38] B. Hess, C. Kutzner, D. van der Spoel, and E. Lindahl, "Gromacs 4: Algorithms for highly efficient, load-balanced, and scalable molecular simulation," *J. Chem. Theory Comput.*, vol. 4, p. 435, 2008.

[39] G. Bussi, D. Donadio, and M. Parrinello, "Canonical sampling through velocity rescaling," *J. Chem. Phys.*, vol. 126, p. 014101, 2007.

[40] H. J. C. Berendsen, J. P. M. Postma, W. F. van Gunsteren, A. DiNola, and J. R. Haak, "Molecular-dynamics with coupling to an external bath," *J. Chem. Phys.*, vol. 81, p. 3684, 1984.

[41] L. Martínez, R. Andrade, E. G. Birgin, and J. M. Martínez, "Packmol: A package for building initial configurations for molecular dynamics simulations," *J. Comp. Chem.*, vol. 30, pp. 2157–2164, 2009.

[42] S. Bogusz, R. M. Venable, and R. W. Pastor, "Molecular dinamics simulations of octyl glucoside micelles: structural properties," *J. Phys. Chem. B*, vol. 104, p. 5462, 2000.

[43] S. Salaniwal, S. Cui, H. D. Cochran, and P. T. Cummings, "Molecular simulations of a dichain surfactant/water/carbon dioxide system. 1. structural properties of aggregates," *Langmuir*, vol. 17, pp. 1773–1783, 2001.

[44] C. J. Fennell, L. Li, and K. A. Dill, "Simple liquid models with corrected dielectric constants," *J. Phys. Chem. B*, vol. 116, pp. 6936–6944, 2012.

[45] I. Boruhhov, "Charge renormalization of cylinders and spheres: ion size effects," *J. Polym. Sci., Part B: Polym. Phys.*, vol. 42, pp. 3598–3615, 2004.

[46] W. R. Inc., "Mathematica, Version 11.3." Champaign, IL, 2018.

[47] G. Hertel and H. Hoffmann, "Lyotropic nematic phases of double chain surfactants," *Trends in Colloid and Interface Science II*, pp. 123–131, 2007.

[48] E. Sloutskin, Z. Sapir, C. D. Bain, Q. Lei, K. M. Wilkinson, L. Tamam, M. Deutsch, and B. M. Ocko, "Wetting, mixing, and phase transitions in langmuir-gibbs films," *Phys. Rev. Lett.*, vol. 99, p. 136102, Sep 2007.

[49] J. Benet, L. G. MacDowell, and E. Sanz, "Computer simulation study of surface wave dynamics at the crystal–melt interface," *J. Chem. Phys.*, vol. 141, p. 034701, 2014.

[50] J. Benet, L. G. MacDowell, and E. Sanz, "A study of the ice-water interface using the tip4p/2005 water model," *Phys. Chem. Chem. Phys.*, vol. 16, pp. 22159–22166, 2014.

[51] J. Benet, P. Llombart, E. Sanz, and L. G. MacDowell, "Premelting-induced smoothening of the ice-vapor interface," *Phys. Rev. Lett.*, vol. 117, p. 096101, Aug 2016.

[52] J. N. Israelachvili, D. J. Mitchell, and B. W. Ninham, "Theory of self-assembly of hydrocarbon amphiphiles into micelles and bilayers," *J. Chem. Soc., Faraday Trans.*, vol. 72, p. 1525, 1976.

[53] R. Nagarajan, "Molecular packing parameter and surfactant self-assembly: the neglected role of the surfactantatail," *Langmuir*, vol. 18, p. 31, 2002.

Chapter 6

Structure of the CTAB agregates adsorbed on the gold surface

Pablo Llombart[1,2], *Luis G. MacDowell*[2] and Eva G. Noya[1]

(1) Instituto de Química Física Rocasolano, CSIC, Calle Serrano 119, 28006 Madrid, Spain
(2) Departamento de Química Física, Facultad de Ciencias Químicas, Universidad Complutense de Madrid, 28040 Madrid, Spain

This chapter is a summary of:

- *Femtosecond laser reshaping yields gold nanorods with ultranarrow surface plasmon resonances, Science,* ***358****, 640-644 (2017)*
- *Disconnecting symmetry breaking from seeded growth for the reproducible synthesis of high quality gold nanorods, ACS Nano,* ***13****, 4424-4435 (2019)*

Abstract

The aim of this chapter is to incorporate an extended version of the research on the complex interface present in the mechanisms of synthesis of gold nanorods. Part of this work was published recently in collaboration with experimental and theoretical groups from University of Antwerp, Universidad Politécnica de Madrid and CIC biomaGUNE. As a result of this collaboration, it was possible to understand the underlying atomistic mechanism in order to optimize two methods of synthesis that allow controlling the size and polydispersity of gold nanorods,that have been published in two articles in journals of high impact.[1, 2]

Both methods are based on the seed growth mechanism, in which gold salts are deposited on preasembled gold seeds by electrochemical reduction. In this method, surfactants such as hexadecyltrimetilamonium bromide CTAB, as well as silver ions, are used commonly as colloidal stabilizer and shape-directing agents.

In the first method of synthesis gold nanorods are irradiated using a femtosecond pulse laser to achieve the reshaping of the nanorods and, as a result, nanorods can be obtained with a very low polidispersity unprecedented to date. The reshaping can be achieved due to the presence of free electrons in the conduction band of the metal nanoparticle surface atoms. These electrons are excited through an incident light beam and a local temperature increase of about 1000 Celsius degrees facilitates the mobility of atoms on the metal surface. This phenomenon of electron excitation is known as surface plasmon resonance (SPR) and only occurs at certain wave frequencies. [3, 4]

The second method consists of using decanol together with the CTAB surfactant that adsorbed as stabilizer and shape-directing agent. Thanks to these change in the morphology of aggregates on the gold surface caused by coassembly with decanol it is possible to control the flow of gold ions during the symmetry breaking and the growth processes.[2] On the one hand, this second method does not achieve polidispersity values as low as the laser-controlled method. However, the reproducibility of this method has been widely proven and allows synthesizing rods not as good from the optical point of view, but easily modulating the width and length of the rod as a function of the concentrations of additives.

- **Femtosecond laser reshaping yields gold nanorods with ultranarrow surface plasmon resonances**

  If we irradiate the gold nanorod colloids with a femtosecond pulse laser it is possible to induce the controlled reshaping of the nanorod, obtaining colloids with surface plasmon resonance bands located with very narrow bands. The reshaping is controlled by finding a balance between energy applies to the rods and the heat transference to the medium (controlled by CTAB). Controlled reshaping occurs within a window of the heat dissipation rate leading to drastic morphological changes when cooling is slow. On the contrary, rapid cooling has almost no effect. Thus delicate balance must be achieved between the irradiation creep and the surface density of the surfactant in the nanorods. The computational contribution that is included in this thesis consists in the study of the interface formed by the CTAB surfactant adsorbed on gold. Molecular Dynamics simulations can help to determine the morphology of the aggregates deposited on the gold surface in this aim as a function of the concentration of surfactant in the synthesis.

  Model and Methods

  In previous studies of CTAB adsorbed on gold [8, 9, 10] the cetyltrimethylammonium ion (CTA^+) was described using an united atom models with Lennard-Jones sites. Partial charges were assigned to the three methyl groups and the methylene group attached to nitrogen, but nitrogen itself remains neutral. The positive charge is divided into equal parts (+0.25e each). This scheme yields the expected charge from the trimethylammonium group, but it seems somewhat artificial if the expected electronegativity for nitrogen is taken into account. Using DFT and second order Moller-Plesset perturbation theory by Prof. Mauricio Alcolea we proposed a new partial charge assignament.

  The *ab-initio* calculations using natural bond orbitals (NBOs) [11] confirmed a negative partial charge on the nitrogen atom (-0.359e), also the methyl (-0.420e) and methylene (-0.206e) carbon atoms. The positive charge of CTA^+ is concentrated on the methyl hydrogens (+0.251e). In base to these NBO charges, we allocated a negative charge on the nitrogen atom and positive charges on the methyl and methylene groups (treated as a single group of united atoms). Apart from this charge assignment, all remaining hydrocarbon sites were considered neutral. The bromide counterions are explicitly simulated as negative point charges within a Lennard-Jones center, as in previous studies. [8] Water molecules are simulated explicitly using SPC model and gold atoms are described by the model proposed by Heinz et al. [8]. Cross Lennard-Jones interactions between atoms were calculated by default GROMACS implementation, the coefficients of r^{-12} and r^{-6} are determined using a geometrical mean combination rule. We find that this model is able to reproduce a number of properties of CTAB aggregates in aqueous solution, such as the radius of the micelles and their eccentricity.[7] It also forms stable micelles of N = 60 aggregates of CTAB that correspond to those expected at critical micelle concentration, cmc. We also find that micelles grow in size as the concentration of CTAB increases, as expected for cationic surfactants. [6, 12] The addition of salts and alcohols promotes the formation of cylindrical and wormlike micelles.

When we try to study the adsorbed bilayers, the surfactants were preassembled on the gold surface using the Packmol software.[13] The structures generated were completely solvated and an energy minimization was carried to relax the initial configuration before being allowed to evolve using Molecular Dynamics. Similarly, to prepare micelles in solution, the surfactants were first assembled in a spherical volume, with bromide ions randomly arranged in the spherical shell next to the CTA^+ cations. Subsequently, aggregates of 60, 75, 90, 100 and 120 molecules were solvated. The initial configurations were relaxed by performing a energy minimization. The system was allowed to equilibrate in a simulation of isotropic NpT. To study the deposition of surfactants in gold, we describe the Au surfaces as a stack of five {100} planes with lateral dimensions $Lx = Ly = 6.26$nm (3600 gold atoms for the two surface). The simulation model consisted of two gold substrates at a distance of approx. 15 nm, placed perpendicular to gold-CTAB-water interface to the z direction of an elongated simulation box of size ca. 25nm. The electrostatic interactions were evaluated using Ewald sums with metallic boundary conditions, using the Particle-Particle-Mesh technique. The cutoff used for the truncation of the electrostatic and core interactions was chosen at 1.2 nm. With the purpose of avoiding spurious electrostatic interactions between periodic images along z axis, a vacuum of 10 nm was left between both gold surfaces. All simulations were performed using the GROMACS 5 package (48). The trajectories were obtained using the velocity-verlet algorithm with a time step dt = 1 fs. The temperature and normal pressure were maintained at T = 298K and p = 1 bar, using the velocity-rescale thermostat and the Berendsen thermostat and set at 2 ps

Results

The aim of our simulations was to study the coverage of surfactants on the nanorods. At first, we considered the hypothesis that there was a fully developed bilayer on the surface of gold. To check this hypothesis we perform simulation for preassembled aggregates with morphologies and expected densities for a bilayer. These inital structures were evolved by Molecular Dynamics simulations. In all simulations the destabilization of the bilayer occurred in less than 0.5 ns in favor of hemispherical micelles (figure 6.1). The resulting hemispherical structure remains stable for tens of nanoseconds in our simulations and leaves a fraction of the gold surface in close contact with water. Furthermore, we found that the bilayer are also not stable in solution and break in spherical micelles with some degree of eccentricity.

These observations are in aggreatment with previous Molecular Dynamics simulations that found that the CTAB is adsorbed as a heterogeneous distribution of hemispheric aggregates. [8] Small-angle neutron scattering measurements [14] indicated that gold is covered by a layer of thickness of 3.2 nm. This is smaller than the expected thickness of a bilayer in solution, ca. h = 4 nm as found in our simulations. For this reason the experimental results had been interpreted as consistent with the formation of highly interdigitaded bilayer. However, nowadays the experiments do not have enough sensitivity to rule out a heterogeneous distribution of surfactants on the surface of the nanorods. Therefore, the experimental results could also be consistent with the formation of hemispheric micelles, which have a maximum height of ca. h = 4.5 nm at the top of the aggregate, but then fall below and can produce an average height of h = 3.2 nm that is well consistent with experiments which have suggested that the formation of such structures is fully compatible with growth anisotropy of nanorods [8]. We would also expect that the finite-size effects of the simulation box would promote rather than destabilize uniform structures such as a bilayer. Therefore, we conclude that the enthalpy gain of surfactants on the nanorod surface was insufficent for the entropy loss necessary for the formation of a bilayer. The behavior found in the simulations suggest a very complex chemical equilibrium between adsorbed and free micelles.

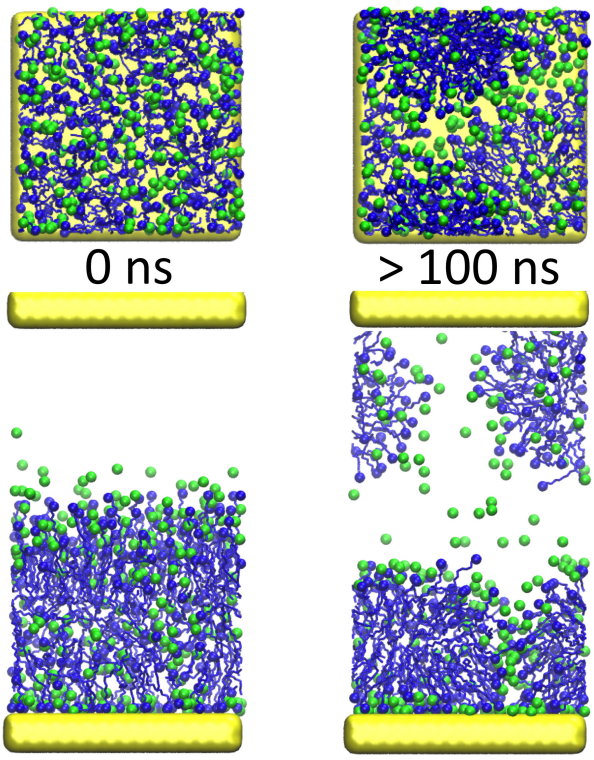

Figure 6.1. Top: top view. Bottom: lateral view. Molecular Dynamics simulations of CTAB bilayers on gold. Preassembled bilayer on a {100} gold surface was subjected to energy minimization and then further allowed to evolve by Molecular Dynamics 100 ns. In all runs, the initial configuration (Left), gets destabilized in less than 500 ps in favor to the formation of hemispherical micelles adsorbed on the both gold surface (Right).

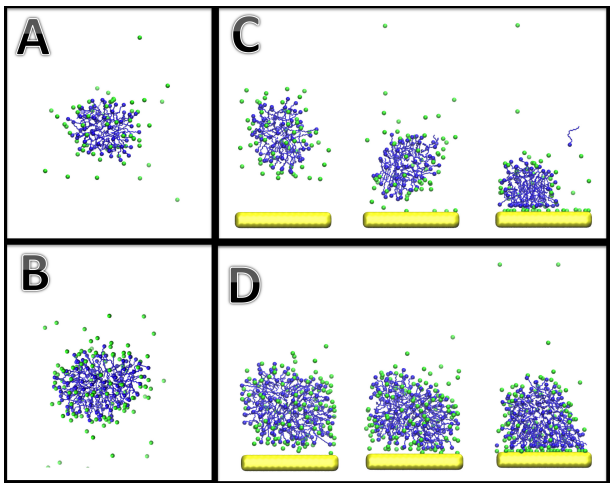

Figure 6.2. Molecular Dynamics simulations of CTAB aggregation and adsorption on gold. Left: Above the cmc, micelles with aggregation numbers 60 (A and C) and 120 (B and D) are spherical and remain stable with life times longer than 100 ns. Right: Free micelles next to the gold substrate evolve spontaneously and strongly adsorb on the gold substrate. At the cmc, micelles with aggregation number 60 (A) retain their quasispherical shape and exhibit partial coverage. At higher surfactant concentrations, the micelles grow significantly in size and cover the gold substrate to a higher extent.

Conclusions

At the cmc and in absence of the gold surface, CTAB aggregates form spherical micelles with approximately 60 molecules. However, the size of the micelles grows steadily as the concentration of surfactant increases. In order to study the adsorption process on the gold surface, we first preassembled free CTAB micelles in solution, with aggregates in the range of 60-120 molecules. The spherical micelles remained stable during very long times (more than 100 ns). The aggregates were more or less spherical, and had an effective positive charge above the surface, loosely neutralized by a cloud of bromide ions. The micelles were placed at a distance of 3, 4 and 5 nm of the substrate and were allowed to evolve, finding in all cases that micelles a slowly approach to the substrate until they are fully adsorbed. At the cmc, micelles with aggregation number 60 retained approximately its spherical shape. On the contrary, micelles with a high number of aggregation also stabilized on the gold substrate but they are no longer spherical and adopt hemispherical shape.

The adsorption of micelles leads to a strong adsorption of Br that neutralizes the charge of the surface of the micelle, but leaves positively charged the part of the micelle in the interface in contact with the water.

We have determined that CTAB aggregates are adsorbed onto gold in the form of micelles. Although bilayer forms are favored due to finite size effects, the repulsions exerted by the surface of the micelle prevent a stable bilayer from forming on gold. We find different water channels depending on the concentration of CTAB. It seems that in the critical micellar concentration of CTAB the optimal conditions have been found in the synthesis method.

- ## Disconnecting Symmetry Breaking from Seeded Growth for the Reproducible Synthesis of High Quality Gold Nanorods

An alternative route from producing nanorods with very small polydispersity and controlled aspect

ratio, consist on adding decanol as a cosurfactant together with CTAB. Our hypothesis is that crystal growth is modulated by the formation of surfactant bilayers on different gold facets. The existence of bilayers in some selected gold facets offer a possible explanation for the anisotropy that may occur in the availability of gold ions that reach the surface of the nanoparticle. In this work, we will try to demonstrate this hypothesis through molecular dynamics simulations. On the other hand, it is very common to use silver salts to selectively control the growth of certain faces of the nanoparticle.

Methods

With the aim of understanding the role of n-decanol on the structure of CTA^+ aggregates and its effect on the nanorod growth, we performed MD simulations of a CTA^+ bilayer deposited on top of a gold surface. The cosurfactant n-decanol was inserted at random positions of the CTAB bilayer. Both amphiphilic molecules were modeled with the GROMOS53–a6 force fields as the starting point. [19] However, the partial charges of CTA^+ and n-decanol were assigned values obtained from the ab initio calculations described in our previous works. [20] Bromide, which acts as the counterion of CTA^+, was described as a Lennard-Jones (LJ) potential with a negative charge at its center. [8] The atoms forming the surface were described with the model developed by Heinz et al. [8] The system was then solvated with single point-charge (SPC) water, adding gold ions in the form of $AuCl_2^+$ and H_3O^+ to neutralize the system. $AuCl_2^+$ was described with the same model used by Mena et al., [21] whereas hydronium was modeled as an LJ center with charges in tetrahedral symmetry. Three positive charges +0.529 were placed one in each hydrogen, and a negative charge (-0.587) at the oxygen atom. The hydronium charges were obtained with the Automated Topology Builder. The O-H bond length was set to 0.0983 nm, and the strength in the bond was constant at 9 831 400 kJ mol^{-1} nm^{-2}. [20] Simulations were performed at varying CTA^+/n-decanol ratios from 0 to 0.5 for 4 different gold surfaces (namely, {100}, {110}, {111}, and {250}). Further details about the simulated systems are provided in Table 6.1.

Simulations were performed with the GROMACS package in the NPT ensemble at 1 bar and 298 K. The temperature was controlled with a velocity-rescale thermostat and the pressure with a Berdensen barostat. [22, 23] Equations of motion were integrated with a time step of 0.003 ps. The relaxation times of the barostat and thermostat were set at 2 ps. The LJ potential as well as the real part of electrostatic interactions were truncated at 1.2 nm. The particle-particle mesh technique was used to deal with electrostatic interactions. [24] Initial preassembled configurations of the CTA^+Br^-/n-decanol bilayers were created using Packmol. [13] The gold surface and the bilayer were placed perpendicular to the z axis. Gold surfaces were placed at the bottom and top of the simulation box. Periodic boundary conditions were applied in the three dimensions of space but leaving 10 nm of vacuum between the two gold surfaces to avoid interactions between neighboring images of the cell. To correct overlaps in the initial configuration, a steep descent minimization was performed until the maximum force converged at 1000 kJ mol^{-1} nm^{-1}. Simulations were extended over rather long times of about 45-425 ns because the diffusion of gold ions through the CTA^+ aggregate to the gold surface is a rather slow process (see Table 6.1). Previous simulations of the assembly of CTAB in the presence of the n-decanol showed that the cosurfactant stabilizes the bilayers over a rather wide n-decanol concentration range.[7] Here, we analyzed the structure of the aggregates as a function of the n-decanol concentration when deposited on top of the gold surfaces by plotting 2D density maps. More details about the systems simulated are provided in Table 6.1) The orientational order of CTA^+ molecules was quantified by evaluating the parameter $S_z = 1/2 < 3\cos\theta^2 - 1 >$, where θ is the angle formed by the head-to-tail vector of each surfactant molecule with the z axis. The availability of gold ions on the gold surfaces was estimated by measuring the distribution of ions as a function of the distance to the surface $P(z)$ along the z axis and calculating the average distribution

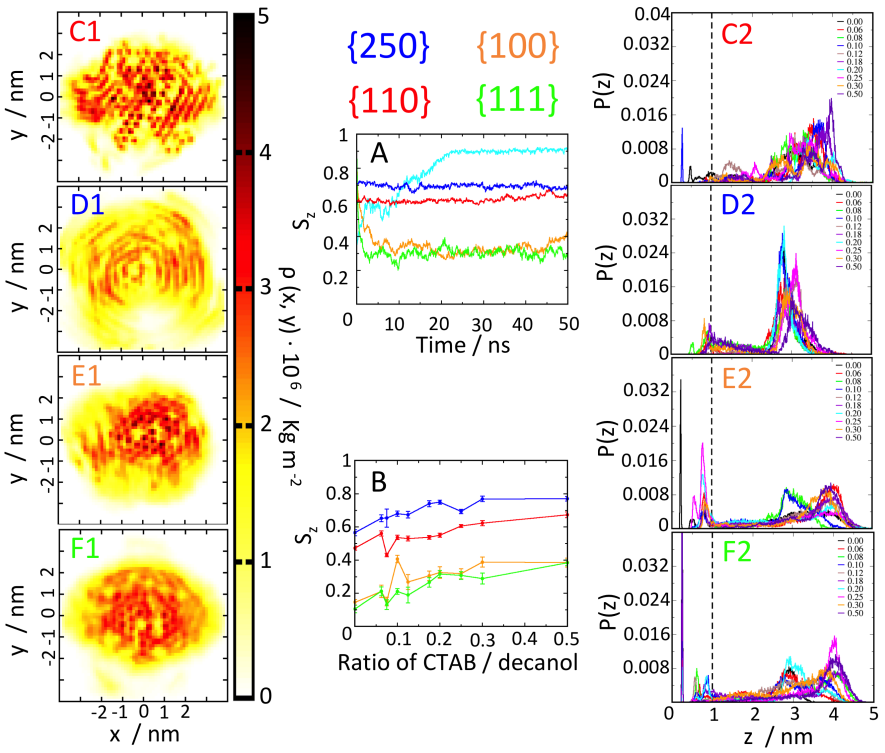

Figure 6.3. Structure of the CTAB-gold interface for different gold facets, as indicated by a color code ({100}, red; {250}, blue; {100}, orange and {111}, green). (A) Time evolution of the bilayer order parameter for different facets at an n-decanol/CTAB ratio of 0.25, compared to that of free bilayers in solution and at an n-decanol/CTAB ratio of 0.20 (cyan line). (B) Bilayer order parameter as a function of n-decanol content for different gold facets. (C1-F1). Center of mass density of CTAB molecules projected on the xy plane. (C2-F2) Probability distribution of gold ions as a function of the distance from the surface, for selected facets at the n-decanol/CTAB ratios indicated in the legend. The dashed black line shows the threshold distance employed in the calculations of $AuCl_2^-$ availability.

Gold crystallographic facet	No. of molecules or atoms			No. of n-decanol molecules	Box dimensions(nm3)	Time (ns)
	water	au	ctab			
{100}	16607	3600	160	0, 10, 12, 16, 20, 28, 32, 40, 48, 80	6.26 x 6.26 x 24.00	300, 207, 130,210, 225, 427, 427, 337, 216, 352
{111}	16607	3024	156	0, 10, 12, 16, 20, 28, 32, 40, 46, 78	6.20 x 6.13 x 24.50	307, 201, 222,220, 190, 197, 202, 102, 135, 172
{110}	16607	3696	156	0, 10, 12, 16, 20, 28, 32, 40, 46, 78	6.49 x 5.84 x 23.00	235, 54, 56, 111, 245, 46, 215, 112, 75, 158
{250}	16952	3780	168	0, 10, 12, 16, 20, 30, 34, 42, 50, 84	7.54 x 6.76 x 26.00	75, 46, 75, 75, 75, 75, 56, 56, 56, 75

Table 6.1. Simulation details. The number of gold ions and protons was 10 in all simulations.

function within a distance of 1 nm from the surface. Given that the silver ions are an shape directing aggent, we study the distribution of silver ions about the gold surface in a similar manner as that for gold ions. We placed 10 silver ions within the simulation box and evolved the system during 150 ns. Simulations were performed for the gold substrate in the presence of surfactant aggregates for systems with either 0 or 0.27 n-decanol/CTA^+ ratios, the latter being close to the optimal ratio for high quality gold nanorod synthesis. The interaction of Ag^+ was modeled using a Lennard-Jones potential center (ϵ=0.4518742 kJ/mol, σ=0.2261 nm) with a unit +e point charge,[25] and bromide as counterions.

Results

Now, we discuss the structure of adsorbed CTAB aggregates, as determined from computer simulations. CTAB forms micelles in aqueous solution, but such micellar aggregates are transformed into ordered bilayers upon addition of n-decanol.[7] At an n-decanol/CTAB ratio of 0.20, the bilayer is stable, with the order parameter remaining constant and close to unity over most of the simulation time (Figure 6.3A, cyan line). A similar order is obtained upon adsorption of micellar aggregates on the gold surface, as reflected by the time evolution of the order parameter shown in Figure 6.3A. The average ordering of the bilayers steadily increases with the n-decanol/CTAB ratio, but the {100} and {111} facets consistently exhibit less order than the {110} and {250} facets (Figure 6.3B). The degree of order correlates to the degree of compaction of the bilayer and surface coverage. To show this, we calculated the density of CTAB carbon atoms relative to the center of mass of the aggregate. Projections of density maps on the xy plane are shown in Figure 6.3C1–F1. Facets {100} and {111}, with a small order parameter, form compact hemispherical micelles that partially cover the gold surface, while facets {110} and {250}, with a large order parameter, afford aggregates that span most of the solid surface. Particularly, we found bilayers fully assembled on the {250} facets, exhibiting almost complete coverage of the gold surface. The structure of adsorbed aggregates determines the distribution of gold ions and their surface availability for the reaction. This can be illustrated by plotting the probability of finding gold ions as a function of the distance to the gold surface (Figure 6.3C2–F2) and its integration up to a threshold distance of 1 nm away to the substrate (Figure 6.4D). Quite generally, gold ions have great tendency to concentrate around trimethylammonium cations avoiding the hydrocarbon tails. For {100} and {111} facets, where aggregates exhibit hemispherical shape, the ions bound to the external surface of the bilayer can easily reach the uncovered surface and are available to undergo reduction and deposition on the surface. For {110} and {250} facets, on the contrary, the gold surface is largely covered, CTAB molecules are ordered vertically, and gold ions can only reach the gold surface via slow and unlikely diffusion across the hydrocarbon region of the aggregates. Particularly, for {250} facets, where the surface is fully covered, the probability of encountering gold ions on the substrate is very rare.

When CTAB forms micelles, e.g., on {100}–type and {111}–type facets, gold ions can readily access the gold surface from solution by diffusion on the micelle surface (Figure 6.4A). On the contrary, when a rigid bilayer is formed on the particle surface, gold ions would be required to cross such a n-decanol/CTAB bilayer to reach the gold surface, but this effect was not observed in the time scale

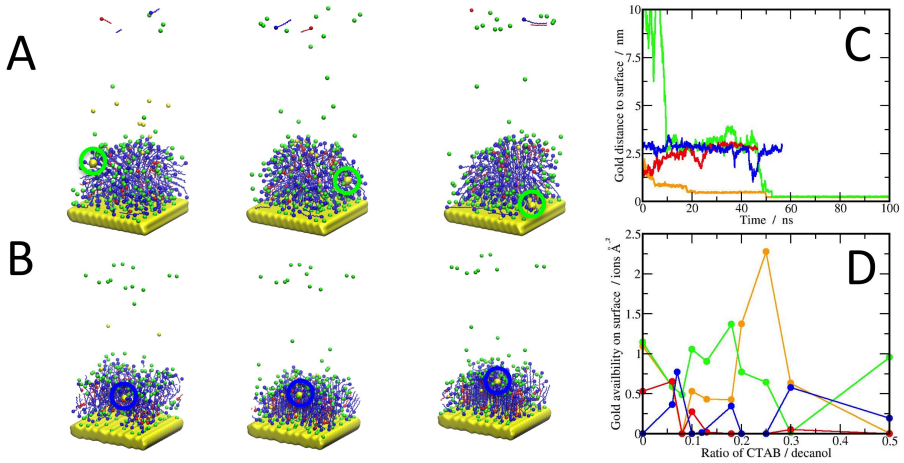

Figure 6.4. Role of n-decanol in the synthesis of small anisotropic seeds. (A, B) Mechanism of diffusion of $AuCl_2^-$ anions in the presence of n- decanol/CTAB aggregates (green and blue circles depict the trajectory of gold ions at different times of the simulation). (A) On {111} surfaces, the micelles cover the surface heterogeneously and the diffusion of gold ions toward the gold surface is facilitated. (B) On {250} surfaces, the surfactants form bilayers with homogeneous coverage, hindering the diffusion of gold ions toward the surface. Gold ions are shown as red spheres, bromide ions as green spheres, surfactant chains as blue lines, n-decanol in orange, and gold surfaces in pink. (C) Distance of gold ions to the gold surface for selected trajectories: orange ({100} facets) and green ({111} facets) lines show the trajectories corresponding to the mechanism in (A), while red ({110} facets) and light blue ({250} facets) lines show the typical diffusion expected for the mechanism shown in panel B. (D) Probability of finding gold ions at a distance smaller than 1 nm from the gold surface for the different facets: 100 (orange), {111} (green), {110} (red), and {250} (blue).

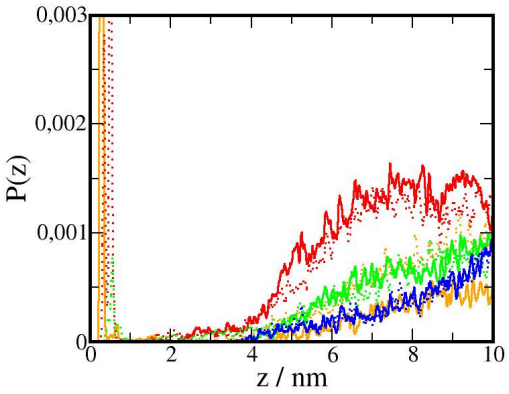

Figure 6.5. Probability distribution function of silver ions as a function of the distance to the gold surface for {100} (orange), {110} (red), {111} (green) and {250} (blue) facets. Results are shown for decanol/CTA^+ ratios of 0 (dotted lines) and 0.25 (solid lines).

of our simulations. Instead, gold ions diffused along the surface of the bilayer, still exposed to the solution (6.4B). We quantified these different behaviors by measuring the separation distance of gold ions to the surface (Figure 6.4C). We found that whereas gold ions were able to reach the gold surface in the presence of micelles, they fluctuated and moved along the bilayer interface when more compact aggregates were present. Upon close observation, one can see that gold ions can also penetrate the aggregates in this instance, but they are swiftly expelled out again. We additionally calculated the probability of finding gold ions at a threshold distance of 1 nm from the surface (Figure 6.4D). The availability of gold ions exhibits a maximum for {100} facets at n-decanol/CTAB ratios between 0.20 and 0.30, in agreement with the concentrations at which the experiments showed growth of more uniform small AuNRs. The availability of gold ions on the {111} surfaces is also significant for n-decanol/CTAB ratios in the range of 0.10–0.30, although much lower than on {100} surfaces. On the contrary, the availability of gold ions on {110} and {250} facets is very low for all the studied n-decanol percentages. Computer simulations thus support a significant influence of n-decanol to enhance the selective CTAB passivation of high-index facets.

The simulation results suggest a small and nonselective adsorption of silver, with random adsorption events found only for {110} and {111} facets in the absence of decanol, and for {100} facets in the case of 0.25 n-decanol/CTA^+ ratio. The results suggest an extremely small permeability of CTAB aggregates to silver, as indicated by the large depletion of silver density in the range between 0 and 4 nm, loosely corresponding to the aggregate is width (see Figure 6.5). For larger distances, the density of silver ions gradually increases, but does not attain an asymptotic density until about 10 nm away from the gold substrate. Whence, a small permeability of silver within the CTA^+ aggregate, together with a slow neutralization of the CTA^+ by the diffusive counterion cloud conspires against the adsorption of silver cations, keeping them away from the gold substrate due to electrostatic repulsion. Apparently, only random and nonselective adsorption events occur rarely, with a somewhat higher probability on facets with more loosely packed aggregates.

Conclusions

In summary, in our molecular dynamics simulations we have found great selectivity depending on the gold face in the morphologies of CTAB aggregates. This fact reflects in the anisotropy of the diffusion of gold ions. On the contrary, there is no selectivity in the availability of silver ions as a

function of the face. The mechanism we propose is justified on the basis of the morphology of the aggregates. Through the order parameter S_z, we find absorbed higly ordered bilayers in the {250} and {110} faces and hemiesferic micelles in the {100} and {111} gold faces. This structural change modifies the growth habit of the nanoparticle through the diffusive process of ions. Therefore that the formation of surfactant bilayers on certain surfaces allows the control of gold ion diffusion and thus of the growth process of nanoparticles.

Because the presence of silver ions is pivotal for the symmetry breaking event to occur, we also studied the role of n-decanol/CTAB aggregates in the avaibility of silver ions on different gold facets. Therefore, in the presence of n-decanol (and silver ions), symmetry breaking in the crystalline gold seed is more efficient. We found that diffusion of silver ions through the n-decanol/ CTAB aggregates is not favored, and the differences between different facets are negligible small anisotropic seeds are systematically obtained with high yields. This result might indicate that the effect of n-decanol is mainly related to changes in the diffusion of gold ions but hardly affecting Ag^+ diffusion.

Bibliography

[1] G. González-Rubio, P. Díaz-Núñez, A. Rivera, A. Prada, G. Tardajos, J. González-Izquierdo, L. Bañares, P. Llombart, L. G. MacDowell, M. Alcolea-Palafox, L. M. Liz-Marzán, O. Peña-Rodríguez, and A. Guerrero-Martínez, "Femtosecond laser reshaping yields gold nanorods with ultranarrow surface plasmon resonances," *Science*, vol. 358, pp. 640–644, 2017.

[2] G. González-Rubio, V. Kumar, P. Llombart, P. Díaz-Núñez, E. Bladt, T. Altantzis, S. Bals, O. Peña-Rodríguez, E. G. Noya, L. G. MacDowell, A. Guerrero-Martínez, and L. M. Liz-Marzán, "Disconnecting symmetry breaking from seeded growth for reproducible synthesis of high quality gold nanorods," *ACS Nano*, vol. submitted, 2018.

[3] V. Myroshnychenko, J. RodrÃguez-FernÃ¡ndez, I. Pastoriza-Santos, A. M. Funston, C. Novo, P. Mulvaney, L. M. Liz-MarzÃ¡n, and F. J. GarcÃa de Abajo, "Modelling the optical response of gold nanoparticles," *Chem. Soc. Rev.*, vol. 37, pp. 1792–1805, 2008.

[4] S. K. Ghosh and T. Pal, "Interparticle coupling effect on the surface plasmon resonance of gold nanoparticles From theory to applications," *Chemical Reviews*, vol. 107, no. 11, pp. 4797–4862, 2007. PMID: 17999554.

[5] L. Scarabelli, A. Sánchez-Iglesias, J. Pérez-Juste, and L. M. Liz-Marzán, "A "tips and tricks" practical guide to the synthesis of gold nanorods," *The Journal of Physical Chemistry Letters*, vol. 6, no. 21, pp. 4270–4279, 2015. PMID: 26538043.

[6] J. Gao, C. M. Bender, and C. J. Murphy, "Dependence of the gold nanorod aspect ratio on the nature of the directing surfactant in aqueous solution," *Langmuir*, vol. 19, no. 21, pp. 9065–9070, 2003.

[7] P. Llombart, L. G. MacDowell, and N. E. G., "Submitted," *Colloids and Surface A*, vol. 0, no. 0, p. null, 0. PMID: 30939242.

[8] S. K. Meena and M. Sulpizi, "From gold nanoseeds to nanorods: The microscopic origin of the anisotropic growth," *Angew. Chemie. Int. Ed.*, vol. 55, pp. 11960–11964, 2016.

[9] S. Pal, B. Bagchi, and S. Balasubramanian, "Hydration layer of a cationic micelle, c10tab: Structure, rigidity, slow reorientation, hydrogen bond lifetime, and solvation dynamics," *The Journal of Physical Chemistry B*, vol. 109, no. 26, pp. 12879–12890, 2005. PMID: 16852599.

[10] M. Tarek, D. J. Tobias, and M. L. Klein, "Molecular dynamics simulation of tetradecyltrimethylammonium bromide monolayers at the air/water interface," *The Journal of Physical Chemistry*, vol. 99, no. 5, pp. 1393–1402, 1995.

[11] J. Carpenter and F. Weinhold, "Analysis of the geometry of the hydroxymethyl radical by the "different hybrids for different spins" natural bond orbital procedure," *Journal of Molecular Structure: THEOCHEM*, vol. 169, pp. 41 – 62, 1988.

[12] M. Pisárčik, F. Devínsky, and M. Pupák, "Determination of micelle aggregation numbers of alkyltrimethylammonium bromide and sodium dodecyl sulfate surfactants using time-resolved fluorescence quenching," *Open Chem.*, vol. 13, pp. 922–931, 2015.

[13] L. Martínez, R. Andrade, E. G. Birgin, and J. M. Martínez, "Packmol: A package for building initial configurations for molecular dynamics simulations," *J. Comp. Chem.*, vol. 30, pp. 2157–2164, 2009.

[14] S. Gómez-Graña, F. Hubert, F. Testard, A. Guerrero-Martínez, I. Grillo, L. M. Liz-Marzán, and O. Spalla, "Surfactant bilayers on gold nanorods," *Langmuir*, vol. 28, pp. 1453–1459, 2012.

[15] S. Pronk, S. Páll, R. Schulz, P. Larsson, P. Bjelkmar, R. Apostolov, M. R. Shirts, J. C. Smith, P. M. Kasson, D. van der Spoel, B. Hess, and E. Lindahl, "GROMACS 4.5: a high-throughput and highly parallel open source molecular simulation toolkit," *Bioinformatics*, vol. 29, pp. 845–854, 02 2013.

[16] M. J. Walsh, W. Tong, H. Katz-Boon, P. Mulvaney, J. Etheridge, and A. M. Funston, "A mechanism for symmetry breaking and shape control in single-crystal gold nanorods," *Accounts of Chemical Research*, vol. 50, no. 12, pp. 2925–2935, 2017. PMID: 29144733.

[17] B. Goris, S. Bals, W. Van den Broek, E. CarbóArgibay, S. Gómez-Graña, L. M. LizMarzán, and G. Van Tendeloo, "Atomic-scale determination of surface facets in gold nanorods," *Nature Materials*, vol. 11, 2012.

[18] E. Carbó-Argibay, B. Rodríguez-González, S. Gómez-Graña, A. Guerrero-Martínez, I. Pastoriza-Santos, J. Pérez-Juste, and L. M. Liz-Marzán, "The crystalline structure of gold nanorods revisited: Evidence for higher-index lateral facets," *Angewandte Chemie International Edition*, vol. 49, no. 49, pp. 9397–9400, 2010.

[19] C. Oostenbrick, A. Villa, A. E. Mark, and W. F. van Gunsteren, "A biomolecular force field based on the free enthalpy of hydration and solvation: the gromos force-field parameter sets 53a5 and 53a6," *J. Comp. Chem.*, vol. 25, pp. 1656–1676, 2004.

[20] A. K. Malde, L. Zuo, M. Breeze, M. Stroet, D. Poger, P. C. Nair, C. Oostenbrink, and A. E. Mark, "An automated force field topology builder (atb) and repository: Version 1.0," *Journal of Chemical Theory and Computation*, vol. 7, no. 12, pp. 4026–4037, 2011. PMID: 26598349.

[21] S. K. Meena and M. Sulpizi, "Understanding the microscopic origin of gold nanoparticle anisotropic growth from molecular dynamics simulations," *Langmuir*, vol. 9, p. 14954, 2013.

[22] H. J. C. Berendsen, J. R. Grigera, and T. P. Straatsma, "The missing term in effective pair potentials," *The Journal of Physical Chemistry*, vol. 91, no. 24, pp. 6269–6271, 1987.

[23] G. Bussi, D. Donadio, and M. Parrinello, "Canonical sampling through velocity rescaling," *J. Chem. Phys.*, vol. 126, p. 014101, 2007.

[24] T. Darden, D. York, and L. Pedersen, "Particle mesh ewald: An n log(n) method for ewald sums in large systems," *The Journal of Chemical Physics*, vol. 98, no. 12, pp. 10089–10092, 1993.

[25] P. Zarzycki, S. Kerisit, and K. M. Rosso, "Molecular dynamics study of the electrical double layer at silver chloride electrolyte interfaces," *The Journal of Physical Chemistry C*, vol. 114, no. 19, pp. 8905–8916, 2010.

Part III

Conclusiones

Conclusiones

A lo largo de estos últimos tres años el candidato ha centrado su investigación en el análisis de interfases sólidas complejas para relacionar las propiedades interfaciales con los hábitos de crecimiento de los cristales. Debido a su interés científico y tecnológico, en esta tesis se han estudiado los hábitos de crecimiento cristalino en los copos de nieve y nanopartículas de oro.

Ambos sistemas tienen un punto en común: la compleja estructura de la interfase y la presencia de una capa de adsorción de espesor nanométrico de la que dependen en buena medida las propiedades de la interfase y que solo pueden ser bien caracterizadas por simulación molecular.

El primer bloque de esta tesis se centra en el estudio de la interfase hielo-vapor con la finalidad de caracterizar las propiedades de la película líquida que se forma sobre la superficie del hielo a temperaturas inferiores a la temperatura de fusión. La mayor parte de nuestro estudio se realizó con el modelo de agua TIP4P/Ice. Este modelo junto al TIP4P/2005 son dos de los modelos rígidos y no polarizables que reproducen un mayor número de propiedades del agua pero, con la ventaja de que el modelo TIP4P/Ice presenta la temperatura de fusión similar al experimental.

Dado que la mayoría de las medidas experimentales se realizan en una atmósfera controlada de nitrógeno, en nuestro primer estudio nos centramos en la caracterización estructural de la interfase hielo-vapor en función de la presión. La adsorción de nitrógeno en la capa líquida no es lo suficientemente intensa y las tasas de crecimiento disminuyen exclusivamente por la reducción del número de moléculas de agua que impactan contra la superficie del hielo.

Nuestras simulaciones muestran que el nitrógeno no tiene un efecto estructural en la interfase y desempeña un papel pasivo. Estas simulaciones nos han permitido relacionar las diferencias en las tasas de crecimiento cristalino medidas en una atmósfera controlada de gas nitrógeno.

Encontramos que cerca del punto triple la fina capa de líquido adsorbido sobre el hielo en la cara prismática principal se comporta como dos superficies independientes de hielo-agua y agua-vapor a pequeñas longitudes de onda (igual que en lascinterfases volumétricas), pero se vuelve suave a longitudes de onda largas. Por otra parte, los espectros de fluctuaciones obtenidos para la cara prismática principal en función de la temperatura muestran un escenario compatible con la transición de rugosidad entorno a 248 K (-2 K con respecto al punto de fusión del modelo de agua TIP4P/2005).

A continuación realizamos el estudio para un intervalo de temperaturas más amplio. En esta ocasión utilizamos el modelo TIP4P/Ice que nos permite simular el sólido a temperaturas más próximas al punto triple experimental del agua.

La superficie del hielo experimenta varias transiciones de fase superficiales, como son: i) una transición de pre-rugosidad (Ordered Flat $\rightarrow$ Disordered Flat) a 225 K para la cara basal y a 215 K para la cara prismática principal, ii) una transción de suavizado (Disordered Flat $\rightarrow$ Reconstructed Flat) a 245 K en la cara basal y 255 K en la prismática principal. En este modelo de agua no hay un escenario compatible cuando el parametro de rugosidad se anula y por tanto no encontramos la transición de rugosidad.

El empleo de hamiltonianos de ondas capilares y de Gordon acoplados permite ajustar los datos

obtenidos en las simulaciones a un modelo teórico y obtener los parámetros termodinámicos que determinan si una superficie es suave o rugosa. Del ajuste al modelo podemos extrar la rigidez interfacial, la tensión superficial y la energía libre de escalón.

El comportamiento no monótono observado para la energía libre de escalón se asemeja al comportamiento cualitativo medido experimentalmente en el crecimiento de los copos de nieve.

Para la película líquida que hay adsorbida sobre la superficie del hielo, encontramos 2 transiciones de estratificación continuas sin presencia de singularidades, en las que espesor de la misma aumenta progresivamente de 1 a 2 capas, alrededor de 235 K, y de 2 a 3 capas moleculares de líquido, alrededor de 257 K.

La separación en microfases de los parches de agua sobre la superficie del hielo es perfectamente compatible con la presencia de transiciones continuas a través de una línea de Fisher-Widom asociada a la prolongación de la línea de transiciones de estratificación más alla del punto crítico.

Nuestros resultados proporcionan una explicación para el hábito cristalino observado en los copos de nieve y allanan el camino para una primera descripción de los principios del crecimiento de los cristales de hielo y las tasas de sublimación en la atmósfera.

En el segundo bloque de este tesis nos hemos centrado en el estudio de la interfase oro-CTAB-agua, con el fin de entender cual es el papel de los agregados del surfactante CTAB en el crecimiento cristalino de las distintas caras del oro.

Con el fin de comprobar la validez de los modelos utilizados y entender el ensamblado de los agregados de CTAB con y sin cosurfactante hemos investigado mediante simulación molecular la estabilidad y estructura de los agregados de CTAB con y sin el cosurfactante decanol en agua pura. En ausencia de decanol, las micelas permanecen estables. De acuerdo con las evidencias experimentales, encontramos una transición estructural de formas esféricas a formas elipsoidales.

El aumento de la fuerza iónica en la disolución determina el cambio de morfología del agregado que pasa de micela a cilindro. Las bicapas de CTAB son inestables cuando no se emplea decanol como cosurfactante.

Cuando se ensamblan junto con el decanol, las bicapas permanecen estables y altamente ordenadas para fracciones intermedias DeOH/CTAB, $0.13 \leq \text{DeOH/CTAB} \leq 0.225$, transformándose en agregados con forma de gusano o cilindros para fracciones inferiores y superiores de DeOH/CTAB, respectivamente.

En agregados adsorbidos sobre las diferentes superficies de oro que exponen diferentes caras atómicas, y sin cosurfactante, encontramos la formación de agregados esféricos o hemiesféricos a medida que aumenta la concentración de surfactante.

En presecia de decanol, el agregado puede disponerse sobre la superficie de las caras cristalográficas estudiadas de dos formas dependiendo en que cara del oro se encuentre: i) Sobre los planos cristalográficos {100} y {111} el agregado se adsorbe en con forma de gota hemiesférica. ii) Sobre los planos {110} y {250} el agregado se encuentra adsorbido en forma de bicapa.

A pesar de que las formas de bicapa se favorezcan debido a efectos de tamaño finito, las repulsiones que ejerce la superficie de la micela impiden que sin decanol se pueda formar una bicapa estable sobre el oro.

La estabilización de las bicapas requiere que la textura de la superficie del oro sea escalonada. Además, la naturaleza ordenada de esta bicapa y la disposición en una red triangular de las cabezas de CTA^+ controla la adsorción selectiva de iones oro sobre determinadas superficies de una nanopartícula de oro.

El decanol aparece como un cosurfactante ideal en la síntesis de nanovarillas de oro, donde se pueden utilizar las variaciones de DeOH/CTAB para ajustar la forma de los agregados de la solución de equilibrio y, por tanto, ajustar la cobertura de agregados adsorbidos en la superficie para mejorar los resultados en

la síntesis de nanovarillas monodispersas con una relación de aspecto controlada.